Exploring the Frontiers of Photoemission Orbital Tomography

Christian Simon Kern

A thesis submitted in partial fulfillment
of the requirements for the degree
Doctor rerum naturalium

Insitute of Physics
University of Graz

Supervisor: Dr. Peter Puschnig

September 2023

Abstract

The technique of angular-resolved photoemission spectroscopy is especially suited to access the quantum mechanical properties of molecules and crystalline surfaces. Within photoemission orbital tomography, we can unambiguously interpret the photoelectron angular distribution as the momentum space signatures of quantum mechanical wave functions. This interpretation relies on certain assumptions for the theoretical modelling of the photoemission process, where especially the assumption of a plane wave as the final state of the liberated photoelectron should be emphasized. This work contains a collection of five publications about applications and extensions of photoemission orbital tomography viewed from a theoretical perspective.

The application of photoemission orbital tomography requires electronic structure calculations, that are, in most cases, only possible within density functional theory, which is due to the large number of degrees of freedom in the considered systems. The necessary approximations in this method lead to an underestimation of long-range electron correlation; this correlation, however, plays an important role for the adsorption of molecules on surfaces, since the resulting van der Waals forces often make a considerable contribution to the binding energy. In three publications that are part of this thesis, it is shown that the correct description of these van der Waals forces poses a serious challenge, especially for the adsorption of organic molecules on the interface between magnesium oxide and Ag(100). On this surface, we specifically examine self-metalation of the porphyrin molecules tetraphenylporphyrin and porphin, and, in addition, observe large structural changes in the organic semiconductor perylenetetracarboxylic dianhydride. For the latter case, the comparison between theory and experiment demonstrates that here, photoemission orbital tomography can serve as precise instrument to quantitatively determine changes in the molecular structure.

When varying the photon energy in angular-resolved photoemission spectroscopy, the dependence of the photocurrent with respect to the photoelectron's momentum component perpendicular to the surface can be measured. From these data, it is possible to gain additional insight into scattering effects in the photoemission process, as well as into the interaction between the photoelectron and the surface. For graphene, an atomically thin two-dimensional modification of carbon, a comparison between theory and experiment reveals that the observed modulations in the photoemission intensity cannot be explained within the plane wave final state assumption. However, in a fourth publication it is demonstrated that the experimental findings can be accounted for by a more direct method, namely the simulation of photoemission spectroscopy within time-dependent density functional theory. Moreover, additional insight is gained when extending the plane wave model to scattered waves, which incorporates scattering effects from different angular momentum channels, as well as from neighboring atoms in the graphene lattice. Within the photoemission orbital tomography interpretation of photoemission data and the help of this understanding, it is now possible to remove artefacts in the experimental data—which result from the photoemission process itself—from the underlying material properties.

In a fifth publication, we extend the applicability of photoemission orbital tomography to a special class of excited states. Optical excitations in semiconductors and isolators below the band gap lead to bound electron-hole pairs, the so-called excitons. Since these quasi-particles are described as correlated wave functions, their treatment within the formalism of photoemission orbital tomography has not been possible before. With the extension to such systems, new consequences for the photoemission from these states arise. Depending on the configuration of the hole state, here our theoretical results predict exciton signatures at different kinetic energies and the electronic part of the exciton demands a coherent sum over the unoccupied single-particle orbitals for each of those momentum space patterns.

Kurzzusammenfassung

Um quantenmechanische Zustände von Molekülen oder Kristalloberflächen sichtbar zu machen, eignet sich vor allem die Technik der winkelaufgelösten Photoemissionsspektroskopie. Die so gewonnen, experimentellen Daten können innerhalb der Photoemissionsorbitaltomographie als eindeutige Signaturen von Wellenfunktionen im Impulsraum interpretiert werden. Diese Interpretation beruht auf bestimmten Annahmen in der theoretischen Modellierung des Photoemissionsprozesses, wobei insbesondere die Verwendung von ebenen Wellen als Endzustand des freien Photoelektrons hervorzuheben ist. Diese Arbeit beinhaltet eine Sammlung von fünf Veröffentlichungen die sich—aus theoretischer Sicht—mit Anwendungen und Erweiterungen der Photoemissionsorbitaltomographie beschäftigen.

Für die Anwendung der Photoemissionsorbitaltomographie wird eine Simulation der elektronischen Struktur benötigt, was auf Grund der großen Anzahl von Freiheitsgraden in den betrachteten Systemen zumeist nur mit Dichtefunktionaltheorie möglich ist. In dieser Methode führen die notwendingen Näherungen dazu, dass langreichweitige Korrelationen von Elektronen unterschätzt werden; diese Korrelationen spielen jedoch für die Adsorption von Molekülen auf Oberflächen eine entscheidende Rolle, da die daraus resultierenden van der Waals Kräfte oft maßgeblich zur Bindung beitragen. In drei Arbeiten, die Teil dieser Dissertation sind, konnte gezeigt werden, dass insbesondere die Adsorption von organischen Molekülen auf der Grenzschicht von Magnesiumoxid und Ag(100) eine besondere Herausforderung für die korrekte Beschreibung der van der Waals Kräfte darstellt. Konkret wurde dabei auf dieser Oberfläche die Selbstmetallierung der beiden Porphyrinmoleküle Tetraphenylporphyrin und Porphin untersucht, sowie eine besonders große strukturelle Veränderung des organischen Halbleiters Perylentetracarbonsäuredianhydrid beobachtet. In letzterem Fall wurde durch den Vergleich von Theorie mit Experiment deutlich, dass die Photoemissionsorbitaltomographie hier ein sehr genaues Instrument zur quantitativen Bestimmung von Veränderung der molekularen Struktur darstellt.

Wird innerhalb der Photoemissionsspektroskopie zusätzlich noch die Photonenenergie variiert, kann dadurch auch die Abhängigkeit des Photostroms von der Impulskomponente des Photoelektrons orthogonal zur Substratoberfläche vermessen werden. Diese Daten liefern zusätzliche Erkenntnisse über Streuprozesse im Photoemissionsprozess sowie der Wechselwirkung des Photoelektrons mit der Oberfläche. Für Graphen, eine zweidimensionale Modifikation des Kohlenstoffs, konnte anhand des Vergleichs experimenteller Daten mit theoretischen Simulationen in einer vierten Arbeit gezeigt werden, dass hier die Annahme einer ebenen Welle als Endzustand nicht mehr ausreicht, um die beobachteten Modulationen in der Photoelektronenintensität zu erklären. Die experimentellen Daten konnten jedoch mit einer direkteren Methode zur Simulation von Photoemissionsspektroskopie mittels zeitabhängiger Dichtefunktionaltheorie sehr gut reproduziert werden. Dies gelang auch anhand einer Erweiterung des ebenen Wellen Modells auf Streueffekte zwischen unterschiedlichen Drehimpulskanälen sowie zwischen Nachbaratomen im Graphen Gitter. Mit diesem Verständnis ist es möglich, bei der Inter-

pretation von Photoemissionsdaten mittels Photoemissionsorbitaltomographie nun Artefakte des Experiments, die sich aus dem Photoemissionsprozess ergeben, von wirklichen Materialeigenschaften zu trennen.

In der fünften Arbeit wurde die Anwendbarkeit der Photoemissionsorbitaltomographie auf spezielle angeregte Zustände erweitert. Optische Anregungen in Halbleitern oder Isolatoren unterhalb der Bandlücke führen zu gebundenen Elektron-Loch Paaren, den so gennanten Exzitonen. Diese Quasiteilchen müssen als korrelierte Wellenfunktionen beschrieben werden und konnten daher bisher nicht im Formalismus der Photoemissionsorbitaltomographie behandelt werden. Durch die Erweiterung auf solche Systeme ergeben sich einige neue Konsequenzen für die Photoemission aus solchen Zuständen. Dabei lassen sich—je nach Konfiguration des Loch-Zustands—Signaturen eines Exzitons bei verschiedenen kinetischen Energien beobachten und der Elektronenanteil der Exziton-Wellenfunktion führt dazu, dass jede dieser Impulsraumsignaturen mit einer kohärenten Summe über die unbesetzten Einteilchenzutände gebildet werden muss.

Acknowledgements

This work would not have been possible without the collaboration of many people that I want to thank for their help and their inspiration. My sincerest gratitude goes to Peter Puschnig for his guidance and motivation and also for giving me the freedom to explore different paths. The atmosphere in his group was always delightful and I want to thank my colleagues Andreas Windischbacher, Daniel Lüftner, Mathias Schwendt, Dominik Brandstetter, Nina Kainbacher, Siegfried Kaidisch and Melvin Hodzic for all our discussions and their contributions to my progress.

I am also greatly indebted to Mike Ramsey and Martin Sterrer for their insights into photoemission, surface science and beyond, as well as for our fruitful collaboration, including the great experimental work by Philipp Hurdax, Francesco Presel, Thomas Boné, Georg Koller, Larissa Egger, Florian Schwarz and Max Niederreiter.

In a steady alliance over the last years, the cooperation with Stefan Tautz, Sergey Subach, Anja Haags, François Bocquet and Xiaosheng Yang from *Forschungszentrum Jülich* and Hans Kirschner, Alexander Gottwald and Mathias Richter from the *Physikalisch-Technische Bundesanstalt Berlin* has lead to significant progress in photoemission orbital tomography and I am grateful to be a part of this team and have always enjoyed our discussions. This also includes the work with Simon Moser, with his persistence and his fresh view on the theory of photoemission.

Furthermore, I want to thank Umberto De Giovannini, Shunsuke Sato and Angel Rubio for sharing their knowledge about TDDFT and for their hospitality at the *Max-Planck-Institut Hamburg*.

With their excitement about excited states, I have also learned a lot from a more recent experimental collaboration with Matthijs Jansen, Wiebke Bennecke, Marcel Reutzel and Stefan Mathias in Göttingen.

I am sincerely grateful to Oliver Hofmann for agreeing to refereeing my thesis on a rather tight schedule.

Computational physics is a lot less fun without working hard- and software and the great IT support by David Schafzahl and Christoph Ruthofer should not be left unmentioned, as well as the enormous help with basically all other university-related problems, that came from Dani Gaar, Eva Holler-Merschnik, Bianca Reicher and Eveline Monschein, who sadly passed away in June 2023.

Finally, I want to thank my friends and my family for their support and for the things in life beyond physics, and especially Sara and Bronágh for being the most beautiful distraction.

There is a crack in everything
That's how the light gets in
L. Cohen

Contents

1 Introduction **1**

2 Methods **5**
2.1 Density Functional Theory . . . 5
2.1.1 Foundations . . . 5
2.1.2 Approximations for Exchange- and Correlation Effects . . . 8
2.1.3 Dispersive Interaction Corrections . . . 11
2.2 Time-dependent Density Functional Theory . . . 15
2.2.1 The Runge-Gross Theorem . . . 15
2.2.2 The van Leeuwen Theorem . . . 17
2.2.3 The Time-dependent Kohn-Sham Scheme . . . 19
2.2.4 The Adiabatic Local Density Approximation . . . 20
2.2.5 Light-matter Interaction and Dipole Moments . . . 21
2.2.6 Optical Excitations from Real-time TDDFT . . . 23
2.2.7 Optical Excitations from Linear Response TDDFT . . . 24
2.3 Simulation of Photoelectron Spectroscopy . . . 28
2.3.1 The Photoemission Experiment . . . 28
2.3.2 Theory of Photoemission – Preliminaries . . . 30
2.3.3 The Plane Wave Final State . . . 33
2.3.4 Simulation of Photoemission from Excitons . . . 35
2.3.5 The Scattered Wave Final State . . . 37
2.3.6 Simulation of Photoemission with Real-Time TDDFT . . . 40

3 Charge-promoted Self-metalation of Porphyrins on an Oxide Surface **45**
3.1 Main Text . . . 46
3.2 Supporting Information . . . 53
3.2.1 Experimental Details . . . 53
3.2.2 Computational details . . . 54
3.2.3 Work function tuning and influence of defects . . . 54
3.2.4 Results of additional experiments . . . 55
3.2.5 Computational results . . . 57

4 Charge and Adsorption Height Dependence of the Self-metalation of Porphyrins on Ultrathin MgO(001) Films **63**
4.1 Introduction . . . 64
4.2 Methods . . . 66
4.2.1 Experimental . . . 66
4.2.2 Theoretical . . . 67

4.3 Results and Discussion . . . 67
4.4 Conclusions . . . 72
4.5 Supporting Information . . . 73

5 Large Distortion of Fused Aromatics on Dielectric Interlayers Quantified by Photoemission Orbital Tomography 77
5.1 Introduction . . . 79
5.2 Results and Discussion . . . 80
5.3 Conclusions . . . 86
5.4 Methods . . . 86
5.5 Supporting Information . . . 87

6 Simple Extension of the Plane Wave Final State in Photoemission: Bringing Understanding to the Photon-energy Dependence of Two-dimensional Materials 93
6.1 Introduction. . . . 95
6.2 Results . . . 96
6.3 Conclusion . . . 103
6.4 Appendix . . . 103
6.4.1 Sample Preparation . . . 103
6.4.2 Photoemission Experiments . . . 104
6.4.3 Photoemission Differential Cross Section . . . 105
6.4.4 Photoemission Initial State . . . 106
6.4.5 TDDFT Calculations . . . 107
6.4.6 Photoemission Final State . . . 108

7 Photoemission Orbital Tomography for Excitons in Organic Molecules 117
7.1 Introduction . . . 118
7.2 Theory . . . 119
7.2.1 Photoemission from Excitons . . . 119
7.2.2 Formulation with Natural Transition Orbitals . . . 121
7.2.3 Generic Exciton Structures . . . 122
7.3 Results and Discussion . . . 125
7.4 Conclusions . . . 128
7.5 Appendix . . . 128
7.5.1 Ground state and linear response calculations . . . 128
7.5.2 Real-time TDDFT calculations . . . 130
7.5.3 Complementing results . . . 132

8 Conclusions 137

Appendices 143

A: Additional Derivations 143

List of Abbreviations 145

Chapter 1

Introduction

The development of quantum mechanics in the beginning of the twentieth century has started a revolution that transformed our fundamental understanding of nature and how we perceive it. Yet consequences like the uncertainty principle have had a formal—not to say philosophical—implication, that had little impact on our everyday life, as compared to other branches of physics and chemistry. In the new millennium, however, a *Second Quantum Revolution* is believed to bring quantum mechanics to more practical relevance by directly exploiting its inner workings in the technology that we use [1]. Among those are the important predictions of quantum information theory [2, 3, 4] and their application for quantum computing, which will become important, if not for the whole of information technology, at least for cryptology once the decoherence time has been sufficiently enlarged [5, 6]. As for the carriers of quantum information, a multitude of different system are currently being explored, including ion traps [7], ultracold atoms [8, 9], superconducting qbits [10, 11, 12], spin defects [13, 14] or topological materials [15].

Moreover, the semiconductor technology for "classical" computing, enabled by modern solid state theory, would have been unthinkable without the fundamental understanding of quantum mechanics. In the future, alternatives to silicon-based semiconductors are expected to become more important; these alternatives are other inorganic material, such as GaAs, but especially the field of *organic electronics* [16, 17, 18, 19, 20, 21] has emerged as a cheap, flexible and resource-efficient alternative to silicon. In organic electronics devices, three important properties of two-dimensional carbon-based chemical networks come together: relative mechanical stability and excellent conduction, both resulting from carbon's ability to form sp^2-bonds, and sheer infinite possibilities to combine molecular building blocks, most of which inspired by nature. Both for the basic research on the constituents of such organic devices, as well as for building the actual combinations of electrodes and the active regions, the study of organic molecules interfaced with metallic and non-metallic contacts is crucial. At the interface, the basic properties of the individual layers and their interplay shape the overall properties of the device, such as the interface geometry, charge rearrangements or transport properties [22, 23]. Most of the aforementioned can be embraced by the term *electronic structure* of such interfaces, which is also the primary concern of this work.

Before going further, another important aspect of organic molecules should not be left unaddressed: their interaction with light. Just as their inorganic counterparts, organic semiconductors can be utilized as active materials in photo diodes [24, 25, 26], organic light-emitting diodes [27, 28, 29, 30, 31] or organic solar cells [32, 33, 34]. Some of these devices have already become commercially available, such as organic light-emitting diode (OLED) displays, and es-

pecially the latter case of organic photovoltaic is of tremendous importance for a green energy future. In order to understand the interaction of organic molecules with light on a fundamental level, it are again the quantum properties of such molecules that need to be understood.

So how do we understand the quantum properties of materials such as organic molecule-substrate interfaces? In an experimental approach, a large palette of different surface science techniques exist, that all have their pros and cons. Arguably the most direct methods to visualize the shape of molecules on ordered (conducting) surfaces, are scanning tunneling microscopy (STM) [35, 36] and the related atomic force microscopy (AFM) [37, 38]. STM utilizes the quantum mechanical tunneling of electron current from the sample to a tip that is scanning the surface and can thereby image the local charge density distribution which builds up the topology of surfaces. By varying the bias voltage or tunneling current conditions, this technique can be turned into a spectroscopy method—scanning tunneling spectroscopy (STS)—that is able to detect the energy levels of the quantum states. Its accessible energy range, however, is limited to only a few eV below and above the Fermi level. In addition, all scanning probe methods have in common that they always show a *local* probe of the system and that the results allow only for a rather rough comparison with the quantum mechanical energy levels and wave functions, which, from a theory perspective, can be seen as the full characterization of a quantum system.

In a complementary method—*photoelectron spectroscopy*—experimental results and theoretical predictions are directly connected. As an application of the photoelectric effect, here the sample is irradiated with light of sufficiently high energy to emit electrons. These photoelectrons then carry most of their quantum properties; most notably, their initial energy level is encoded in their final kinetic energy in relation to the energy of the photons. The photon energy in turn can be varied from few eV to the keV range, thereby giving access to the complete spectrum of electron binding energies in a material. When probing the deep-lying core levels with x-ray radiation, x-ray photoelectron spectroscopy (XPS) [39, 40] can detect the atom species and their chemical states, which was therefore termed *electron spectroscopy for chemical analysis* by its inventor [41, 42]. In angular-resolved photoemission spectroscopy (ARPES), also the emission angle of the photoelectrons is detected, which allows to deduce the parallel components of their initial momentum and is therefore the probe that yields the most direct information of the quantum states of a material [43, 44, 45].

At the same time, results of ARPES measurements are often more difficult to interpret and in many cases the combination of experimental and theoretical effort is expedient. This has resulted in a technique termed photoemission orbital tomography (POT), where a direct connection between molecular orbitals and their momentum space signatures arises from a simple model of the photoemission process as an one-step transition from an initial state, describing the bound electron in the system, and the final state of the photoelectron [46]. In particular, the photoelectron is modeled as a free particle by a plane wave, which then establishes a Fourier transform-like relation between real- and momentum space. This relation has been used to determine the geometry of adsorbate layers [47, 48, 49], the hybridization between these layers and the substrate [50, 51, 52] or the nature of reaction products on the surface [53]. Inverting the connection between real- and momentum space, POT can even be used to reconstruct real-space images of orbitals from photoemission data [54, 55, 56, 57, 58]. While the complex-valued phase of the wave function cannot be fully retrieved in ARPES, nevertheless, POT and its real-space reconstruction protocol emphasizes the role of orbitals and brings them into the realm of quantum mechanical observables.

In this work, the frontiers of POT are being explored in three different directions. First, the theoretical description of the electronic structure, i.e., the *initial state* of the photoelectron process is explored. This many-electron state is described by means of density functional theory (DFT) [59, 60, 61, 62, 63, 64], which allows for an accurate yet economic simulation of the collec-

tive nature of hundreds to thousands of electrons under the influence of the electron-electron and electron-ion interaction. The necessary approximations to allow for such a description typically neglect or underestimate long-range correlation interactions, the so-called *van der Waals interactions* [65, 66]. These attractive forces originate from temporal fluctuations in the charge density and play an important role for the binding of molecules to surfaces [67, 68], but are also encountered in two-dimensional systems [69, 21, 70], soft matter [71, 72] or biology [73, 74, 75]. In the context of POT, organic molecules have mainly been studied when adsorbed on metal surfaces, while here we are exploring their interaction with a special surface: thin layers of MgO on the Ag(100)-surface. This system has the interesting property that, despite MgO being an insulator, it can promote charge transfer from the metal through the interlayer into the adsorbed molecules via electron tunneling [76]. In addition, the magnesium ions in the substrate allow for an important type of on-surface reactions, namely the self-metalation of porphyrine-based molecules. This organic building block is at the heart of many important molecules in nature, such as haemoglobin, cytochromes, chlorophyll or vitamin B12, and gains its functionality from the ability to incorporate metal ions in its center [77, 78]. Wether the self-metalation of such molecules is possible on the MgO/Ag(100) surface and how the charge transfer is related to this process, is studied in this work, with special emphasis on the role of van der Waals interactions and their approximate treatment in a DFT framework for the energetics of the metalation. If an organic molecule has some of its carbon replaced by oxygen, such as in the case of perylene-tetracarboxylic dianhydride (PTCDA) adsorbed on MgO/Ag(100), the Mg^{2+}-ions offer strong binding to the molecule's oxygen atoms. This constitutes a further interesting case for POT, since it poses the question if, and to which extent, structural changes of the molecular geometry can be observed by changes in the momentum space signatures of the corresponding orbitals.

Despite its merits, POT has also been criticized for its simplifications regarding the final state [79, 80] and even shown to be insufficient in certain circumstances [81, 82], which is mostly attributed to the plane wave assumption. Thus, as a second major topic of this work, the role of the *final state* in POT is therefore explored. The assumption of a plane wave as the final state in photoemission can be avoided in by following two routes: replacing it by another, explicit final state or avoiding an assumption about the final state at all. Borrowed from the quantum mechanical scattering problem, the scattered wave approximation (SWA) [83, 84] can be used to follow the road in the one direction. The other route leaves the realm of time-independent quantum mechanics altogether. With time-dependent DFT (TDDFT), the photoemission process can be modeled very closely to the experiment: by coupling a light field to the electrons, they are ejected from the sample and by measuring their energy and angular distribution at a detector surface placed around the sample, ARPES can be directly simulated [85, 86]. Importantly, on their way to the detector, the photoelectrons interact with each other and with the rest of the sample and we thus can use this method to study final state effects. Such effects emerge primarily if photoemission from light with different polarization directions or with different photon energies is compared and here the final state is explored for the prototypical two-dimensional material graphene.

Beyond the control of initial states from DFT and the consideration of different final states, we finally push the frontiers of POT to the description of photoemission from excited states as a third research direction followed in this thesis. Very recently, enabled by laser high-harmonic generation or free-electron lasers, it has become possible to study also the dynamics of excited states in time- and angle-resolved photoemission spectroscopy (trARPES) experiments. While the case of optical population of formally unoccupied states above the band gap should, in principle, be covered by the established formulation of POT, the situation is somewhat different for excitation energies lower than the band gap in non-metallic systems. Here, quasi-particles

form—the excitons—that are not straightforward to include in the formalism of POT due to their entangled character stemming from the electron-hole interaction. In the last part of this work, we therefore undertake the effort to include the description of excitons into the formalism of POT, where the control of results is possible by the comparison to simulations from TDDFT.

This thesis is organized as follows. In Chapter 2, an overview over the methods used in this thesis is given, which covers a brief introduction to DFT and its approximations with regard to exchange-correlation functionals and the inclusion of van der Waals interactions. Subsequently, the time-dependent fashion of DFT, TDDFT is established by recapitulating its principle thereoms: the Runge-Gross theorem and the van Leeuwen thereom. After a short note on the implications of light-matter interaction on a semiclassical level, the two major approaches of excited states calculations from TDDFT are reviewed: the time-propagation method and the linear-response formalism. The methodology is concluded by describing photoelectron spectroscopy in going from the experiment to its simulation at different levels of sophistication. After some general remarks about the Golden Rule matrix element for photoemission and its relation to other formalisms, we introduce the plane wave approximation (PWA) and deduce a formalism for the simulation of excitons with POT. Touching the subject of different final states, in addition, the SWA is introduced and, finally, the simulation of photoemission from TDDFT via the *surface-flux method* is reviewed. After introducing the methodology, the Chapters 3-7 present the results of this work by incorporating the respective publications into the thesis. Each publication is introduced by a short significance statement and its author contributions. The publications are then presented with slight adaptions to layout and standards for references etc., but have not been altered in terms of content. To each publication, respective appendices or supporting material are also included in the chapters. Note that in this way, the notation and the choice of units are not standardized throughout this thesis. The presentation of the results is completed by the concluding Chapter 8 and a list of publications.

Chapter 2

Methods

2.1 Density Functional Theory

DFT is arguably the most important tool for electronic structure simulations in physics and chemistry and the interfaces between organic molecular layers and (metal) substrates are no exception. The success of DFT lies in a well proportioned balance between accuracy and computational effort, such that its key papers are the most cited in physics and its implementations are among the codes that consume the most CPU time on current supercomputers. With more computing power, the future is even brighter and DFT is considered to endow our increasing demand for simulations in key fields of the present, such as green energy, nanotechnology, opto-electronics or materials science.

In this section, a brief introduction into the foundations of DFT is given, focusing on concepts that will be used for the extension of DFT to the time-domain in Section 2.2. Subsequently, different approximations of exchange-correlation effects, inherent in DFT, are discussed with reference to our work on the electronic structure of various molecule-substrate interfaces. In close relation, we also compare different methods to treat non-local van der Waals interactions; these are especially important for molecular interfaces with metal-isolator surfaces, as in the magnesium oxide-silver substrates. For more complete introductions on the foundations of DFT and its various approximations for the exchange-correlation effects, the devoted readers are referred to the literature [61, 62, 63, 64, 87, 88, 89].

2.1.1 Foundations

The electronic and optical properties of matter are governed by the motion of the electrons and their description requires quantum theory, if we are interested in systems of the size of individual molecules. On this level, a system of N electrons is characterized by the Hamiltonian

$$\boldsymbol{H} = \boldsymbol{T} + \boldsymbol{U} + \boldsymbol{V}, \tag{2.1}$$

with contributions from the kinetic energy

$$\boldsymbol{T} = \frac{1}{2}\sum_{i}^{N} \boldsymbol{p}_i^2, \tag{2.2}$$

the Coulomb interaction

$$\boldsymbol{U} = \sum_{j>i}^{N} \frac{1}{|\boldsymbol{r}_i - \boldsymbol{r}_j|}, \tag{2.3}$$

as well as any external potential that the electrons may feel:

$$\boldsymbol{V} = \sum_{i}^{N} v(\boldsymbol{r}_i). \tag{2.4}$$

In the latter, the potential of the ions is included and we employ the *Born-Oppenheimer approximation*. Unless stated otherwise, we use atomic units such that $\hbar = m = e^2/4\pi\epsilon_0 = 1$.

Many-body quantum mechanics is commonly formulated in terms of the wave function $\Psi(\boldsymbol{r}_1, \boldsymbol{r}_2, \ldots, \boldsymbol{r}_N)$, where we suppress the spin degree of freedom in following. Although formally the N-electron non-relativistic, stationary and non-magnetic Schrödinger equation,

$$\boldsymbol{H}\Psi = E\Psi \tag{2.5}$$

contains all desired information in the wave functions, there exists no closed solution for more than two electrons. Even worse, the complexity of the problem scales exponentially with the number of electrons and for $N \gtrsim 10^3$ it thus ceases to remain a valid scientific concept [60].

In DFT we instead use the electron density of the ground-state Ψ_0 as the main variable, thereby moving from 3^N to $3N$ spatial variables:

$$n_0(\boldsymbol{r}) = N \int \mathrm{d}\boldsymbol{r}_2 \cdots \int \mathrm{d}\boldsymbol{r}_N |\Psi_0(\boldsymbol{r}, \boldsymbol{r}_2, \ldots, \boldsymbol{r}_N)|^2. \tag{2.6}$$

The mathematical proof that in a finite system of interacting electrons in its ground state, there exists a one-to-one mapping of the external potential and the ground-state density—the electron-electron interaction given—was stated by Hohenberg and Kohn in 1964 [59]:

$$v(\boldsymbol{r}) \leftrightarrow n(\boldsymbol{r}). \tag{2.7}$$

Essentially, this means that all observables can indeed be expressed as functionals of the ground-state density. Proving the Hohenberg-Kohn theorem is straightforward by *reductio ad absurdum* [59, 87, 64, 61]. The ground state energy, as one specific observable, is expressed as a functional of the density in the following way:

$$\begin{aligned} E[n] &= \langle \Psi[n] | \boldsymbol{T} + \boldsymbol{U} + \boldsymbol{V} | \Psi[n] \rangle \\ &= F[n] + \int \mathrm{d}\boldsymbol{r}\, n(\boldsymbol{r}) v(\boldsymbol{r}), \end{aligned} \tag{2.8}$$

thereby defining the universal functional $F[n]$. It is universal in the sense that it is the same for all systems under the influence of the same electron-electron interaction and one could, in principle, minimize Equation 2.8 with respect to some trial wave functions and thus find the ground state energy and density. Aside from formal aspects, such as the v-representability problem [90, 91, 92, 93], the constrained search for the universal functional [94, 95] is impracticable and the exact form of $F[n]$ remains unknown.

The great success of DFT began only when Kohn and Sham [96] established a recipe on how to calculate, at least approximately, the ground state density along the following lines. The Hohenberg-Kohn theorem holds for *any* given form of the electron-electron interaction, one

could therefore also choose zero interaction, i.e. $\boldsymbol{U} = 0$. The Kohn-Sham (KS) system represents such a collection of N non-interacting electrons and can be written with the Hamiltonian

$$\boldsymbol{H}_{\mathrm{KS}} = \boldsymbol{T}_{\mathrm{KS}} + \boldsymbol{V}_{\mathrm{KS}} = \sum_{i}^{N} \left(\frac{\mathbf{p}_i^2}{2} + v_{\mathrm{KS}}(\boldsymbol{r}_i) \right), \tag{2.9}$$

with the important restriction that this system must lead to same ground state density as the interacting system. The ground state of such a non-interacting system can be written as a Slater determinant

$$\Psi_0(\boldsymbol{x}_1, \ldots, \boldsymbol{x}_N) = \frac{1}{\sqrt{N!}} \begin{vmatrix} \varphi_N(\boldsymbol{r}_1) & \varphi_N(\boldsymbol{r}_2) & \cdots & \varphi_N(\boldsymbol{r}_N) \\ \vdots & \vdots & & \vdots \\ \varphi_1(\boldsymbol{r}_1) & \varphi_1(\boldsymbol{r}_2) & \cdots & \varphi_1(\boldsymbol{r}_N) \end{vmatrix}, \tag{2.10}$$

with the KS orbitals φ_i satisfying the effective one-body Schrödinger equation

$$\boldsymbol{H}_{\mathrm{KS}} \varphi_i(\boldsymbol{r}) = \varepsilon_i \varphi_i(\boldsymbol{r}). \tag{2.11}$$

The ground state density is then obtained from

$$n_{\mathrm{KS}}(\boldsymbol{r}) = \sum_{j}^{N} \left| \varphi_j(\boldsymbol{r}) \right|^2. \tag{2.12}$$

The crucial part here lies in demanding that the KS system reproduces the exact ground state density,

$$n_{\mathrm{KS}}(\boldsymbol{r}) \stackrel{!}{=} n(\boldsymbol{r}). \tag{2.13}$$

Obviously, this can only be achieved by modifying the potential v_{KS} accordingly. In other words: the difference between a system of interacting and non-interacting electrons, i.e. all many-body effects, must be hidden in the difference between v and v_{KS} (and the differences in kinetic energy, see below). Rewriting the ground state energy of the interacting system, as in Equation 2.8, with

$$\begin{aligned} E[n] &= \boldsymbol{T}[n] + \boldsymbol{U}[n] + \int \mathrm{d}\boldsymbol{r}\, n(\boldsymbol{r}) v(\boldsymbol{r}) \\ &= \boldsymbol{T}_{\mathrm{KS}}[n] + \int \mathrm{d}\boldsymbol{r}\, n(\boldsymbol{r}) v(\boldsymbol{r}) + E_{\mathrm{H}}[n] + E_{\mathrm{xc}}[n], \end{aligned} \tag{2.14}$$

we have brought the two systems together. Moreover, we have defined the exchange-correlation energy as a new entity that should take care of the differences between both systems, i.e. the difference between the true kinetic energy, $\boldsymbol{T}$, and the kinetic energy of the KS system, $\boldsymbol{T}_{\mathrm{KS}}$, as well as the electron-electron interaction beyond the mean-field. The latter is the known as the Hartree energy E_{H}:

$$E_{\mathrm{H}}[n] = \frac{1}{2} \int \mathrm{d}\boldsymbol{r}\, \mathrm{d}\boldsymbol{r}'\, \frac{n(\boldsymbol{r}) n(\boldsymbol{r}')}{|\boldsymbol{r} - \boldsymbol{r}'|}. \tag{2.15}$$

Having reformulated Equation 2.8 with Equation 2.14, we still do not know the exact form of E_{xc}, but we are now in the position to at least evaluate the energy as a functional of a density that can be easily computed in terms of single-particle orbitals φ_i. Assuming for a moment that E_{xc} would be known, then it can be stated that the above formalism is an exact mapping of the many-body problem on an effective single-particle system. Moreover, we then could compute the *true* ground state density in a self-consistent scheme, the KS scheme, that requires the following steps:

(i) Make an initial guess for the density $n^{(0)}$

(ii) Compute $v_{\mathrm{KS}}^{(0)}[n]$

(iii) Construct the KS Hamiltonian $\boldsymbol{H}_{\mathrm{KS}}^{(0)}$

(iv) Solve $\boldsymbol{H}_{\mathrm{KS}}^{(0)}\varphi_i^{(1)} = \varepsilon_i\varphi_i^{(1)}$

(v) Compute $n^{(1)} = \sum_i \left|\varphi_i^{(1)}\right|^2$ and the total energy $E_{\mathrm{tot}}^{(1)}$

After step (v), one can evaluate a convergence criterion, e.g. $\epsilon = \left|E_{\mathrm{tot}}^{(j)} - E_{\mathrm{tot}}^{(j-1)}\right|$ and stop the calculation at some desired value of ϵ, otherwise the scheme is repeated from step (ii). The first numerical bottleneck of this scheme is step (ii), since the Poisson equation needs to solved, which is usually done in momentum space. The second is step (iv), which usually involves diagonalizing a large matrix and which is where most of the CPU time in DFT codes is spent. It could be further remarked that a critical point in the self-consistent evaluation of (ii)-(v) is feeding in the new density, which can be potentially overshooting the changes and is therefore prone to instabilities. One therefore usually uses a mixing scheme between the old and the new density and numerical algorithms, such as the conjugate gradient algorithm [97], to ensure faster convergence.

With the KS scheme described above, a practical method has been established that allows for computing the many-electron problem with the help of the density and some auxiliary system of non-interacting electrons. In principle, this description is formally exact, *if* we were in possession of the exchange-correlation energy E_{xc}. Since we are not, the price that we have to pay is living with a more or less appropriate formulation of E_{xc} as a functional of the density, depending on the level of computational effort we are willing to invest. Before turning to the following paragraph, which is devoted to the approximations for exchange-correlation effects, some general remarks to DFT with regard to this work can be made.

(i) Although the foundations of DFT guarantee that all observables can be expressed as functionals of the ground-state density, the quantum mechanical wave function is not an observable and we will frequently treat the KS orbitals as the true orbitals, which is customary but formally not justified [98].

(ii) Coming from Hartree-Fock (HF) theory, Koopmans theorem [99] gives an interpretation of the energy levels as electron-removal energies in finite systems. In DFT, this only holds for the highest occupied orbital but is, in contrast to the HF equivalent, exact [100]. In general, however, the energy eigenvalues ε_i are non-physical.

(iii) Related with (ii) is also the infamous "band gap problem" of DFT, which consists in the fact the fundamental gap of semiconductors and insulators is severely underestimated when relying on KS energies.

2.1.2 Approximations for Exchange- and Correlation Effects

With the KS scheme described in the preceding paragraph, we have obtained a formal method for computing the electronic structure in terms of the density. To make this method practical, however, an approximation for the exchange-correlation energy (or its potential) as defined in Equation 2.14 has to be found.

The Local Density Approximation

The first example of such an approximation was already given by Hohenberg and Kohn in their seminal paper [59], guided by the following considerations. If the density is only slowly varying in space, one might as well take properties of the homogeneous electron gas (with constant density) for the construction of an exchange-correlation functional. The exchange expression for the homogeneous electron gas (HEG) had already been derived by Dirac in 1930 [101] such that only the correlation part has to be calculated. This can be done by Quantum Monte Carlo techniques [102], leading to a suitable parametrization, e.g. as given by Perdew and Zunger [103] or Perdew and Wang [104]. Accordingly, this approximation is termed the local density approximation (LDA) and can be expressed as an integral over the exchange- and correlation parts of the HEG energy per electron [64]:

$$\begin{aligned} E_{\mathrm{xc}}^{(\mathrm{LDA})}[n] &= \int \mathrm{d}\boldsymbol{r}\; n(\boldsymbol{r}) \left(e_{\mathrm{x}}^{(\mathrm{HEG})}[n] + e_{\mathrm{c}}^{(\mathrm{HEG})}[n] \right) \\ &= \int \mathrm{d}\boldsymbol{r}\; n(\boldsymbol{r}) \left(-\frac{3}{4\pi} \frac{(9\pi/4)^{1/3}}{r_{\mathrm{S}}} + e_{\mathrm{c}}^{(\mathrm{HEG})}[n] \right), \end{aligned} \tag{2.16}$$

with the Wigner-Seitz radius r_{S} and e.g. the correlation energy per electron from Perdew and Wang [104]

$$e_{\mathrm{c}}^{(\mathrm{HEG})}[n] = -2c_0(1+\alpha_1 r_{\mathrm{S}}) \ln\left\{ 1 + \frac{1}{2c_0(\beta_1 r_{\mathrm{S}}^{1/2} + \beta_2 r_{\mathrm{S}} + \beta_3 r_{\mathrm{S}}^{3/2} + \beta_4 r_{\mathrm{S}}^2)} \right\}, \tag{2.17}$$

with fit parameter $c_0, \alpha_1, \beta_1, \beta_2, \beta_3$ and β_4. Given the crudeness of the LDA, some results are remarkably accurate, for instance the lattice constants in bulk metals [105], which is attributed to fortunate error-cancellation and some exact properties that the LDA fulfills, e.g. the sum rules for the exchange-, correlation- and exchange-correlation holes from coupling constant-integration [64] or the coordinate-scaling behavior of the density [106]. Note that the LDA can also be extended to spin-polarized systems [107] and is then called the local spin density approximation (LSDA). In this work, the LDA is primarily used in its time-dependent fashion, the adiabatic LDA, which is described in Section 2.2.

Generalized Gradient Approximations

The next step on the so-called *Jacob's ladder* [108] is the generalized-gradient approximation (GGA), which, as the name suggests, takes also the gradient of the density into account:

$$E_{\mathrm{xc}}^{(\mathrm{GGA})}[n] = \int \mathrm{d}\boldsymbol{r}\; n(\boldsymbol{r}) F\left(n(\boldsymbol{r}), \nabla n(\boldsymbol{r})\right). \tag{2.18}$$

For the exact form of $F\left(n(\boldsymbol{r}), \nabla n(\boldsymbol{r})\right)$, many variants exist. Among the most successful ones are the formulations of Becke [109] or Perdew, Burke and Ernzerhof (PBE) [110]. Improvements of the latter over LDA are most pronounced for binding- or ionization energies in molecules, while some metal lattice constants are even inferior [105]. Nonetheless, the original paper for PBE is the most cited reference of all physics and in this work we also partly rely on the PBE functional for the calculations of metal-organic interfaces.

Meta-GGAs

A direct extension of GGA functionals are Meta-GGA (MGGA) functionals, which do not only take gradients but also second derivatives of the density, as well as the KS orbital kinetic-energy

density,

$$\tau(\boldsymbol{r}) = \frac{1}{2}\sum_i |\nabla\phi_i(\boldsymbol{r})|^2, \tag{2.19}$$

into account:

$$E_{\mathrm{xc}}^{(\mathrm{MGGA})}[n,\tau] = \int \mathrm{d}\boldsymbol{r}\; n(\boldsymbol{r}) F\left(n(\boldsymbol{r}), \nabla n(\boldsymbol{r}), \Delta n(\boldsymbol{r}), \tau\right). \tag{2.20}$$

In this way, MGGAs achieve a higher flexibility that can be used to partly remove the self-interaction error [111] and fulfill exact constraints like global properties of the exchange and correlation energies, the scaling of the density or the asymptotic behavior of the xc potential when $r \to 0$ or $r \to \infty$ [112]. Earlier forms of MGGAs include the PKZB [113] and TPSS [114] functionals, while a more recent implementation was introduced by the SCAN functional [115].

Hybrid Functionals

One of the most dissatisfying shortcomings of local and semi-local exchange-correlation functionals, such as LDA and PBE, is the wrong prediction of energy levels. Despite the fact that only the highest occupied molecular orbital (HOMO) has a well-defined physical meaning, both the occupied- and unoccupied frontier orbitals from DFT calculations are utilized e.g. for the interpretation of energies of molecular adsorbates or the electronic band-gap where especially the latter is often very wrong in (semi-) local functionals. One way of overcoming this deficiency is to use a portion of Fock-exchange, also termed exact-exchange in DFT, from HF theory, which is defined in its energy expression as

$$E_{\mathrm{x}}^{\mathrm{HF}} = -\sum_{j>i}\int \mathrm{d}\boldsymbol{r}\,\mathrm{d}\boldsymbol{r'}\;\frac{\varphi_i^*(\boldsymbol{r})\varphi_j^*(\boldsymbol{r'})\varphi_j(\boldsymbol{r})\varphi_i(\boldsymbol{r'})}{|\boldsymbol{r}-\boldsymbol{r'}|}. \tag{2.21}$$

For the mixing ratios of semi-local exchange-correlation functionals with $E_{\mathrm{x}}^{\mathrm{HF}}$, different families of functionals exist. In quantum chemistry, one of the most widely used implementations is B3LYP [116, 117], defined as

$$E_{\mathrm{x}}^{\mathrm{B3LYP}} = (1-\alpha)E_{\mathrm{x}}^{\mathrm{LDA}} + \alpha E_{\mathrm{x}}^{\mathrm{HF}} + \beta E_{\mathrm{x}}^{\mathrm{B88}} + \gamma E_{\mathrm{c}}^{\mathrm{LYP}} + (1-\gamma)E_{\mathrm{c}}^{\mathrm{LDA}}, \tag{2.22}$$

with $\alpha = 0.2$, $\beta = 0.72$, $\gamma = 0.81$ and the GGA-type functionals $E_{\mathrm{x}}^{\mathrm{B88}}$ from Becke [109] and $E_{\mathrm{c}}^{\mathrm{LYP}}$ from Lee, Yang and Parr [118]. Incorporating Fock-exchange increases the computational burden at least by an order of magnitude, since computing the two-body integrals is expensive and has a quadratic scaling with system size, which is especially unfavorable for metal-organic interfaces where a large number of atoms have to be computed. A way to overcome this was proposed by Heyd, Scuseria and Ernzerhof (HSE) [119], where the idea is to rewrite the Coulomb interaction,

$$\frac{1}{r} \to \frac{1-\mathrm{erf}(\omega r)}{r} + \frac{\mathrm{erf}(\omega r)}{r}, \tag{2.23}$$

with the error function

$$\mathrm{erf}(x) = \frac{2}{\sqrt{\pi}}\int_0^x \mathrm{d}x' \mathrm{e}^{-x'^2}. \tag{2.24}$$

The two terms in Equation 2.23 can now be evaluated with different means of exchange-correlation, thereby introducing an effective range-separation parameter ω controlling the spatial distance where Fock-exchange is mixed in or not, which reduces the number of non-local integrals that need to be evaluated. The HSE energy functional reads

$$E_{\mathrm{x}}^{\mathrm{HSE}} = (1-\alpha)E_{\mathrm{x}}^{\mathrm{PBE,SR}}(\omega) + \alpha E_{\mathrm{x}}^{\mathrm{HF,SR}}(\omega) + E_{\mathrm{x}}^{\mathrm{PBE,LR}}(\omega) + E_{\mathrm{c}}^{\mathrm{PBE}}, \tag{2.25}$$

where the long-range part of the exchange energy, as well as the correlation, is taken from PBE. In the revised form of HSE [120], the mixing parameter in the short range is $\alpha = 0.25$ and $\omega = 0.11\ \mathrm{bohr}^{-1}$.

The step from B3LYP to HSE can be seen as going from a global hybrid to a range-separated hybrid (RSH), where the mixing- and range-separation parameter α and ω define the functional. Generalizing this concept, such a set of parameter can be optimized for each individual system, where for molecules in the gas-phase the optimal parameter can be found by comparison of one aforementioned exact property in DFT: the HOMO level being equal to the ionization potential. One therefore computes e.g. a N-electron molecule in its neutral electronic configuration, additionally as the anion with $N+1$ electrons and then compares their energy difference with the HOMO level. By minimizing this difference in the two-parameter space of α and ω, the so-called optimially-tuned range-separated hybrid (OT-RSH) [121, 122] functionals are invoked, which are reported to give very accurate results, especially for the KS-gap [123]. Recently, this method has been extended to solids [124].

The steps taken on *Jacob's ladder* have so far lead to the improvement of the exchange part in the missing many-body interactions only. Improving on the correlation part is considerably harder. In DFT, the random phase approximation (RPA) [125] would provide such means but the implementations of the RPA are prohibitively expensive for our systems of interest. We therefore have to resort to other methods for describing long-range correlation effects, a topic which is raised in the next paragraph.

2.1.3 Dispersive Interaction Corrections

Beyond static classical electromagnetic forces that are taken into account by the Hartree term already, quantum fluctuations induce small, non-permanent dipole moments that lead to additional attractive forces. These forces would be included by the long-range correlation of the true electron-electron interaction, but are not incorporated in the exchange-correlation approximations discussed so far. While at first glance this influence might seem small compared to chemical bonding, it can be particularly important for organic molecules physisorbed on (metal) surfaces. Without such dispersive forces, a molecule might even not bind to the surface at all [67] and van der Waals-interactions play an important role in widespread areas of research, such as metal-organic interfaces [126, 127, 128, 129], vertically stacked 2D systems [69, 21, 70], soft matter [71, 72] or biology [73, 74, 75]. Consequently, a large amount of literature and review articles [130, 131, 132, 66, 133] exist that deal with the numerous ways to incorporate van der Waals interactions into DFT. In the following, three types of such approximations, at different levels of sophistication, are briefly described and will be classified with respect to the interfaces that are subject to this work.

Empirical Corrections after Grimme

Already in the early works of London [134, 65] a long-range, attractive behavior between molecules was inferred, that, together with a short-ranged part to account for Pauli repulsion,

culminated in the famous Lennard-Jones potential [135],

$$U(\boldsymbol{R}) = U_0 \left[\left(\frac{\boldsymbol{R}_0}{\boldsymbol{R}} \right)^{12} - 2 \left(\frac{\boldsymbol{R}_0}{\boldsymbol{R}} \right)^{6} \right], \tag{2.26}$$

with $\boldsymbol{R}$ being the distance between the constituents and where the constants $\boldsymbol{R}_0$ and U_0 are used to set the minimum position and magnitude. It is exactly this $\boldsymbol{R}^{-6}$-law that is used in the original method after Grimme [136]. Here, van der Waals corrections enter as an additional term in the exchange-correlation energy, i.e.

$$E_{xc} = E_{xc}^{\mathrm{DFT}} + E_{\mathrm{vdW}}. \tag{2.27}$$

Note that this energy is added to the total energy *after* each self-consistent electronic cycle, such that it will only affect the system for geometry optimizations and not the electronic structure obtained from single-point calculations. The van der Waals energy E_{vdW} according to Grimme was initially defined as

$$E_{\mathrm{vdW}} = -s_6 \sum_{i<j} \frac{C_6^{ij}}{\boldsymbol{R}_{ij}^6} f_{\mathrm{damp}} \left(\boldsymbol{R}_{ij} \right), \tag{2.28}$$

with the sum running over all pairs of atoms i, j and a coefficient C_6^{ij} for each pair, as well as a global scaling factor s_6 and a function f_{damp} to damp the interaction at small inter-atomic distances where covalent bonding should dominate. In practice, the C_6 coefficients are not needed for each pair of atoms but an average of the form

$$C_6^{ij} = 2 \frac{C_6^i C_6^i}{C_6^i + C_6^i} \tag{2.29}$$

is taken, such that a single coefficient is supposed to account for an atom sort in all of its possible configurations and hybridization states. In an updated version of the method [137], usually termed DFT-D3, the coefficients are geometry-dependent and are also adjusted according to their local chemical coordination. Moreover, three-body interactions are also taken into account via an additional term with $\boldsymbol{R}^{-8}$-scaling and C_8^{ij}-coefficients. This makes the DFT-D3 method a very versatile yet cost-efficient way to incorporate van der Waals forces in DFT calculations, also for periodic systems [138]. From a conceptional point of view, however, criticism may arise for the empiricism introduced by the open parameter in the description, although the C_6-coefficients may be also calculated from TDDFT [139].

The Method of Tkatchenko and Scheffler

As a second example, we describe a family of methods initialized by Tkatchenko and Scheffler [140], which still make use of equations 2.27 and 2.28 but put the parameter of the method on a more sound basis. In contrast to Grimme's method, the physical environment is respected in such a way that the C_6 coefficients are functionals of the relative, dynamic polarizability of each atom in the system. This connection arises from the Casimir-Polder integral [141]:

$$C_6^{ij} = \frac{3}{\pi} \int_0^\infty \mathrm{d}\omega \; \alpha_i \left(\mathrm{i}\omega \right) \alpha_j \left(\mathrm{i}\omega \right). \tag{2.30}$$

Since the α_i are tensor-valued entities at imaginary frequencies, their practical calculation involves tracing over spatial directions and truncating the Padé series [142, 143], leading to an

effective frequency dependency. While for free atoms, the calculation is rather straightforward and polarizabilities α_i^{free} can be computed from TDDFT [139], for atoms in molecules and solids this task is more involved. In this case, one can make use of a general property, namely that there exists a direct relation between volume and polarizability [144], such that the effective atomic volumes scale the polarizability of free atoms:

$$\alpha_i = \frac{V_i^{\text{eff}}}{V_i^{\text{free}}} \alpha_i^{\text{free}}, \tag{2.31}$$

and, ultimately, the van der Waals-coefficients as

$$C_6^{ii} = \left(\frac{V_i^{\text{eff}}}{V_i^{\text{free}}} \right)^2 C_{6,\text{free}}^{ii}. \tag{2.32}$$

In the case of interaction between unlike atomic species, a combination rule is defined by

$$C_6^{ij} = \frac{2 C_6^{ii} C_6^{jj}}{\left(\frac{\alpha_j}{\alpha_i} C_6^{ii} + \frac{\alpha_i}{\alpha_j} C_6^{jj} \right)}. \tag{2.33}$$

Effective volumes are obtained from Hirshfeld partitioning [145, 146] as

$$\frac{V_i^{\text{eff}}}{V_i^{\text{free}}} = \frac{\int \mathrm{d}\boldsymbol{r}\, w_i(\boldsymbol{r}) r^3 n(\boldsymbol{r})}{\int \mathrm{d}\boldsymbol{r}\, r^3 n_i^{\text{free}}(\boldsymbol{r})}, \tag{2.34}$$

with the Hirshfeld weights $w_i(\boldsymbol{r})$ defined as

$$w_i(\boldsymbol{r}) = \frac{n_i^{\text{free}}(\boldsymbol{r})}{\sum_j n_j^{\text{free}}(\boldsymbol{r})}. \tag{2.35}$$

In this way, the van der Waals coefficients are functionals of the electron density and therefore respect the local charge environment. Employing the additivity of C_6-coefficients [140], the sum of these atomic C_6-coefficients then make up the van der Waals-parameter of the entire (sub-) system, e.g. the molecule and the surface, respectively. As before, the van der Waals force has to be damped at small distances, where the correct behavior is already represented by the (semi-) local xc-functional. Here, the damping function

$$f_{\text{damp}} = \frac{1}{1 + \exp\left\{ -d \left(\frac{R_{ij}}{R_{ij}^0 s} + 1 \right) \right\}} \tag{2.36}$$

depends on the shape parameter d, s, as well as on the van der Waals radii $\boldsymbol{R}_{ij}^0$. The latter can be computed from their atom-in-molecule counterparts, $\boldsymbol{R}_i^0$, as $\boldsymbol{R}_{ij}^0 = \boldsymbol{R}_i^0 + \boldsymbol{R}_j^0$, with the $\boldsymbol{R}_i^0$ being defined via the free-atom van der Waals radii ($\boldsymbol{R}_i^{0,\text{free}}$) as

$$\boldsymbol{R}_i^0 = \left(\frac{V_i^{\text{eff}}}{V_i^{\text{free}}} \right)^{\frac{1}{3}} \boldsymbol{R}_i^{0,\text{free}}. \tag{2.37}$$

Surpassing the original scheme of Tkatchenko and Scheffler, several noteworthy extensions have been developed. First, with iterative Hirshfeld partitioning [147, 148], free atoms are no longer used as a reference method for the atoms-in-molecules approach. Instead, atomic reference charges are determined self-consistently, which leads leads to an improvement in the description of ionic solids [149]. Second, electrodynamic response effects can be incorporated with the self-consistent screening equation [150, 151],

$$\alpha_i^{\mathrm{SCS}}(\mathrm{i}\omega) = \alpha_i(\mathrm{i}\omega) - \alpha_i(\mathrm{i}\omega) \sum_{j>i} \tau_{ij} \alpha_j^{\mathrm{SCS}}(\mathrm{i}\omega), \tag{2.38}$$

although results are mixed [152], especially in the case of ionic solids. For metals, an atoms-in-molecules approach is even more problematic due to the large number of quasi-free electrons. As a remedy and a third example, the set of optimized van der Waals parameter of Ruiz et. al. [153] should respect the enhanced screening in metal surfaces and were also used in part of this work. Forth, an extension via the many-body dispersion method includes long-range contributions based on the random-phase approximation of the correlation energy [151, 154, 155]. Tests for the many-body dispersion method in its plane wave implementation [156] in systems that incorporated ionic solids were, however, numerically problematic, such that this method has not been used in this work. Overall, the methods to treat van der Waals interaction after Tkatchenko and Scheffler represent a direct generalization of the London theory of dispersion and are computationally flexible and cheap. While their performance in metal and ionic solids may be enhanced, the general concept of atoms-in-solids remains questionable in the cases of organic molecules on metal-oxide substrates.

Van der Waals Density Functionals

The major similarity between all methods for van der Waals interactions in DFT that have been discussed so far, is that they are applied *after* one electronic cycle. In this way, they affect only energies and forces but the electron density itself is affected only implicitly in relaxations. For overcoming this limitation, one would need to explicitly incorporate long-range correlation into the exchange-correlation functional applied in the KS scheme. From a fundamental point of view, an exact expression of the correlation energy exists in form the adiabatic connection fluctuation-dissipation (ACFD) theorem [157, 158, 159, 160], which formally connects the exchange-correlation energy to the electronic response when adiabatically switching from the exact many-body interaction to the KS system. Correlation energy functionals developed from this expression commonly make use of the RPA [125, 161, 162, 163, 164, 165, 166] but are limited to atoms, simple solids or small molecules due to their scaling with system size as $\mathcal{O}(N^4)$ or worse [157].

As a feasible alternative, the family of van der Waals density functional (vdW-DF)s split the correlation part of the xc functional in a short-range part, treated in the LDA, and a non-local long-range part, such that

$$E_{\mathrm{xc}}^{\mathrm{vdW-DF}}[n] = E_{\mathrm{x}}^{\mathrm{GGA}}[n] + E_{\mathrm{c}}^{\mathrm{LDA}}[n] + E_{\mathrm{c}}^{\mathrm{nl}}[n]. \tag{2.39}$$

For deriving the non-local correlation part, $E_{\mathrm{c}}^{\mathrm{nl}}$, one starts from the ACFD theorem and, after some approximations for the response functions and the dielectric function [167, 157], arrives at the result that the long-range correlation energy can be expressed in the form

$$E_{\mathrm{c}}^{\mathrm{nl}}[n] = \int \mathrm{d}\boldsymbol{r}\, d\boldsymbol{r}'\; n(\boldsymbol{r}) \Phi(\boldsymbol{r}, \boldsymbol{r}') n(\boldsymbol{r}'), \tag{2.40}$$

with a non-local integration kernel $\Phi(\boldsymbol{r}, \boldsymbol{r}')$. Depending on the functionals used for exchange and short-range correlation, as well as on the exact form of the kernel Φ, several fashions of vdW-DFs exist alongside the original method [167]; among those are vdW-DF2 [168], optPBE-vdW [169], optB88-vdW [169], optB86b-vdW [170], VV10 [171], rVV10 [172] and SCAN+rVV10 [173].

2.2 Time-dependent Density Functional Theory

Very much alike DFT being a formally exact replacement of the time-independent many-body Schrödinger equation (SE), the time-dependent many-body SE can be recast into a time-dependent fashion of DFT called TDDFT. With this method, we have access to explicitly time-dependent phenomena, like the temporal evolution of the electrons in a molecule under the influence of a photon field, which is exactly the physical process in photoemission. TDDFT thus allows to directly simulate the photoemission experiment in real-time by adding a photoelectron detector to the simulation environment. Moreover, TDDFT provides access to the calculation of excited states, both in the linear response regime and with a real-time formalism. For the latter, no restrictions on the field strength need to made, thereby allowing for non-linear phenomena, such as laser high-harmonic generation. In a combination of different laser pulses and a real-time photoelectron detection scheme, we can directly simulate photoemission from excited states, such as in pump-probe experiments. These different methods therefore make TDDFT a very promising tool to investigate different aspects of the foundations and extensions of POT.

In this section, a brief introduction in the theoretical foundations of TDDFT is given, centering around the Runge-Gross and van Leeuwen theorems and the resulting time-dependent KS equations. This is accompanied by an overview of methods for the calculation of excited states, namely Casida's equation [174] in the linear response regime and the real-time propagation [175]. In the presentation of the topics, we loosely follow Reference [157], which is an excellent resource for both a didactic and complete treatment of the subject. For work presented in this thesis, we mainly have used the real-space real-time code OCTOPUS [176, 177], which will be used in the scheme for the detection of photoelectrons (see Paragraph 2.3.6).

2.2.1 The Runge-Gross Theorem

For a system of N electrons under the influence of a time-dependent potential $v(\boldsymbol{r}, t)$, the potential operator

$$\boldsymbol{V}(t) = \sum_{i}^{N} v(\boldsymbol{r}, t) \tag{2.41}$$

and with it the Hamiltonian $\boldsymbol{H}(t)$ become explicitly time-dependent and we thus seek a solution of the time-dependent many-body SE

$$\mathrm{i}\partial_t \Psi = \boldsymbol{H}(t)\Psi. \tag{2.42}$$

For a given initial state Ψ_0 at time t_0, a formal solution exists,

$$\Psi(t) = \boldsymbol{U}(t, t_0)\Psi_0, \tag{2.43}$$

with the time-propagation operator

$$\boldsymbol{U}(t, t_0) = \mathcal{T}\mathrm{e}^{-\mathrm{i}\int_{t_0}^{t} \mathrm{d}t' \boldsymbol{H}(t')}. \tag{2.44}$$

Here, $\mathcal{T}$ is the time-ordering operator to ensure causality. Since a closed-form solution of the many-electron SE of the ground state in terms of wave functions turned out to be hopeless, it is even more so for the time-dependent case. We therefore would like to have a time-dependent version of the Hohenberg-Kohn theorem that would allow us to express all observables in terms of the—now potentially time-dependent—densities $n(\boldsymbol{r}, t)$. The rigorous proof that there exists a one-to-one correspondence (up to certain modifications of the potential, see below) of the time-dependent potentials and densities was given by Runge and Gross [178] and will be summarized in the following.

Relying on the principle of *reductio ad absurdum*, it will be shown that two different potentials, v and v', lead to different densities at a later time, if the system has evolved from the same initial state Ψ_0. It is noteworthy that Ψ_0 is not necessarily an eigenstate of v or v' at initial time t_0 [157] and that v and v' have to differ by more than a purely time-dependent function $f(t)$, i.e.

$$v(\boldsymbol{r}, t) - v'(\boldsymbol{r}, t) \neq f(t). \tag{2.45}$$

The latter condition is required, since adding a time-dependent scalar function $f(t)$ to the potential leads to a simple time-dependent phase-factor of the wave function, which would then vanish when computing the density. It is further assumed that both potentials can be expanded in a Taylor series about the initial time t_0:

$$v(\boldsymbol{r}, t) = \sum_{k}^{\infty} \frac{1}{k!} v_k(\boldsymbol{r})(t - t_0)^k. \tag{2.46}$$

The condition 2.45 then translates to

$$\exists k \geq 0 \ : \ v_k(\boldsymbol{r}) - v'_k(\boldsymbol{r}) \neq \text{const.} \tag{2.47}$$

As a first step, starting from the current density operator,

$$\boldsymbol{J}(\boldsymbol{r}) = \frac{1}{2\mathrm{i}} \sum_{j}^{N} \left[\nabla_j \delta(\boldsymbol{r} - \boldsymbol{r}_j) + \delta(\boldsymbol{r} - \boldsymbol{r}_j) \nabla_j \right], \tag{2.48}$$

and the equation of motion of the current density,

$$\mathrm{i} \frac{\partial}{\partial t} \boldsymbol{j}(\boldsymbol{r}, t) = \langle \Psi(t) | \left[\boldsymbol{J}(\boldsymbol{r}), \boldsymbol{H}(t) \right] | \Psi(t) \rangle, \tag{2.49}$$

we can compute the time evolution of the difference in current density between the unprimed and the primed system at time t_0:

$$\begin{aligned} \partial_t \left\{ \boldsymbol{j}(\boldsymbol{r}, t) - \boldsymbol{j}'(\boldsymbol{r}, t) \right\} \Big|_{t=t_0} &= -\mathrm{i} \langle \Psi_0 | \left[\boldsymbol{J}(\boldsymbol{r}), \left\{ \boldsymbol{H}(t_0) - \boldsymbol{H}'(t_0) \right\} \right] | \Psi_0 \rangle \\ &= -n(\boldsymbol{r}, t_0) \nabla \left\{ v(\boldsymbol{r}, t_0) - v'(\boldsymbol{r}, t_0) \right\}. \end{aligned} \tag{2.50}$$

A detailed derivation of how to get to the second line of Equation 2.50 is shown in Appendix A. As a consequence, if the two potentials differ at time t_0, the two current densities $\boldsymbol{j}$ and $\boldsymbol{j}'$ will differ at some time infinitesimally later. With the requirement that the potentials may be Taylor-expandable around t_0, and k now denoting the smallest k for which Equation 2.47 holds, we need to evaluate the equation of motion, i.e. Equation 2.49, k times to find

$$\frac{\partial^{k+1}}{\partial t^{k+1}} \left\{ \boldsymbol{j}(\boldsymbol{r}, t) - \boldsymbol{j}'(\boldsymbol{r}, t) \right\} \Big|_{t=t_0} = -n(\boldsymbol{r}, t_0) \nabla \left\{ v_k(\boldsymbol{r}) - v'_k(\boldsymbol{r}) \right\}, \tag{2.51}$$

thereby concluding that the current densities differ at $t > t_0$ if the potentials differ by more than a purely time-dependent function.

In a second step, it needs to be shown that if the current densities differ, so will the densities, both of which being related to each other by the continuity equation:

$$\frac{\partial}{\partial t} n(\boldsymbol{r}, t) = -\nabla \boldsymbol{j}(\boldsymbol{r}, t). \tag{2.52}$$

Taking the $(k+1)$-th time derivative, we get

$$\begin{aligned} \frac{\partial^{k+2}}{\partial t^{k+2}} \left\{ \boldsymbol{n}(\boldsymbol{r}, t) - \boldsymbol{n}'(\boldsymbol{r}, t) \right\} \Big|_{t=t_0} &= -\nabla \frac{\partial^{k+1}}{\partial t^{k+1}} \left\{ \boldsymbol{j}(\boldsymbol{r}, t) - \boldsymbol{j}'(\boldsymbol{r}, t) \right\} \Big|_{t=t_0} \\ &= \nabla \left(n(\boldsymbol{r}, t_0) \nabla \left\{ v_k(\boldsymbol{r}) - v_k'(\boldsymbol{r}) \right\} \right). \end{aligned} \tag{2.53}$$

It is now left to show that, under the conditions stated above, the right-hand side of Equation 2.53 cannot vanish, for which we define the shorthand notation

$$\nabla \left(n(\boldsymbol{r}, t_0) \nabla \left\{ v_k(\boldsymbol{r}) - v_k'(\boldsymbol{r}) \right\} \right) =: \nabla (n_0 \nabla \Delta v_k). \tag{2.54}$$

Taking the integral over all space of $\nabla(\Delta v_k n_0 \nabla \Delta v_k)$, we can make use of the divergence theorem:

$$\int_V \mathrm{d}\boldsymbol{r}\, \nabla(\Delta v_k n_0 \nabla \Delta v_k) = \int_{\partial V} \mathrm{d}\boldsymbol{S}\, \Delta v_k n_0 \nabla \Delta v_k, \tag{2.55}$$

where the flux integral on the right-hand side vanishes for realistic potentials [179]. Applying the product rule on the left-hand side leads to

$$\begin{aligned} &\int_V \mathrm{d}\boldsymbol{r}\, \Delta v_k \nabla (n_0 \nabla \Delta v_k) + \int_V \mathrm{d}\boldsymbol{r}\, n_0 (\nabla \Delta v_k)^2 = 0 \\ \Rightarrow &\int_V \mathrm{d}\boldsymbol{r}\, \Delta v_k \nabla (n_0 \nabla \Delta v_k) = -\int_V \mathrm{d}\boldsymbol{r}\, n_0 (\nabla \Delta v_k)^2. \end{aligned} \tag{2.56}$$

It is now straightforward to see that the integrand on the right-hand side of Equation 2.56 is non-zero, since Δv_k is non-zero by construction and therefore the right-hand side of Equation 2.53 cannot vanish, which completes the proof of the Runge-Gross theorem.

In summary, it has been shown that two densities, $n(\boldsymbol{r}, t)$ and $n'(\boldsymbol{r}, t)$, both evolving from the same initial many-body state $\Psi(t_0)$ will start to differ at infinitesimal time later than t_0, if their potentials $v(\boldsymbol{r}, t)$ and $v'(\boldsymbol{r}, t)$ differ by more than a merely time-dependent function and are both Taylor-expandable around t_0. This establishes the fundamental existence theorem of TDDFT: for a given initial state, there exists an invertible mapping of the time-dependent density on the time-dependent potentials. All observables are therefore unique functionals of the density and the many-body initial state. The additional dependency on the initial state is not a consequence of the construction of TDDFT but rather an unavoidable facet of any initial-value problem, such as the time-dependent SE. For practical calculations, we would like to establish a representation in analogy to the KS scheme, which is yet to be shown and will be part of the subsequent paragraph.

2.2.2 The van Leeuwen Theorem

Aiming at a time-dependent fashion of the KS scheme, we want to map the problem on a different two-particle interaction, i.e. non-interacting particles. Therefore, consider the Hamiltonian

$$\boldsymbol{H}'(t) = \boldsymbol{T} + \boldsymbol{U}' + \boldsymbol{V}'(t), \tag{2.57}$$

which differs in the interaction potential $u'(\boldsymbol{r}-\boldsymbol{r}')$ and the external potential $v'(\boldsymbol{r})$ from the reference Hamiltonian $\boldsymbol{H}(t)$. Imposing the same conditions on the external potentials as before, namely being Taylor-expandable around time t_0, we assume furthermore that the primed system starts from a different initial state $\Psi'(t_0)$ than the reference system. The task is now to show that, under these conditions, the primed system can lead to the same density as the reference system. As a first step, consider an equation of motion for the current density, i.e.

$$\partial_t \boldsymbol{j}(\boldsymbol{r},t) = -\mathrm{i}\langle\Psi(t)|\left[\boldsymbol{J}(\boldsymbol{r}),\boldsymbol{H}(t)\right]|\Psi(t)\rangle, \tag{2.58}$$

which leads to

$$\frac{\partial}{\partial t}\boldsymbol{j}(\boldsymbol{r},t) = -n(\boldsymbol{r},t)\nabla v(\boldsymbol{r},t) - \boldsymbol{F}(\boldsymbol{r},t), \tag{2.59}$$

with additional force densities arising from internal kinetic- and interaction effects in the many electron system [180, 157], that we subsume under $\boldsymbol{F}(\boldsymbol{r},t)$ for the following. Taking the divergence,

$$\frac{\partial}{\partial t}\nabla\boldsymbol{j}(\boldsymbol{r},t) = -\nabla\left(n(\boldsymbol{r},t)\nabla v(\boldsymbol{r},t)\right) - \nabla\boldsymbol{F}(\boldsymbol{r},t), \tag{2.60}$$

and using the continuity equation, Equation 2.52, produces

$$\frac{\partial^2}{\partial t^2}n(\boldsymbol{r},t) = \nabla\left(n(\boldsymbol{r},t)\nabla v(\boldsymbol{r},t)\right) - \nabla\boldsymbol{F}(\boldsymbol{r},t). \tag{2.61}$$

Writing the same equation for the primed system and subtracting it from the unprimed, we get

$$\nabla\left(n(\boldsymbol{r},t)\nabla\left\{v(\boldsymbol{r},t)-v'(\boldsymbol{r},t)\right\}\right) = \nabla\left\{\boldsymbol{F}(\boldsymbol{r},t)-\boldsymbol{F}'(\boldsymbol{r},t)\right\}, \tag{2.62}$$

where it has been assumed that both densities are identical at all times. Equation 2.62 is a second order differential equation in time (reminiscent from Equation 2.61) and as initial conditions we require that for both initial states, $\Psi(t_0)$ and $\Psi'(t_0)$, the densities $n(\boldsymbol{r},t_0)$ and $n'(\boldsymbol{r},t_0)$ are equal. Additionally, we demand that

$$\partial_t n(\boldsymbol{r},t)\Big|_{t=t_0} = \partial_t n'(\boldsymbol{r},t)\Big|_{t=t_0}. \tag{2.63}$$

Note that from this requirement, it also follows that the linear momentum of both systems must be equal at initial time t_0, since

$$\boldsymbol{P}(t) = \int \mathrm{d}\boldsymbol{r}\; \boldsymbol{j}(\boldsymbol{r},t) = \int \mathrm{d}\boldsymbol{r}\; \boldsymbol{r}\frac{\partial}{\partial t}n(\boldsymbol{r},t), \tag{2.64}$$

where the continuity equation has been used in the last step and it has been assumed that the currents vanish at infinity. It turns out, however, that it is possible to construct initial states for which the densities, and their time-derivatives, are equal at t_0, while the currents do not vanish at infinity [180]. Such cases can be excluded with the condition $\boldsymbol{P}(t_0) < \infty$. As boundary condition, one can demand that $v(\boldsymbol{r},t) = v'(\boldsymbol{r},t)$ for $\boldsymbol{r}\to\infty$, which also fixes $c(t)$ in $v'(\boldsymbol{r},t)$. Then Equation 2.62 is a Sturm-Liouville differential equation [180, 157]. Using the abbreviations $\Delta v(\boldsymbol{r},t) := v(\boldsymbol{r},t) - v'(\boldsymbol{r},t)$ and $\Delta\boldsymbol{F}(\boldsymbol{r},t) := \boldsymbol{F}(\boldsymbol{r},t) - \boldsymbol{F}'(\boldsymbol{r},t)$, we can write our differential equation at time t_0 as

$$\nabla\left(n(\boldsymbol{r},t_0)\nabla\Delta v(\boldsymbol{r},t_0)\right) = \nabla\Delta\boldsymbol{F}(\boldsymbol{r},t_0). \tag{2.65}$$

A solution for $\Delta v(\boldsymbol{r}, t_0)$ exists, since $\Delta \boldsymbol{F}(\boldsymbol{r}, t_0)$ can be constructed from the given initial states $\Psi(t_0)$ and $\Psi'(t_0)$ and we thus obtain $v'(\boldsymbol{r}, t_0)$. Remember that $v'(\boldsymbol{r}, t_0)$ is, by construction, Taylor-expandable around t_0, i.e.

$$v'(\boldsymbol{r}, t) = \sum_k^{\infty} \frac{1}{k!} v'_k(\boldsymbol{r})(t - t_0)^k, \tag{2.66}$$

with

$$v'_k(\boldsymbol{r}) = \frac{\partial^k}{\partial t^k} v'(\boldsymbol{r}, t)\Big|_{t=t_0} \tag{2.67}$$

By obtaining $v'(\boldsymbol{r}, t_0)$, we have therefore determined the term $v'_0(\boldsymbol{r})$ in the Taylor expansion of $v'(\boldsymbol{r}, t)$. Taking the first time-derivative of Equation 2.65 at time t_0 leads to

$$\nabla \left(\frac{\partial}{\partial t} n(\boldsymbol{r}, t_0)\Big|_{t=t_0} \nabla \Delta v(\boldsymbol{r}, t_0) + n(\boldsymbol{r}, t_0) \nabla \frac{\partial}{\partial t} \Delta v(\boldsymbol{r}, t_0) \right)\Big|_{t=t_0} = \tag{2.68}$$

$$= \nabla \left(\frac{\partial}{\partial t} n(\boldsymbol{r}, t_0)\Big|_{t=t_0} \nabla (v_0(\boldsymbol{r}) - v'_0(\boldsymbol{r})) + n(\boldsymbol{r}, t_0) \nabla (v_1(\boldsymbol{r}) - v'_1(\boldsymbol{r})) \right)\Big|_{t=t_0} = \frac{\partial}{\partial t} \nabla \Delta \boldsymbol{F}(\boldsymbol{r}, t_0)\Big|_{t=t_0},$$

from which we infer $v'_1(\boldsymbol{r})$. For higher orders in k, we always get $v'_k(\boldsymbol{r})$ from $v'_{k-1}(\boldsymbol{r})$ and thus recursively get $v'(\boldsymbol{r}, t)$ by explicit construction. This completes the proof of the van Leeuwen theorem, that can be summarized in the following statement. For a given electron interaction $u(\boldsymbol{r}, \boldsymbol{r}')$, external potential $v(\boldsymbol{r}, t)$ and initial state $\Psi(t_0)$, there exists a different system with an interaction $u'(\boldsymbol{r}, \boldsymbol{r}')$ and an external potential $v'(\boldsymbol{r}, t)$, which is unique up to a purely time-dependent function $c(t)$, that reproduces the *same* time-dependent density.

Just as in the case of ground state DFT, we are especially interested in the case $u'(\boldsymbol{r}, \boldsymbol{r}') = 0$, because we want to map the system of interacting electrons onto an auxiliary system of non-interacting electrons and thus obtain a time-dependent version of the KS scheme. With the theoretical foundations provided by the van Leeuwen theorem, this is indeed possible. The academic questions if *any* system can be represented by a potential that is Taylor-expandable around t_0 and if this condition can be relaxed, are still open [181, 182, 183, 184, 185]. For practical calculations in the systems of our interest, however, everything is well-defined and in the following we will turn to the description of the time-dependent KS scheme and further approximations.

2.2.3 The Time-dependent Kohn-Sham Scheme

For a numerical propagation of a many-electron system in an non-interacting KS Hamiltonian, that is now explictily time-dependent, we suppose that from a preceding DFT calculation for the ground state, a solution to the Schrödinger equation

$$\boldsymbol{H}_{\mathrm{KS}} \varphi_i^0(\boldsymbol{r}) = E_i \varphi_i^0(\boldsymbol{r}) \tag{2.69}$$

exists. From the wave functions, we know the density of the ground state:

$$n_{\mathrm{KS}}^0(\boldsymbol{r}) = \sum_j^N \left| \varphi_j^0(\boldsymbol{r}) \right|^2. \tag{2.70}$$

At a later time $t > t_0$, we add a time-dependent potential and therefore get the time-dependent Kohn-Sham (TDKS) potential as

$$v_{\mathrm{KS}}[n, \Psi_0, \Phi_0](\boldsymbol{r}, t) = v(\boldsymbol{r}, t) + \int \mathrm{d}\boldsymbol{r}' \frac{n(\boldsymbol{r}', t)}{|\boldsymbol{r} - \boldsymbol{r}'|} + v_{\mathrm{xc}}[n, \Psi_0, \Phi_0](\boldsymbol{r}, t). \tag{2.71}$$

There are several things to remark for the TDKS potential. First of all, the entities are now functionals of the time-dependent density $n(\boldsymbol{r}, t)$, with the exception of the external potential $v(\boldsymbol{r}, t)$ of course. Just as in ground state DFT, the above equation should be seen as the definition of the time-dependent exchange-correlation potential v_{xc}, since v_{KS} must reproduce the same time-dependent density as the full system. As mentioned in the paragraphs dealing with the Runge-Gross- and the van Leeuwen-theorem, v_{xc} carries an additional dependence on the many-body initial state Ψ_0, and on the KS ground state Φ_0. While Ψ_0 is of course not accessible, we assume that the system is initially in its ground state and Φ_0 to be a single Slater determinant, constructed of the $\varphi_j(\boldsymbol{r})$. Note that while we do know the density at time t_0, this is not enough since also the phase information of the wave function needs to be fixed at initial time.

Before we describe the local density approximation for v_{xc} in the next paragraph, an additional property of the TDKS scheme needs to be discussed. For obtaining the minimal energy of the ground state, we needed a self-consistency cycle, as described in the foundations of DFT, see Paragraph 2.1.1. For the TDKS scheme, an exact analogy would mean that we could adhere to the following procedure.

(i) Take the density and wave functions at t_0 from the ground state calculation.

(ii) Make an initial guess for the density $n^{(0)}(\boldsymbol{r}, t)$ at *all* times $t > t_0$.

(iii) Compute $v_{\mathrm{KS}}[n^{(0)}](\boldsymbol{r}, t)$.

(iv) Construct the KS Hamiltonian $\boldsymbol{H}_{\mathrm{KS}}[n^{(0)}]$.

(v) Solve the TDKS equation for the orbitals $\varphi_j^{(1)}(\boldsymbol{r}, t)$.

(vi) Obtain new density $n^{(1)}(\boldsymbol{r}, t)$ from $\varphi_j^{(1)}(\boldsymbol{r}, t)$.

(vii) Compare new density $n^{(1)}(\boldsymbol{r}, t)$ with old density $n^{(0)}(\boldsymbol{r}, t)$.

If the convergence criterion is not fulfilled in step (vii), then repeat the procedure of steps (iii)-(vi) until the desired convergence is reached. Clearly, already the second step of guessing a global time-dependent density seems hopeless for the general case and in practice, we go a different way by propagating the TDKS equation using a numerical propagator for time-dependent Schödinger equations, such as the Crank-Nicolson algorithm [186] or one of the many other available [187]. All of these methods discretize the time variable and approximate the quantum mechanical time-evolution operator. Then, the global self-consistency requirement can be limited to one that is only local in time by, for instance, a predictor-corrector scheme.

2.2.4 The Adiabatic Local Density Approximation

In contrast to ground state DFT, the approximations for exchange-correlation effects in TDDFT introduce very little new physics, despite exhibiting an additional degree of freedom, i.e. the time variable. Excluding a few exceptions [188, 189, 190], in almost all cases the adiabatic approximation to the respective ground state DFT functionals is used. If $n_0(\boldsymbol{r})$ is the ground state

density and $v_{\mathrm{xc}}^0[n_0](\boldsymbol{r})$ the ground state xc functional, then the adiabatic approximation is defined as

$$v_{\mathrm{xc}}^a(\boldsymbol{r},t) = v_{\mathrm{xc}}^0[n_0](\boldsymbol{r})\Big|_{n_0\to n(\boldsymbol{r},t)}. \tag{2.72}$$

This means essentially that the adiabatic exchange-correlation potential is a functional of the density at the *actual* time and thus carries no memory of the past of the system. For most systems, this works surprisingly well. Counterexamples are e.g. double excitations [191, 192] or resonantly-driven systems [193, 194]. In this work, the adiabatic local density approximation (ALDA) is used exclusively for time-dependent calculations. As in the static case, we use the energy density of the homogeneous electron gas $e_{\mathrm{xc}}^{(HEG)}$ (see Paragraph 2.1.2):

$$v_{\mathrm{xc}}^{(\mathrm{ALDA})}(\boldsymbol{r},t) = \frac{\mathrm{d}e_{\mathrm{xc}}^{(HEG)}(n)}{\mathrm{d}n}\bigg|_{n=n(\boldsymbol{r},t)}. \tag{2.73}$$

As a consequence, the ALDA will of course inherit all the shortcomings of the static LDA, in addition to the problems introduced by the adiabatic approximation discussed above. Nonetheless, excitation energies of molecular systems computed with the ALDA and real-time TDDFT are remarkably good, which will be shown in detail in Paragraph 2.2.6.

2.2.5 Light-matter Interaction and Dipole Moments

Before we discuss how excited states or spectroscopic observables can be computed within TDDFT, we need to set the stage and introduce miscellaneous entities that occur in quantum mechanical light-matter interaction. First of all, let us take a step back from the TDKS Hamiltonian and write the non-relativistic, electronic N-body Hamiltonian with an electromagnetic vector field $\boldsymbol{A}(\boldsymbol{r},t)$ coupled to the system. In the Coulomb gauge, we write

$$\boldsymbol{H}(t) = \sum_{j=1}^{N}\left[\frac{1}{2}\left(\boldsymbol{p}_j + \frac{1}{c}\boldsymbol{A}(\boldsymbol{r}_j,t)\right)^2 + \frac{\mu_B}{c}\boldsymbol{\sigma}\nabla_j\times\boldsymbol{A}(\boldsymbol{r}_j,t) + v_{\mathrm{ext}}(\boldsymbol{r}_j) + \sum_{k>j}^{N}\frac{1}{|\boldsymbol{r}_j-\boldsymbol{r}_k|}\right], \tag{2.74}$$

where μ_B is the Bohr magneton and $\boldsymbol{\sigma}$ denotes the vector of Pauli matrices. This implies that the photon field can be treated as a classical field, which is justified for photon numbers larger than one per cubic wavelength (typically >4 orders of magnitude larger for the fields treated in this work, see e.g. Reference [157]).

As a next step, we make use of the dipole approximation. If the photon field varies only slowly on the characteristic length scale of the electrons, we can treat the electromagnetic field as uniform in space, i.e. $\boldsymbol{A}(\boldsymbol{r},t)\to\boldsymbol{A}(t)$. Then the curl of $\boldsymbol{A}$ vanishes and we are left with

$$\boldsymbol{H}(t) = \sum_{j=1}^{N}\left[\frac{1}{2}\left(\boldsymbol{p}_j + \frac{1}{c}\boldsymbol{A}(t)\right)^2 + v_{\mathrm{ext}}(\boldsymbol{r}_j) + \sum_{k>j}^{N}\frac{1}{|\boldsymbol{r}_j-\boldsymbol{r}_k|}\right]. \tag{2.75}$$

Moreover, one often makes the additional approximation to ignore terms proportional to $\mathcal{O}(\boldsymbol{A}^2)$, which is justified when the momenta induced by the photon field are small in reference to the electrons' kinetic momenta. In this case, Equation 2.75 reduces to

$$\boldsymbol{H}(t) = \sum_{j=1}^{N}\left[\frac{1}{2}\boldsymbol{p}_j^2 + \frac{1}{c}\boldsymbol{p}_j\boldsymbol{A}(t) + v_{\mathrm{ext}}(\boldsymbol{r}_j) + \sum_{k>j}^{N}\frac{1}{|\boldsymbol{r}_j-\boldsymbol{r}_k|}\right]. \tag{2.76}$$

Inherited from the gauge freedom in electrodynamics, we can similarly represent the electron-photon coupling in the Hamiltonian within different gauges. In the length gauge, the $\boldsymbol{p}_j \boldsymbol{A}(t)$-term is replaced by $\boldsymbol{r}_j \boldsymbol{E}(t)$, with the electromagnetic field

$$\boldsymbol{E}(t) = -\frac{1}{c}\frac{\partial \boldsymbol{A}(t)}{\partial t}. \tag{2.77}$$

Note that the length gauge is only defined in the dipole approximation.

Gauge freedom also applies if we want to consider optical matrix elements of the static Hamiltonian $\boldsymbol{H}_0$, for which we assume a system of eigenstates $\{|n\rangle\}$, i.e.

$$\boldsymbol{H}_0|n\rangle = \varepsilon_n|n\rangle. \tag{2.78}$$

Dipole matrix elements in the length form are then defined as

$$\boldsymbol{d}_{nm} = \sum_{j=1}^{N} \langle n|\boldsymbol{r}_j|m\rangle, \tag{2.79}$$

and are a measure of the probability for transitions of the system between different eigenstates $|n\rangle \to |m\rangle$. Using the commutation relation

$$\left[\boldsymbol{r}_j, \boldsymbol{H}_0\right] = \mathrm{i}\boldsymbol{p}_j, \tag{2.80}$$

we can write

$$\boldsymbol{d}_{nm} = \sum_{j=1}^{N} \frac{\mathrm{i}}{\varepsilon_m - \varepsilon_n} \langle n|\boldsymbol{p}_j|m\rangle, \tag{2.81}$$

which is usually referred to as the *velocity form* of the dipole matrix element. In addition, there exists also the *acceleration form*, which reads

$$\boldsymbol{d}_{nm} = \sum_{j=1}^{N} \frac{1}{(\varepsilon_m - \varepsilon_n)^2} \langle n|\nabla_j v_{\mathrm{ext}}(\boldsymbol{r}_j)|m\rangle. \tag{2.82}$$

If the exact eigenstates of the N-electron system were known, all the formulations of the dipole matrix elements would be equal; in practice, however, differences can arise due to the approximations introduced in DFT or due to numerical parameter, such as basis set truncation. If non-local pseudopotentials are used to approximate the core electrons, additional care has to be taken since the non-local part of v_{ext} does not commute with the momentum- or position operator and extra terms arise [195, 196].

For a time-dependent Hamiltonian $\boldsymbol{H}(t)$, we can define the time-dependent dipole moment with the time-dependent density $n(\boldsymbol{r}, t)$ as

$$\boldsymbol{d}(t) = \sum_{j=1}^{N} \int \mathrm{d}\boldsymbol{r}\, \boldsymbol{r}_j\, n(\boldsymbol{r}, t). \tag{2.83}$$

Its time-derivatives can be obtained by the Ehrenfest theorem for an observable O:

$$\frac{\mathrm{d}}{\mathrm{d}t}\langle O\rangle = -\mathrm{i}\,\langle [O, \boldsymbol{H}(t)]\rangle + \left\langle \frac{\partial}{\partial t} O \right\rangle, \tag{2.84}$$

as

$$\frac{\mathrm{d}}{\mathrm{d}t}\boldsymbol{d}(t) = \sum_{j=1}^{N} \int \mathrm{d}\boldsymbol{r}\ \Psi^*(t)\boldsymbol{p}_j\Psi(t), \tag{2.85}$$

and

$$\frac{\mathrm{d}^2}{\mathrm{d}t^2}\boldsymbol{d}(t) = -\sum_{j=1}^{N} \int \mathrm{d}\boldsymbol{r}\ n(\boldsymbol{r},t)\nabla_j v_{\mathrm{ext}}(\boldsymbol{r}_j,t). \tag{2.86}$$

Having gained access to the dipole moments, we will show in the following how this quantity can be related to observables in spectroscopy. As stated above, the dipole moments can on the one hand be formulated in terms of matrix elements with eigenstates of the time-independent problem. This treatment will be subject to the paragraph about linear-response TDDFT (Paragraph 2.2.7). On the other hand, we can use the time-dependent density in order to obtain time-dependent dipole moments. The questions of how this entity can be recorded from real-time propagation of the TDKS equations and how the time-dependent dipole moment is related to optical spectroscopy, are discussed in the following paragraph.

2.2.6 Optical Excitations from Real-time TDDFT

Optical spectroscopy probes the excitations of quantum systems with light in the energy range from hundreds of meV to few eV, an energy window somewhat correlated to the human visible range. In this energy window, transitions involving the frontier orbitals of molecules, or, respectively, the highest occupied and lowest unoccupied bands in solids, play the most important role. In addition, the low-energy part of the optical spectrum and the infrared part can be sensitive to vibrations, which are not part of this work since we ignore the influence of nuclear degrees of freedom and their imprint on the electronic structure, as expressed by the Franck-Condon principle [197, 198], for instance.

In general, we could couple a monochromatic electromagnetic field to our system, propagate it in time and watch how much the electrons respond to this perturbation. If we hit an eigenmode of the system, this response will be drastically enhanced and we could then vary the frequency of the field to find all the eigenmodes versus the photon energy. Although possible, there is a more efficient way. By taking a Dirac delta pulse, we achieve a perturbation that acts instantly on the system. Written as an electric field polarized in the Cartesian ν-direction, we have

$$E_\nu(t) = E_\nu^0\delta(t). \tag{2.87}$$

This field has the important property that it can excite all eigenmodes of the system, which can be seen by taking the Fourier transform,

$$E_\nu(\omega) = E_\nu^0, \tag{2.88}$$

and thereby going from the time- to the frequency domain. Adding a few more items to the list, we define $p_\mu = -d_\mu$, and with it the polarizability tensor as

$$p_\mu(t) = \sum_\nu \alpha_{\mu\nu}(t)E_\nu(t). \tag{2.89}$$

In this way, its off-diagonal elements can also give a measure of how a system can respond in a different direction than it was initially perturbed. In the frequency domain, we have

$$\alpha_{\mu\nu}(\omega) = \frac{1}{E_\nu^0} \int \mathrm{d}t \; \mathrm{e}^{\mathrm{i}\omega t} p_\mu(t), \tag{2.90}$$

and the imaginary part of the polarizability can be directly connected to the photoabsorption cross section,

$$\sigma_{\mu\nu}(\omega) = \frac{4\pi\omega}{c} \Im(\alpha_{\mu\nu}), \tag{2.91}$$

and can therefore be compared to experimental data.

The possibility to extract the time-dependent dipole moment from a real-time TDDFT calculation and compute optical properties with it, was first described by Yabana and Bertsch [175] for gas-phase molecules and later extended to clusters [199, 200] and the dielectric function in periodic systems [201]. The approach can be summarized as follows. For one polarization direction ν of the field, apply a delta kick at initial time t_0. Note that for this step, it is also possible to either switch on or off a constant electric field at t_0, such that $E_\nu = E_\nu^0 \Theta(t \pm t_0)$, with Θ denoting the Heaviside step-function. Then the system is propagated for time T, while all three μ-components of the time-dependent dipole moment are recorded. If this procedure is repeated for the other two Cartesian directions of the field polarization ν, we obtain $\alpha_{\mu\nu}$ from Equation 2.90 and, subsequently, $\sigma_{\mu\nu}$ from Equation 2.91. As a technical remark, when evaluating the Fourier transform over the finite time interval T, one needs to introduce a window function or an additional damping parameter in order to eliminate numerical instabilities [202].

While the optical absorption spectrum can also be computed in the linear-response formulation, which is detailed in the next paragraph, the real-time propagation method has the advantage that it is not restricted to the linear response of the system to some external perturbation and therefore arbitrarily high field strengths can be applied. This allows for the description of non-linear phenomena, such as high-harmonic generation [203] or field-induced effects [204].

2.2.7 Optical Excitations from Linear Response TDDFT

In this paragraph the linear response formalism of TDDFT is reviewed with the computation of optical excitations in mind. Although in the case of Casida's equation [174], which we will restrict ourselves to here, no observables are actually calculated from time-propagation, the apparatus of TDDFT is required for the formal derivation of the method. In fact, the majority of applications of TDDFT fall in the linear response regime and therefore a large body of introductory and review literature exist [205, 206, 207, 208, 209, 210] beyond the original formulation of local density linear response TDDFT [211, 212].

Consider a system of electrons in the ionic potential v_0 in its ground state at initial time t_0. We now assume that a perturbation in the form of a scalar potential $v_1(\boldsymbol{r}, t)$ will modify the external potential $v_{\mathrm{ext}}(\boldsymbol{r}, t_0) = v_0$ and the ground state density $n(\boldsymbol{r}, t_0) = n_0(\boldsymbol{r})$ at some later time $t > t_0$. We can then write the external potential as $v_{\mathrm{ext}}(\boldsymbol{r}, t) = v_0 + v_1(\boldsymbol{r}, t)$ and the time-dependent density as

$$n(\boldsymbol{r}, t) = n_0(\boldsymbol{r}) + n_1(\boldsymbol{r}, t) + n_2(\boldsymbol{r}, t) + \ldots, \tag{2.92}$$

where the n_i result from a Taylor expansion with respect to the perturbation, labeled by the order in v_1. A converging perturbation expansion requires the interaction to be sufficiently

small and in the linear order we can write can write the density response as

$$n_1(\boldsymbol{r},t) = \int \mathrm{d}t' \int \mathrm{d}\boldsymbol{r}' \chi(\boldsymbol{r},t,\boldsymbol{r}',t') v_1(\boldsymbol{r}',t'). \tag{2.93}$$

For defining the response function χ, different routes can be followed. With the many-body ground state Ψ_0 given, the density-density response is defined as

$$\chi(\boldsymbol{r},t,\boldsymbol{r}',t') = -\mathrm{i}\Theta(t-t')\langle\Psi_0|\left[\boldsymbol{n}(\boldsymbol{r},t),\boldsymbol{n}(\boldsymbol{r}',t')\right]|\Psi_0\rangle, \tag{2.94}$$

where $\boldsymbol{n}$ is the density operator in the interaction picture and where the step function ensures causality. In frequency space, this expression can be written in the Källén-Lehmann representation [213, 214, 157]:

$$\chi(\boldsymbol{r},\boldsymbol{r}',\omega) = \lim_{\eta\to 0^+} \sum_{n=1}^{\infty} \left\{ \frac{\langle\Psi_0|\boldsymbol{n}(\boldsymbol{r})|\Psi_n\rangle\langle\Psi_n|\boldsymbol{n}(\boldsymbol{r}')|\Psi_0\rangle}{\omega-\Omega_n+\mathrm{i}\eta} - \frac{\langle\Psi_0|\boldsymbol{n}(\boldsymbol{r}')|\Psi_n\rangle\langle\Psi_n|\boldsymbol{n}(\boldsymbol{r})|\Psi_0\rangle}{\omega+\Omega_n+\mathrm{i}\eta} \right\}. \tag{2.95}$$

Here, the sum runs over all excited states Ψ_n of the many-body system and it is obvious that $\chi(\boldsymbol{r},\boldsymbol{r}',\omega)$ will have poles at the true excitation energies Ω_n. Alternatively, and more in a density functional spirit, we can define the density-density response function as a change of the density induced by the external potential and write (in the time domain)

$$\chi(\boldsymbol{r},t,\boldsymbol{r}',t') = \left.\frac{\delta n[v_{\mathrm{ext}}](\boldsymbol{r},t)}{\delta v_{\mathrm{ext}}(\boldsymbol{r}',t')}\right|_{v_{\mathrm{ext}}[n_0]}. \tag{2.96}$$

This definition requires that the functional $n[v_{\mathrm{ext}}]$ can be inverted, i.e. $v_{\mathrm{ext}}(\boldsymbol{r},t) = v_{\mathrm{ext}}[n](\boldsymbol{r},t)$, which is guaranteed by the Runge-Gross theorem. In addition, χ can then be viewed as a functional of the ground-state density, a manifestation of the fact that the linear response of a system is encoded in its ground state properties.

Supported by the van Leeuwen theorem, we can also invoke the non-interacting TDKS system and define an analogous response function:

$$\chi_{\mathrm{KS}}(\boldsymbol{r},t,\boldsymbol{r}',t') = \left.\frac{\delta n[v_{\mathrm{KS}}](\boldsymbol{r},t)}{\delta v_{\mathrm{KS}}(\boldsymbol{r}',t')}\right|_{v_{\mathrm{KS}}[n_0]}. \tag{2.97}$$

We can now make the connection between the external potential and the TDKS system, which is given, in analogy to Equation 2.14, as

$$v_{\mathrm{KS}}(\boldsymbol{r},t) = v_{\mathrm{ext}}(\boldsymbol{r},t) + \int \mathrm{d}\boldsymbol{r}' \frac{n(\boldsymbol{r}',t)}{|\boldsymbol{r}-\boldsymbol{r}'|} + v_{\mathrm{xc}}(\boldsymbol{r},t). \tag{2.98}$$

With the chain rule for functional derivatives, we can relate the response function, defined as in Equation 2.96, with the TDKS system:

$$\chi(\boldsymbol{r},t,\boldsymbol{r}',t') = \int \mathrm{d}\boldsymbol{r}'' \int \mathrm{d}t'' \left.\frac{\delta n[v_{\mathrm{ext}}](\boldsymbol{r},t)}{\delta v_{\mathrm{KS}}(\boldsymbol{r}'',t'')} \frac{\delta v_{\mathrm{KS}}(\boldsymbol{r}'',t'')}{\delta v_{\mathrm{ext}}(\boldsymbol{r}',t')}\right|_{v_{\mathrm{ext}}[n_0]}. \tag{2.99}$$

Then, we calculate the functional derivative of v_{KS} with respect to v_{ext} as

$$\begin{aligned}\left.\frac{\delta v_{\mathrm{KS}}(\boldsymbol{r}'',t'')}{\delta v_{\mathrm{ext}}(\boldsymbol{r}',t')}\right|_{v_{\mathrm{ext}}[n_0]} =& \delta(\boldsymbol{r}''-\boldsymbol{r}')\delta(t''-t') \int \mathrm{d}\boldsymbol{r}''' \int \mathrm{d}t''' \left(\frac{\delta(t''-t''')}{|\boldsymbol{r}''-\boldsymbol{r}'''|} + \right. \\ &\left. + \frac{\delta v_{\mathrm{xc}}(\boldsymbol{r}'',t'')}{\delta n(\boldsymbol{r}''',t''')} \right) \frac{\delta n(\boldsymbol{r}''',t''')}{\delta v_{\mathrm{ext}}(\boldsymbol{r}',t')}.\end{aligned} \tag{2.100}$$

Inserting Equation 2.100 into Equation 2.99 leads to

$$\chi(\boldsymbol{r},t,\boldsymbol{r}',t') = \chi_{\mathrm{KS}}(\boldsymbol{r},t,\boldsymbol{r}',t') + \int \mathrm{d}\boldsymbol{r}'' \int \mathrm{d}t'' \int \mathrm{d}\boldsymbol{r}''' \int \mathrm{d}t''' \, \chi_{\mathrm{KS}}(\boldsymbol{r},t,\boldsymbol{r}'',t'') \cdot \\ \cdot \left(\frac{\delta(t''-t''')}{|\boldsymbol{r}''-\boldsymbol{r}'''|} + \left.\frac{\delta v_{\mathrm{xc}}(\boldsymbol{r}'',t'')}{\delta n(\boldsymbol{r}''',t''')}\right|_{n_0} \right) \chi(\boldsymbol{r}''',t''',\boldsymbol{r}',t'). \tag{2.101}$$

It is common to define the time-dependent exchange-correlation kernel as

$$f_{\mathrm{xc}}[n_0](\boldsymbol{r}'',t'',\boldsymbol{r}''',t''') := \left.\frac{\delta v_{\mathrm{xc}}[n_0](\boldsymbol{r}'',t'')}{\delta n(\boldsymbol{r}''',t''')}\right|_{n_0}, \tag{2.102}$$

and rewrite

$$\chi(\boldsymbol{r},t,\boldsymbol{r}',t') = \chi_{\mathrm{KS}}(\boldsymbol{r},t,\boldsymbol{r}',t') + \int \mathrm{d}\boldsymbol{r}'' \int \mathrm{d}t'' \int \mathrm{d}\boldsymbol{r}''' \int \mathrm{d}t''' \, \chi_{\mathrm{KS}}(\boldsymbol{r},t,\boldsymbol{r}'',t'') \cdot \\ \cdot \left(\frac{\delta(t''-t''')}{|\boldsymbol{r}''-\boldsymbol{r}'''|} + f_{\mathrm{xc}}[n_0](\boldsymbol{r}'',t'',\boldsymbol{r}''',t''') \right) \chi(\boldsymbol{r}''',t''',\boldsymbol{r}',t'). \tag{2.103}$$

This expression is a Dyson-type equation and has to to be solved self-consistently. If we further multiply it by the perturbing potential, i.e. $v_1(\boldsymbol{r}',t')$, and integrate over $\boldsymbol{r}'$ and t', we get the linear density response as

$$n_1(\boldsymbol{r},t) = \int \mathrm{d}\boldsymbol{r} \int \mathrm{d}t' \, \chi_{\mathrm{KS}}(\boldsymbol{r},t,\boldsymbol{r}',t') v_{\mathrm{KS},1}(\boldsymbol{r}',t'), \tag{2.104}$$

with the effective (TDKS) perturbing potential

$$v_{\mathrm{KS},1}(\boldsymbol{r}',t') := v_1(\boldsymbol{r}',t') + \int \mathrm{d}\boldsymbol{r}'' \, \frac{n_1(\boldsymbol{r}'',t)}{|\boldsymbol{r}'-\boldsymbol{r}''|} + \int \mathrm{d}\boldsymbol{r}'' \int \mathrm{d}t'' \, f_{\mathrm{xc}}[n_0](\boldsymbol{r}',t',\boldsymbol{r}'',t') n_1(\boldsymbol{r}'',t''). \tag{2.105}$$

Combining Equations 2.104 and 2.105, we have a formalism that is an *exact* representation of the linear response of a many-body system in terms of the auxiliary time-dependent Kohn-Sham system and the ground state density. The computation, however, has to be carried out in a self-consistent manner and $f_{\mathrm{xc}}[n_0]$ has to be approximated in a suitable way. Changing from the time domain to the frequency domain once more, we can also write the combination of Equations 2.104 and 2.105 as

$$n_1(\boldsymbol{r},\omega) = \int \mathrm{d}\boldsymbol{r}' \, \chi_{\mathrm{KS}}(\boldsymbol{r},\boldsymbol{r}',\omega) v_1(\boldsymbol{r}',\omega) + \\ + \int \mathrm{d}\boldsymbol{r}' \int \mathrm{d}\boldsymbol{r}'' \, \chi_{\mathrm{KS}}(\boldsymbol{r},\boldsymbol{r}',\omega) \left(\frac{1}{|\boldsymbol{r}'-\boldsymbol{r}''|} + f_{\mathrm{xc}}[n_0](\boldsymbol{r},\boldsymbol{r}',\omega) \right) n_1(\boldsymbol{r}'',\omega). \tag{2.106}$$

The response function of the KS system can be expressed in terms of pairs of occupied (valence) orbitals ϕ_v and unoccupied (conduction) orbitals ϕ_v from the ground state calculation,

$$\chi_{\mathrm{KS}}(\boldsymbol{r},\boldsymbol{r}',\omega) = \sum_{v,c} \frac{\varphi_v(\boldsymbol{r})\varphi_c^*(\boldsymbol{r})\varphi_v^*(\boldsymbol{r}')\varphi_c(\boldsymbol{r}')}{\omega - (\varepsilon_v - \varepsilon_c) + \mathrm{i}\eta}, \tag{2.107}$$

such that all necessary ingredients are on the table and optical spectra of molecules or clusters can be calculated.

In practice, the linear response of the density, as written in Equation 2.106, can be recast in to an anti-hermitian eigenvalue problem, which is known as the Casida equation [174]. The derivations that lead to this equation are beyond the scope of this thesis and we only present its final form and refer to the literature [174, 206, 207, 208, 209, 210]. For a set of real-valued occupied and unoccupied orbitals φ_v and φ_c, and neglecting the spin component, one can define

$$\begin{aligned} B_{vc,v'c'}(\omega) &= \delta_{vv'}\delta_{cc'}(\varepsilon_v - \varepsilon_c) + K_{vc,v'c'}(\omega), \\ K_{vc,v'c'}(\omega) &= \int \mathrm{d}\boldsymbol{r} \int \mathrm{d}\boldsymbol{r}' \; \varphi_v^*(\boldsymbol{r})\varphi_c(\boldsymbol{r}) f_{\mathrm{xc}}(\boldsymbol{r}', \boldsymbol{r}'', \omega)\varphi_{v'}(\boldsymbol{r}')\varphi_{c'}^*(\boldsymbol{r}'), \end{aligned} \tag{2.108}$$

and obtain the resonance energies Ω and solutions $\boldsymbol{X}$, $\boldsymbol{Y}$ from

$$\begin{pmatrix} \boldsymbol{B} & \boldsymbol{K} \\ \boldsymbol{K} & \boldsymbol{B} \end{pmatrix} \begin{pmatrix} \boldsymbol{X} \\ \boldsymbol{Y} \end{pmatrix} = \Omega \begin{pmatrix} -1 & 0 \\ 0 & 1 \end{pmatrix} \begin{pmatrix} \boldsymbol{X} \\ \boldsymbol{Y} \end{pmatrix}. \tag{2.109}$$

Finally, we want to address some aspects that are of relevance for the calculation of excitation energies via the Casida formalism. First, the choice of the exchange-correlation functional in the underlying DFT calculation for obtaining the set of occupied orbitals $\{\varphi_v\}$ and unoccupied orbitals $\{\varphi_c\}$ will influence the associated energies ε_v and ε_c and therefore the peak positions in the optical spectrum. It is known that the incorporation of a portion of exact exchange, as in hybrid functionals described in Paragraph 2.1.2, leads to a better agreement with experimental values [121, 123] and excitation energies from many-body Green's function approaches [215]. Second, the sum over unoccupied orbitals needs to be truncated, and it turns out that the method is rather sensitive to this cutoff. In convergence tests related to this work, we found that often times it can be necessary to incorporate a number of unoccupied orbitals that exceeds the number of occupied orbitals by a factor of five or more to converge the energy positions of first few optical excitations within 0.1 eV. Third, we restrict ourselves to the adiabatic approximation of the exchange-correlation kernel which also neglects the frequency-dependency. This excludes the applicability to systems with strong excitonic effects [216] or double excitations [217].

In comparison with the time-propagation method described in the preceding paragraph, some differences are noteworthy. While both methods give very similar results for the (adiabatic) LDA, the time-progation method is often restricted to the ALDA as hybrid functionals are very expensive. Therefore, the agreement with experimental data is usually superior for molecules in the gas-phase or in solution when optical spectra are computed with the linear response Casida method, if hybrid functionals are used for the ground state calculation. Moreover, excitations can be tracked down to the specific orbitals involved and give therefore generally more insight into the character of the excitation, for instance via natural transition orbitals [218], although a transition analysis is also possible for the time-propagation method [219, 220]. The biggest general advantage of the time-propagation method is the scaling with the number of electrons N: different implementations of the Casida equation scale from $\mathcal{O}(N^2)$ to $\mathcal{O}(N^3)$ while real-time TDDFT achieves a scaling between linear to $\mathcal{O}(N^2)$ and can therefore be much more efficient for large systems [157]. Moreover, the dependency on a large number of unoccupied orbitals in linear response TDDFT is also absent. It is the flexibility of the time-propagation method that makes it possible to be combined with the numerical simulation of the photoemission process, which will be described at the end of the following section and which will then enable us to directly simulate pump-probe photoemission experiments.

2.3 Simulation of Photoelectron Spectroscopy

In this section, we will briefly describe the photoemission experiment, which is the central measurement we compare our theoretical results to. Subsequently, different methods for making the connection between this experiment and electronic structure calculations are reviewed. Conceptually, in going from the plane wave approximation (PWA), to the scattered wave approximation (SWA), we incorporate important final state effects into the simulation of photoemission experiments. Altering the applicability of photoemission orbital tomography (POT), we show how the PWA can be extended to the description of bound electron-hole pairs, the excitons. Finally, we review how photoemission from both the ground state, as well an excited state, can be simulated within real-time time-dependent DFT (TDDFT).

2.3.1 The Photoemission Experiment

The observation that light of a certain wavelength can release electrons from a sample, i.e. the photoelectric effect, was first made by Hertz [221] and later explained by Einstein [222]. This explanation was one of the key corroborations of Planck's postulation of an elementary quantum of energy [223] and the reason for Einstein's Nobel prize of the year 1921. For the first time, light would be regarded as *photons* carrying the energy $\hbar\omega$ ($\hbar = 1$ in our system of units). When a sufficiently large photon energy is transferred to the electrons in a sample, they can leave the system and carry the maximum kinetic energy

$$E_{\text{kin}} = \omega - E_b - \Phi. \tag{2.110}$$

This energy conservation respects that a particular portion of the photon energy is neccesary to break the binding of the electron to the rest of the system, i.e. the *binding energy* E_b, and that while escaping the sample, the electron experiences electromagnetic attraction by the sample that has to be overcome until it reaches the energy level of the vacuum. This energy is usually called the *work function* Φ of the sample and the remainder is the kinetic energy of the photoelectron, E_{kin}.

The first observation of the photoelectric effect by Hertz, as well as refined experiments by Millikan [224]—who called energy quantization "a reckless hypothesis" despite confirming it—were done with metal samples. Due to the high density of states at the Fermi level, the binding energy played a minor role for the observation of the maximum kinetic energy. Decades later, and most notably due to the work of Siegbahn (Nobel prize 1981) for energies in the x-ray regime and Vilesov [225] and Turner [226] for UV energies, the observable of interest had changed: when recording the kinetic energy, one could actually deduce the binding energy from Equation 2.110 and thereby establish a spectroscopic technique. If not only energy conservation but also momentum conservation is considered, this method can even be pushed further. While the magnitude of the photoelectron momentum is given by the kinetic energy,

$$|\boldsymbol{k}| = \sqrt{2E_{\text{kin}}}, \tag{2.111}$$

different conservation laws for the individual components of $\boldsymbol{k}$ apply. It is commonly assumed that the component parallel to the surface is conserved, while the momentum perpendicular to the surface may be affected by the process itself. In order to further elucidate the momentum conservation, in Figure 2.1 the geometry of the quantities of interest in the process is depicted. The incoming photon impinges on the sample under the incidence angle ϑ_γ with respect to the surface normal (the Cartesian z-direction). In the dipole approximation, as detailed in Paragraph 2.2.5, the electromagnetic field is fully characterized by the photon energy ω and the

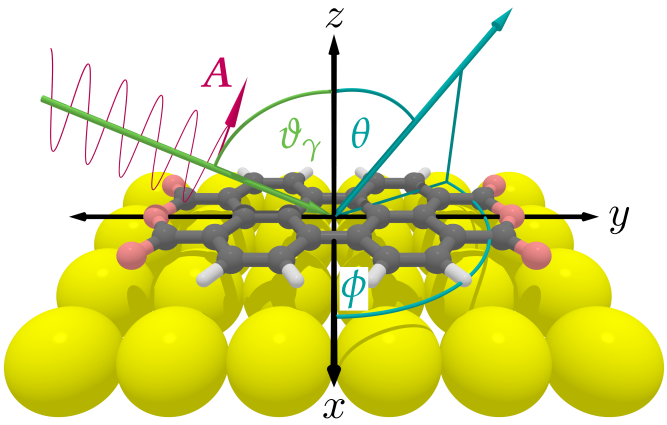

Figure 2.1: **Sketch of the photoemission process.** An incoming photon is depicted by its incident direction (green), the angle ϑ_γ with respect to the surface normal (z) and the corresponding polarization vector of the electromagnetic field vector $\boldsymbol{A}$ (red). The outgoing photoelectron (blue) leaves the sample under the polar- and azimuthal angles θ and ϕ, respectively.

polarization vector $\boldsymbol{A}$, which we consider as spatially constant over the atomistic dimensions in the following. After the process, the photoelectron leaves the sample under the angles θ and ϕ. These angles can be measured with different techniques and instruments, where we focus on two generally different setups with different consequences for the simulation of the experiment. Either, the sample is rotated around its azimuthal angle ϕ and photoelectrons are recorded through a narrow slit that ranges from about $\theta = 0°$ to $\theta = 90°$. This setup is referred to as the *toroid* geometry, in reference to the toroidal electron analyzer developed at the La Trobe University [227]. If, on the other hand, the sample orientation is at rest and the full upper hemisphere can be recorded, we will refer to this setup as an hemispherical analyzer or NanoESCA geometry, in reference to a commercially available electron microscope [228]. The reason to discriminate between the two general setups is that in the toroid geometry, the plane of incidence coincidences with the plane of emission, while this is not the case when the full hemisphere is recorded at once.

From a condensed matter point of view, perfect surfaces of crystals, and in general also oriented layers of molecules on such surfaces, show momentum conservation. This statement has to be restricted to the conservation of momentum up to integer multiples of the crystal lattice, as induced by the Bloch theorem, and to the periodic directions of the sample since the surface obviously breaks the periodicity and therefore the momentum conservation. In an ARPES experiment, it is therefore assumed that the initial momentum parallel to the surface, $\boldsymbol{k}_\parallel$, is conserved in the process, while the momentum perpendicular, $k_\perp$, is not conserved due to the potential step at the surface [229]. This situation is occasionally compared to the diffraction at the boundary of different media in optics [230] and can be mimicked in a phenomenological way by the addition of an inner potential [231, 232]. From measuring the kinetic energy and the angles θ and ϕ as denoted in Figure 2.1, the parallel components of the photoelectron

momentum can be obtained from the relations

$$\begin{aligned} k_x &= |\boldsymbol{k}| \sin(\theta) \cos(\phi), \\ k_y &= |\boldsymbol{k}| \sin(\theta) \sin(\phi). \end{aligned} \tag{2.112}$$

Then, the measured photoelectron intensity I becomes a function of the kinetic energy E_{kin}, $\boldsymbol{k}_{\parallel}$ and, in principle, the photon energy ω:

$$I = I(\boldsymbol{k}_{\parallel}, E_{\text{kin}}, \omega). \tag{2.113}$$

For a fixed photon energy, the three dimensional data set $I(k_x, k_y, E_{\text{kin}})$ can be either analyzed for a fixed kinetic energy, i.e. $I(k_x, k_y)$, which is referred to as a *momentum map*, or along a one-dimensional path in $\boldsymbol{k}_{\parallel}$ and the kinetic energy, which is called a *band map*. If the work function Φ is known, the band map can be plotted versus the binding energy instead of the kinetic energy and is then a visualization of the spectral function of the system. The reasons for this direct connection will be further elaborated in the next paragraph, which is an introduction to the theoretical description of the photoemission process.

2.3.2 Theory of Photoemission – Preliminaries

Even more than the theoretical description of the collective quantum nature of electrons in their ground state, their interaction with light, as in the photoelectric effect, is a very complicated task. Consequently, different levels of sophistication, from simple optical arguments down to the microscopic description of quantum electrodynamics, exist. It is therefore expedient to start the following introduction to the theoretical description of photoemission with its placement within the literature and describe a number of restrictions.

Historically, photoemission from surfaces has partly been described in the *three-step model*, where the process is divided into three independent steps: an electron in the crystal is excited by light, transported to the surface and then escapes to the vacuum level and the detector [233]. In this work, however, we will only consider models that treat photoemission as a coherent *one-step* process, with the only exception being the real-time TDDFT simulations described in Paragraph 2.3.6, where no final state has is assumed. This restriction also excludes many-body Green's functions techniques [229, 234, 235, 83, 236, 237, 238, 239], where retardation effects in the process and correlation effects between photoelectrons and the rest of the sample can be considered. Neglecting the latter effect is usually referred to as the *sudden approximation* [44]. Without explicitly defining the nature of the initial many-body N electron state $|\Psi_i^N\rangle$, as well as the final $N-1$-electron state $|\Psi_f^{N-1}\rangle$, we can write the process in this approximation as

$$|\Psi_i^N\rangle \longrightarrow |\Psi_f^N\rangle = \mathcal{A}|\boldsymbol{k}\rangle|\Psi_f^{N-1}\rangle, \tag{2.114}$$

where $|\boldsymbol{k}\rangle$ denotes the wave function of the photoelectron and $\mathcal{A}$ anti-symmetrizes the product wave function.

Adopting the approximations for light-matter interaction made in Paragraph 2.2.5, we assume that the photon field varies only slowly on the length scale of our systems of interest. Then we can ignore the spatial variation of the photon field, i.e.

$$\boldsymbol{A}(\boldsymbol{r}, t) = \boldsymbol{A}_0 \mathrm{e}^{-\mathrm{i}\omega t} \mathrm{e}^{\mathrm{i}\boldsymbol{p}_\gamma \boldsymbol{r}} = \boldsymbol{A}_0 \mathrm{e}^{-\mathrm{i}\omega t} \left(1 + \mathrm{i}\boldsymbol{p}_\gamma \boldsymbol{r} + \dots\right) \approx \boldsymbol{A}_0 \mathrm{e}^{-\mathrm{i}\omega t} = \boldsymbol{A}(t). \tag{2.115}$$

Here we have denoted the photon momentum with $\boldsymbol{p}_\gamma$ and used the Taylor expansion of the exponential function. While this is certainly a good approximation with the photon energies

utilized in ultra-violet photoemission experiments ($\omega \leq 100$ eV), the spatial variation of the photon field can become relevant for photon energies in the keV-regime, as used e.g. in core-level photoemission spectroscopy, and additional terms in Taylor expansion of Equation 2.115 may become important [240, 241]. Assume now that the N-electron Hamiltonian $\boldsymbol{H}_0$ describes the time-independent system and has the solutions $|\Psi_i^N\rangle$:

$$\boldsymbol{H}_0|\Psi_i^N\rangle = E_i|\Psi_i^N\rangle. \tag{2.116}$$

Adding light-matter interaction to $\boldsymbol{H}_0$ leads to the full Hamiltonian $\boldsymbol{H}$ for the electron-photon system:

$$\boldsymbol{H} = \boldsymbol{H}_0 + \boldsymbol{H}_{\text{int}}. \tag{2.117}$$

In the velocity gauge (see Paragraph 2.2.5), this is achieved by replacing the kinematic momentum by the canonical momentum, i.e.

$$\boldsymbol{p} \to \boldsymbol{p} - \frac{1}{c}\boldsymbol{A}. \tag{2.118}$$

Then the interaction Hamiltonian reads

$$\boldsymbol{H}_{\text{int}} = -\frac{1}{c}\boldsymbol{p}\boldsymbol{A} + \frac{1}{2c^2}\boldsymbol{A}^2. \tag{2.119}$$

For small enough field strengths, we ignore the term of $\mathcal{O}(\boldsymbol{A}^2)$ and view the electromagnetic field as a small perturbation of the system. This allows us to use the *Fermi golden rule* from time-dependent perturbation theory [242], where the probability that the system—under the additional influence of $\boldsymbol{H}_{\text{int}}$—undergoes a transition from its initial state $|\Psi_i^N\rangle$ to a final state $|\Psi_f^N\rangle$ is given by

$$\Gamma_{i\to f} = 2\pi \left|\langle\Psi_f^N|\boldsymbol{H}_{\text{int}}|\Psi_i^N\rangle\right|^2 \delta\big(\omega - (E_f - E_i)\big). \tag{2.120}$$

Before elaborating on the energy conservation or simplifying this expression any further, we need to specify the description of the N-electron system and clarify the approximations made for the matrix element $\mathcal{M}$ in Equation 2.120, i.e.

$$\mathcal{M}(\boldsymbol{k}) = \langle\Psi_f^N|\boldsymbol{H}_{\text{int}}|\Psi_i^N\rangle. \tag{2.121}$$

Writing $\mathcal{M}$ as a real space integral, and suppressing the spin degree of freedom once more, we get (up to an irrelevant minus sign)

$$\mathcal{M}(\boldsymbol{k}) = \int \mathrm{d}\boldsymbol{r}_1 \ldots d\boldsymbol{r}_N \; \gamma_{\boldsymbol{k}}^*(\boldsymbol{r}_1)\overline{\Psi}_f^{N-1}(\boldsymbol{r}_2,\ldots,\boldsymbol{r}_N)\, \boldsymbol{A}\boldsymbol{P}\, \Psi_i^N(\boldsymbol{r}_1,\ldots,\boldsymbol{r}_N), \tag{2.122}$$

where we used $\gamma_{\boldsymbol{k}}(\boldsymbol{r}) = \langle\boldsymbol{r}|\boldsymbol{k}\rangle$ and $\boldsymbol{P} = \sum_i^N \boldsymbol{p}_i$. It can be shown [243] that this expression is considerably simplified by the introduction of Dyson orbitals [244, 98, 245], which are defined as

$$D(\boldsymbol{r}) = \frac{1}{\sqrt{N}} \int \mathrm{d}\boldsymbol{r}_2 \ldots d\boldsymbol{r}_N \; \overline{\Psi}_f^{N-1}(\boldsymbol{r}_2,\ldots,\boldsymbol{r}_N)\Psi_i^N(\boldsymbol{r},\boldsymbol{r}_2,\ldots,\boldsymbol{r}_N), \tag{2.123}$$

and which are therefore a measure of the overlap between the N- and the $N-1$-electron system. The matrix element then reads [243]

$$\mathcal{M}(\boldsymbol{k}) = \int \mathrm{d}\boldsymbol{r}\, \gamma_{\boldsymbol{k}}^{*}(\boldsymbol{r}) \boldsymbol{A}\boldsymbol{p} D(\boldsymbol{r}). \tag{2.124}$$

It should be stressed that this expression holds for the formally exact many-body wave function, albeit only neglecting the correlation between the photoelectron and Ψ_f^{N-1}. In principal, Dyson orbitals are therefore the most appropriate way to describe the quantity that is actually measured in photoemission experiments [246], and simulations based on multi-reference wave function methods have been shown to yield accurate results for gas-phase molecules [247, 248]. For situations where electron correlation would play a greater role, as well as systems of interest in this work, however, these calculations are prohibitively expensive and, in comparison to the experiment, approximate Dyson orbitals calculated from DFT have shown to improve ARPES simulations only slightly over Kohn-Sham orbitals [243]. In the following we will therefore resort to KS orbitals as the basis for the initial state and identify the Dyson orbitals with solutions from the effective, single-particle KS equation

$$\boldsymbol{H}_{\mathrm{KS}} \varphi_{j\boldsymbol{q}}(\boldsymbol{r}) = \varepsilon_{j\boldsymbol{q}} \varphi_{j\boldsymbol{q}}(\boldsymbol{r}). \tag{2.125}$$

In contrast to the discussion about the foundations of DFT in Section 2.1, we now add an additional label $\boldsymbol{q}$ for the crystal momentum, in order to also describe Bloch electrons in periodic systems, for which a direct correspondence to Dyson orbitals is not straightforward due to their extension over the, in principle infinite, crystal. We will use Dyson orbitals, however, as a theoretical concept to derive a method for the simulation of ARPES from excitons in Paragraph 2.3.4.

Having obtained an expression for the matrix element from single-particle bands, i.e.

$$\mathcal{M}_{j\boldsymbol{q}}(\boldsymbol{k}) = \int \mathrm{d}\boldsymbol{r}\, \gamma_{\boldsymbol{k}}^{*}(\boldsymbol{r}) \boldsymbol{A}\boldsymbol{p} \varphi_{j\boldsymbol{q}}(\boldsymbol{r}), \tag{2.126}$$

we can now turn to the term which ensures energy conservation in the expression for the transition probability in Equation 2.120. The δ-function essentially states that the energy difference between the final state and the initial state amounts to the photon energy. Note that this an approximation and, in general, the δ-function is replaced by the *spectral function* if many-body effects are properly taken into account [44]. Regarding this energy conservation, the difference $E_f - E_i$ can be thought of being composed from three different parts, which is also illustrated in Figure 2.2. First, the energy that was used to overcome the binding energy of the electron in the system, $E_B = \varepsilon_{j\boldsymbol{q}}$. This energy is negative and usually referenced to the Fermi level, E_F. At the Fermi level, however, the electron still feels the Coulomb attraction of the $N-1$-electron system. In our static description, we will treat the escaping of the photoelectron to the vacuum level, E_{vac}, as a phenomenological energy contribution, which is the work function Φ. At the vacuum level, the rest of the photon energy ω results in the third contribution: the kinetic energy of the photoelectron, E_{kin}. Summing over all initial states in Equation 2.120 and ignoring possible scaling factors, we get the total photoelectron intensity I as a function of the photoelectron momentum $\boldsymbol{k}$ [249]:

$$I(\boldsymbol{k}) \propto \sum_{j}^{N} \sum_{\boldsymbol{q}}^{\mathrm{BZ}} \left| \int \mathrm{d}\boldsymbol{r}\, \gamma_{\boldsymbol{k}}^{*}(\boldsymbol{r}) \boldsymbol{A}\boldsymbol{p} \varphi_{j\boldsymbol{q}}(\boldsymbol{r}) \right|^2 \delta\big(\omega - |\varepsilon_{j\boldsymbol{q}}| - E_{\mathrm{kin}} - \Phi\big). \tag{2.127}$$

Note that the summation over all occupied states N can be extended to unoccupied states and smeared out at the Fermi edge, if, for instance, systems with metallic character are considered.

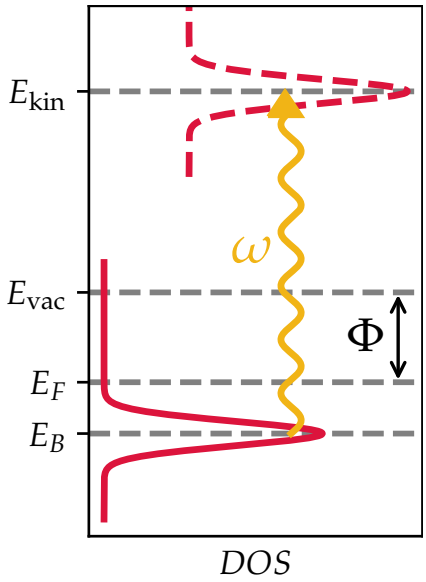

Figure 2.2: **Energy conservation in the photoemission process.** Sketched is the density of states (DOS) at the x-axis versus the energy on the y-axis. The photon energy ω results in shifting the initial DOS to E_{kin}.

While the initial state, as well as the work function, can be obtained from a DFT calculation, nothing has been said about the nature of the final state so far. In principle, γ_k can be seen as an unbound scattering solution of the Hamiltonian $\boldsymbol{H} = \boldsymbol{H}_{\text{KS}} + \boldsymbol{H}_{\text{int}}$ and several ways to compute such scattering states have been used in regard to a description of the photoelectron. These methods include an iterative solution of the Lippman-Schwinger equation [250, 251, 29] or the incorporation of scattering effects via the Kohn-Korringa-Rostocker technique [252, 253, 254]. In what follows, we encompass a route that takes different levels of sophistication for the description of the final state in photoemission. Starting from a simple plane wave, which is ignorant to any scattering effects that the photoelectron may experience, we describe POT for photoemission from the ground state in the following paragraph and, subsequently, extend this method to photoemission from excitons in Paragraph 2.3.4. As an intermediate step, scattering effects are taken into account in a phenomenological way in Paragraph 2.3.3 before we describe photoemission with real-time TDDFT in Paragraph 2.3.6, which may also be seen as a full ab-initio method for final state effects complementary to Greens function techniques.

2.3.3 The Plane Wave Final State

In an ARPES experiment the detector is far away from the system, as compared to the characteristic length scale of bound electrons. It thus stands to reason that the influence of the system on the photoelectron can be neglected and approximating such a quasi-free electron by a plane wave might suffice. This description has, in fact, a long history in the theory of photoemission [255, 256] but was considered too simplictic relative to more sophisticated descriptions [229, 234, 83, 235, 83]. It then took until the new millennium that the plane wave final state approximation was revived by Puschnig et. al. [46] for the theoretical description of measured orbital signatures from organic molecules, which is the foundation of POT. Inserting

a plane wave into Equation 2.127 and absorbing the normalization factor, we get

$$I(\boldsymbol{k}) \propto \sum_{j}^{N} \sum_{\boldsymbol{q}}^{\mathrm{BZ}} \left| \int \mathrm{d}\boldsymbol{r}\, \mathrm{e}^{-\mathrm{i}\boldsymbol{k}\boldsymbol{r}} \boldsymbol{A}\boldsymbol{p}\varphi_{j\boldsymbol{q}}(\boldsymbol{r}) \right|^2 \delta\big(\omega - |\varepsilon_{j\boldsymbol{q}}| - E_{\mathrm{kin}} - \Phi\big). \tag{2.128}$$

With $\boldsymbol{p} = -\mathrm{i}\nabla$, we can integrate this expression by parts and drop the boundary term, assuming that $\varphi_{j\boldsymbol{q}}$ vanishes at infinity [249]. Then we get

$$\begin{aligned} I(\boldsymbol{k}) &\propto |\boldsymbol{A}\boldsymbol{k}|^2 \sum_{j}^{N} \sum_{\boldsymbol{q}}^{\mathrm{BZ}} \left| \int \mathrm{d}\boldsymbol{r}\, \mathrm{e}^{-\mathrm{i}\boldsymbol{k}\boldsymbol{r}} \varphi_{j\boldsymbol{q}}(\boldsymbol{r}) \right|^2 \delta\big(\omega - |\varepsilon_{j\boldsymbol{q}}| - E_{\mathrm{kin}} - \Phi\big) = \\ &= |\boldsymbol{A}\boldsymbol{k}|^2 \sum_{j}^{N} \sum_{\boldsymbol{q}}^{\mathrm{BZ}} \big|\mathcal{F}[\varphi_{j\boldsymbol{q}}](\boldsymbol{k})\big|^2 \delta\big(\omega - |\varepsilon_{j\boldsymbol{q}}| - E_{\mathrm{kin}} - \Phi\big), \end{aligned} \tag{2.129}$$

such that the ARPES intensity is proportional to the absolute square of the Fourier-transformed initial state, modulated by a factor $|\boldsymbol{A}\boldsymbol{k}|^2$ that is called the *polarization factor*.

If periodic systems are considered, it is common to calculate the initial state in terms of a plane wave basis set,

$$\varphi_{j\boldsymbol{q}}(\boldsymbol{r}) = \mathrm{e}^{\mathrm{i}\boldsymbol{q}\boldsymbol{r}} u_{j\boldsymbol{q}}(\boldsymbol{r}) = \sum_{\boldsymbol{G}}^{|\boldsymbol{G}_{\max}|} c_{j\boldsymbol{q}}(\boldsymbol{G}) \mathrm{e}^{\mathrm{i}(\boldsymbol{q}+\boldsymbol{G})\boldsymbol{r}}, \tag{2.130}$$

where $u_{j\boldsymbol{q}}$ denotes the lattice-periodic part of the Bloch function such that $u_{j\boldsymbol{q}}(\boldsymbol{r}) = u_{j\boldsymbol{q}}(\boldsymbol{r} + \boldsymbol{R})$ for all lattice vectors $\boldsymbol{R} = \sum_i^3 n_i \boldsymbol{a}_i \ \forall \ n_i \in \mathbb{Z}$. Then, the matrix element in the photoemission intensity becomes a simple sum over the plane wave coefficients $c_{j\boldsymbol{q}}(\boldsymbol{G})$:

$$\begin{aligned} I(\boldsymbol{k}) &\propto |\boldsymbol{A}\boldsymbol{k}|^2 \sum_{j}^{N} \sum_{\boldsymbol{q}}^{\mathrm{BZ}} \left| \sum_{\boldsymbol{G}}^{|\boldsymbol{G}_{\max}|} \int \mathrm{d}\boldsymbol{r}\, \mathrm{e}^{-\mathrm{i}(\boldsymbol{q}+\boldsymbol{G}-\boldsymbol{k})\boldsymbol{r}} c_{j\boldsymbol{q}}(\boldsymbol{G}) \right|^2 \delta\big(\omega - |\varepsilon_{j\boldsymbol{q}}| - E_{\mathrm{kin}} - \Phi\big) = \\ &= |\boldsymbol{A}\boldsymbol{k}|^2 \sum_{j}^{N} \sum_{\boldsymbol{q}}^{\mathrm{BZ}} \left| \sum_{\boldsymbol{G}}^{|\boldsymbol{G}_{\max}|} c_{j\boldsymbol{q}}(\boldsymbol{G}) \right|^2 \delta_{\boldsymbol{k},\boldsymbol{q}+\boldsymbol{G}}\, \delta\big(\omega - |\varepsilon_{j\boldsymbol{q}}| - E_{\mathrm{kin}} - \Phi\big). \end{aligned} \tag{2.131}$$

The latter expression weights contributions from all states equally, while in reality photoemission is restricted to electrons near the surface due to the decreased mean free path for states deeper in the bulk. When simulating (molecular) adsorbates on several layers of substrate, this can be accounted for in a phenomenological way by damping the plane wave in z-direction into the substrate [257, 249].

Instead of the simulation of molecule-substrate interfaces as discussed above, often times it can be sufficient to calculate the gas-phase orbitals of molecules only, in order to get a first impression how the momentum space signatures of these orbitals might look like. Then, one can benefit from the considerably lower computational cost in many quantum chemistry codes that use local orbitals as basis sets (e.g. Refs. [258, 259]), especially when using hybrid functionals for exchange-correlation effects. The resulting orbitals can be exported on a real-space grid and momentum maps can be efficiently computed with the Fast Fourier Transform (FFT), for instance with the software *kmap.py* [260]:

$$I(\boldsymbol{k}) \propto |\boldsymbol{A}\boldsymbol{k}|^2 \sum_{j}^{N} \big|\mathrm{FFT}[\varphi_j](\boldsymbol{k})\big|^2 \delta\big(\omega - |\varepsilon_j| - E_{\mathrm{kin}}\big). \tag{2.132}$$

In addition, numerical algorithms allow for a fitting of experimental data to gas-phase momentum maps [260], which can be useful when measured momentum signatures are stemming from multiple contributions of states that are too close in energy to resolve experimentally. In the following paragraph, we will extend the method of POT to the description of excitons in molecules.

2.3.4 Simulation of Photoemission from Excitons

DFT is very successful in describing properties of occupied electrons in terms of their density while the method notoriously fails for unoccupied states. This holds especially true for the energy position of these states and is related to the derivative discontinuity in E_{xc} which is absent in (semi-) local functionals, as also mentioned in Section 2.1. Nonetheless, orbitals of unoccupied states can be interpreted in POT. In a photoemission experiment, however, one can only observe occupied states. This may include formerly unoccupied states that become filled, either through charge transfer from the substrate or through optical excitation. For the latter case, an additional state of matter exists: if the material possesses a band gap, charge-neutral states can form as bound electron-hole pairs below the band-gap. These bosonic quasi-particles are then called *excitons* and the extension of POT to such systems is very desirable because of their important role in organic semiconductors. The reason why this is not straightforward, lies in the correlated nature of the electron-hole pair. As detailed in Chapter 7, we recapitulate the ideas that led to a plane wave description of photoemission from excitons in the following.

In order to express the exciton wave function, we use a basis of occupied states, $\{\phi_v\}$, as well as unoccupied states $\{\chi_c\}$, which need to be separated by a band-gap. Then the exciton wave function can be written as [261]

$$\psi_m(\boldsymbol{r}_h, \boldsymbol{r}_e) = \sum_{v,c} X_{vc}^{(m)} \phi_v^*(\boldsymbol{r}_h)\chi_c(\boldsymbol{r}_e). \tag{2.133}$$

Here, the label m states that we consider the m-th exciton, with excitation energy Ω_m, and the sum runs over all occupied (valence) and unoccupied (conduction) states ϕ_v and χ_c, depending on spatial coordinates of the hole, $\boldsymbol{r}_h$, and the electron, $\boldsymbol{r}_e$, respectively. The $X_{vc}^{(m)}$ mix the individual contributions v, c of the m-th exciton and are called the *transition density matrix elements*. They can be obtained from solving the Casida equation, as described in Paragraph 2.2.7, or from the Bethe-Salpter equation (BSE) [261]. Both methods have their own advantages and disadvantages [215] and in this work we will only consider Casida's equation to obtain the $X_{vc}^{(m)}$. From Equation 2.133 it is obvious that, due to the correlation between electron- and hole-states, a direct simulation of photoemission is not possible, with the exception of the trivial case when the $X_{vc}^{(m)}$ vanish but for one transition $v \to c$. This could be, for instance, the direct transition from the HOMO to the lowest unoccupied molecular orbital (LUMO), which is often observed as the dominant low-energy excitation in organic molecules [262]. Then the experimantally observed mometum map equals the LUMO map and the kinetic energy equals the kinetic energy of the HOMO emission, plus the excitation energy Ω_m. In the general case, however, an exciton is composed of multiple transitions and both the signatures in momentum space, as well as their kinetic energy positions, are unknown.

In order to resolve this problem, we take a step back from a single-particle description of the involved states and consider the N-electron system in a many-body description, this time in Fock space to allow for the creation of holes (annihilation of electrons), as well as the population of formally unoccupied states (creation of electrons) due to the optical excitation. With the general N-electron many-body ground state $|\Psi_0^N\rangle$ known, we might as well write the exciton

wavefunction of Equation 2.133, together with rest of the system, as

$$\left|\Psi^N_{\mathrm{i},m}\right\rangle = \sum_{v,c} X^{(m)}_{vc} a^\dagger_c a_v \left|\Psi^N_0\right\rangle, \tag{2.134}$$

such that for each pair of $\{v, c\}$ an electron is annihilated in the v-th state and created in the c-th state. The additional label "i" denotes that this object will be the initial state for the photoemission matrix element. The final state can be written, in analogy to Equation 2.114, as

$$|\Psi^N_{\mathrm{f},j,\boldsymbol{k}}\rangle = \mathcal{A}|\boldsymbol{k}\rangle|\Psi^{N-1}_{\mathrm{f},j}\rangle = \mathcal{A}|\boldsymbol{k}\rangle a_j|\Psi^N_0\rangle, \tag{2.135}$$

and is characterized by the photoelectron momentum $\boldsymbol{k}$ and the label j, which keeps track of the state from which the electron is ejected. Next, we construct a Dyson orbital from these states, hoping to get rid of the $N-1$ passive electrons in the process. Owing to the splitting of the basis set in $\{\phi_v\}$ and $\{\chi_c\}$, the projection of the Dyson orbital on this basis contains two terms (the projections are also called Dyson amplitudes [263, 248]):

$$D_{j,m}(\mathbf{r}) = \sum_{v'} \left\langle \Psi^N_{\mathrm{i},m}\middle|a^\dagger_{v'}\middle|\Psi^{N-1}_{\mathrm{f},j}\right\rangle \phi_{v'}(\mathbf{r}) + \sum_{c'} \left\langle \Psi^N_{\mathrm{i},m}\middle|a^\dagger_{c'}\middle|\Psi^{N-1}_{\mathrm{f},j}\right\rangle \chi_{c'}(\mathbf{r}). \tag{2.136}$$

Note that there exists a different Dyson orbital for each state j from which the electron has been removed and that the summation over v' runs over all occupied states, while the summation over over c' is, in principle, infinite and has to be truncated along with the basis set considered for the calculation of the exciton properties. Inserting the initial state (Equation 2.134) and the final state (Equation 2.135) into the Dyson orbital expression, we get

$$\begin{aligned} D_{j,m}(\mathbf{r}) = &\sum_{v'}\sum_{v,c} X^{(m)}_{vc} \left\langle \Psi^N_{\mathrm{i},0}\middle|a^\dagger_v a_c a^\dagger_{v'} a_j\middle|\Psi^N_{\mathrm{i},0}\right\rangle \phi_{v'}(\mathbf{r}) + \\ &+ \sum_{c'}\sum_{v,c} X^{(m)}_{vc} \left\langle \Psi^N_{\mathrm{i},0}\middle|a^\dagger_v a_c a^\dagger_{c'} a_j\middle|\Psi^N_{\mathrm{i},0}\right\rangle \chi_{c'}(\mathbf{r}). \end{aligned} \tag{2.137}$$

Here, the sum over v' gives zero because of orthogonality relations, which also demand that $c = c'$ in the second term. Exploiting those orthogonality relations requires an important assumption that has not been discussed so far: while the final and initial states defined in Equations 2.134 and 2.135 are general many-body states, here we now explicitly assume that those states are constructed from the *same* single-particle orbitals. This implies that no electronic relaxation effects are considered upon ionizing the N-electron system. We finally thus get (up to normalization constants)

$$\begin{aligned} D_{j,m}(\mathbf{r}) &= \sum_{v,c} X^{(m)}_{vc} \left\langle \Psi^N_{\mathrm{i},0}\middle|a^\dagger_v a_c a^\dagger_c a_j\middle|\Psi^N_{\mathrm{i},0}\right\rangle \chi_c(\mathbf{r}) = \\ &= \sum_{c} X^{(m)}_{jc} \left\langle \Psi^N_{\mathrm{i},0}\middle|a^\dagger_j a_j a_c a^\dagger_c\middle|\Psi^N_{\mathrm{i},0}\right\rangle \chi_c(\mathbf{r}) = \\ &= \sum_{c} X^{(m)}_{jc} \chi_c(\mathbf{r}). \end{aligned} \tag{2.138}$$

We have therefore shown that the Dyson orbital for the electron missing in the j-th valence state simplifies to a coherent sum over unoccupied orbitals, weighted by their contribution to the j-th row of the transition density matrix. Note that this derivation implicitly assumes that the many-body electron state can be simplified to a single Slater determinant, which is a restriction

that may be problematic for static correlation effects but, in principle, the above construction for the Dyson orbital could be also extended to multi-reference methods [264].

For the total photoelectron intensity originating from the m-th exciton, we have to sum over all possible hole configurations j and insert the respective Dyson orbitals into Equation 2.132:

$$\begin{aligned} I_m(\boldsymbol{k}) &\propto |\boldsymbol{A}\boldsymbol{k}|^2 \sum_j^N \left|\mathcal{F}[D_{j,m}](\boldsymbol{k})\right|^2 \delta\big(\omega - (E_\mathrm{f} - E_\mathrm{i})\big) = \\ &= |\boldsymbol{A}\boldsymbol{k}|^2 \sum_j^N \left| \mathcal{F}\left[\sum_c X_{jc}^{(m)} \chi_c\right](\boldsymbol{k}) \right|^2 \delta\big(\omega - (E_\mathrm{f}^N - E_\mathrm{i}^N)\big), \end{aligned} \tag{2.139}$$

where E_i^N and E_f^N denote the energy of the N-electron initial and final states, respectively. For the initial state on the one hand, we identify its energy with the ground state energy of the N-electron system, E_0^N, plus the excitation energy, such that $E_\mathrm{i}^N = E_0^N + \Omega_m$. The final state energy, on the other other hand, is the energy of the $N-1$-electron system, where the hole resides in state j, plus the kinetic energy E_kin: $E_\mathrm{f}^N = E_{\mathrm{f},j}^{N-1} + E_\mathrm{kin}$. Inserting both energy expressions into the energy conservation of Equation 2.139 leads to

$$\omega = E_\mathrm{f}^N - E_\mathrm{i}^N = E_{\mathrm{f},j}^{N-1} + E_\mathrm{kin} - E_0^N - \Omega_m = E_\mathrm{kin} + \varepsilon_j - \Omega_m, \tag{2.140}$$

where we have inserted the j-th ionization potential as $\varepsilon_j := E_{\mathrm{f},j}^{N-1} - E_0^N$ ($\varepsilon_j > 0$). Utilizing this energy conservation, we arrive at the final result

$$I_m(\boldsymbol{k}) \propto |\boldsymbol{A}\boldsymbol{k}|^2 \sum_j^N \left| \sum_c X_{jc}^{(m)} \mathcal{F}\left[\chi_c\right](\boldsymbol{k}) \right|^2 \delta\big(\omega - E_\mathrm{kin} - \varepsilon_j + \Omega_m\big), \tag{2.141}$$

which renders an expression of the photoelectron intensity for the emission from the m-th exciton and where all possible configurations that the electron and hole can take are respected.

The result for photoemission from excitons, originally presented in Chapter 7, has remarkable consequences that are summarized in the following. For each possible configuration of the hole left behind after the photoemission, energy conservation with the respective ionization potential has to be obeyed. For excitons that are composed of transitions with multiple contributions from different occupied states v, the measurement can therefore lead to photoemission signatures at different kinetic energies. At each allowed kinetic energy, photoemission momentum maps are proportional to the absolute squared Fourier transform of a *coherent sum* over unoccupied orbitals, weighted by their transition density matrix elements. While for the extension of POT to excitons we still relied on the plane wave final state approximation, in the following paragraph we will lift this restriction and present a model for scattering effects in the final state of photoemission.

2.3.5 The Scattered Wave Final State

Despite the success of the plane wave approximation, it is a very simplified model where the photoelectron does not encounter any influence of the sample at all. As mentioned in Paragraph 2.3.2, one way to incorporate some of the effects of the sample can be achieved with quantum mechanical scattering theory. This ansatz has been used in the theoretical description of photoemission for decades already, and was pioneered by Liebsch [265, 266, 267], Davenport [268, 269, 270] and others [271, 272, 273, 274, 275, 276, 277].

For the subsequent incorporation of scattering effects on an intermediate level, we write the initial state in terms of local, i.e. atom-centered, orbitals that are eigenstates of the angular momentum operator. In addition to the basis sets for DFT calculations discussed so far—namely plane waves and real-space grids—we now represent the initial state of the photoemission matrix element in terms of a local combination of atomic orbitals (LCAO) basis:

$$\varphi_j(\boldsymbol{r}) = \sum_a^{N_a} \sum_j^N \sum_l^\infty \sum_{m=-l}^{l} c^a_{jlm} R_{jl}(r_a) Y_{lm}(\hat{\boldsymbol{r}}_a). \tag{2.142}$$

In this expression we have a sum over all N_a atoms, with each atom located at $\boldsymbol{R}_a$, and we use the shorthand notation $\boldsymbol{r}_a := \boldsymbol{r} - \boldsymbol{R}_a$. At each site a, the atomic contribution to the electronic wave function in the j-th orbital is represented in a basis composed of radial functions R_{jl} and the spherical harmonics Y_{lm}. Here and in the following, we consider gas-phase molecules and ignore the crystal momentum, but will extend the method to periodic systems at a later stage. Inserting this initial state in the matrix element expression in the velocity gauge, e.g. as in Equation 7.10, leads to

$$\begin{aligned}\mathcal{M}_j(\boldsymbol{k}) &= \int \mathrm{d}\boldsymbol{r}\, \gamma^*_{\boldsymbol{k}}(\boldsymbol{r}) \boldsymbol{A}\boldsymbol{p} \varphi_j(\boldsymbol{r}) = \\ &= \sum_a^{N_a} \sum_j^N \sum_l^\infty \sum_{m=-l}^{l} \int \mathrm{d}\boldsymbol{r}\, \gamma^*_{\boldsymbol{k}}(\boldsymbol{r}) \boldsymbol{A}\boldsymbol{p}\, c^a_{jlm} R_{jl}(r_a) Y_{lm}(\hat{\boldsymbol{r}}_a) =: \sum_a^{N_a} \mathcal{M}^a_j(\boldsymbol{k}).\end{aligned} \tag{2.143}$$

From the definition in the last step, it can be seen that the matrix element can now be expressed as a sum of atomic matrix elements, which is referred to as the *independent atomic center approximation* [271]. Next, we will consider the action of the nabla operator on the contribution from one angular momentum channel $\{l, m\}$ only:

$$\begin{aligned}\nabla_a R_{jl}(r_a) Y_{lm}(\hat{\boldsymbol{r}}_a) &= \\ &= -N^{(\mathrm{hi})}_l \left(\frac{\mathrm{d}}{\mathrm{d}r_a} - \frac{l}{r_a} \right) R_{jl}(r_a) \boldsymbol{\mathcal{Y}}^m_{ll+1}(\hat{\boldsymbol{r}}_a) + \\ &\quad + N^{(\mathrm{lo})}_l \left(\frac{\mathrm{d}}{\mathrm{d}r_a} - \frac{l+1}{r_a} \right) R_{jl}(r_a) \boldsymbol{\mathcal{Y}}^m_{ll-1}(\hat{\boldsymbol{r}}_a) = \\ &=: \left[\boldsymbol{f}^{(\mathrm{hi})}_{lm}(\boldsymbol{r}_a) + \boldsymbol{f}^{(\mathrm{lo})}_{lm}(\boldsymbol{r}_a) \right].\end{aligned} \tag{2.144}$$

Here we have made use of an analytical expression for the gradient acting on such functions in terms of the vector spherical harmonics [278], which are defined as

$$\boldsymbol{\mathcal{Y}}^M_{Jl}(\hat{\mathbf{r}}) = \sum_{m=-l}^{l} \sum_{\mu=-1}^{1} c_{\mathrm{CG}}(l, 1, J; m, \mu, M) Y_{lm}(\hat{\mathbf{r}}) \xi_\mu, \tag{2.145}$$

using the Clebsch-Gordan coefficients c_{CG} and

$$\xi_{-1} = \frac{1}{\sqrt{2}} (\hat{x} - \mathrm{i}\hat{y}), \quad \xi_0 = \hat{z}, \quad \xi_1 = -\frac{1}{\sqrt{2}} (\hat{x} + \mathrm{i}\hat{y}). \tag{2.146}$$

For the sake of a more compact notation, we have also abbreviated l-dependent prefactors with

$$N^{(\mathrm{hi})}_l = \left[\frac{l+1}{2l+1} \right]^{1/2} \quad \text{and} \quad N^{(\mathrm{lo})}_l = \left[\frac{l}{2l+1} \right]^{1/2}. \tag{2.147}$$

As shown in the last step of Equation 2.144, the action of the nabla operator results in *two* angular momentum contributions for each l-channel in the initial state, which we subsume with the functions $\boldsymbol{f}_{lm}^{(\mathrm{hi})}$ (high) for raising or $\boldsymbol{f}_{lm}^{(\mathrm{lo})}$ (low) for lowering the angular momentum, which is, essentially, the consequence of the optical selection rule in any matrix element within the dipole approximation. As an example, for photoemission from a p orbital, the dipole matrix element results in the combination of both an s and d channel, with m depending on the incidence field due to its scalar product with the ξ_ν, as well as on additional selection rules resulting from the Clebsch-Gordan coefficients c_{CG}.

Concerning the final state in the matrix element, we begin by writing a generic scattered wave as

$$\gamma_{\boldsymbol{k}}(\boldsymbol{r}) = \frac{4\pi}{(2\pi)^{\frac{3}{2}}} \sum_{l'm'} \mathrm{e}^{\mathrm{i}\delta_{l'}(k)} R_{l'}(kr) \mathrm{i}^{l'} Y^*_{l'm'}(\hat{\boldsymbol{k}}) Y_{l'm'}(\hat{\boldsymbol{r}}), \tag{2.148}$$

where the radial functions, $R_{l'}$, and the phase-shifts, $\delta_{l'}$, determine the scattering character. Such a solution exists if it can be assumed that the atomic potentials at each site a are well-separated and spherically-symmetric, which is the realm of the apparatus of quantum mechanical scattering theory [279] and which is, strictly speaking, only valid for the Coulomb problem in the hydrogen atom. In this case, the radial function is proportional to the confluent hypergeometric function of the first kind and Equation 2.148 describes a Coulomb wave that is shaped by the Sommerfeld parameter [279]. Despite the lack of formal justification, the Coulomb wave final state has been successfully applied to small molecules [280] and even solid state systems [84]. In this work, we use the SWA in the generic sense and treat radial functions and phase-shifts as model fit parameters. Note that when identifying $R_{l'}$ with the spherical Bessel functions of the first kind and setting $\delta_{l'} = 0 \ \forall \ l'$, we recast the *Rayleigh expansion* of the plane wave in Equation 2.148 [281].

Inserting the SWA, as well as Equation 2.144, into the matrix element of Equation 2.143, we get the following expression:

$$\mathcal{M}_j(\boldsymbol{k}) \propto \sum_a^{N_a} \sum_j^N \sum_l^\infty \sum_{m=-l}^{l} \int \mathrm{d}\boldsymbol{r} \, \mathrm{e}^{\mathrm{i}\delta_l(k)} R_l(kr) \mathrm{i}^l Y^*_{lm}(\hat{\boldsymbol{k}}) Y_{lm}(\hat{\boldsymbol{r}}) \boldsymbol{A} \, c^a_{jlm} \left[\boldsymbol{f}_{lm}^{(\mathrm{hi})}(\boldsymbol{r}_a) + \boldsymbol{f}_{lm}^{(\mathrm{lo})}(\boldsymbol{r}_a) \right], \tag{2.149}$$

where the orthogonality relations between the spherical harmonics had demanded that $l' = l$ and $m' = m$. At the expense of more algebra, especially when we would insert the expressions for the $\boldsymbol{f}_{lm}^{(\mathrm{hi/lo})}$ as well, we have thus obtained a matrix element that serves as a model for final state scattering. With the l-dependent phase-shifts, it is now possible that two photoemission channels, with different l, can have different interference patterns, depending on the kinetic energy of the final state. Especially when comparing photoemission from measurements with different (orthogonal) light polarizations, this can lead to a dichroism and the described mechanism of l-channel interference has been used to explain the circular dichroism effect by Schönhense [282]. Moreover, the k- or E_{kin}-dependence of the phase-shifts can lead to an oscillation of intensity when varying the energy of the incident light, which has been successfully used to explain observed variations in the photoemission from C60 thin films [231]. In principle, the phase-shifts could also be functions of the atom position a, thereby respecting different chemical environments , or the m quantum number.

As shown in Chapter 6, this model can also be extended to periodic systems, where local orbitals can be obtained with the mapping on a tight-binding Hamiltonian [283]. If a well-defined phase relation between nearest-neighbors exists, as in graphene, scattering of the photoelectron wave function from the nearest-neighbors can also be included, as described in Chapter 6 where

experimental data could be reproduced by fitting to the SWA model and thus confirming that all relevant physics in the photoemission process of such a system is captured by the SWA. Despite this success, it should be mentioned that l-dependent phase-shifts for the description of scattering effects are only well-defined for spherically-symmetric potentials and are therefore not straight-forward to compute from full-potential DFT methods, such that tight-binding approximations [284] or muffin-tin potential descriptions may become neccesary [285, 286, 287]. This is in contrast to ab-initio simulations of photoemission from TDDFT, which is subject to the following paragraph.

2.3.6 Simulation of Photoemission with Real-Time TDDFT

For the time being, the photoemission process has been described with Fermi's golden rule as a static, one-step process. In the following, we will recapitulate a formulation in which the emission of photoelectrons is treated as an actual process in real time. With TDDFT, we have a method where the time evolution of electrons, coupled to a photon field, is captured, as previously described for optical excitations in Paragraph 2.2.6. For the real-time simulation of the ARPES experiment, however, we need to modify the setup in two regards. First, we want to use monochromatic light and, second, we need to somehow detect the photoelectrons. The latter can be achieved with a method that was initially developed when time-propagating the time-dependent Schrödinger equation (TDSE) on a real-space real-time grid for recording photoelectrons as the flux integral through a detector surface [288]. In this way, the flux per unit area can be interpreted as photoelectron intensity, given that the detector surface is positioned far enough from the system, as to record only quasi-free electrons that are not part of the system's bound states. If the flux density is recorded with angular resolution, the same considerations as for the experiment can be made (see Paragraph 2.3.1) and photoemission intensity from such a simulation can be regarded as $I(\boldsymbol{k}, \omega, T) = I(E_{\text{kin}}, \boldsymbol{k}_{||}, \omega, T)$, i.e. as a function of kinetic energy, parallel momentum, photon energy and, in principle, the time duration of the observation, T.

Subsequently, the surface-flux method was adopted to the KS formalism and integrated into the OCTOPUS code [176, 177] by De Giovannini et. al. for excited states in small systems [289], molecules [85] and periodic systems [86], where the former two kinds of systems require slightly different computational setups than the latter one. For molecules or clusters in the gas-phase, a spherical simulation box with radius R is used for the real-space grid, as depicted in Figure 2.3 (a). With the molecule in the center of the domain, the spherical detector surface is placed at the distance R_S from the center. For reasons that will become clear in the following, the detector surface thus separates an inner region, A, from the outer region, B, of the simulation domain. Suppose that the inner region A is well-described by the KS Hamiltonian for N electrons, coupled with the light field:

$$\boldsymbol{H}_{\text{KS}}(t) = \frac{1}{2}\left(\boldsymbol{p} - \frac{\boldsymbol{A}(t)}{c}\right)^2 + v_{\text{ext}}(\mathbf{r}, t) + \int \mathrm{d}\boldsymbol{r}' \, \frac{n(\mathbf{r}', t)}{|\mathbf{r} - \mathbf{r}'|} + v_{\text{xc}}[n](\mathbf{r}, t). \tag{2.150}$$

In region B, we assume that the photoelectrons are essentially free particles in the presence of an electromagnetic field, which is described by the Volkov Hamiltonian of the form

$$\boldsymbol{H}_{\text{V}}(t) = \frac{1}{2}\left(\boldsymbol{p} - \frac{\boldsymbol{A}(t)}{c}\right)^2, \tag{2.151}$$

and therefore also respects the imprint of (strong) fields on the photoelectron momentum, which

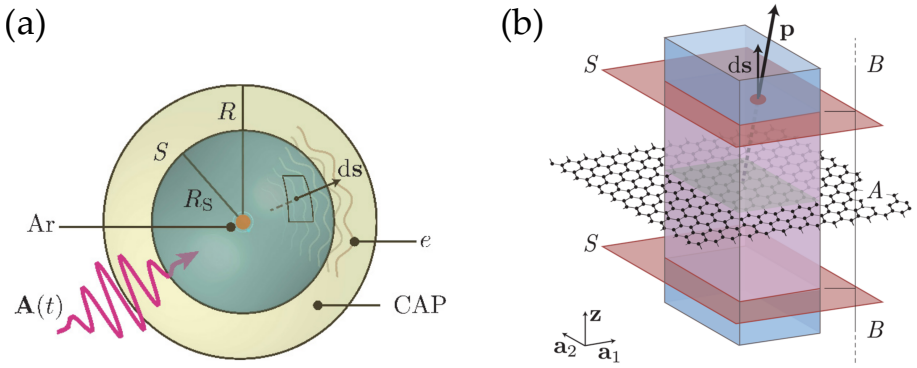

Figure 2.3: **Overview of the geometry for photoemission simulations.** In panel (a), the geometry for molecules is depicted (figure from Reference [290]), in panel (b) the corresponding setup for (semi-) periodic systems is shown (figure from Reference [86]).

is in contrast to pure plane waves. The total system is then governed by the Hamiltonian

$$\boldsymbol{H}(t) = \begin{cases} \boldsymbol{H}_{\mathrm{KS}}(t) & \text{if } \boldsymbol{r} \in A \\ \boldsymbol{H}_{\mathrm{V}}(t) & \text{if } \boldsymbol{r} \in B, \end{cases} \tag{2.152}$$

and we assume that—if the system has been subjected to the field for some time T—the charge density associated with either region A or B is spatially separated at some later time $t > T$. In other words: all photoelectrons have passed the detector and are far away from the system whereas the electrons which are still bound to the system remain there and no charge density is flowing in the interstitial region any longer. This condition can only be fulfilled if the detector is placed far enough from the system, if the field strengths remain moderate and if the simulation time exceeds T long enough that even the slowest photoelectrons have made it through the detector.

Under the conditions just stated, we can propagate the system with the Hamiltonian $H_{\mathrm{KS}}(t)$ in order to get the solutions $\varphi_j^A(\boldsymbol{r}, t)$ of the subsystem A described with TDDFT. For subsystem B, analytical solutions exist [85] that have the the form

$$\gamma_{\boldsymbol{k}}(\boldsymbol{r}, t) = (2\pi)^{-3/2}\, \mathrm{e}^{\mathrm{i}\chi(\boldsymbol{k},t)} \mathrm{e}^{\mathrm{i}\boldsymbol{k}\boldsymbol{r}}, \tag{2.153}$$

which are thus plane waves with an additional time-dependent phase factor acquired by the photon field,

$$\chi(t) = \frac{1}{2} \int_0^t \mathrm{d}\tau \left(\boldsymbol{k} - \frac{\boldsymbol{A}(t)}{c} \right)^2. \tag{2.154}$$

Since these Volkov states form a complete set, we can expand the KS states in region B in this basis, which gives

$$\varphi_j^B(\boldsymbol{r}, t) = \int \mathrm{d}\boldsymbol{k}\; b_j(\boldsymbol{k}, t) \gamma_{\boldsymbol{k}}(\boldsymbol{r}, t). \tag{2.155}$$

The density in B, $n^B(\boldsymbol{r}, t) = \sum_j^N |\varphi_j^B(\boldsymbol{r}, t)|^2$, is a measure of the photoelectrons that have escaped

through the detector after time T:

$$N_{\text{photo}}(T) = \sum_j^N \int \mathrm{d}\boldsymbol{k}\ |b_j(\boldsymbol{k}, T)|^2, \tag{2.156}$$

and the derivative with respect to $\boldsymbol{k}$ gives the momentum- and energy resolved photoemission probability, and, directly related, the photoemission intensity

$$I(\boldsymbol{k}) \propto \frac{\partial N_{\text{photo}}(T)}{\partial \boldsymbol{k}}. \tag{2.157}$$

From the point of view of a continuity equation, we may also express N_{photo} als the flux of electrons through the detector surface S:

$$N_{\text{photo}}(T) = -\int_0^T \mathrm{d}t \oint_S \mathrm{d}\boldsymbol{s}\ \boldsymbol{j}(\boldsymbol{r}, t), \tag{2.158}$$

where $\boldsymbol{j}$ is the current density that can be obtained from the current denity operator $\boldsymbol{J}$, defined in Equation 2.48, as

$$\boldsymbol{j}(\boldsymbol{r}, t) = \sum_j^N \langle \varphi_j(t) | \boldsymbol{J}(t) | \varphi_j(t) \rangle. \tag{2.159}$$

With the projection defined in Equation 2.155, this can be written as

$$\boldsymbol{j}(\boldsymbol{r}, t) = \sum_j^N \int \mathrm{d}\boldsymbol{k}\ b_j^*(\boldsymbol{k}, t) \langle \gamma_{\boldsymbol{k}}(t) | \boldsymbol{J}(t) | \varphi_j(t) \rangle. \tag{2.160}$$

Expanding the ket instead of the bra in a similar fashion, inserting both results into Equation 2.158 and comparing with Equation 2.156 (see Ref. [85]), we get the final result that the photoelectron intensity is proportional to a flux integral, integrated over time and summed over all states:

$$I(\boldsymbol{k}) \propto \sum_j^N \left| \int_0^T \mathrm{d}t \oint_S \mathrm{d}\mathbf{s} \langle \gamma_{\boldsymbol{k}}(t) | \boldsymbol{J}(t) | \varphi_j(\boldsymbol{r}, t) \rangle \right|^2. \tag{2.161}$$

For periodic systems, we have an additional dependence of the initial state on the crystal momentum, i.e. $\varphi_j \to \varphi_{j\boldsymbol{q}}$, and therefore an additional sum over the sampled points of the Brillouin zone occurs in Equation 2.161. From a computational point of view, the simulation box is now represented differently, as shown for a 2D system that is periodic in the x-y-plane in Figure 2.3 (b). The detector surface is then a plane, in general both above and below the sample, and electron density on its way to the detector gets backfolded to the cell as a consequence of the periodic boundary conditions, thereby reducing the size of the real-space grid for the simulation box considerably. In momentum space, however, the resolution is limited by the sampling of the Brillouin zone, which somewhat outweighs the advantages of the reduced simulation box in the case of (semi-) periodic systems.

In the way described above, real-time TDDFT thus allows for the most direct way of simulating ARPES: just as in the experiment, we detect the flux of electrons through a surface and by resolving both the solid angle and the kinetic energy (trough the projection on Volkov states), we obtain the photoelectron intensity $I(\boldsymbol{k}_{||}, E_{\text{kin}}, \omega)$. In stark contrast to the methods described

before, here we do not have to assume a final state for the photoelectron and its movement in time, under the influence of the the photon field and the remaining system, is governed by the TDDFT Hamiltonian and scattering effects are therefore naturally accounted for. Moreover, density originating from spatially different photoelectrons mutually interfere with each other, at least on the mean field level, which is achieved by updating the Hartree potential during the time-evolution. Consequently, photoemission simulations from real-time TDDFT were shown to reproduce final state effects like circular dichroism [291] or, as demonstrated in Chapter 6 for graphene, the correct variation of angle-resolved photoemission spectra with photon energy. In addition, the method can also be combined with pump fields in the optical regime and thereby gives access to photoelectron spectroscopy for exited systems [289, 292, 290, 293, 294, 295]. In Chapter 7, we could show that the photoelectron momentum maps for excitons within the PWA, as described in Paragraph 2.3.4, are in very good agreement with those from real-time TDDFT, which could therefore serve as a reference method for pump-probe spectroscopy. We finally remark that, despite the success in capturing final state effects and the possibility of simulating excited states photoemission, this method is, by and large, restriced to the ALDA and to rather small systems due to its great computational burden.

Chapter 3

Charge-promoted Self-metalation of Porphyrins on an Oxide Surface

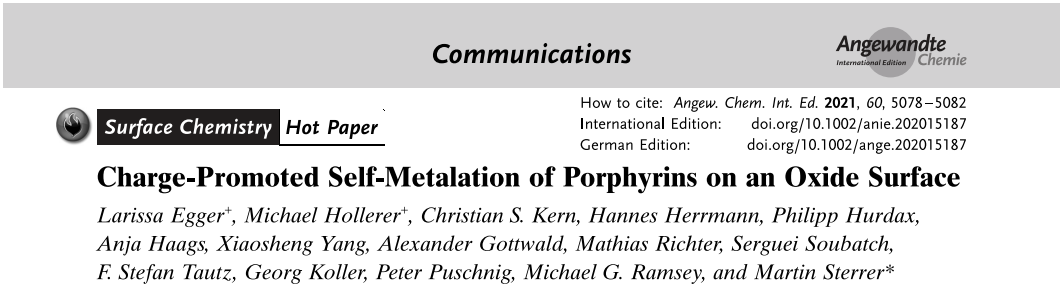

Figure 3.1: **Header of the article as published in *Angewandte Chemie, International Edition* [296].**

Significance Statement

Porphyrin complexes occur in nature in haemoglobin, cytochromes, chlorophyll and in vitamin B12 and their versatility to incorporate different metal ions has a multitude of possible applications [77, 78]. Free-base porphyrins with H_2 in their center were shown to self-metalate when adsorbed on various metal surfaces [297, 298]. In addition to these metal surfaces, thin films of oxides adsorbed on metal surfaces have recently gained interest, where especially the 2 ML MgO/Ag(001) interface has been shown to promote electron transfer into molecules adsorbed on such surfaces, despite the isolating property of MgO [76, 299]. The self-metalation of porphyrins on oxide surfaces had been observed [300, 301, 302, 303], but previous computational studies found that this self-metalation on MgO nano-cubes was limited to edges and cornes [304, 305], while experimental evidence exists that self-metalation is indeed possible on MgO(001) thin films [304, 306].

In this work we could confirm the self-metalation of tetra-phenyl-porphyrins on the 2 ML MgO/Ag(001) surface. In contrast to previous work, we additionally varied the work function of the MgO/Ag(001) surface, which enabled us to pinpoint the effect of self-metalation to the

charge transfer from the surface into the molecules. While charge transfer occurred for standard preparations of MgO/Ag(001), we found that the self-metalation is suppressed on high work function surfaces where no charge transfer occurs. The metalation of porphyrins was experimentally confirmed by x-ray photoemission spectroscopy and the characterization of the geometric and electronic structure of the molecule-substrate interface was achieved with scanning tunneling microscopy, low-energy electron diffraction and valence photoemission spectroscopy. For the latter techniques, our DFT simulations agreed very well, although the direct verification of the metalation process in terms of energy preference could not unambiguously be achieved for all different work function surfaces. This is due to the fact that the simulation of the electronic structure is, in this case, especially sensitive to the treatment of van der Waals interactions, which is a recognition that also helped to understand the discrepancies arising from different previous studies.

Author Contributions

The sample preparation as well as the low-energy electron diffraction, XPS, STM and lab-based ARPES experiments in this work were done by Larissa Egger, Michael Hollerer, Hannes Hermann, Georg Koller, Michael G. Ramsey and Martin Sterrer in Graz. Tomography ARPES measurements were undertaken by Larissa Egger, Philipp Hurdax, Anja Haags and Xiaosheng Yang at the Physikalisch-Technische Bundesanstalt Berlin, supervised by Serguei Soubatch, Alexander Gottwald, Mathias Richter, F. Stefan Tautz, Georg Koller and Michael G. Ramsey. Calculations for structural and electronic properties were carried out by me, under the supervision of Peter Puschnig. Martin Sterrer was responsible for overall project coordination and wrote the initial draft of the manuscript, with contributions from all co-authors.

Abstract

Metalation and self-metalation reactions of porphyrins on oxide surfaces have recently gained interest. The mechanism of porphyrin self-metalation on oxides is, however, far from being understood. Herein, we show by a combination of results obtained with scanning tunneling microscopy, photoemission spectroscopy, and DFT computations, that the self-metalation of 2H-tetraphenyl-porphyrin on the surface of ultrathin MgO(001) films is promoted by charge transfer. By tuning the work function of the MgO(001)/Ag(001) substrate, we are able to control the charge and the metalation state of the porphyrin molecules on the surface.

3.1 Main Text

Due to their versatility, porphyrins and metalloporphyrins have attained major attention in all aspects of organic-inorganic hybrid materials science. In particular, surface-mediated processes of and with porphyrins have strongly contributed to the unbroken fascination of these materials [77]. Surface science investigations of porphyrin self-assembly, on-surface synthesis of 2D covalently linked metal-organic frameworks and building of 3D hetero-architectures [307], or studies on directed metalation [298, 308] and ligation to control their magnetic, sensing and catalytic properties, have provided fundamental insight into their chemical and physical properties [78].

The surface-confined porphyrin metalation is typically achieved by pre- or post-deposition of metal adatoms, or by self-metalation, which occurs on specific metal substrates such as Cu,

Ni, and Fe [298]. These redox-type reactions, which include conformational intermediates, hydrogen-transfer processes and, finally, H_2 release, are reasonably well understood [309, 310]. Recently, self-metalation reactions have also been observed on several single-crystalline oxide surfaces, including TiO_2[110] [300, 301, 302], Co_xO_y thin films [303] and MgO thin films [304]. In contrast to the metalation with metal adatoms, self-metalation on oxides can be viewed as an ion exchange process, where the two protons of a free-base porphyrin are replaced by a metal cation. Detailed mechanistic aspects of this reactions remain, however, still elusive. In the present work, we provide compelling evidence that the self-metalation of 2H-tetraphenylporphyrin (2H-TPP) is promoted by charge transfer on the surface of ultrathin MgO(001) films. Furthermore, by controlling the support properties, we show that uncharged/unmetalated and charged/metalated molecules can be deliberately formed.

The protons released from the free-base porphyrin during the self-metalation process on oxides are suggested to contribute to hydroxylation of the surface [304, 306, 305]. In the case of the self-metalation of 2H-TPP on bulk MgO the hydroxyl formation indeed provides a substantial energy contribution that makes the metalation reaction thermodynamically feasible [304]. However, this process is strongly morphology-dependent and studies on MgO nanocubes show that the reaction is limited to low-coordinated sites such as edges and corners, where the Mg^{2+} vacancy formation energy is lower and hydroxyls are more stable than on regular surface sites [304, 305]. In contrast to this finding is the observation of self-metalation of a complete 2H-TPP monolayer on MgO(001) thin films [306]. While MgO thin film samples also exhibit a certain concentration of surface defects [311], their limited abundance can, however, not explain the high degree of metalation occurring on the regular surface of the films, which remains a mystery. This calls for a different mechanism of the self-metalation reaction on the thin film surface that requires detailed knowledge and understanding of the morphology and electronic properties of the combined molecule-substrate system to be unraveled. Herein, we tackle this problem by a combination of experiments using scanning tunneling microscopy (STM) and photoemission spectroscopy, and density function theory (DFT) computations (Supporting Information in Paragraph 3.2.1 and Paragraph 3.2.2)

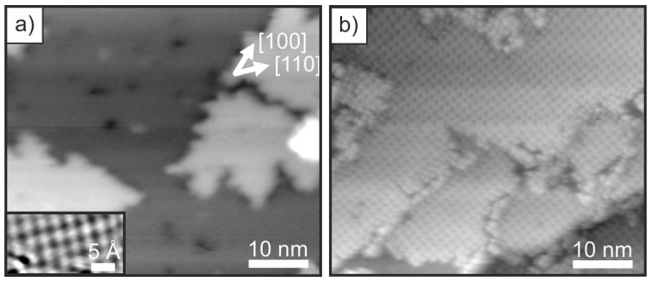

Figure 3.2: STM images of (a) 2 ML MgO(001)/Ag(001) (U_{bias} = 3.0 V, i_t = 29 pA), (b) 1 ML 2H-TPP adsorbed on 2 ML MgO(001)/Ag(001) at room temperature and annealed at 473 K (U_{bias} = 2.0 V, i_t = 28 pA). Inset in (a): Atomically resolved image of MgO(001).

Large-scale STM images of the thin MgO(001) film before and after 2H-TPP adsorption are shown in Figures 3.2 (a) and (b), respectively. As we discuss later, our x-ray photoelectron spectroscopy (XPS) results confirm the spontaneous metalation of a monolayer of 2H-TPP on the films, such that it can be assumed that in the STM images most of the porphyrin molecules are already in the metalated, Mg-TPP, state. The molecules are arranged in a highly ordered square phase with two rotational domains. This is also evident from the low energy electron diffraction (LEED) pattern shown in Paragraph 3.2.1, which can straightforwardly be interpreted in

terms of a $\begin{pmatrix} 4 & -2 \\ 2 & 4 \end{pmatrix}$ superstructure with a square unit mesh with a unit vector of 13.3 Å. More

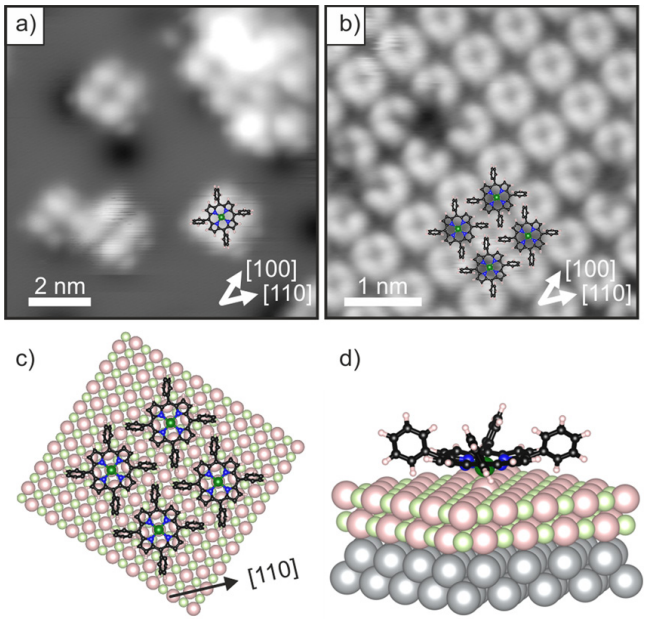

Figure 3.3: STM images of (a) a low-coverage 2H-TPP film adsorbed at 80 K on 2 ML MgO(001)/Ag(001) ($U_{\text{bias}} = 1.2$ V, $i_t = 25$ pA) and (b) its ordered monolayer ($U_{\text{bias}} = 3.2$ V, $i_t = 55$ pA). (c) Tentative structural model of the monolayer phase derived from STM and LEED (top view). (d) DFT-derived adsorption model of Mg-TPP on 2 ML MgO(001)/Ag(001) (3D view). In this model calculation charge transfer occurs from the substrate into the molecule.

detailed STM images of isolated molecules and of the monolayer phase are presented in Figures 3.3 (a) and (b), respectively. The isolated molecules appeared as a 4-lobe structure with a depression in the center (Figure 3.3 (a)). The four lobes are associated with the phenyl groups and the axes connecting opposing phenyl groups point in the [110] directions. The identification of the individual molecules is less straightforward in the case of the monolayer phase but is aided by the appearance of a molecular vacancy, as in Figure 3.3 (b). This reveals that the circularly arranged 4-lobe structure does not correspond to the four phenyl groups of a single molecule, but to the phenyls of 4 neighboring molecules, as depicted in Figure 3.3 (b). The STM of the monolayer phase is in perfect agreement with the LEED structure and leads to the schematic surface model presented in Figure 3.3 (c). This arrangement clearly maximizes T-type interaction between phenyl rings of neighboring molecules [312]. The 4-lobe appearance of the TPP molecules in STM is in accordance with a tilting and twisting of the phenyl groups of TPP in the adsorbed state due to the strong interaction of the macrocycle with the surface (Figure 3.3 (d)) [51]. The upward-tilted phenyl groups dominate the image contrast and, thus, prevent the observation of detailed orbital structure, which is mostly localized at the macrocycle. However, this information would be required to gain information about the electronic structure of the adsorbed TPP molecules and their charge state. Therefore, we now turn to the more detailed investigation of the occupied electronic states using angular-resolved ultraviolet photoemission spectroscopy (ARUPS) and XPS.

The ARUPS and N 1s XP spectra of clean MgO(001)/Ag(001) and increasing doses of 2H-

TPP on MgO(001)/Ag(001) are presented in Figure 3.4. Considering the XP spectra first, we

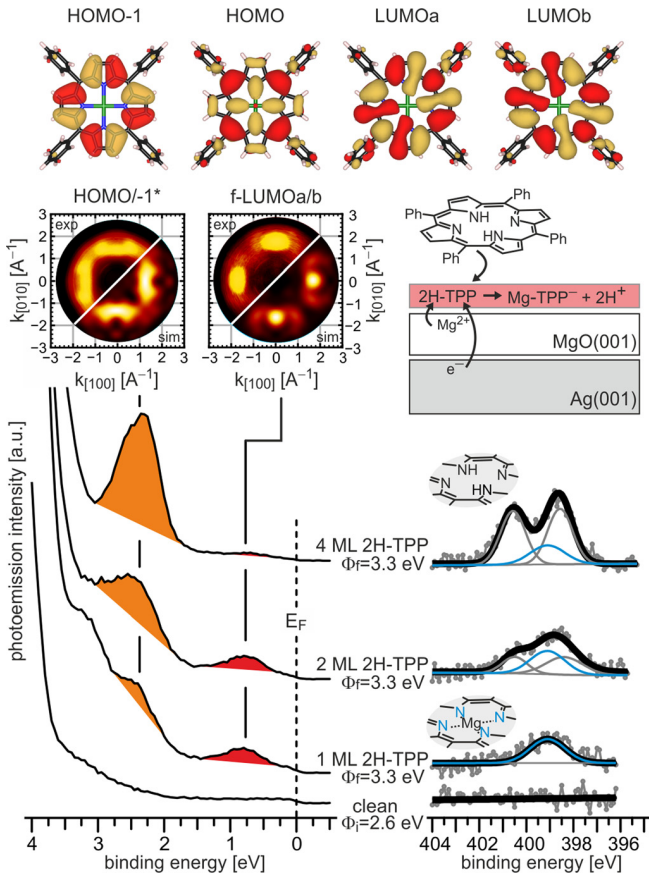

Figure 3.4: Top: real-space representation of the HOMO-1, HOMO, and the degenerate LUMOa and LUMOb of gas-phase Mg-TPP. ARUPS (bottom, left) and XPS (bottom, right) spectra of clean 2 ML MgO(001)/Ag(001) and increasing doses of 2H-TPP (1, 2, and 4 ML) at room temperature. Here, Φ_i is the work function of clean MgO(001)/Ag(001) and Φ_f is the work function after adsorption of 2H-TPP. Middle, left: comparison of experimental and simulated momentum maps of 1 ML 2H-TPP on MgO(001)/Ag(001). The experimental maps were taken at the peak maxima of the PE peaks at 0.75 eV, showing the pattern of the superposition of the molecular LUMOa/b, and at 2.3 eV, showing the pattern of the superposition of the HOMO and HOMO-1. Middle, right: schematic model of charging and metalation upon adsorption of 2H-TPP on MgO(001)/Ag(001).

observe a single N 1s peak at 399 eV binding energy (BE) upon adsorption of a monolayer 2H-TPP, suggesting a similar chemical environment of the four N atoms as in metalated TPP [309]. This peak remains upon increasing the 2H-TPP dose beyond a monolayer, while a pair of additional N 1s peaks at 400.5 eV and 398 eV, corresponding to the aminic and iminic nitrogen pairs in unmetalated 2H-TPP [309], grows in intensity upon further 2H-TPP adsorption. This confirms the results of previous investigations of the same system and indicates that the 2H-TPP molecules in the monolayer are metalated to Mg-TPP, while the molecules in the second and all subsequent layers remain unmetalated 2H-TPP [306]. At this point we note again that the large

concentration of metalated TPP on the thin MgO films together with the rather flat terrace-like morphology of the films (Figure 3.2) is not consistent with a defect-mediated self-metalation reaction suggested in the literature (Paragraph 3.2.3) [304, 305]. Thus, another driving force for the metalation must be present on the thin MgO films.

It is well established that the deposition of MgO films on Ag(001) significantly reduces the Ag(001) work function, which leads to promotion of charge transfer into adsorbates with sufficiently high electron affinity (EA) through electron tunneling [313, 314]. 2H-TPP has a similar EA (1.6-1.8 eV) [315] as pentacene, which has been shown to become negatively charged on the MgO(001)/Ag(001) substrate [76]. Proof for the charge transfer into the TPP molecules in the present experiments comes from the ARUPS results presented in Figure 3.4, left. The deposition of 2H-TPP on 2 ML MgO(001)/Ag(001) thin films, which had an initial work function of Φ_i = 2.6 eV, leads to new states in the MgO band gap region that can be associated with the frontier orbitals of 2H-TPP. Two molecular emissions with BE's of 0.75 eV and 2.3 eV are immediately present after adsorption of a 2H-TPP monolayer at room temperature. Simultaneously, the work function increased to 3.3 eV, which is a first indication that charge transfer into the TPP molecules has occurred [299, 316]. Upon increasing the 2H-TPP coverage to 2 ML and 4 ML, the 0.75 eV emission is attenuated, while the intensity of the 2.3 eV emission increases with 2H-TPP coverage, proving that the former is solely due to molecular species in the first monolayer. The additional 2H-TPP layers do not lead to further work function changes, which indicates that the charge transfer is restricted to the interfacial TPP monolayer.

Identification of the molecular orbitals from which the photoemitted electrons arise is possible with a technique known as photoemission tomography, where the angular intensity distribution of the photoemitted electrons is recorded and converted into a momentum map, which, approximately, corresponds to the reciprocal space image of the real-space electron density distribution [46]. For the two emissions observed in the MgO bandgap region, the experimental momentum maps obtained at BE's corresponding to the peak maxima are displayed in Figure 3.4 along with simulated maps of the degenerate TPP LUMO's (for the 0.75 eV BE emission) and of the superposition of the HOMO and HOMO-1 (for the 2.3 eV BE emission). See Figure 3.4, top, for the real-space representations of the orbitals. Note that the HOMO and HOMO-1 are too close in energy to be resolved in the present experiments. Because of the perfect agreement, the peak at 0.75 eV BE can be identified as emission from an occupied state that has the electron density distribution of the molecular LUMO. This unambiguously confirms the charge transfer into the 2H-TPP molecules upon adsorption and the corresponding state will henceforth be termed former LUMO (f-LUMO). Furthermore, since charge transfer through the thin MgO film is accomplished by tunneling, this state is an integer charge transfer state, in agreement with previous observations [76, 299, 316].

From the combined XPS/ARUPS data in Figure 3.4 we conclude that two processes simultaneously take place upon adsorption of 2H-TPP on ultrathin MgO(001) films: (i) integer charge transfer into the molecules via electron tunneling and (ii) a self-metalation reaction to Mg-TPP. Whether these processes are independent of each other, or if one process is the precondition for the other to occur, cannot be answered with the information provided by the experimental data of Figure 3.4 alone. To prove the interplay between charge transfer and metalation, we block the charge transfer utilizing the recipe developed recently [299, 316]. It relies on chemical modification of the MgO/Ag interface by introducing either oxygen or magnesium. With this, the work function can be tuned over a wide range, from 2.3 eV to 4.4 eV (Paragraph 3.2.3). When charging occurs, the saturation sample work function reached after adsorption of the molecules is equivalent to the critical work function that marks the transition from charging to non-charging (Paragraph 3.2.4) [299, 316]. From the experiment shown in Figure 3.4 the critical work function is at around Φ_{crit} = 3.3 eV. Thus, we expect charge transfer into adsorbed 2H-TPP to be blocked

when adsorbed on an MgO(001)/Ag(001) substrate with $\Phi > 3.3$ eV.

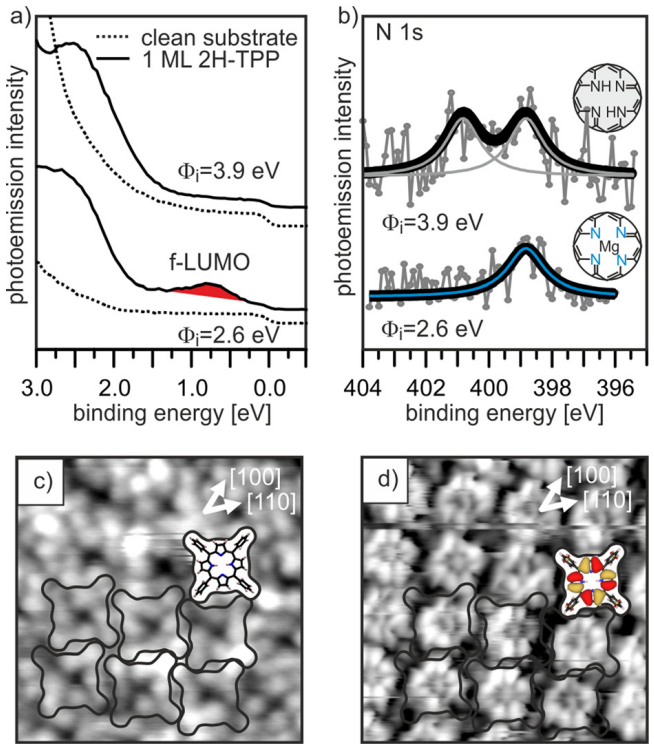

Figure 3.5: (a,b) ARUPS (a) and N 1s XPS (b) for 2H-TPP adsorbed on 2 ML MgO(001)/Ag(001) films with different initial work function, Φ_i. (c,d) STM of 2H-TPP on high work function MgO(001)/Ag(001) at U_{bias} = +2.9 V (c) and U_{bias} = -2.6 V (d).

In Figure 3.5 (a) and (b) we compare the photoemission spectra of 2H-TPP monolayers adsorbed on MgO(001)/Ag(001) with different initial work function, 2.6 eV and 3.9 eV, i.e., below and above Φ_{crit} for charging. The spectra for 2H-TPP on the low work function substrate resemble the results reported in Figure 3.4, where both, charge transfer and self-metalation occur, as shown by the observation of the occupied former LUMO in ARUPS and a single N 1s component in the XPS spectrum. If 2H-TPP is instead adsorbed on the high work function substrate, the band-gap state in the ARUPS is absent, confirming that the molecules are not charged. In addition, we observe the typical signature of non-metalated 2H-TPP in the corresponding XP spectrum.

The absence of charge transfer has also consequences for the appearance of the molecules in STM. Instead of the phenyl-dominated 4-lobe appearance as in Figure 3.3, at similar tunneling conditions both, the peripheral phenyls and the pyrrole groups of the macrocycle are imaged (Figure 3.5 (c)). Furthermore, at negative tunneling voltage, submolecular contrast resembling the electron density distribution of the HOMO-1 was achieved (Figure 3.5 (d)). In addition, we find that, compared to the arrangement shown in Figure 3.3, the 2H-TPP molecules are rotated by 45°, i.e., the phenyl axis is now aligned with the [100] crystallographic direction. The different STM contrast suggests that the 2H-TPP molecules are flatter, and the strong tilting and twisting of the phenyl groups, as seen for the charged and metalated TPP, is absent. This implies a weaker interaction of uncharged 2H-TPP with the surface compared to the charged

and metalated molecule, which also affects the stability of the monolayer phases. While the charged and metalated monolayer is stable up to at least 473 K (see Figure 3.2 (b)), a similar thermal treatment led to the structural disintegration of the uncharged and unmetalated 2H-TPP monolayer.

We could thus show that self-metalation of 2H-TPP on ultrathin MgO films is promoted by integer charge transfer from the MgO/Ag interface into the 2H-TPP LUMO. Most remarkable, this process is not restricted to defects such as low-coordinated sites at edges and corners but occurs also on defect-free terrace sites. Previous computational studies revealed that the self-metalation reaction is energetically unfavored on the terraces of bulk-like MgO [304]. There, the energy gain due to the formation of hydroxyl groups next to the Mg^{2+} vacancy is too small to compensate the high vacancy formation energy. It is obviously the charging of the 2H-TPP molecules on the ultrathin MgO films that provides the energetic balance to make the metalation reaction on terrace sites thermodynamically more favorable. This can be rationalized in terms of the stronger interaction energy and the reduced surface-to-molecule distance for the charged 2H-TPP molecules. Moreover, the presence of a charged molecule on top of the MgO surface leads to significant rumpling of the surface ions, which could further aid the self-metalation reaction by lowering the vacancy formation energy. We note that our findings provide also an explanation for the somewhat contradicting results of previous 2H-TPP monolayer adsorption studies on MgO thin films, where 50 % metalation has been reported on 10 ML thin MgO films [304], whereas complete (100 %) metalation was observed on 2 ML thin MgO films [306]. The reason for this can be found in the electrostatics of the system. The charging is a consequence of potential equilibration in the combined adsorbate-substrate system, which, for the present case, can be explained with a simple capacitor model [299, 316]. In this model, an increase of the dielectric thickness necessitates a decrease of transferred charge to keep a constant potential. Thus, on thicker MgO films less molecules in the monolayer get charged and, consequently, less molecules become metalated (Paragraph 3.2.4). It has to be noted that, while our DFT simulations succeeded in describing the charging of 2H-TPP molecules and the associated work function changes on MgO(001)/Ag(001), the results for the related self-metalation reaction were not in good agreement with the experimental findings, even with inclusion of various van-der-Waals corrections schemes (Paragraph 3.2.5). In general, the metalation reaction of 2H-TPP on the MgO(001)/Ag(001) surface is a complicated process to simulate, since it bridges ionic binding, weak physisorption and metal-organic charge transfer, all situations that can be well described by ab-initio methods individually, but in combination impose a serious challenge and an open task for further computational investigations.

In summary, we have unraveled the mystery of the high 2H-TPP self-metalation activity on ultrathin MgO(001)/Ag(001) films by showing that the metalation is promoted by charge transfer. This finding provides important hints for the mechanism of the self-metalation of porphyrins on oxide surfaces. The charge-induced conformational changes in the molecule, the decrease of the molecule-substrate distance, and the enhanced surface rumpling may all be relevant parameters that positively influence the reaction pathway. Remarkably, our results suggest a method to control electric and chemical (charged/metalated vs uncharged/unmetalated) states of porphyrins by tuning the work function of the substrate or thickness of the dielectric, which opens the way for a selective surface functionalization.

3.2 Supporting Information

3.2.1 Experimental Details

All experiments were performed under ultrahigh vacuum conditions in three separate preparation and analysis systems. All chambers were equipped with the tools necessary for sample cleaning/preparation (electron beam heating, sputter gun, metal and molecule evaporators, gas dosing) and basic characterization (low energy electron diffraction, quadrupole mass spectrometer).

Sample preparation

The Ag(001) substrate was cleaned by repeated cycles of sputtering (Ar^+ ions at 0.8-1 kV) and annealing (773 K, 2 min). MgO(001) films were grown by Mg evaporation from an e-beam evaporator in an oxygen environment. Mg fluxes used were of the order of 1 Å/min as monitored by a quartz microbalance. The MgO deposition was done at a substrate temperature of 553 K and in an O_2 pressure of 10^{-6} mbar, followed by slow cooling (roughly 2.5 °C/min), the accepted procedure providing epitaxial MgO(100) films with high structural quality [317]. 2H-TPP was deposited onto the MgO(001)/Ag(001) substrate either at room temperature or 80 K from a Knudsen type molecular evaporator heated to 433 K. The molecular flux was calibrated using a quartz microbalance. The low energy electron diffraction (LEED) pattern of a full monolayer of 2H-TPP adsorbed on MgO(001)/Ag(001) thin films shows a $\begin{pmatrix} 4 & -2 \\ 2 & 4 \end{pmatrix}$ superstructure with a square unit mesh with a unit vector of 13.3 Å.

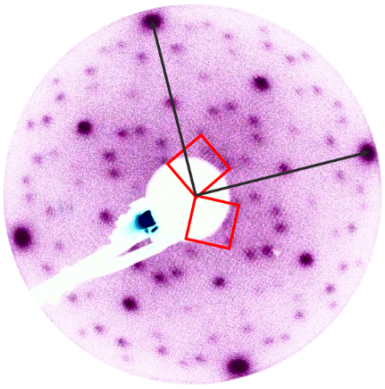

Figure 3.6: LEED image of the 2H-TPP monolayer on MgO(001)/Ag(001).

Scanning tunneling microscopy (STM)

STM measurements were performed at 77 K with a Createc low-temperature STM attached to an ultrahigh-vacuum preparation chamber (base pressure 2×10^{-10} mbar) using electrochemically etched tungsten tips. The bias was applied to the sample.

Photoemission experiments

Photoemission experiments were performed at the Metrology Light Source of the Physikalisch-Technische Bundesanstalt (Berlin, Germany) at the insertion device beamline using a toroidal electron-energy analyzer. A photon energy of 35 eV and an incidence angle of χ = 40° with respect to the surface normal were used. The polarization direction is in the specular plane, which is also the measured photoelectron trajectory. The emitted electrons were simultaneously recorded with polar angles of -80° to 80° with respect to the surface normal. For the shown momentum maps, the photoelectron intensity on the positive polar angle range was used. Note that this direction corresponds to the maximal molecular emission relative to the substrate emission. To measure the momentum maps for a chosen binding energy, the sample was rotated in the azimuthal direction in 1° steps, which results in a full photoelectron distribution in the (k_x, k_y)-plane perpendicular to the sample normal. The energy distribution curves were obtained by integration of photoemission intensity over the entire available $k_{||}$ range. Coverage-dependent UPS (He I) and XPS (Mg K_α) experiments were taken in-house with a hemispherical Scienta SES-200 analyser in angular and spatial mode, respectively. ARUPS spectra were taken along the [100] azimuthal direction at θ = 40° take-off angle. XP spectra were taken at normal emission.

3.2.2 Computational details

DFT calculations for the gas-phase orbitals of both 2H-TPP and Mg-TPP have been performed with the ab-initio quantum chemistry software NWChem [318]. We have used a 6-31G* basis set and the GGA-PBE approximation for exchange-correlation effects [319]. Theoretical momentum maps of the angular photoelectron distribution have been simulated within the plane wave final state approximation, from the Fourier transform of the real space orbitals of the isolated molecule, as described in Ref [46]. In order to shed light on the metalation of 2H-TPP, we have additionally simulated the adsorption of 2H-TPP and Mg-TPP on the MgO/Ag-surface in various configurations by means of DFT utilizing the VASP code and employing the projector-augmented wave method [320, 321]. Using a repeated slab approach, with 5 Ag-layers, 2 MgO layers and one molecule per unit cell, an inter-layer vacuum layer of 13 Å thickness and a dipole-correction in z-direction, all investigated structures have been optimized using a van der Waals corrected GGA functional for exchange and correlation effects [319, 137]. All atomic positions except those of the lowest 3 layers of Ag have been relaxed, and we have used the experimental lattice parameter of Ag with a = 4.076 Å. Subsequent to the geometry optimization, the electronic structure has been calculated using an energy cutoff of 400 eV, a Gaussian-type smearing with a broadening of 0.2 eV and a Brillouin zone-sampling with 8x8x1 points centered around the Gamma point.

3.2.3 Work function tuning and influence of defects

A typical MgO thin film preparation results in samples with an average work function of 2.8 $\pm$0.2 eV, which is similar to the calculated work function for an MgO(001)/Ag(001) system with ideal, i.e. stoichiometric, interface (see below and Ref. [322, 323]). Based on previous experimental reports [324] and theoretical predictions [323] we applied various treatments to alter the work function. To reduce the WF, we typically mildly annealed the samples after preparation in UHV or evaporated additional Mg during annealing. To increase the WF, the samples were exposed to oxygen (5×10^{-7} to 2×10^{-4} mbar) at elevated temperature after preparation. For the experiments presented in this paper, the MgO films were either used as obtained

from a typical preparation (WF = 2.7 eV), or additionally exposed to oxygen to increase the WF (WF = 3.9 eV). As shown below (Computational results 3.2.5), the work function variation can be accomplished by inserting additional oxygen atoms in the interstitial sites of the topmost Ag layer (WF increase), or be replacing Ag atoms in the topmost Ag layer by Mg (WF reduction). Neither of these treatments changes the stoichiometry of the MgO film on top of the Ag(001) substrate. (We mention that it is also possible to change the work function by introducing either oxygen or magnesium vacancies in the interfacial MgO layer [299], but this is experimentally less likely at the applied conditions.)

Of course, some defects can and will be formed during the MgO film growth and several previous studies have reported on defect characterization on MgO thin films. The most obvious surface defects on MgO thin films are low coordinated sites at step edges [325, 326]. Additionally, color centers (oxygen vacancies) have attracted a lot of interest in the past [327]. They can either exist with 0, 1, or 2 electrons trapped inside the vacancy. In particular, the F^+ and F^0 centers (1 and 2 trapped electrons, respectively) lie energetically above the MgO valence band and, therefore, can influence the reactivity of the MgO surface. There are, however, no indications for a large and countable abundance of color centers on freshly prepared MgO thin film samples, neither from scanning tunneling microscopy [328], electron spin resonance [329, 328], UPS and metastable impact electron spectroscopy [326, 330], and electron energy loss spectroscopy [331] studies. It is known that color centers can be formed on thin MgO films by relatively harsh measures such as electron bombardment [329, 328, 331]. It is, therefore, safe to say that for the results presented in this manuscript, defects do not play a significant role for the observed charge transfer into 2H-TPP on the ultrathin MgO films. This is supported by both the initial work function dependence and the MgO layer thickness dependence of charging and metalation, which follows the expectations of the capacitor model and relies only on charge transfer from the MgO-Ag interface to the molecules on the surface. If surface defects would be responsible for the charge transfer into the 2H-TPP molecules, the capacitor model would not be valid anymore, which is not observed (see Paragraph 3.2.4).

3.2.4 Results of additional experiments

Adsorption of Mg-TPP on high work function MgO(001)/Ag(001)

To provide an additional proof that the state at 0.75 eV binding energy is due to charge transfer into the LUMO of 2H-TPP, and is not related to an intrinsic electronic state of Mg-TPP, which is formed by self-metalation on the MgO surface, we have deposited Mg-TPP on a high WF 2 ML MgO(001)/Ag(001) substrate. In Figure 3.7 we compare the UPS spectra of this preparation with the UPS spectra of 2H-TPP deposited on low WF and high WF 2 ML MgO(001)/-Ag(001). As reported in Section 3.1, only on low WF MgO(001)/Ag(001) the state at 0.75 eV is present, according to charge transfer from the substrate into the molecular LUMO. The deposition of 1 ML Mg-TPP on a high WF substrate, where no charge transfer occurs, gives rise to an UPS spectrum without any new features directly below the Fermi energy. The broad peak at 2 eV BE is related to the HOMO and HOMO-1 emissions of neutral Mg-TPP.

Work function and MgO film thickness dependence of charging and self-metalation

According to our previous findings [299, 299], if the work function is low enough for charge transfer to occur into adsorbates on MgO(001)/Ag(001) thin films (Fermi level pinning regime), the number of charged molecules on the surface is related to the potential difference $\Delta\Phi$ (work

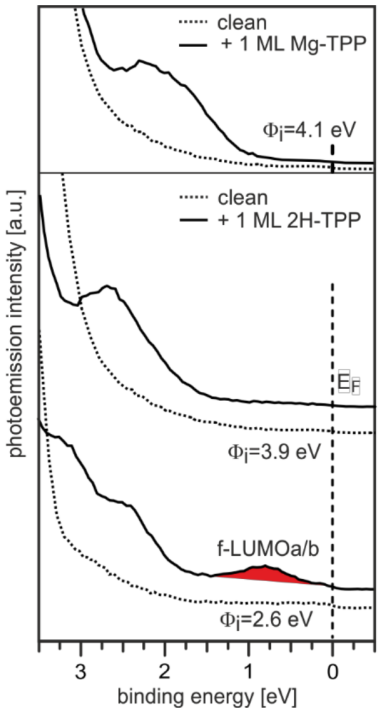

Figure 3.7: Comparison of UPS spectra after adsorption of a monolayer 2H-TPP on 2 ML MgO(001)/Ag(001) films with different initial work function (bottom) and for a monolayer Mg-TPP on a high work function 2 ML MgO(001)/Ag(001) film.

function difference before and after adsorption) according to the capacitor model:

$$\Delta\Phi = \frac{\sigma d_{cs}}{\varepsilon_0 \varepsilon_r}, \tag{3.1}$$

where σ is the average charge density in the molecular film [C/m^2], ε_r is the dielectric constant of the thin film and d_{cs} (charge separation distance) is the distance between the charge at the molecule and the interface. Thus, for the same MgO film thickness (same d_{cs}), the number of charged molecules depends on the initial work function and decreases as Φ_i increases. We have tested this hypothesis by studying the charge transfer into and self-metalation of 2H-TPP on 2 ML MgO(001)/Ag(001) preparations with different initial work function. As shown in Figure 3.8, the experimental results are in agreement with the expectations from the capacitor model: as the initial work function is increased, the intensity of the state at 0.75 eV BE in UPS (Figure 3.8, left), which is related to the occupied former LUMO of the TPP molecules, decreases until it is no longer present on samples with high initial work function, where no charge transfer takes place. Concomitant with the decrease of the former LUMO intensity in UPS, the N 1s XPS peak related to metalated TPP (Mg-TPP) decreases and the fraction of unmetalated 2H-TPP increases (Figure 3.8, right). Note that for an initial work function of 3.3 eV, which is the same as the observed pinning work function that marks, in an ideal system, the transition from charging to non-charging, there is still a large fraction of charged and metalated TPP present on the surface. This result can be understood based on the creation of an additional dipole due to a push-back effect of the adsorbed TPP molecules, which partly counterbalances the charge-

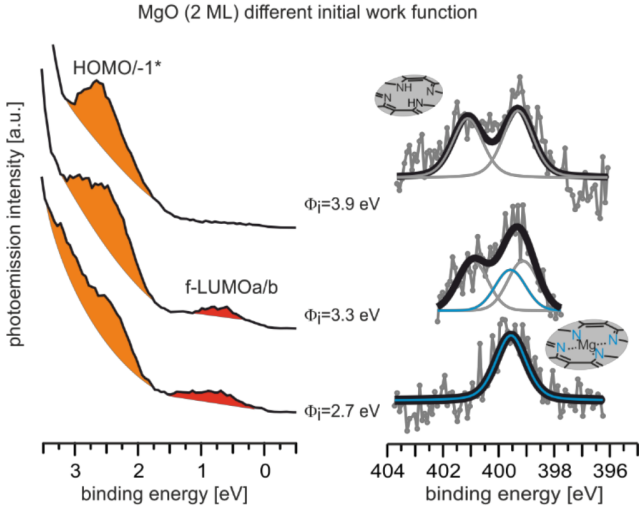

Figure 3.8: ARUPS (left) and N 1s XPS (right) spectra of 2H-TPP adsorbed on 2ML MgO(001)/Ag(001) samples with different initial work function (Φ_i). Increasing initial work function reduces charge transfer (f-LUMO) and metalation.

induced dipole. The "true" pinning work function is therefore a few tenths of an eV above the observed pinning work function (see also the discussion in Ref. [299]). From the relative intensities of the N 1s XP signals the fraction of charged/metalated and uncharged/unmetalated TPP molecules in the monolayer can be calculated. For the Φ = 3.3 eV work function sample shown in Figure 3.8, around 30% of the molecules in the monolayer are charged/metalated and 70% of the molecules are uncharged/unmetalated. This is also consistent with the f-LUMO intensity seen in the ARUPS.

Next, we have studied the MgO film thickness dependence of the charging and self-metalation process. According to Equation 3.1, the number of charged molecules should decrease at constant potential difference $\Delta\Phi$ if the MgO film thickness (and thus d_{cs}) is increased [299]. We have prepared MgO films with the same initial work function (Φ_i = 2.7 eV) but different thickness (nominally 2 ML, 4 ML and 8 ML) and show in Figure 3.9 the UPS (left) and N 1s XPS (right) results for the adsorption of a monolayer 2H-TPP on these samples. For the 2 ML and 4 ML thin MgO(001) films the results are almost identical and suggest that only charged and metalated TPP molecules are present on the surface. However, we observe a decrease of the occupied former LUMO peak in UPS and, as a result, the co-presence of metalated (50%) and non-metalated TPP (50%) molecules according to XPS, for the 8 ML thin MgO film, in perfect agreement with the expectations from the capacitor model (Equation 3.1). The additional results presented here thus provide further proof for the direct relation between charge transfer into and self-metalation of 2H-TPP on the surface of ultrathin MgO(001)/Ag(001) films.

3.2.5 Computational results

An overview over the simulated structures can be seen in Figure 3.10. Importantly, we have also investigated the influence of the substrate's work function (WF) on the electronic structure of the adsorbed molecule. The DFT calculation for two stoichiometric layers of MgO on five layers of Ag results in an initial WF of 3.0 eV prior to the adsorption of the molecule (Figure 3.10, middle row). When incorporating an additional 1/4 monolayer of oxygen atoms at interstitial

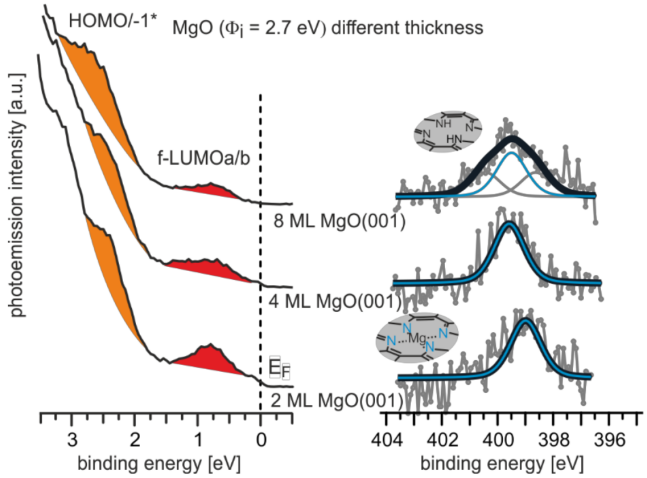

Figure 3.9: ARUPS (left) and N 1s XPS (right) spectra of 2H-TPP adsorbed on MgO(001)/Ag(001) samples with different MgO film thickness. Increasing MgO thickness (with the same initial work function) reduces charge transfer (f-LUMO) and metalation (XPS).

sites in the topmost Ag-layer, the WF rises to 4.7 eV (Figure 3.10, top row) as has already been described in Ref [323]. Conversely, substituting 1/4 of the Ag atoms in the topmost Ag layer by Mg lowers the initial WF to 2.1 eV (Figure 3.10, bottom row) [324]. Using these three model substrates, both the adsorption of 2H-TPP (Figure 3.10, middle column) and Mg-TPP (Figure 3.10, right column) has been simulated. Note that for the adsorption of Mg-TPP, the metalation reaction has been simulated as an exchange reaction consisting of the removal of a Mg^{2+} from the topmost MgO layer and the concomitant creation of a hydroxyl group in the so-created Mg vacancy. As can be seen from Figure 3.10, the preferred adsorption site of 2H-TPP is the center of the molecule being on top of an oxygen ion (red balls) with the nitrogen atoms sitting on top of Mg^{2+} (orange balls) resulting in an azimuthal orientation of the molecule in agreement with experimental findings. When studying the exchange reaction for the metalation process we have tested several relative positions of the hydroxyl groups (protons highlighted as green balls) with respect to the molecule's central Mg^{2+} ion (highlighted as dark blue ball). It turns out that in the most favorable adsorption configuration, Mg-TPP's center is again situated on top of an oxygen atom and the hydroxl groups are located in the topmost MgO layer at the position of the Mg^{2+} vacancy underneath a nitrogen atom of Mg-TPP.

The resulting electronic structures have been analyzed in Figure 3.10 in terms of their total density of states (DOS, black lines) and the DOS projected onto the molecule (red lines). In all cases one can clearly identify the energetic positions of the frontier molecular orbitals as indicated in the figure. While for the high WF case no charge transfer into the LUMO takes place, neither for the 2H-TPP nor the Mg-TPP case, the situation is markedly different for the initial WF of 3.0 eV. Here the calculation results in the formerly doubly degenerate LUMO peak to be centered at the Fermi energy, clearly indicating 1e charge transfer into the LUMO. It should be noted that the energy of the LUMO peak truncated by E_F must be taken as an artifact of the computational treatment. As has been shown for other molecular systems adsorbed on thin insulating layers on metals integer charge transfer leads to the singularly occupied molecular orbital (SOMO) appearing well below E_F and the singularly unoccupied molecular orbital (SOMO) well above it [316, 76]. The creation of supercells containing more than one molecule and the usage of a hybrid functional with a substantial fraction of exact exchange [76, 332]

would be necessary to realize conditions that allow for integer charge transfer. Unfortunately, in the present case, such a theoretical treatment is prevented by the large number of atoms per unit cell owing to computational reasons. Nevertheless, from our experience [76], we expect that the electronic structure shown for the initial WF of 3.0 eV would lead to an integer charge transfer corresponding to the experimentally observed situation of the f-LUMO (SOMO) 0.8 eV below E_F. Finally, when reducing the initial WF to 2.1 eV by incorporating additional Mg atoms in the topmost Ag layer, the LUMO peak moves almost entirely below the Fermi energy thereby further promoting the charge transfer into the molecule with the LUMO fully occupied (2 electrons). In order to tackle the question of the relative energetic stability of the adsorption of intact 2H-TPP on MgO(001)/Ag(001) compared to the metalated Mg-TPP on MgO(001)/Ag(001) as resulting from the exchange reaction described above, we now analyze the adsorption energies resulting from our DFT total energy calculations. We define the adsorption energy as follows:

$$E_{\text{ads}} = E_{\text{tot}} - (E_{\text{surf}} + E_{\text{mol}}). \tag{3.2}$$

Here, E_{tot} refers either to the total energy of 2H-TPP on MgO(001)/Ag(001) or the Mg-TPP on MgO(001)/Ag(001) complex subsequent to the metalation reaction, and E_{surf} and E_{mol}, respectively, refer to the total energies of the uncovered MgO(001)/Ag(001) substrate prior to the adsorption and the gas-phase 2H-TPP molecule's total energy. With this definition of the adsorption energy, negative values correspond to bonding to the surface while positive values suggest that adsorption is not favored. To investigate the role that van-der-Waals (vdW) corrections play for the adsorption energies and to demonstrate possible complications inherently present in state-of-the-art vdW-corrected DFT functionals when applied to mixed metallic/ionic/molecular hybrid systems, we have evaluated the adsorption energies for four different functionals. First, we disregard vdW corrections entirely, that is, we employ the standard PBE-GGA functional (GGA) [319]. Second, we use Grimme's empirical D3 method [137], which we have already used for the electronic structure analysis discussed above. In addition, we have employed two more vdW-correction schemes, namely the SCAN+rVV10 method (SCAN) [115, 173] and the Tkatchenko-Scheffler (TS) [140, 151, 152] method with parameters obtained from the self-consistent screening equation. It should be noted that for each functional all structures have been relaxed prior to the evaluation of Equation 3.2. The resulting adsorption energies as well as the final work function values are listed in Table 3.1. First, we note that in a pure GGA calculation without vdW correction, neither 2H-TPP nor the metalated Mg-TPP would bind at all, or at least only very lightly, on the high and medium WF substrates. This finding is in agreement with earlier GGA calculations for Mg-TPP on bulk MgO cubes [304], where the self-metalation reaction was found to be thermodynamically favorable at step edges of MgO but not on a defect-free MgO surface. Only for the very low initial WF does PBE predict binding, which can be explained by the substantial electron transfer. Importantly, when comparing the situation before and after the metalation, we observe that PBE predicts the metalation reaction to be favored except for the low WF substrate where PBE yields almost equal adsorption energies for the two molecules. It is a well-known fact that vdW interactions, which are not properly accounted for in a GGA functional, play an essential role in the adsorption of organic molecules on all organic and inorganic substrates. When inspecting the adsorption energies obtained for Grimme's empirical DFT+D3 correction, we indeed notice the strong influence of dispersive long-range interactions on the energy balance for the adsorption. First, the adsorption energies now clearly indicate that, both, 2H-TPP and Mg-TPP will stick to the MgO(001)/Ag(001). Secondly, we observe that the binding becomes more favorable with the increased charge transfer into the molecule on decreasing the substrate's initial WF. However, DFT+D3 predicts the metalation reaction to be endothermic except for the high WF substrate. There are several reasons which might explain this theoretical outcome conflicting somewhat

Initial WF (eV)	Adsorbate	Adsorption energy (eV)				Final WF (eV)			
		GGA	D3	SCAN	TS	GGA	D3	SCAN	TS
4.7	2H-TPP	0.42	-3.41	-5.01	-7.1	4.52	4.16	3.96	4.17
4.7	Mg-TPP	-0.08	-3.61	-5.18	-6.62	4.55	4.43	4.32	4.46
3	2H-TPP	0.72	-4	-6.22	-7.76	3.17	3.2	3.36	3.19
3	Mg-TPP	0.44	-3.7	-5.9	-6.87	3.12	3.16	3.25	3.13
2.1	2H-TPP	-1.84	-6.22	-8.55	-8.43	3.03	3.17	3.24	3.12
2.1	Mg-TPP	-1.72	-5.71	-7.79	-6.42	3.06	3.07	3.11	2.98

Table 3.1: Adsorption energies according to Equation 3.2 and final work functions for 2H-TPP and Mg-TPP for different initial WFs for four the different DFT functionals GGA, D3, SCAN and TS, respectively. See text for more details.

with the experimental findings. First, it should be noted that, although we have tested several configurations for the position of the hydroxyl group relative to the Mg-TPP adsorption position, we may have missed the global energy minimum of the metalated Mg-TPP complex on the surface. Secondly, it should be stressed that the present case of an organo-metallic complex adsorbed on an ionic crystal double-layer residing on a metallic substrate challenges common vdW correction schemes. For instance, while pure GGA is known to describe ionic crystals well, it fails to correctly describe weak physisorption of molecules on surfaces [333]. Thus, the known deficiencies of common vdW-correction schemes for ionic bonds may prevent the delicate interplay between bonding of Mg to the MgO-lattice and the Mg-N interaction inside Mg-TPP to be correctly accounted for. We have indeed tested how other vdW-correction schemes perform for the present systems. Summarizing the results listed in Table 3.1, we find quite a strong effect on the absolute size of the adsorption energies, e.g., the adsorption energies from the SCAN and TS schemes are significantly larger than those from the D3 approach. However, also the latter approaches would predict the metalation to be less favored. As a third and final reason for this discrepancy, it should be emphasized that the charge transfer into the molecule plays a key role for the metalation. While the GGA+vdW approach captures the overall correct trend as a function of the substrate's WF (compare discussion above and results of Figure 3.10), it must be noted that a more realistic description of the charge transfer would probably require the utilization of hybrid DFT functionals [332]. Unfortunately, however, a full geometry relaxation using hybrid functionals is presently computationally out of reach for such large unit cells.

In general, the metalation reaction of 2H-TPP on the MgO(001)/Ag(001) surface is a complicated system to simulate, since it bridges ionic binding, weak physisorption and metal-organic charge transfer, all situations that can be well described by ab-initio methods individually, but in combination impose a serious challenge and an open task for further computational investigations and developments.

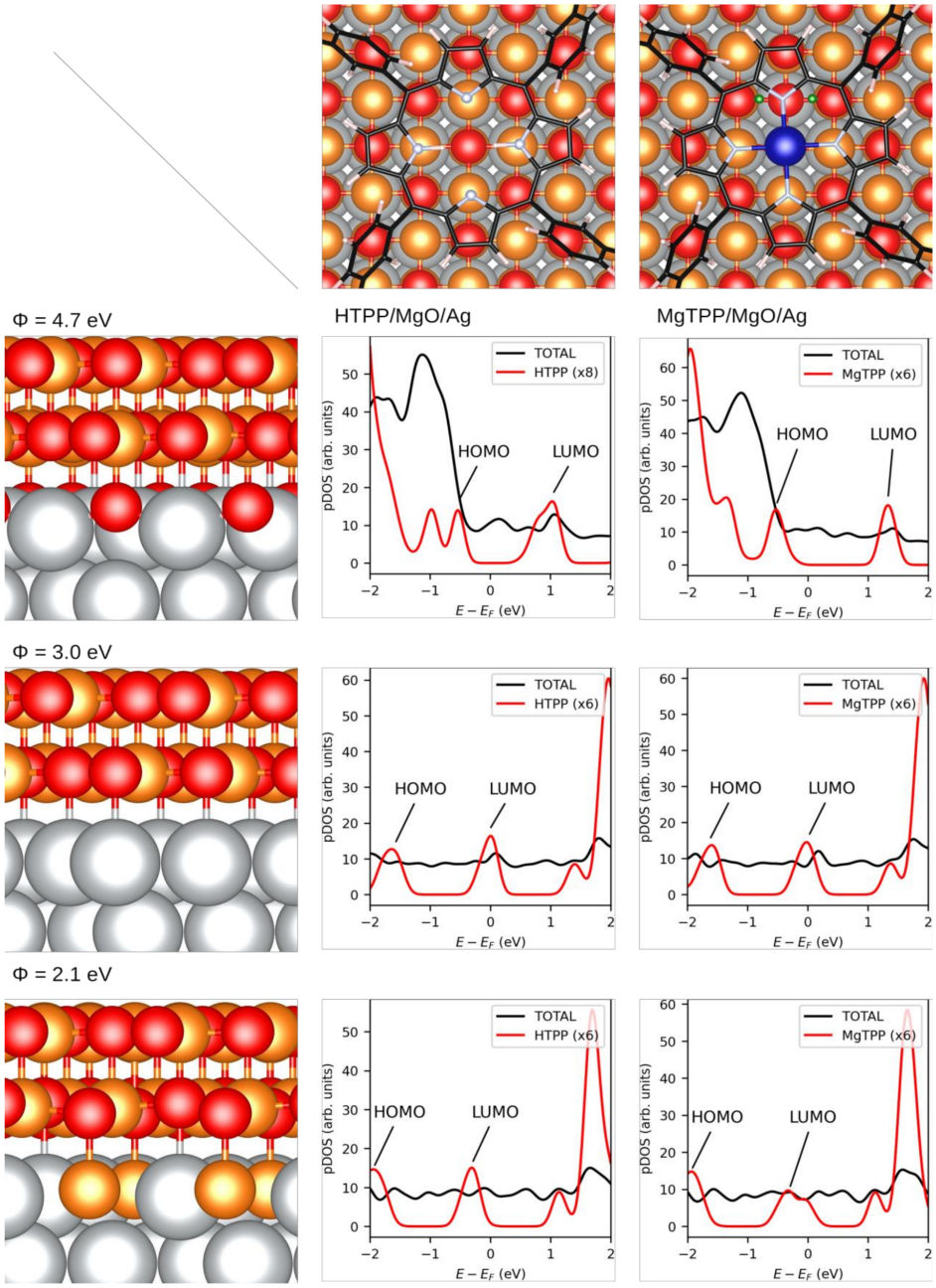

Figure 3.10: Overview of total DOS (black) and DOS projected on molecule (red) for 3 different initial WF (rows) for 2H-TPP and Mg-TPP on MgO(001)/Ag(001) (columns). In the real space models the red, orange and grey balls represent O, Mg and Ag atoms, respectively, while the small green balls represent the displaced hydrogen.

Chapter 4

Charge and Adsorption Height Dependence of the Self-metalation of Porphyrins on Ultrathin MgO(001) Films

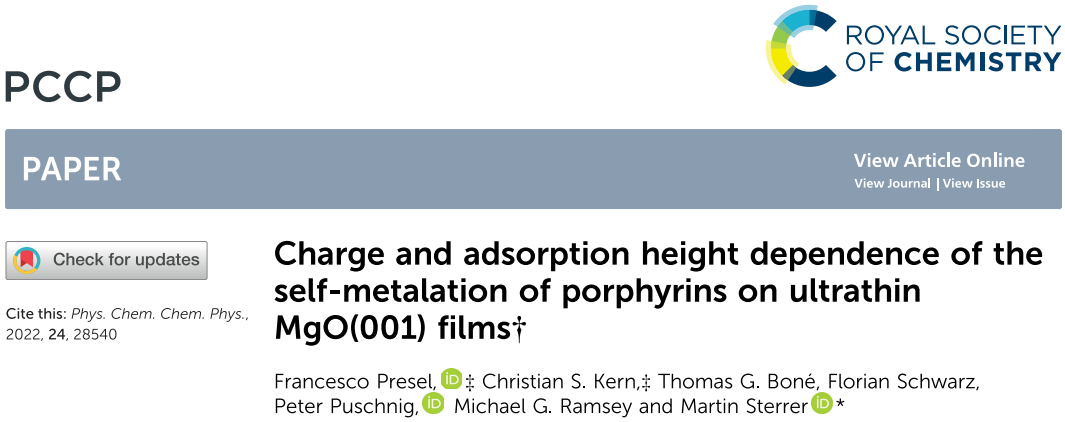

Figure 4.1: **Header of the article as published in *Journal of Physical Chemistry Chemical Physics* [334].**

Significance Statement

This work is a follow-up project of the self-metalation of tetra-pehyl-porphyrins as described in Chapter 3. Here we studied the adsorption of the smaller parent-molecule, porphin, instead of tetra-pehyl-porphyrin, on the same surface of 2 ML MgO/Ag(100). In contrast to its larger relative, porphin lacks the upstanding phenyl side-groups of tetra-pehyl-porphyrin and could therfore serve for two tasks. Firstly, more extensive computational studies were possible due

to the smaller unit cell of the molecule. This fact was especially important for resolving the open questions about the incorporation of different treatments for van der Waals interaction in such systems, as raised by the previous work. Secondly, the flat porphin molecules are believed to adsorb closer to the surface, as the non-planar tetra-pehyl-porphyrin. This allowed us to examine the self-metalation in a regime of stronger molecule-surface interaction where different mechanisms for the metalation-process could become relevant.

Indeed, when varying the surface work function as in the previous study on tetra-pehyl-porphyrins, we found that porphin self-metalates, irrespective of charge transfer from the surface to the molecules, which could also be reproduced with DFT calculations by employing a dedicated van der Waals functional.

Author Contributions

The sample preparation, as well as the low-energy electron diffraction, scanning tunneling microscopy and x-ray photoemission measurements of this work were carried out by Francesco Presel, Florian Schwarz and Martin Sterrer. Additional valence photoemission experiments were done by Thomas G. Boné, supervised by Michael G. Ramsey. The DFT calulations, as well as the analysis of their results, were done by me, under the supervision of Peter Puschnig. Martin Sterrer was responsible for overall project coordination and wrote the initial draft of the manuscript, together with Francesco Presel. All authors contributed to the scientific discussion and to the finalization of the manuscript.

Abstract

We have experimentally determined the adsorption structure, charge state, and metalation state of porphin, the fundamental building block of porphyrins, on ultrathin Ag(001)-supported MgO(001) films by scanning tunneling microscopy and photoemission spectroscopy, supported by calculations based on density functional theory. By tuning the substrate work function to values below and above the critical work function for charging, we succeeded in the preparation of 2H-P monolayers which contain negatively charged and uncharged molecules. It is shown that the porphin molecules self-metalate at room temperature, forming the corresponding Mg–porphin, irrespective of their charge state. This is in contrast to self-metalation of tetraphenyl porphyrin (TPP), which occurs on planar MgO(001) only if the molecules are negatively charged. The different reactivity is explained by the reduced molecule-substrate distance of the planar porphin molecule compared to the bulkier TPP. The results of this study shed light on the mechanism of porphyrin self-metalation on oxides and highlight the role of the adsorption geometry on the chemical reactivity.

4.1 Introduction

Tailoring the properties of molecules of the tetrapyrrole family by metalation and functionalization is potentially useful for targeting specific applications, e.g., in the fields of catalysis, sensing, and optoelectronics. To this end, on-surface preparation strategies, mostly carried out on metal surfaces, for variously functionalized porphyrins and phthalocyanines have been developed, that provided detailed insight into their hierarchical organization and allowed their structural, electronic and chemical properties to be studied in great detail [77, 78, 335]. However, for specific applications, e.g., if porphyrins are to be used in solar energy harvesting de-

vices [336], it is desirable to switch to semiconducting substrates such as oxides. Compared to metal surfaces, atomic-scale investigations into the interfacial properties of hybrid systems oxide/porphyrin are just emerging. Herein, we present a study of the interface between the basic tetrapyrrole macrocycle, the free-base porphin (2H-P), and welldefined MgO(001) surfaces, to elucidate the role of the distance between the macrocycle and the surface, and of the charging of the molecules, on its self-metalation activity.

The controlled synthesis of metal-tetrapyrrole complexes and assemblies is possible by surface-confined methods such as post-metalation or self-metalation of adsorbed molecules [298]. It is established that free-base porphyrins self-metalate in a redox process on specific metal substrates, e.g. Fe, Ni, Co, Pd, Cu, Ag, Au, where it often requires thermal activation or the aid by adsorbed oxygen [337, 338, 308, 339, 340, 341]. Recent studies have also provided insight into the anchoring and self-metalation of porphyrins, specifically of 2H-tetraphenyl-porphyrin (2H-TPP) and its derivatives, on oxide surfaces such as MgO [304], TiO_2 [300], or cobalt oxides [303]. In contrast to on metal surfaces, the self-metalation reaction on oxides can be viewed as an ion-exchange process, where the two aminic protons in the macrocycle are replaced by a substrate cation and either desorb, or form hydroxyls on the surface.

2H-TPP adsorbs flat, that is, with the macrocycle parallel to the surface, on most oxide surfaces. Its self-metalation has been shown to depend on the type of oxide. For example, TPP readily metalates on CoO(111) and Co_3O_4(111) [339, 303] films at room temperature, but requires thermal activation on TiO_2(110) [300], where initially the diacid (4H-TPP) is formed and the metalation process might be triggered by the diffusion of interstitial Ti to the surface [342, 343, 344]. In addition, a strong dependence of the self-metalation activity on oxides on the adsorption geometry has been noted. The introduction of specific anchor groups, e.g. carboxylic or phosphonic acid groups attached to the phenyls of TPP, can shift the preferred adsorption geometry from flat-lying to upright standing, which generally leads to suppression of self-metalation, depending on coverage and temperature [345, 346, 347, 348, 349, 350, 351, 352, 353, 354].

While for some flat oxides the high self-metalation yield points to a high activity of regular surface sites in this process, the possible involvement of surface defects has to be considered as well [355]. A specific case evolved for MgO, for which self-metalation of 2H-TPP was originally demonstrated for MgO nanostructures on the edges of cubic nano-crystals, where the energy needed to extract a magnesium ion is lower and the energy balance due to the formation of hydroxyls is favorable [305]. Subsequent experiments suggested that also on flat, single-crystalline substrates it only occurs at undercoordinated sites [304]. In contrast, we have recently shown that it can occur on the regular surface sites of a planar Ag(001)-supported MgO(001) ultrathin film, where the metalation process is facilitated by charge transfer (CT) of electrons from the metal substrate, through the MgO film, into the adsorbed porphyrins [296].

However, the underlying mechanism allowing or preventing self-metalation based on charge transfer has not been fully understood. One possible explanation is suggested by our previous observation that charge transfer leads to electrostatic attraction, pulling the porphyrin macrocycle of 2H-TPP closer to the MgO surface compared to the uncharged case, where the distance to the surface is larger because of the steric effect of the bulky phenyl ligands [296]. By similar arguments, the self-metalation activity of 2H-TPP on the edges and corners of nanoparticulate MgO [305] could be explained by the macrocycle making a closer approach at corners and edges without interference of the steric repulsion of the phenyls [356].

To provide support for this hypothesis, we present in this work an experimental and computational study about the self-metalation of the free-base porphin (2H-P) on the surface of ultrathin MgO(001) films. Compared to 2H-TPP, the porphin molecule is lacking the four external phenyl ligands and is therefore completely planar, which should allow the macrocycle to get closer to the surface even without the help of electrostatic attraction due to charging. In addi-

tion, since the phenyl ligands contribute only little to the frontier molecular orbitals of 2H-TPP, the electronic structures of 2H-TPP and 2H-P in the energy range of interest are almost identical and should therefore not be accountable for any observed differences in self-metalation activity.

Experimentally, we follow a similar approach as previously reported for the study of the self-metalation of 2H-TPP on ultrathin MgO(001) films on Ag(001) [296]. By variation of the work function Φ of the MgO(001)/Ag(001) substrate, we are able to control the charge transfer into the 2H-P molecular monolayer and, thus, can study the self-metalation of charged and uncharged molecules. The basic structural characterization of the 2H-P monolayers was performed with scanning tunneling microscopy (STM) and low energy electron diffraction (LEED). The charge and the metalation state of the 2H-P molecules was determined using ultraviolet photoemission spectroscopy (UPS) and X-ray photoemission spectroscopy (XPS), respectively. The result of these measurements, that the self-metalation of 2H-P on ultrathin Ag(001)-supported MgO(001) films does not depend on the charge state of the molecules, is supported by calculations based on density functional theory (DFT).

4.2 Methods

4.2.1 Experimental

The experiments were performed in two separate ultrahigh vacuum apparatuses, one specifically designed for low-temperature scanning tunneling microscopy studies, and the other one for photoemission experiments. The Ag(001) crystal was cleaned by repeated sputtering (sample current I_S = 4 μA, HV = 750 V) and annealing (T = 750 K) cycles. The ultrathin MgO films were then grown *via* reactive Mg deposition, using slightly different growth conditions to obtain films with either standard or high-Φ [299]. The growth rate was controlled by the Mg deposition rate, which was calibrated with a quartz microbalance. To obtain a standard-Φ film, Mg was evaporated in $p = 1.0 \times 10^{-6}$ mbar O_2 onto the sample kept at T = 550 K; the O_2 flow was then promptly switched off together with the Mg flux and the sample was slowly cooled to RT (10 $K\ min^{-1}$). The high-Φ film was obtained likewise, however the O_2 pressure was slightly higher ($p = 2.0 \times 10^{-6}$ mbar); moreover, after interrupting the Mg flux the O_2 flow was left at the same pressure and the sample temperature was firstly kept constant for 10 minutes, then slowly cooled at the same rate always in O_2 flow, and the gas flow was only switched off once the sample temperature reached below 400 K. 2H-P (95% purity) from Frontier Scientific was used without further purification and was deposited onto the MgO film held at RT from a home-built evaporator with the porphin powder contained in a crucible, which was heated to 430 K for sublimation. The calibration of the deposited amount was again based on the quartz micro-balance and the Φ behavior during a dosing series was used to determine the dose corresponding to a monolayer (here we define 1 ML as the single layer completion coverage).

UPS measurements were performed using a NanoESCA system by ScientaOmicron, with a custom-designed preparation chamber attached to it, which is equipped with a sputter gun, a heating stage, the Mg (FOCUS EFM 3T) and molecule (resistively heated crucible) evaporators, leak valves and an XPS setup from SPECS (Phoibos 150 analyzer and XR50 Al-K_α source). The sample temperature during all photoemission experiments was room temperature. Ultraviolet He I ($h\nu$ = 21.22 eV) light was produced by a HIS 14 HD excitation source by Focus and reflected onto the surface at an angle of 68° to the surface normal by a toroidal mirror. UPS spectra were collected with a channeltron detector, and the work function Φ was determined from the secondary electron cutoff in a sample bias configuration. LEED and STM measurements were carried out in another set-up, also equipped with the necessary sample preparation equipment. Since the electron beam can damage or even destroy molecular overlayer structures,

LEED experiments were always performed after STM experiments. For 2H-P on standard-Φ samples LEED images of reasonable quality could be obtained, while for 2H-P on high-Φ samples the diffuse pattern present disappeared too quickly. Therefore, no LEED images could be obtained for the corresponding preparations. STM images were obtained at T = 77 K in a low-temperature STM system from Createc. Electrochemically etched tungsten tips were used, and the bias voltage was applied to the sample.

4.2.2 Theoretical

The geometric and electronic properties of adsorbed (Mg-)porphin molecules were computed in the repeated slab-approach, using 5 layers of Ag plus 2 layers of MgO as a substrate and a minimum of 18 Å vacuum between the slabs. We used the plane-wave code VASP [357, 320, 358] with the projector-augmented wave method [321] and a dipole-correction in z-direction to avoid spurious electric fields. Since systems with organic molecules on dielectric interlayers on metal substrates have proven to be challenging [296], we used the explicit van der Waals-functional optb86b-vdW [169, 170] for exchange-correlation effects, including long-range dispersion. All geometries were relaxed to a total energy convergence of 0.001 eV, with the 3 lowest layers of Ag held fixed (lattice constant: 4.092 Å). We sampled the Brillouin zone with a Monkhorst-Pack [359] mesh of 4×4×1 and used a kinetic energy cutoff of 450 eV. For the simulation of the electronic structure, refined settings with 8×8×1 k-point sampling and 500 eV energy cutoff were used.

4.3 Results and Discussion

Charge transfer into adsorbates weakly interacting with MgO(001)/Ag(001) can be well described by the parallel plate capacitor model. Within this model, the amount of transferred charges depends on the work function (Φ) and on the thickness of the oxide film [299]. An important property for charge transfer is the pinning work function (Φ_{pin}), which is determined by the electronic properties of the adsorbate and describes the highest substrate work function, where charging can still be observed. The Φ_{pin} for the 2H-P/MgO(001)/Ag(001) system studied here is 3.8 eV and thus similar to the one of 2H-TPP on the same substrate [296]. For samples with an initial work function before molecule deposition (Φ_{ini}) smaller than Φ_{pin}, charge transfer into the molecules will occur, whereas for samples with $\Phi_{\text{ini}} > \Phi_{\text{pin}}$ no charging will occur. In order to investigate the self-metalation of 2H-P molecules on ultrathin MgO(001) films and its dependence on the charge state of 2H-P, we have prepared 2 monolayer (ML) thin MgO(001) films on Ag(001) with different initial work functions: one, with a $\Phi_{\text{ini}} < \Phi_{\text{pin}}$, will be denoted as "standard-Φ" and has been obtained following the typical preparation procedure for flat MgO films [360, 317]; the other, with $\Phi_{\text{ini}} > \Phi_{\text{pin}}$, is denoted "high-Φ". The high Φ is obtained by treatment of the standard MgO(001)/Ag(001) thin film with oxygen at elevated temperature, which introduces excess O at the MgO/Ag interface [323].

As shown by our LEED and STM results reported in Figure 4.2, monolayers of 2H-P form a well-ordered overlayer structure on the MgO(001)/Ag(001) substrate. Figure 4.2 (a) shows an STM image of 2H-P on the standard-Φ sample after deposition at room temperature (RT) and mild heating to 400 K. The corresponding LEED pattern is displayed in Figure 4.2 (c). The lattice formed by the adsorbates corresponds to a commensurate (1,4 | 4,1) super-structure. Two 90° rotated domains (indicated by the red and blue unit cells in Figure 4.2 (c)) are observed in the LEED pattern. In STM, at the shown tunneling conditions, the molecules have a slight rhombic appearance, i.e., with a 2-fold symmetry. It is interesting to note that, although 2H-P forms

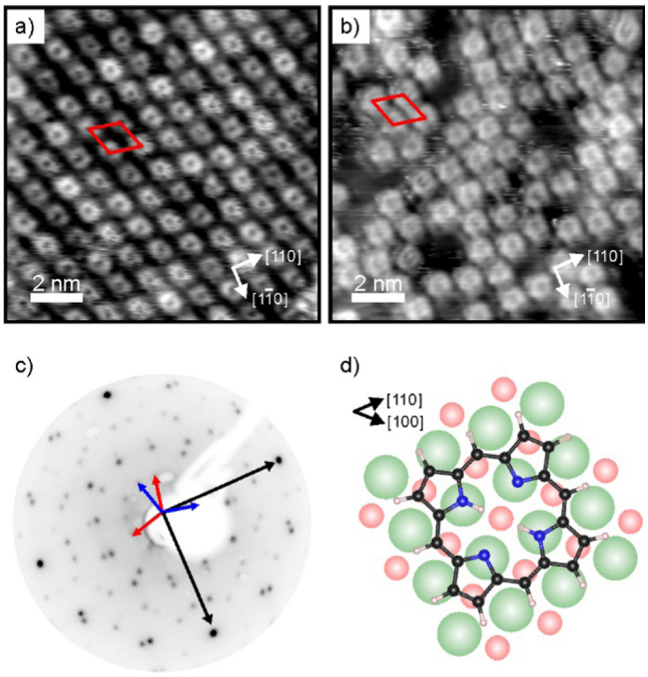

Figure 4.2: (a) and (b): STM images (12 nm × 12 nm) of a 2H-P monolayer on (a) standard-Φ, and (b) high-Φ 2 ML MgO(001)/Ag(001), taken at 77 K. Tunneling conditions: (a) I_t = 58 pA, V_{bias} = +0.1 V; (b) I_t = 53 pA, V_{bias} = +0.39 V. (c) LEED image (55 eV) of 2H-P on standard-Φ MgO(001)/Ag(001). The unit cell vectors of the MgO substrate (black) and two mirror domains of the 2H-P superstructure (red and blue) are indicated by arrows. (d) Schematic of the 2H-P adsorption geometry on MgO(001) (green: Mg; red: O; black: C; blue: N; white: H).

a supercell not aligned with the high-symmetry directions of the MgO, the symmetry axes of the individual molecules are closely aligned to a ⟨100⟩ direction of the substrate (as shown in Figure 4.2 (d)). In Figure 4.2 (b) the STM image of 2H-P on a high-Φ sample is shown. The 2H-P coverage here is slightly below full monolayer, and the sample has not been annealed to prevent work function changes due to thermal-induced desorption of oxygen from the MgO/Ag interface. Despite the slightly worse quality of the image, it can clearly be seen that the molecules adsorb with the same orientational alignment as in the standard-Φ case and locally arrange in the same superlattice.

To determine the degree of charge transfer into the 2H-P monolayer on the two substrates, we have measured their ultraviolet photoemission spectra (UPS). The region between the Fermi level (E_F) and the strong MgO valence band (VB) emission differs significantly for the standard-Φ and high-Φ samples, as can be appreciated in Figure 4.3 (a). For the case of the standard-Φ sample, two distinct emissions are detected, at a binding energy (BE) of 2.8 eV and 1.0 eV, respectively. In contrast, on the high-Φ sample only a single 2H-P-related emission is apparent at 2.3 eV BE. The UPS spectra obtained here are similar to the ones of 2H-TPP on MgO(001)/Ag(001) thin films of different Φ_{ini} [296]. Following similar arguments as in our previous study, the emission at 1.0 eV on the standard-Φ sample is assigned to a former lowest unoccupied molecular orbital (fLUMO) of the porphin, which is populated on charging. Note that in an isolated porphin molecule the two lowest unoccupied MO's (LUMO and LUMO+1) are

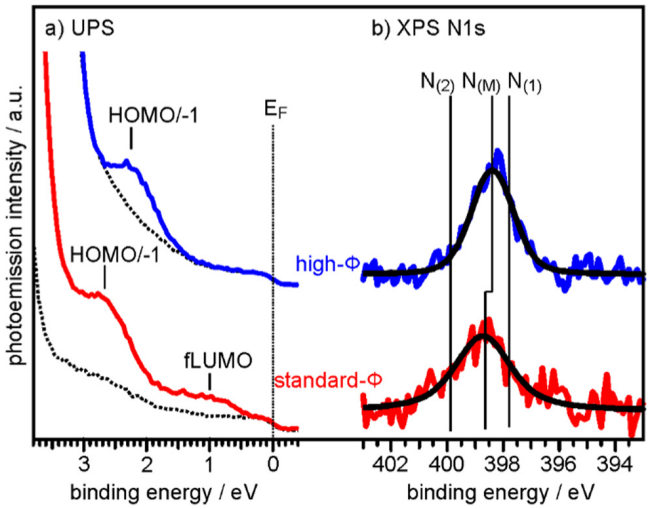

Figure 4.3: (a) UPS spectra of the clean 2 ML MgO(001)/Ag(001) substrate (broken lines) and of 1 ML 2H-P deposited at RT on a standard-Φ (red line, Φ_{ini} = 2.73 eV) and a high-Φ (blue line, Φ_{ini} = 4.08 eV) sample, respectively. The Fermi energy (E_F) and the major emissions corresponding to fLUMO and HOMO/-1 are indicated. (b) N 1s XP spectra of the same sample preparations. Colored lines are raw data and black lines are the corresponding fits assuming only a single N 1s component on each sample. $N_{(M)}$ indicates the BE of the N 1s peaks for the metalated Mg-P, while $N_{(1)}$ and $N_{(2)}$ are the BE's expected for unmetalated 2H-P (see Section 4.5).

degenerate and no distinction between them is made at this point. The emissions between 1.5 eV and 3 eV on both, the standard and high-Φ sample, are a superposition of the 2H-P HOMO and HOMO-1, which are too close in energy to be resolved. Since no molecular emissions appear on the high-Φ sample between E_F and the HOMO/HOMO-1 emissions, we conclude that the 2H-P molecules remain uncharged on this surface. This interpretation is supported by the observation of the work function change upon 2H-P adsorption. While the work function remained constant in the case of the high-Φ sample, an increase of about 1 eV was noted for the standard-Φ sample, which is consistent with the formation of a charge transfer dipole due to the presence of negatively charged porphin molecules.

To determine if the different charge states of the molecules affect the self-metalation, N 1s XP core level spectra have been acquired from the same samples. As shown in Figure 4.3 (b), the corresponding spectra of 2H-P on high-Φ and standard-Φ MgO(001)/Ag(001) have a very similar appearance and can both be fitted with a single component, $N_{(M)}$, which is centered at a BE of 398.4 eV for the high-Φ sample and at 398.7 eV for the standard-Φ sample. The larger width of the spectrum for the standard-Φ sample (full-width at half maximum of 2.1 eV compared to 1.6 eV for high-Φ) arises from the presence of two species of metalated molecules, namely charged and uncharged ones, which are too close in BE to be resolved. The presence of both charged and uncharged species on an ultrathin MgO(001) film is not unexpected and has, for example, previously been observed within an adsorbed pentacene monolayer [299].

The appearance of a single component in the N 1s spectrum of porphyrins is the accepted fingerprint of their metalation: unmetalated molecules have two inequivalent nitrogen atoms, as within each molecule two are protonated and two are not, whereas in the metalated case the metal ion is equivalently bonded to all 4 nitrogen atoms, making them equivalent [309]. For

comparison, the XPS of a sample with partially populated second (unmetalated) 2H-P layer is shown in Section 4.5, from which we could identify the N 1s BE components originating from unmetalated molecules ($N_{(1)}$ and $N_{(2)}$ in Figure 4.3 (b)), separated by 2 eV. In addition, the appearance of a high-BE shoulder in the O 1s XP spectrum after 2H-P deposition, due to the formation of hydroxyl groups, provides further confirmation of the metalation reaction (see Section 4.5).

From the combined XPS and UPS results we can conclude that the porphin monolayers are fully metalated on, both, high-Φ and standard-Φ MgO(001)/Ag(001) substrates. Thus, the self-metalation reaction of 2H-P to Mg-P on the planar MgO(001) surface occurs irrespective of the charge state of the molecules. This contrasts with the previously investigated 2H-TPP, which remained unmetalated on a high-Φ substrate and was metalated only if charge transfer into the molecules was possible [296]. Our suggestion that the charging of 2H-TPP is necessary to bring the porphyrin macrocycle closer to the MgO surface, thereby facilitating the self-metalation, is thus strongly supported by the experimental observations.

To corroborate the experimental findings, we performed DFT calculations for a standard-Φ (3.1 eV) and a high-Φ (4.7 eV) system, respectively. The former is obtained with a stoichiometric MgO(001) film on Ag(001), while the latter is achieved by adding 1/2 ML of oxygen in interstitial sites at the MgO/Ag interface [299, 323]. We have performed the calculations for two unit cell sizes, one resembling the full monolayer (high coverage, HC), and one with a larger unit cell (low coverage, LC) to simulate the situation of a more or less isolated 2H-P(Mg-P) molecule.

Firstly, we discuss the adsorption configuration (side views and top views in Figure 4.4 (a)) for the low coverage case. The adsorption geometry was found to be the same regardless of the work function (Figure 4.4, left panel: standard-Φ; right panel: high-Φ). The inner part of the macrocycle is slightly bent towards the surface with an average height of 2.69 Å and 2.83 Å, respectively (Table 4.1). The pyrrolic nitrogen atoms are located on top of surface Mg^{2+} ions with the two aminic protons pointing towards a surface O^{2-} ion below the center of the molecule. The calculated density of states (DOS) is shown in Figure 4.4 (b). Here, a significant difference is observed between the two systems: for high Φ, the DOS has a clear gap around the Fermi level (E_F), with the LUMO located about 0.5 eV above it, while for standard Φ the LUMO crosses E_F. These results agree qualitatively with the experimental data, showing that on the high-Φ sample the molecules remain neutral, whereas on the standard-Φ sample the molecules get negatively charged.

The self-metalation was simulated by exchanging an Mg^{2+} ion from the surface with the aminic protons. The subsequent geometry relaxation shows that the protons bind with the O^{2-} in the Mg^{2+} vacancy forming hydroxyls, and that the exchanged Mg^{2+} is positioned slightly below the molecular backbone. As shown in Figure 4.4 (a), the overall adsorption geometry is hardly modified by metalation. For high Φ, there is a significant stabilization of the metalated state over the unmetalated one by 0.83 eV, whereas for standard Φ the energy difference is small (Table 4.1). This is most likely related to the fact that the unmetalated 2H-P, due to charging, adopts already an energetically favorable adsorption height for metalation. Indeed, on the standard-Φ surface the N-surface distance is only marginally reduced upon metalation (Table 4.1). Regardless of the work function, the Mg^{2+} ion in the macrocycle (Mg_P) is coordinated to a surface O^{2-}, which is significantly lifted from the surface plane (by 0.25 Å). The Mg_P-O_{surf} distance is 2.06 Å, which is only slightly larger than the Mg–O distance in the film (2.04 Å in our calculation) and shows that in the metalated case, the extracted Mg^{2+} ion adopts a position that resembles the continuation of the Mg-O lattice in vertical direction. Qualitatively, the DOS of the metalated molecules shows a similar charging behavior to that observed for 2H-P, with the LUMO crossing E_F in the case of standard Φ, and a clear HOMO-LUMO gap around E_F for high Φ (Figure 4.4 (b)).

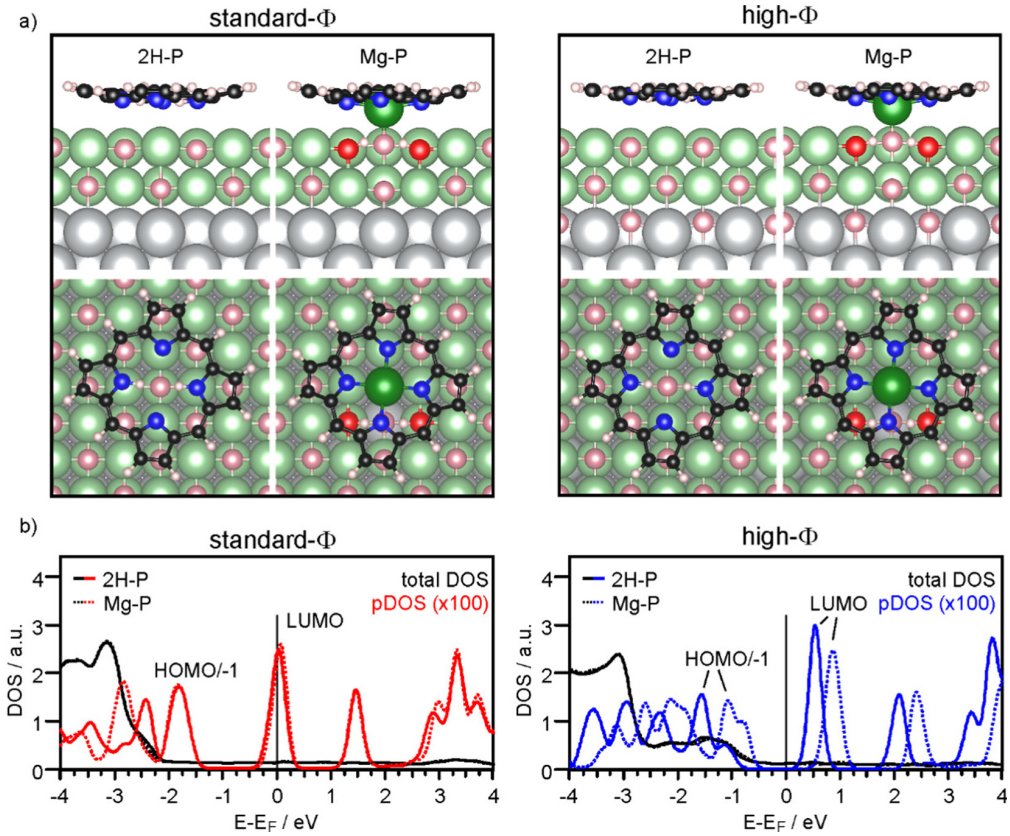

Figure 4.4: (a) Side views and top views of the DFT (optb86b)-optimized geometry for 2H-P and Mg-P on standard-Φ (left panel) and high-Φ (right panel) 2 ML MgO(001)/Ag(001). Colors: grey: Ag; pink: O; red: O of OH; green: Mg; black: C; blue: N; white: H. Note that the high Φ was obtained by adding 1/2 ML O at interstitial sites of the interfacial Ag layer. (b) Calculated density of states (DOS) for 2H-P (full lines) and Mg-P (dotted lines) on standard-Φ (left panel) and high-Φ (right panel) 2 ML MgO(001)/Ag(001). The black and colored lines represent the total DOS and the DOS projected onto the C atoms of 2H-P/Mg-P, respectively.

To investigate the role of lateral interactions between molecules in the adsorbed ML, we repeated all calculations with a smaller unit cell (corresponding to the experimental ML). The adsorption geometry and DOS obtained for these systems is shown in Section 4.5. Most significantly, the favorable adsorption site for the unmetalated molecules is with their center above a surface Mg^{2+} ion, and they are further away from the surface than at lower coverage: the d(N-surface) increases from 2.75 Å to about 3.1 Å for, both, high-Φ and standard-Φ. By contrast, for Mg-P a similar geometry and molecule-to-surface heights were obtained as in the low coverage case (Table 4.1). Also the DOS shows some differences at quantitative level, but the qualitative behavior is the same (see Section 4.5). For the high-Φ, the LUMO shifts up in energy. For standard-Φ, a similar upward shift results in a smaller area of the LUMO DOS being below E_F, representing a smaller CT. This is expected based on the capacitor model, as the same charge must be distributed between more molecules to reach the same pinning work function. The smaller CT can, however, not account for the increased d(N-surface) alone. This is clear by comparing the d(N-surface) of the high and low coverage cases on the high-Φ system, where

Table 4.1: Calculated distance d(N-surface) between the average position of the 4 nitrogen atoms in the porphyrin macrocycle and the average position of the Mg ions in the topmost MgO layer, and metalation energy, ΔE_{met} (= $E_{\text{Mg-P/MgO(001)/Ag(001)}}$ - $E_{\text{2H-P/MgO(001)/Ag(001)}}$), for 2H-P and Mg-P on 2 ML MgO(001)/Ag(001) as a function of the initial work function, Φ_{ini}. For comparison, the d(N-surface) for 2H-TPP and Mg-TPP on 2 ML MgO(001)/Ag(001) are also shown. Results for 2H-P are reported for calculations employing the optb86b vdW functional for the high-coverage case (HC) and the low-coverage case (LC). All energies are given eV, all distances in Å.

	d(N-surface)			d(N-surface)			d(N-surface)[b]	
Φ_{ini}	2H-P(LC)	Mg-P(LC)	ΔE_{met}	2H-P(HC)	Mg-P(HC)	ΔE_{met}	2H-TPP	MgTPP
3.1	2.69	2.62	-0.04	3.09[a]	2.74	-0.25	2.74	2.77
4.7	2.83	2.71	-0.83	3.10[a]	2.74	0.68	3.08	2.97

[a] The d(N-surface) of 2H-P provided for the HC case refers to adsorption with the center of the molecule above an Mg ion, which is energetically slightly more favorable than adsorption above an O ion. [b] The results for the TPP's were computed with a different treatment of van der Waals forces (see Supporting Material of Ref. [296]).

no charge transfer takes place. The difference of 0.27 Å (Table 4.1) results primarily from intermolecular interactions. Finally, also for the full ML case, metalation is, at least thermodynamically, still favored, with a calculated energy gain of 0.25 eV (standard-Φ) and 0.68 eV (high-Φ), respectively.

It is instructive to compare the N-surface heights for the 2H-P/Mg-P systems with those of TPP, where metalation was strongly dependent on the charge state. For standard-Φ, where significant CT into TPP takes place, the d(N-surface) is about 2.75 Å for 2H-TPP and Mg-TPP, whereas for high-Φ, where no CT takes place and no metalation was observed in experiment, it is around 3 Å (Table 4.1). By contrast, for 2H-P in the larger unit cell, the dependence of d(N-surface) on Φ and thus CT is much weaker, with values of 2.62 Å (standard-Φ) and 2.73 Å (high-Φ), respectively. This shows that in uncharged 2H-P, when isolated on the surface, the center of the macrocycle can indeed approach closer to the surface than in uncharged 2H-TPP, which substantiates our conclusion about the critical role of the distance between the macrocycle and the surface for the self-metalation. Care has to be taken, however, when comparing the results on oxides with those for the self-metalation on metal surfaces, where molecular hydrogen is formed as byproduct of the redox reaction. For example, the self-metalation of 2H-TPP and 2H-P on copper surfaces requires elevated temperature, even though both molecules receive a significant amount of charge on copper and the d(N-surface) is only 2.2 Å [361, 297, 362]. On the other hand, the process proceeds readily at room temperature upon water formation in the presence of additional oxygen [363], which highlights the decisive role of the reaction pathway and the involved energetics.

4.4 Conclusions

Our experimental data, supported by DFT calculations, clearly shows that charge transfer in the 2H-P/MgO(001)/Ag(001) system is strongly affected by the work function of the MgO(001)/-

Ag(001) substrate. By tuning the preparation conditions, we were able to prepare 2H-P monolayer films, which are either uncharged or charged, similar as previously reported for 2H- TPP on the same substrate [296]. Compared to the latter, however, the metalation behavior is remarkably different. Whereas 2H-TPPs were only able to self-metalate when charge transfer occurred, a 2H-P monolayer can self-metalate completely, regardless of whether the molecules are charged or not. This provides an important insight into the self-metalation process, as it proves that charge transfer does not play a direct role in this reaction. Our results suggest instead that the key factor enabling it is the distance between the macrocycle and the surface. In the case of the bulkier 2H-TPP, electrostatic attraction induced by charging provides the force that pulls the macrocycle so close to the surface that self-metalation is facilitated. On the other hand, the planar 2H-P can reach this critical distance without the help of charging.

Since a MgO(001)/Ag(001) thin film substrate with a high work function can be considered as bulk-like MgO in terms of its charge transfer properties, the results presented in this work suggest that the self-metalation of 2H-P on planar MgO(001) faces is not restricted to thin film substrates, but should be observable also on the (001) facets of, e.g. MgO nanocubes, where the self-metalation of 2H-TPP is not possible [305].

4.5 Supporting Information

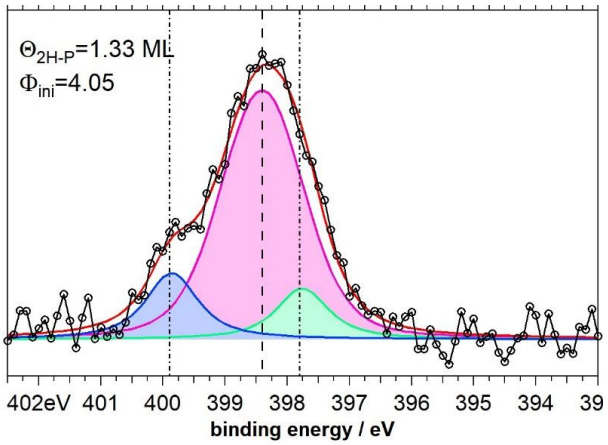

Figure 4.5: XP spectrum of 1.33 ML 2H-P on high-Φ 2 ML MgO(001)/Ag(001). The spectrum has been fitted with three peaks, corresponding to the 4 equivalent N atoms in metalated MgP ($N_{(M)}$, BE = 398.4 eV)) and the iminic ($N_{(1)}$, BE = 397.8 eV) and aminic ($N_{(2)}$, BE = 399.8 eV) N atoms in unmetalated 2H-P, which grows on top of the metalated monolayer.

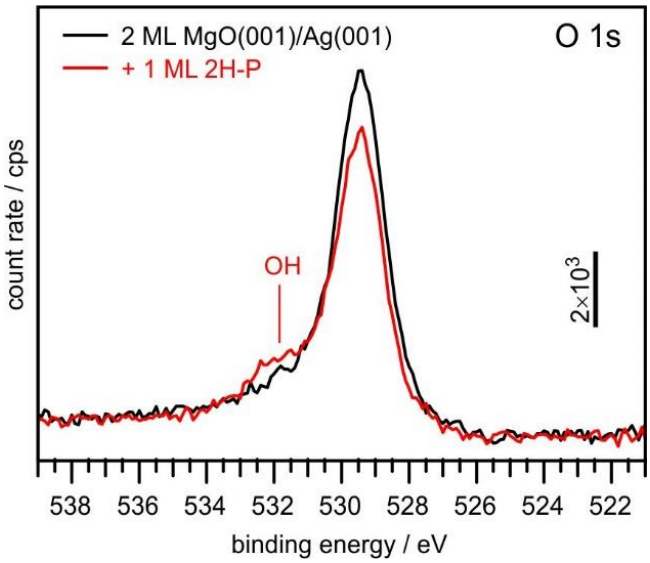

Figure 4.6: O 1s XP spectrum of clean 2 ML MgO(001)/Ag(001) (black) and of the same surface after deposition of 1 ML 2H-P (red). In addition to the attenuation of the main O 1s signal from the MgO film (529.5 eV), a shoulder grows in at higher binding energy (532 eV), which is associated with the formation of hydroxyl groups [306].

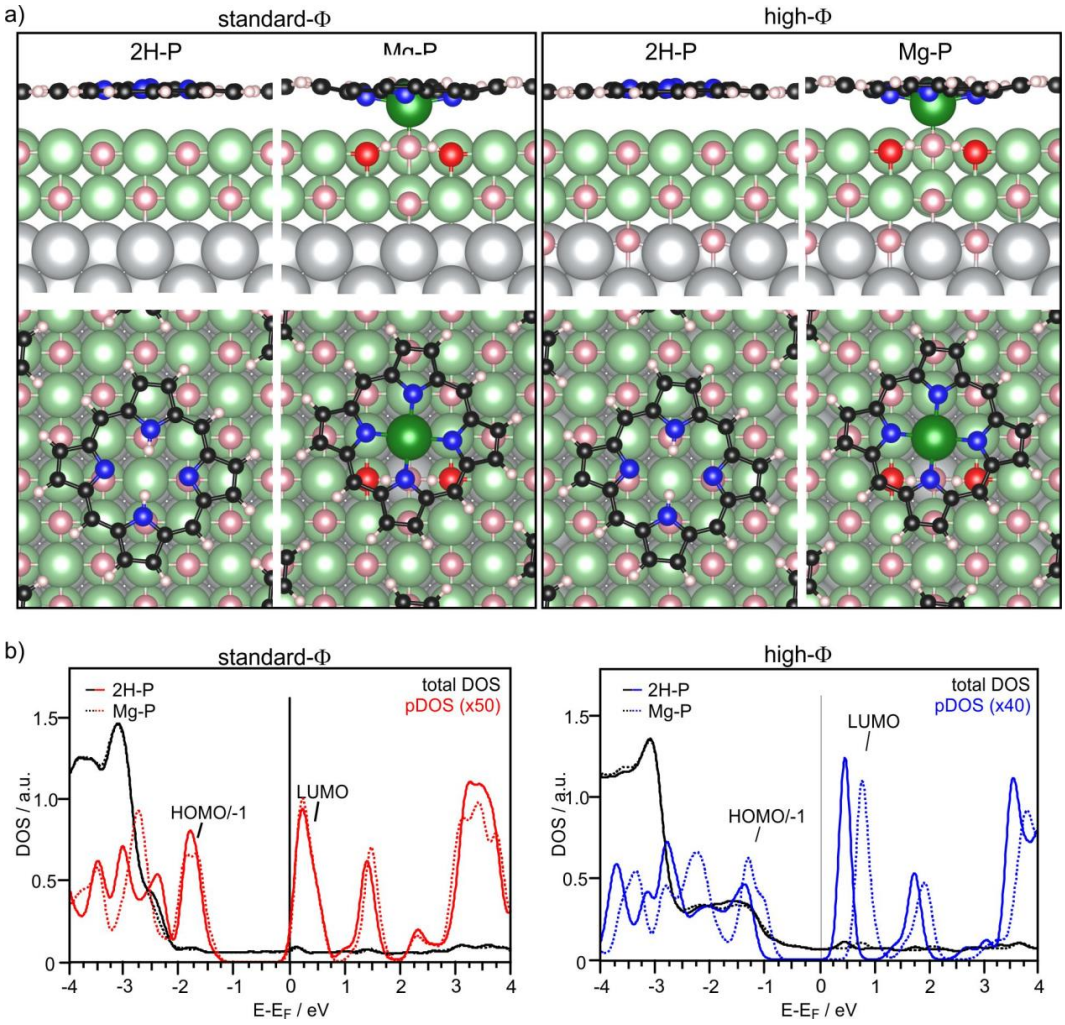

Figure 4.7: (a) Side views and top views of the DFT (optb86b)-optimized geometry for 2H-P and Mg-P on standard-Φ (left panel) and high-Φ (right panel) 2 ML MgO(001)/Ag(001). Colors: grey: Ag; pink: O; red: O of OH; green: Mg; black: C; blue: N; white: H. Note that the high Φ was obtained by adding 1/4 ML O at interstitial sites of the interfacial Ag layer. (b) Calculated density of states (DOS) for 2H-P (full lines) and Mg-P (dotted lines) on standard-Φ (left panel) and high-Φ (right panel) 2 ML MgO(001)/Ag(001). The black and colored lines represent the total DOS and the DOS projected onto the C atoms of 2H-P/Mg-P (enhanced by a factor of 50), respectively.

Chapter 5

Large Distortion of Fused Aromatics on Dielectric Interlayers Quantified by Photoemission Orbital Tomography

www.acsnano.org

ARTICLE

Large Distortion of Fused Aromatics on Dielectric Interlayers Quantified by Photoemission Orbital Tomography

Philipp Hurdax, Christian S. Kern, Thomas Georg Boné, Anja Haags, Michael Hollerer, Larissa Egger, Xiaosheng Yang, Hans Kirschner, Alexander Gottwald, Mathias Richter, François C. Bocquet, Serguei Soubatch, Georg Koller, Frank Stefan Tautz, Martin Sterrer, Peter Puschnig, and Michael G. Ramsey*

Figure 5.1: **Header of the article as published in *ACS Nano* [49].**

Significance Statement

Most flat, π-conjugated molecules also adsorb flat on pristine metal surfaces since their carbon backbones are comprised of rather stiff sp^2-bonds. If, in addition, inter- and intra-molecular dispersion plays only a minor role, the momentum space signatures of their frontier p_z-orbitals are very robust, both in terms of a band picture and upon the variation of the photon energy when probed with ARPES. The latter aspect is in contrast to organic molecules with a more

three-dimensional carbon network, such as buckminsterfullerene for instance, where the orbitals in momentum space vary with k_z and their momentum maps will therefore vary with kinetic energy.

Continuing the work on MgO/Ag(100) surfaces, here, we detected a large distortion of the dye molecule perylene-tetracarboxylic dianhydride with photoemission orbital tomography. This extreme bending could be explained with a peculiar interplay between the molecule's oxygen atoms and the Mg^{2+}-ions of the MgO surface. With measuring photoemission maps of the HOMO and former LUMO at three different photon ergies, we were able to quantify the bend in relation to simulations from DFT. In comparison, the molecular bends deduced from experiment turned out to be slightly larger than those theoretically predicted from calculations with different correction for van der Waals interaction. Therefore, we could establish photoemission orbital tomography as a quantitative method to detect conformal changes via momentum space signatures of orbitals and, furthermore, as a benchmark tool for electronic structure calculations.

Author Contributions

The experiments for the three different photon energies were carried out at different times and places. Philipp Hurdax, Anja Haags, Larissa Egger and Xiaosheng Yang measured the data with 35 eV photon energy under the supervision of François C. Bocquet, Serguei Soubatch, Georg Koller, F. Stefan Tautz and Michael G. Ramsey. Those experiments were carried out at the Physikalisch-Technische Bundesanstalt, Berlin, provided with support and supervision from Hans Kirschner, Alexander Gottwald and Mathias Richter. Additional experiments with He I and He II photon energy were carried out in Graz by Thomas G. Boné and Philipp Hurdax, with additional support for sample preparation and characterization by Michael Hollerer, Georg Koller, Martin Sterrer and Michael G. Ramsey. Calculations with DFT, a model for the extrapolation of the bend from those calculations, as well as additional control calculations with TDDFT were done by me, supervised by Peter Puschnig. Philipp Hurdax and Michael G. Ramsey wrote the initial draft of the manuscript, with contributions from all co-authors. Michael G. Ramsey was responsible for overall project coordination.

Abstract

Polycyclic aromatic compounds with fused benzene rings offer an extraordinary versatility as next-generation organic semiconducting materials for nanoelectronics and optoelectronics due to their tunable characteristics, including charge-carrier mobility and optical absorption. Nonplanarity can be an additional parameter to customize their electronic and optical properties without changing the aromatic core. In this work, we report a combined experimental and theoretical study in which we directly observe large, geometry-induced modifications in the frontier orbitals of a prototypical dye molecule when adsorbed on an atomically thin dielectric interlayer on a metallic substrate. Experimentally, we employ angle-resolved photoemission experiments, interpreted in the framework of the photoemission orbital tomography technique. We demonstrate its sensitivity to detect geometrical bends in adsorbed molecules and highlight the role of the photon energy used in experiment for detecting such geometrical distortions. Theoretically, we conduct density functional calculations to determine the geometric and electronic structure of the adsorbed molecule and simulate the photoemission angular distribution patterns. While we found an overall good agreement between experimental and theoretical data, our results also unveil limitations in current van der Waals corrected density functional approaches for such organic/dielectric interfaces. Hence, photoemission orbital tomography

provides a vital experimental benchmark for such systems. By comparison with the state of the same molecule on a metallic substrate, we also offer an explanation why the adsorption on the dielectric induces such large bends in the molecule.

5.1 Introduction

Fused aromatic molecules are shaped by sp^2 hybridization, which results in a planar network of bonds and an electronic structure characterized by a series of σ-orbitals and π-orbitals, the latter having their electron densities on either side of the molecular plane. This electronic configuration results in a stiffness of carbon skeletons ranging from small molecules such as benzene over to one or two-dimensional structures such as linear acenes or coronene to graphene. Thus, those structures are comparably resistant to geometric distortions, which actually may be desirable, as distortion has profound effects on the optoelectronic [364, 365, 366, 367, 368, 369, 370, 371] and chemical properties [372, 373, 374, 375] of various materials. Bonding on metal surfaces is expected to soften the carbon backbone through hybridization, thereby allowing for bonds, e.g., with functional groups, to induce geometric distortions. Indeed, molecular distortions have been observed on metal surfaces, such as a bend of perylene-3,4,9,10-tetracarboxylic dianhydride (PTCDA) detected by X-ray standing waves (XSW) [376] or a corrugation of graphene detected by atomic force microscopy (AFM) [377]. However, in these cases, the out-of-plane distortion of the carbon backbone is small ($\leq$0.1 Å). Here, we report a much larger distortion of a π-conjugated planar molecule. Moreover, we observe it on a dielectric thin film, where there is no hybridization between the substrate states and the π-system of the carbon core of the molecule.

Geometric distortions can be inferred by several methods, such as dynamic low-energy electron diffraction, X-ray photoelectron diffraction, and XSW. These, however, pose strict requirements to the systems investigated. For instance, the XSW technique has been used successfully to detect adsorption heights of constituent atoms [378, 379, 380, 381, 382, 383, 384, 385, 386], but it requires atomic species to be energetically distinguishable in X-ray photoelectron spectroscopy (XPS) and therefore cannot discern between carbon atoms with the same local chemical environment.

The photoemission orbital tomography (POT) technique essentially produces images of molecular orbitals in momentum space (k-space), which are related to the real space orbitals by the square of their Fourier transform [46, 54]. Since orbitals are a direct result of the details of the internal atomic structure, POT should be able to detect conformational changes on adsorption directly. Indeed, POT has been demonstrated to shed light on subtle questions such as the degree of aromaticity in kekulene [53]. POT has also been used successfully to detect and quantify geometric changes of p-sexiphenyl, namely the planarization of the molecule upon adsorption on metals and oxide thin films, when there is charge transfer to the molecule, thereby removing the torsional angle between the phenyl rings around the nominal single bonds of the molecule [46, 387, 316]. In this work, we show that POT can be used to detect and quantify even more subtle geometric changes, namely the bend of the molecule PTCDA.

PTCDA has been studied on various substrates as a model molecule. POT of PTCDA has been conducted on metals such as Ag(001) [388], Ag(110) [50, 389, 55, 390, 58], Ag(111) [391, 392], Cu(100) [393], and oxidized Cu(100) [394, 262]. In all these cases, the patterns of the photoemission distribution from the frontier orbitals were in close agreement with the patterns calculated for flat, oriented molecules in the gas phase (approximating the final state of photoemission by a plane wave) [260] and showed no photon energy dependence [55, 57].

On oxide films, deviations of the orbitals on adsorption might be deemed even more un-

likely, since the dielectric interlayer decouples the molecular wave function from the metallic wave function, thereby preventing any hybridization [395]. Indeed, POT momentum maps of the frontier orbitals of both pentacene [76] and p-sexiphenyl [316] on epitaxial MgO(001) films on Ag(001) were in very good agreement with gas-phase simulations of planar molecules.

Here, we show that for PTCDA on MgO(001)/Ag(001), there are large differences between the experimental momentum maps of the frontier orbitals and theoretical ones simulated for the gas phase. Most notably, for this system, the momentum maps display a very strong photon energy dependence. With the support of density functional theory (DFT) calculations, this is identified as the result of a significant bend in the molecular backbone arising on adsorption. By contrasting the situation to adsorption on Ag(001), with the same adsorption configuration, we can understand the bend on MgO as arising from the higher electronic hardness of the dielectric film compared to the metal surface.

5.2 Results and Discussion

MgO forms well-ordered (001)-oriented films on Ag(001) due to the close match of their lattices [396, 360]. Adsorbed monolayers (MLs) of PTCDA on MgO(001)/Ag(001) are identical to PTCDA on Ag(001) in terms of the superstructure. This is evident in the low-energy electron diffraction (LEED) image in Figure 5.2 (a), which reveals a PTCDA superlattice with the epitaxial matrix:

$$\begin{pmatrix} 4 & 4 \\ -4 & 4 \end{pmatrix}.$$

The scanning tunneling microscopy (STM) image in Figure 5.2 (b) confirms this and shows the orientation of the long molecular axes aligned alternatingly along the two principal crystallographic directions, [110] and [1$\bar{1}$0], of the substrate. Thus, PTCDA adopts the same structure on MgO(001)/Ag(001) as on Ag(001) [376], as illustrated in Figure 5.2 (c).

Despite this close similarity, the POT momentum maps of the frontier molecular orbitals are different on the two substrates. Figure 5.2 (d) shows momentum maps of the PTCDA lowest unoccupied and highest occupied molecular orbitals (LUMO and HOMO), respectively, on Ag(001) measured at a photon energy of 57 eV. Significantly, their appearance is in close agreement with momentum maps measured at lower photon energy [388] and with that of the maps simulated for two gas-phase planar molecules oriented 90° with respect to each other shown in Figure 5.2 (e). In contrast, the measured momentum maps of PTCDA on MgO(001)/Ag(001) displayed in Figure 5.2 (f), although recognizable from their nodal structures [394], are strikingly different from the gas-phase maps simulated for the same photon energy (Figure 5.2 (e)). Of note, for the LUMO, which is occupied by tunneling from the underlying metal, is the elongation of the minor lobes and the appearance of emissions at ($\pm$0.5, $\pm$0.5) Å^{-1}. For the HOMO the distinct "W" shape in each quadrant is replaced by a more diffuse emission pattern containing a number of maxima, the most intense one located at ($\pm$1.2, $\pm$1.2) Å^{-1}. We formulate the hypothesis that these significant changes of the emission patterns of PTCDA adsorbed on MgO are caused by a distortion of the molecular orbitals on adsorption due to a significant bend of the backbone of PTCDA.

The presence of a bend can already be inferred, even without involved DFT calculations of the PTCDA/MgO(001)/Ag(001) heterostructure, by considering momentum maps at different photon energies. This is illustrated in Figure 5.3 for a planar (Figure 5.3 (a)) and bent (Figure 5.3 (b)) PTCDA molecule with the example of its HOMO. Momentum maps can be viewed as spherical cuts through the square of the orbitals in k-space projected, in the case of a flat-lying molecule, onto the molecular plane [46]. The radius of the sphere, representing the

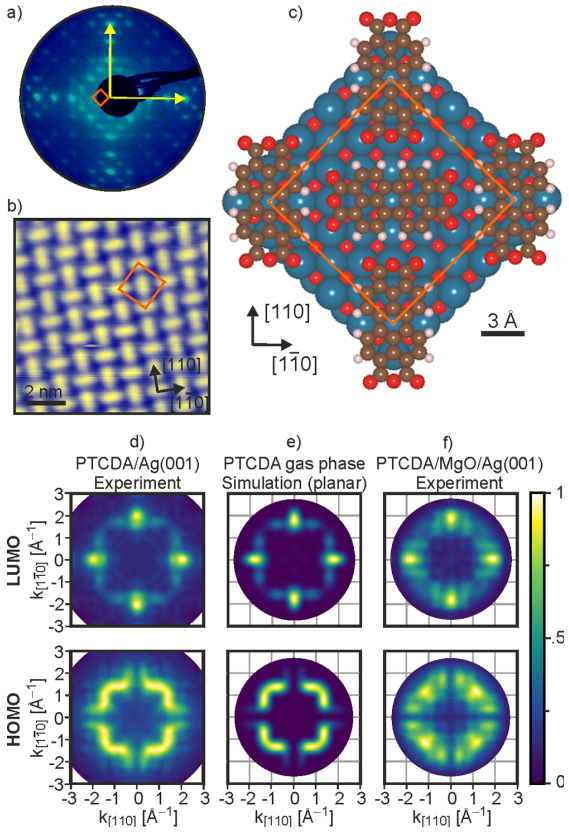

Figure 5.2: Identical structure but different momentum maps of PTCDA on Ag(001) and on MgO(001)/Ag(001). (a) LEED pattern of the PTCDA monolayer on 2 ML MgO(001)/Ag(001) at an energy of 50 eV. The substrate unit cell vectors are indicated by yellow arrows, and the unit cell of the PTCDA overlayer is shown as an orange square. (b) Structure of the PTCDA monolayer measured by STM (V_{bias} = 1.35 V, I_t = 61 pA). (c) Schematic of the adsorption geometry. (d) Experimental momentum maps of the LUMO and the HOMO of PTCDA/Ag(001) measured at a photon energy of 57 eV. (e) Simulated maps for LUMO and HOMO of gas-phase PTCDA at a photon energy of 35 eV with two orthogonal orientations. (f) Experimental momentum maps of LUMO and HOMO of PTCDA/MgO(001)/Ag(001) measured at a photon energy of 35 eV. The binding energies of the measured LUMO and HOMO with respect to the Fermi level are, respectively, 0.5 and 1.7 eV in (d) and 1.6 and 2.8 eV in (f).

Ewald sphere of photoemission, increases with the square root of the photon energy. Changing the photon energy therefore entails a change in the vertical component of the momentum (k_z) across the map. Planar π-systems as the PTCDA HOMO shown in Figure 5.3 (a) have practically no photon energy dependence of the (k_x, k_y) position of the main emissions, because the periodicities of the wave function in the x,y plane do not depend on the z-coordinate. In other words, their wave function can be approximated by the product of a part depending on the in-plane coordinates and a part depending on the vertical coordinate z. In momentum space (Figure 5.3 (a)), this leads to lobes which are oriented perpendicular to the molecular plane. Thus, as the Ewald sphere expands with increasing photon energy, it will always intersect the orbital at the same (k_x, k_y) corresponding to a particular periodicity of the wave function. Experimentally,

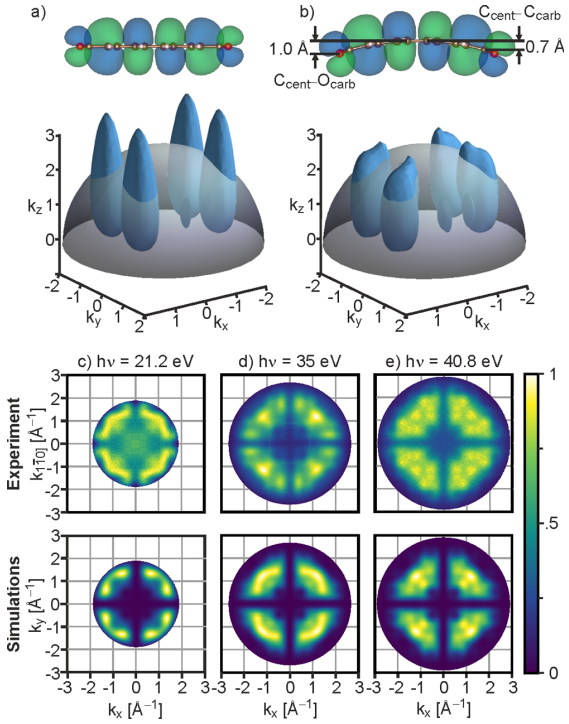

Figure 5.3: Momentum maps of PTCDA on MgO(001)/Ag(001) at different photon energies. (a, b) Side view in real space and corresponding three-dimensional k-space density (square of the Fourier transform of the real space orbital) of the HOMO of the PTCDA molecule in its planar geometry (a) and in the bent geometry (b) as obtained by on-surface DFT calculations. The bend across the carbon backbone (0.7 Å) and the total bend of the molecule (1.0 Å), including the end oxygens, are indicated. The gray hemispheres represent the Ewald sphere for a photon energy of 35 eV. (c-e) Symmetrized experimental momentum maps (upper panel) of the PTCDA HOMO on MgO(001)/Ag(001) taken at photon energies of (c) 21.2 eV, (d) 35 eV, and (e) 40.8 eV, and (lower panel) simulated momentum maps of the HOMO for isolated molecules in the bent geometry at the experimental photon energies.

this has indeed been observed for PTCDA monolayers on the three facial Ag surfaces as well as on bare and oxidized Cu(100) [55]. However, if the molecule adopts a nonplanar geometry, such as the bent one shown in Figure 5.3 (b), the orbitals must be slightly deformed due to local distortions of atomic orbitals constituting the molecular π-system. Thus, k_z-dependent substructures are introduced in the lobes of the three-dimensional k-space orbital (Figure 5.3 (b)), which will result in a strong photon energy dependence of the momentum maps.

To investigate whether the emission patterns in the momentum maps of PTCDA-/MgO(001)/Ag(001) are photon energy dependent, additional momentum maps were measured with a lab-based instrument using unpolarized He I and He II radiation of 21.2 and 40.8 eV, respectively. In Figure 5.3 (c-e) (upper panel), the symmetrized experimental maps of the HOMO are shown together with the momentum map recorded at 35 eV with p-polarization obtained with synchrotron radiation. At low photon energy ($h\nu$ = 21.2 eV, Figure 5.3 (c)), the measured momentum map is almost identical to the simulated map of the gas-phase planar PTCDA molecule shown in Figure 5.2 (e). This is in contrast to the map recorded at 35 eV

shown in Figure 5.3 (d), which exhibits notable differences as already mentioned. Further significant changes in the number of emission maxima can be seen when increasing $h\nu$ from 35 to 40.8 eV (Figure 5.3 (e)). Note that the map of the LUMO, which is available in Section 5.5 (Figure 5.6), also undergoes clear changes with photon energy. We can thus conclude that a photon energy-dependent study of PTCDA momentum maps on MgO(001)/Ag(001) with POT indeed supports the hypothesis of a nonplanar molecular geometry.

DFT calculations of PTCDA on MgO(001)/Ag(001) also suggest a significant bend of the molecule. In order to separate the effect of the bend on the momentum maps from a possible influence of the environment at the adsorption site, we first calculate the orbitals for an isolated gas-phase molecule but in the geometry obtained from the calculation on the surface. Also note that in the simulation, the structure of the molecular layer is taken into account by superimposing momentum maps of two perpendicularly oriented PTCDA molecules. The resulting HOMO momentum maps simulated for the same photon energies as used in the experiment are shown in Figure 5.3 (c-e) (lower panel, see Section 5.5, Figure 5.7, for the photon energy dependence of the simulated LUMO maps). At a low photon energy of 21.2 eV (Figure 5.3 (c)), like the experimental map, the simulated map resembles that of the planar molecule. As the photon energy rises (Figure 5.3 (d-e)), the simulated maps show clear changes, which qualitatively reproduce the trend seen in the experimental maps. However, the quantitative agreement is not perfect. We notice that systematically a higher photon energy in the simulations would be required to achieve a better match with the experimental maps. The theoretical map at a photon energy of 35 eV is in closest agreement to the experimental map at 21.2 eV, and the theoretical map at 40.8 eV resembles the experimental map at 35 eV. This discrepancy between theoretical and experimental maps, also seen in the more subtle changes of the LUMO (see Section 5.5, Figure 5.6), might be the consequence of a bend larger than this particular DFT calculation would suggest.

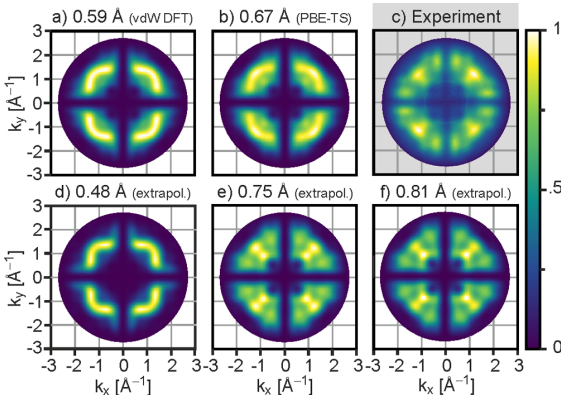

Figure 5.4: Dependence of the PTCDA HOMO momentum map on the bend. (a, b) Simulated momentum maps of isolated PTCDA with the geometry obtained by on-surface calculations using the van der Waals correction schemes vdW-DFT and PBE-TS, respectively. (c) Experimental momentum map of PTCDA on MgO(001)/Ag(001). (d-f) Simulated momentum maps of isolated PTCDA for bends extrapolated from the vdW-DFT geometries (see Section 5.5). All simulated maps are shown at an energy corresponding to the experimental photon energy of 35 eV and for two orthogonal orientations of the molecule. The bends, C_{cent}-C_{carb} height differences, are listed on top of the images.

To test if a different bend of the molecule can account for the remaining mismatch between theory and experiment and to gain a better understanding of the effect of the bend on the emis-

sion patterns, additional DFT calculations for the PTCDA/MgO(001)/Ag(001) heterostructure have been carried out. These were performed for perfectly stoichiometric MgO interlayers and MgO layers for which oxygen was introduced at the MgO/Ag interface in order to account for a realistic range of work functions [397, 323, 299]. Moreover, as it is yet unclear which theoretical methodology is best suited for the complex dielectric/metal substrate system, two different van der Waals correction schemes have been employed: the Tkatchenko-Scheffler method [140] on top of Perdew-Burke-Ernzerhof DFT methodology (PBE-TS) and a van der Waals DFT functional (vdW-DFT) [169, 170]. To quantify the degree of bending, we take the height difference between the central carbon atoms of the molecule (C_{cent}) and the carbon atoms of the carboxyl groups (C_{carb}), as illustrated in Figure 5.3 (b). Using this definition, the calculated bends are found to vary by 0.05 Å depending on the work function of the substrate (which controls the degree of charge transfer into the LUMO) and by 0.1 Å depending on the van der Waals correction scheme applied (see Section 5.5, Table 5.1). On a stochiometric MgO film, PBE-TS yields a bend of 0.67 Å, while vdW-DFT leads to a bend of only 0.59 Å. Based on these geometries, we have simulated maps of the HOMO for $h\nu$ = 35 eV using the same procedure as described above, see Figure 5.4 (a,b). Although the larger bend obtained with PBE-TS yields a slightly better agreement, neither can be considered to well reproduce the experimental map shown in Figure 5.4 (c). Thus, we have also simulated momentum maps for a larger range of bends by extrapolating to smaller and larger values, respectively. When the bend is reduced to 0.48 Å (Figure 5.4 (d)), the momentum map adopts the distinct W pattern in each of the four quadrants characteristic for the planar molecule (cf. Figure 5.2 (e)). Conversely, increasing the bend slightly to 0.75 Å (Figure 5.4 (e)) leads to further significant changes: The former W shaped pattern has broken up into four separate maxima, more similar to the experiment. A further increase in the bend to 0.81 Å (Figure 5.4 (f)) causes the simulation to diverge from the experiment: The region of high intensity 45° to the principal azimuth becomes sharper and its dominant maximum changes from the experimental ($\pm$1.2, $\pm$1.2) Å^{-1} to ($\pm$0.9, $\pm$0.9) Å^{-1}. Therefore, a bend of 0.81 Å overshoots the experimental momentum map and the best match is achieved at a bend around 0.75 Å.

The fact that the momentum map at a bend of 0.48 Å is hardly distinguishable from the map of the planar molecule suggests that the effect of the bend on photoemission patterns is nonlinear and the method only becomes highly sensitive above a critical threshold of the distortion. This also partly explains why the deviations from the planar conformation have not been observed in POT on any metal despite the presence of a small bend [376]. Moreover, it needs to be considered that while on MgO the molecular bend extends across the entire molecular backbone, on Ag(001), as on other Ag surfaces, most of the height difference arises from the oxygens bending toward the substrate with the central carbon core of the molecule remaining essentially flat (see side view in Figure 5.5 (a)) [376, 398]. The maximum atomic height difference among carbon atoms amounts to only 0.1 Å for PTCDA on Ag(001) according to X-ray standing wave measurements and dispersion-corrected DFT [376]. This is shown in the top view of Figure 5.5 (a), where atoms are colored according to their calculated heights. A bend restricted to the oxygens at the edges of the molecule leaves the frontier π orbitals mostly unaffected, since the latter are located predominantly in the region of the carbon backbone. In contrast, on MgO(001)/Ag(001), the bend is calculated to extend over the whole range of the molecule, as shown in Figure 5.5 (b).

To test if the discrepancy between experimental and simulated momentum maps might be explained by factors other than an altered shape of the molecular backbone, additional calculations have been carried out. These comprised (i) a more accurate description of the final state with time-dependent DFT (TD-DFT), (ii) accounting for intermolecular interactions in the free-standing monolayer as well as (iii) including the substrate. An overview of all these calculations

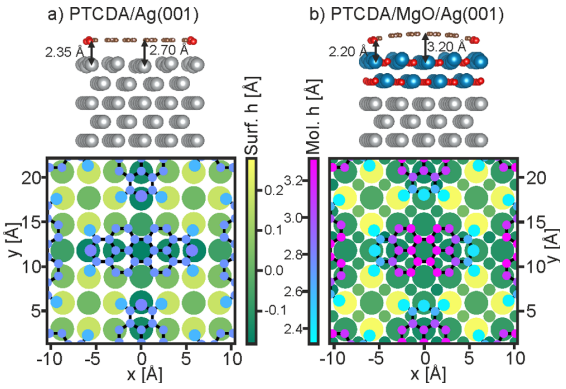

Figure 5.5: Comparing the atomic positions of PTCDA on Ag(001) and MgO(001)/Ag(001). Side view and top view of PTCDA on Ag(001) (a) and on 2 ML MgO(001)/Ag(001) (b). Both structures have been obtained from PBE-TS DFT calculations. In the side views, the O atoms are shown in red, the C atoms in bronze, the Ag atoms in silver, and the Mg atoms in blue. In the top views, atoms of both the substrate surface (Surf. h) and the molecule (Mol. h) are color-coded according to their elevations relative to the average height of the top substrate layer (atoms from smallest to largest are C, O, Ag, Mg).

can be found in Section 5.5 (Figures 5.8-5.10). Of the three factors, point (iii) has the most significant effect on the momentum maps. However, none of them leads to a clear improvement in the agreement between theory and experiment. While the effects of these three factors impose an uncertainty on a quantification of the bend using POT, their investigation still confirms that a bend larger than suggested by DFT is required for theory to reproduce the experiment. Hence, we conclude that momentum maps are very sensitive to the magnitude of the bend and POT can thus serve as a benchmark to select the best computational approach for a given system.

To understand the origin of the strong bend of the molecular backbone when PTCDA adsorbs on MgO(001)/Ag(001), it is instructive to compare the situation to the one on Ag(001), where no significant bend occurs [376]. As depicted in Figure 5.5, on both substrates the principle bonding is effectuated by the interaction of the carboxylic oxygens (O_{carb}) at the corners of the molecule with the metal atoms underneath them. This leads to the latter being pulled above the substrate surface plane on both substrates, albeit to a greater extent for MgO, with O_{carb}-Ag and O_{carb}-Mg bond lengths of 2.35 and 2.2 Å, respectively. However, despite the carboxylic oxygens having similar heights above the substrate surface planes (∼2.5 Å), on Ag the carbon backbone is drawn close to the surface (2.7 Å) and remains essentially planar, while on MgO it bends with its center calculated to be 3.2 Å above the surface. This large height is similar to that obtained for a variety of aromatic molecules without functional anchor groups on MgO and can be attributed to the pushback effect of Pauli exclusion. While the quasi-free electrons of the Ag substrate can give way to create space for the electrons of the perylene core, the electrons of the dielectric are confined and cannot retract, thus preventing a closer approach of the molecular backbone. We suggest that the large bend of PTCDA on MgO/Ag expresses a more general aspect of adsorption on dielectrics, whose electronic hardness can lead to significantly stronger alterations of molecular geometries compared to metals.

5.3 Conclusions

With the POT technique, we have shown that compared to metal surfaces, dielectric interlayers have the capacity to lead to greatly increased geometric distortions of adsorbed molecules containing anchor groups. POT can detect these structural modifications via the changes in the orbital structure of the molecules. As such, it has advantages over diffraction techniques whose requirement of long-range order can make them difficult to apply to heterogeneous systems such as the MgO/Ag substrate considered here. A noticeable photon energy dependence of the photoemission patterns of the frontier π-orbitals serves as a clear indication of a nonplanar adsorption geometry. In combination with simulations of the photoemission patterns, our experiments revealed the bend of the PTCDA backbone induced on adsorption on MgO(001)/Ag(001) to be larger than that predicted by DFT calculations with different methodologies. This suggests that POT can serve also as a benchmark for DFT.

We suggest that, as photoemission momentum maps reflect the orbital structure in k-space, when combined with DFT, the POT technique has the potential to determine the exact shape of nonplanar adsorbates by detailed studies of the photon energy dependence. Moreover, the sensitivity of POT to the bending of adsorbed molecules in conjunction with the possibility to combine POT with ultrafast time-resolved photoemission [262] in principle provides the opportunity to study the nuclear dynamics, e.g., in surface chemical reactions, through its influence on molecular orbitals.

5.4 Methods

All sample preparations and photoemission orbital tomography (POT) experiments were performed under ultrahigh-vacuum (UHV) conditions at a base pressure of about 3×10^{-10} mbar. A clean Ag(001) surface was obtained by cycles of Ar^+ ion sputtering and annealing at 500 °C. MgO(001) films were grown by Mg evaporation in an oxygen environment (O_2 pressure of 10^{-6} mbar) at a substrate temperature of 270 °C. Mg fluxes were of the order of 1 Å/min as calibrated by a quartz microbalance. After the growth of MgO, the sample was slowly (approximately 2.5 °C/min) cooled to room temperature (RT). All MgO films grown for this study had a nominal thickness of 2 ML. A monolayer of perylene-3,4,9,10-tetracarboxylic dianhydride (PTCDA) on 2 ML MgO(001)/Ag(001) was prepared by sublimation of solid PTCDA from a home-built evaporator with the substrate held at RT.

POT experiments were carried out at RT in two different UHV chambers. The experiments at a photon energy of 35 eV were conducted at the Metrology Light Source insertion device beamline of the Physikalisch-Technische Bundesanstalt [399] using a toroidal electron analyzer [400]. The sample was illuminated by p-polarized light at an angle of 40° to the surface normal. As momentum maps were acquired by recording the photoemission intensity in the incidence plane while rotating the sample around its normal, the polarization factor $|\boldsymbol{Ak}|^2$ depends only on the radial coordinate of the momentum maps.

For additional POT experiments at photon energies of 21.22 and 40.80 eV, we used a NanoESCA system by Scienta Omicron. The He I and II radiation from an unpolarized HIS 14 HD excitation source (Focus GmbH) was incident at an angle of 68° to the surface normal. Due to the focusing mirror, the sample was illuminated by 30.6% s-polarized and 69.4% p-polarized light. This results in a decrease of intensity in the lower half of the momentum maps due to the polarization factor $|\boldsymbol{Ak}|^2$ and a corresponding asymmetry of the momentum maps. In order to obtain a symmetric appearance more easily comparable to the k maps obtained with the toroidal electron analyzer, and to improve the signal-to-noise ratio, the data were subsequently

symmetrized by mirroring the half of the map with more significant contributions of the orbitals to the intensity and averaging the map over instances rotated by 0°, 90°, 180°, and 270°.

In POT, the momentum map of photoemission from a molecule is the projection of Ewald-sphere cuts through the orbital distribution in k-space onto a plane representing the experimental geometry, e.g., the molecular plane in case of a molecule lying flat on a surface. The radius of the Ewald sphere is related to the kinetic energy of photoelectrons and thus to the photon energy: It is given by the latter minus the orbital energy with respect to the vacuum level. Note the common discrepancy between orbital energy as measured in experiment and calculated by theory. To account for this, we adapted the theoretical photon energy so that it results in the same kinetic energy for each experimental photon energy. However, for the sake of clarity and since the photon energy is the free-to-choose experimental parameter, momentum maps of identical kinetic energy are labeled according to the corresponding experimental photon energy.

Scanning tunneling microscopy (STM) measurements were performed at 77 K with a low-temperature STM apparatus attached to an UHV preparation chamber. Electrochemically etched tungsten tips were used.

The calculations for the molecular monolayer on three layers of Ag(001) and two layers of MgO(001) were carried out with the Vienna Ab initio Simulation Package [357, 320, 358] plane wave code in the repeated-slab approach, where an interlayer vacuum of 18 Å was inserted alongside a dipole-correction in order to avoid spurious electric fields. We utilized the projector augmented wave method [321] with an energy cutoff of 450 eV. The Brillouin zone was sampled with a Γ-centered mesh of $4\times4\times1$ points, and we used a Gaussian-type smearing of the unoccupied states with 0.2 eV width.

In order to account for van der Waals (vdW) interactions, we have used two different approximations for the exchange-correlation treatment: PBE [319] and the Tkatchenko-Scheffler method [140] with iterative Hirshfeld-partitioning [149, 147] (PBE-TS) as well as the vdW-functional optb86b-vdw (vdW-DFT) [169, 170]. The respective geometries were relaxed such that the maximum of the norm of the forces was lower than 0.005 eV/Å, while the 2 lowest layers of Ag(001) were held fixed (lattice constant: 4.16 Å). After geometry relaxation, the electronic structure was computed with the same parameters, albeit with a plane-wave cutoff of 500 eV and a Brillouin zone sampling of $8\times8\times3$ points. Photoemission momentum maps for the full system as well as the molecular monolayer in the adsorbed geometry were simulated in the plane-wave final-state approximation, as described, e.g., in Reference [401]. To calculate momentum maps of a gas-phase molecule, we used the molecular geometries from the aforementioned calculations and used the DFT module of the Gaussian orbitals based code NWChem [259] to obtain the molecular orbitals. Here, the 6-31G** basis set and the B3LYP exchange-correlation functional [116, 118] were used. The momentum maps were then simulated from the real-space orbitals, as shown in Reference [260].

5.5 Supporting Information

Dependence of the Calculated PTCDA Bend on the Approach to Treat the van der Waals Interaction and on the Work Function of the MgO(001)/Ag(001) Substrate

Table 5.1 summarizes the values of the PTCDA bend obtained with different approaches for treating the van-der-Waals forces and different densities of extra oxygen at the oxide-metal interface, which strongly affects the work function of the MgO(001)/Ag(001) substrate. The magnitude of the bend clearly depends on the type of calculation employed with the argueably

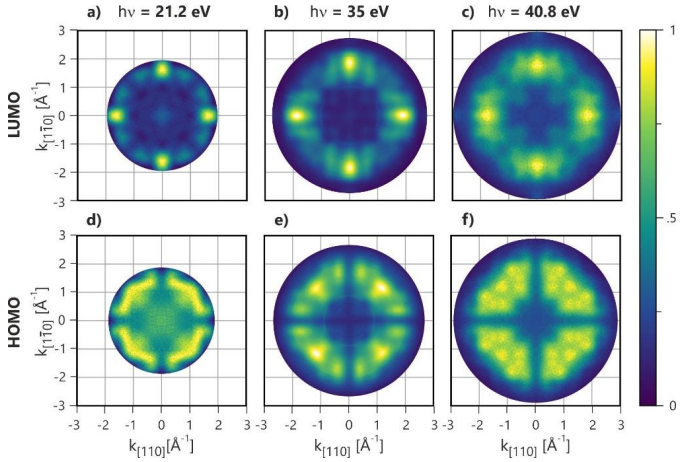

Figure 5.6: LUMO (a, b, c) and HOMO (d, e, f) maps taken at photon energies of (a, d) 21.2 eV, (b, e) 35 eV and (c, f) 40.8 eV. The symmetrized maps of (a), (c), (d) and (f) were measured with a Scienta Omicron NanoESCA system, while (b) and (e) were measured at the Metrological Light Source in Berlin with p polarized synchrotron radiation and a toroidal analyzer.

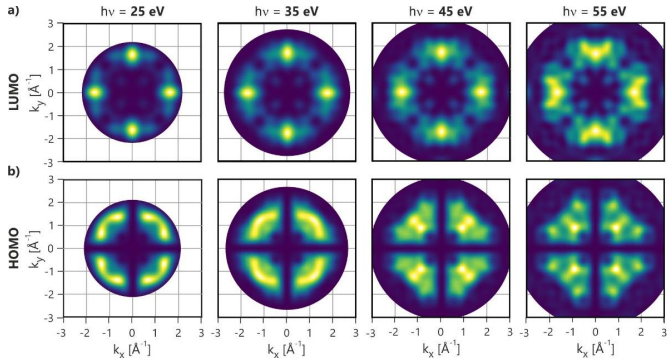

Figure 5.7: Displayed are (a) the LUMO and (b) the HOMO of PTCDA in the top and bottom rows, respectively. The molecular geometry with a C_{cent}-C_{carb} bend of 0.67 Å has been derived by DFT calculations on MgO(001)/Ag(001) using the PBE-TS approach.

more objective vdW DFT methodology resulting in a ∼0.1 Å lower bend than that of the PBE-TS calculations. The bend decreasing for lower substrate work functions is related to the increase in charge transfer to the LUMO and concomitant increase in electrostatic attraction.

Table 5.1: Calculated bends (C_{cent}-C_{carb}) in the carbon backbone of PTCDA on 2 ML of MgO(001) on Ag(001) for different oxygen content at the MgO-Ag interface resulting in different work functions calculated with two different van der Waals correction schemes.

	vdW DFT		PBE-TS	
Substrate	Φ_{sub} [eV]	C-Bend [Å]	Φ_{sub} [eV]	C-Bend [Å]
MgO/Ag(001)	2.96	0.59	2.84	0.67
MgO/$\frac{1}{4}$ ML O/Ag(001)	3.67	0.62	3.42	0.72
MgO/$\frac{1}{2}$ ML O/Ag(001)	4.25	0.64	3.95	0.71
Ag(001)	4.23			

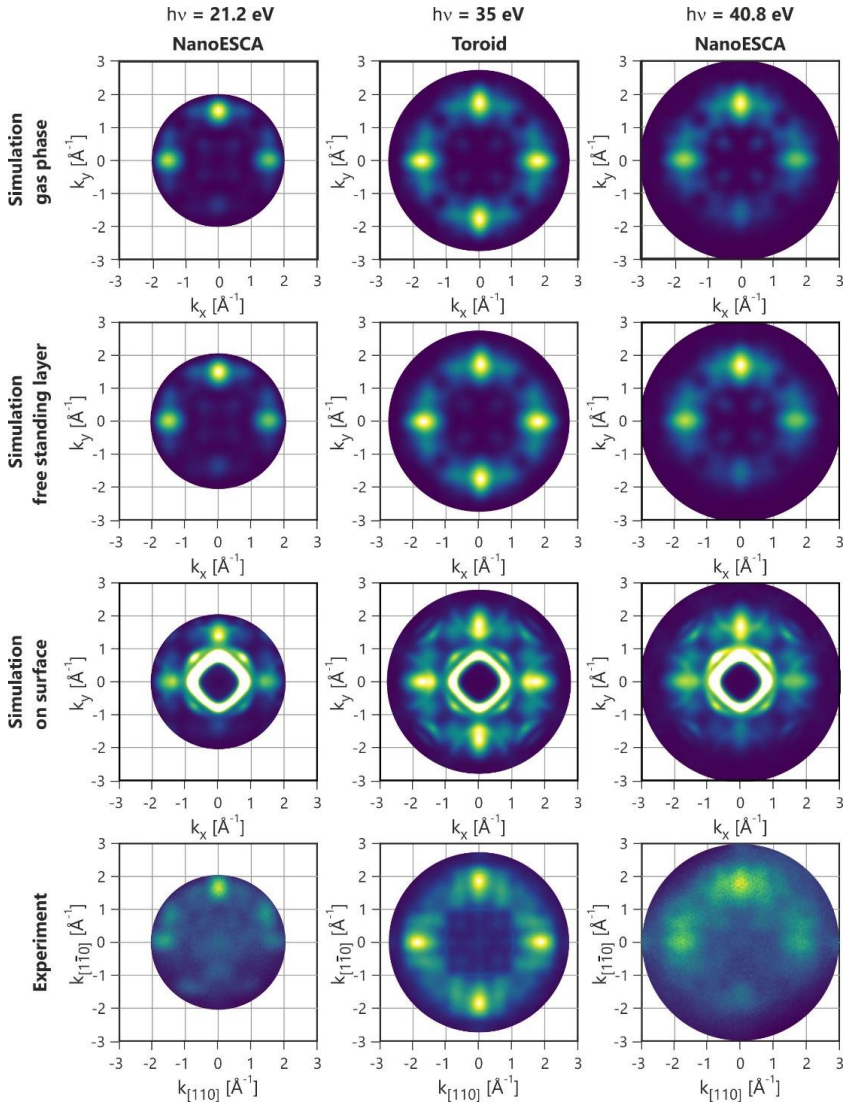

Figure 5.8: Momentum maps of PTCDA on MgO(001)/Ag(001) at different photon energies. (a, b) Side view in real space and corresponding three-dimensional k-space density (square of the Fourier transform of the real space orbital) of the HOMO of the PTCDA molecule in its planar geometry (a) and in the bent geometry (b) as obtained by on-surface DFT calculations. The bend across the carbon backbone (0.7 Å) and the total bend of the molecule (1.0 Å), including the end oxygens, are indicated. The gray hemispheres represent the Ewald sphere for a photon energy of 35 eV. (c-e) Symmetrized experimental momentum maps (upper panel) of the PTCDA HOMO on MgO(001)/Ag(001) taken at photon energies of (c) 21.2 eV, (d) 35 eV, and (e) 40.8 eV, and (lower panel) simulated momentum maps of the HOMO for isolated molecules in the bent geometry at the experimental photon energies.

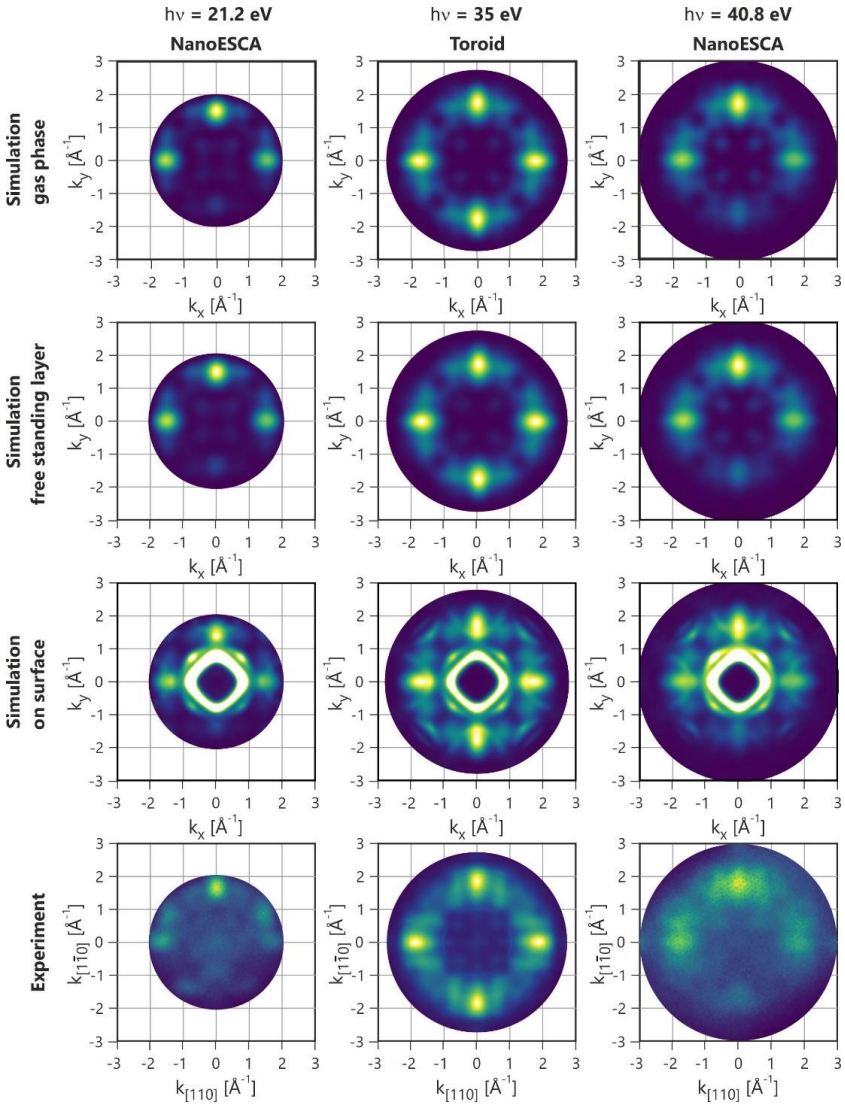

Figure 5.9: Momentum maps of PTCDA on MgO(001)/Ag(001) at different photon energies. (a, b) Side view in real space and corresponding three-dimensional k-space density (square of the Fourier transform of the real space orbital) of the HOMO of the PTCDA molecule in its planar geometry (a) and in the bent geometry (b) as obtained by on-surface DFT calculations. The bend across the carbon backbone (0.7 Å) and the total bend of the molecule (1.0 Å), including the end oxygens, are indicated. The gray hemispheres represent the Ewald sphere for a photon energy of 35 eV. (c-e) Symmetrized experimental momentum maps (upper panel) of the PTCDA HOMO on MgO(001)/Ag(001) taken at photon energies of (c) 21.2 eV, (d) 35 eV, and (e) 40.8 eV, and (lower panel) simulated momentum maps of the HOMO for isolated molecules in the bent geometry at the experimental photon energies.

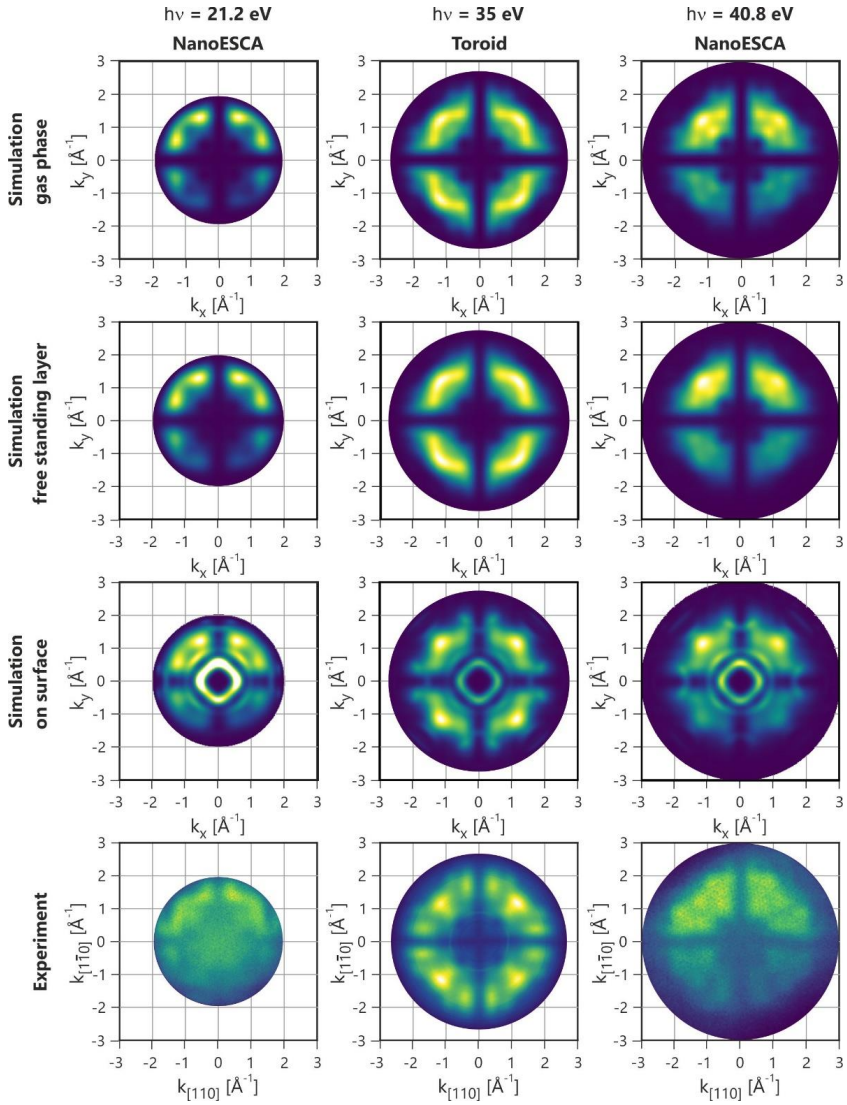

Figure 5.10: Momentum maps of PTCDA on MgO(001)/Ag(001) at different photon energies. (a, b) Side view in real space and corresponding three-dimensional k-space density (square of the Fourier transform of the real space orbital) of the HOMO of the PTCDA molecule in its planar geometry (a) and in the bent geometry (b) as obtained by on-surface DFT calculations. The bend across the carbon backbone (0.7 Å) and the total bend of the molecule (1.0 Å), including the end oxygens, are indicated. The gray hemispheres represent the Ewald sphere for a photon energy of 35 eV. (c-e) Symmetrized experimental momentum maps (upper panel) of the PTCDA HOMO on MgO(001)/Ag(001) taken at photon energies of (c) 21.2 eV, (d) 35 eV, and (e) 40.8 eV, and (lower panel) simulated momentum maps of the HOMO for isolated molecules in the bent geometry at the experimental photon energies.

Chapter 6

Simple Extension of the Plane Wave Final State in Photoemission: Bringing Understanding to the Photon-energy Dependence of Two-dimensional Materials

PHYSICAL REVIEW RESEARCH **5**, 033075 (2023)

Editors' Suggestion

Simple extension of the plane-wave final state in photoemission: Bringing understanding to the photon-energy dependence of two-dimensional materials

Christian S. Kern,[1] Anja Haags,[2,3,4] Larissa Egger,[1] Xiaosheng Yang,[2,3,4] Hans Kirschner,[5] Susanne Wolff,[6,7] Thomas Seyller,[6,7] Alexander Gottwald,[5] Mathias Richter,[5] Umberto De Giovannini,[8,9] Angel Rubio,[8,10] Michael G. Ramsey,[1] François C. Bocquet,[2,3] Serguei Soubatch,[2,3] F. Stefan Tautz,[2,3,4,*] Peter Puschnig,[1,†] and Simon Moser[11,‡]

Figure 6.1: **Header of the article as published in *Physical Review Research* [402].**

Significance Statement

ARPES is arguably the most important technique to experimentally extract the bandstructure of crystalline solids. This direct connection arises from the interpretation of measured data as the sample's one-electron removal spectral function. In reality, however, the spectral function is also modulated by so-called matrix-element effects, which are not stemming from the electronic structure of the sample itself, but are a result of the photoemission process and depend, for instance, on the polarization and the photon energy of the light field. To account for such effects, the photoemission process has to be modeled with an appropriate final state that describes the outgoing photoelectron accordingly. The most simple final state—a plane wave—does not

account for these effects sufficiently and an extension that would allow to fully reproduce the experimentally observed ARPES intensities is therefore desirable.

In this work, we studied the final-state effects in the prototypical 2D material graphene by approaching the problem from three different angles. First, with the metrology beamline at the Physikalisch-Technische Bundesanstalt Berlin, it was possible to extract calibrated ARPES intensities when varying the photon energy of the incidence light over a wide range. Second, sophisticated TDDFT simulations which naturally account for the final-state effects in question, could reproduce the experimental data very well and thereby allowed to exclude possible influences of the substrate. Third, with extending a scattered wave approximation for the final state to periodic systems, we could show that the physics in the process is essentially captured by a model of two interacting, dipole-allowed emission channels of the photoelectron. Depending on the incidence light polarization, we could further show that it can be necessary to also include nearest-neighbor scattering from the two invariant sublattices in graphene. Since 2D quantum materials are a very active field of research, with ARPES being one of the most important tool to investigate their electronic structure, our study therefore provides valuable insights that will help to disentangle the contributions from the material and the measuring process.

Author Contributions

Following an initial idea from Simon Moser to study the photoemission distribution along the graphene horse-shoe as a function of incident photon energy, the experiments were carried out at the Physikalisch-Technische Bundesanstalt Berlin. The expertise for metrology, necessary to extract calibrated ARPES data, came from Hans Kirschner, Alexander Gottwald and Mathias Richter. The preparation of the graphene samples was done by Susanne Wolff and Thomas Seyller and the sample characterization and ARPES measurements were carried out by Anja Haags, Larissa Egger and Xiaosheng Yang, under the supervision of Michael G. Ramsey, François C. Bocquet, Serguei Soubatch and F. Stefan Tautz. The experimental data was then processed by Anja Haags, Simon Moser, Serguei Soubatch, Peter Puschnig and myself. The TDDFT calculations were carried out by myself, with additional expertise from Umberto De Giovannini, Angel Rubio and Peter Puschnig. Simon Moser developed the scattered wave model and wrote the initial draft of the manuscript, with contributions from all co-authos. Overall project coordination was shared between Peter Puschnig, F. Stefan Tautz and Simon Moser.

Abstract

Angle-resolved photoemission spectroscopy (ARPES) is a method that measures orbital and band structure contrast through the momentum distribution of photoelectrons. Its simplest interpretation is obtained in the plane-wave approximation, according to which photoelectrons propagate freely to the detector. The photoelectron momentum distribution is then essentially given by the Fourier transform of the real-space orbital. While the plane-wave approximation is remarkably successful in describing the momentum distribution of aromatic compounds, it generally fails to capture kinetic-energy-dependent final-state interference and dichroism effects. Focusing our present study on quasi-freestanding monolayer graphene as the archetypical two-dimensional (2D) material, we observe an exemplary E_{kin}-dependent modulation of, and a redistribution of spectral weight within, its characteristic *horseshoe* signature around the $\overline{\mathrm{K}}$ and $\overline{\mathrm{K}}'$ points: both effects indeed cannot be rationalized by the plane-wave final state. Our data are, however, in remarkable agreement with *ab initio* time-dependent density functional simulations of a freestanding graphene layer and can be explained by a simple extension of the plane-wave

final state, permitting the two dipole-allowed partial waves emitted from the C $2p_z$ orbitals to scatter in the potential of their immediate surroundings. Exploiting the absolute photon flux calibration of the Metrology Light Source, this scattered-wave approximation allows us to extract E_{kin}-dependent amplitudes and phases of both partial waves directly from photoemission data. The scattered-wave approximation thus represents a powerful yet intuitive refinement of the plane-wave final state in photoemission of 2D materials and beyond.

6.1 Introduction.

Angle-resolved photoemission spectroscopy (ARPES) is a standard probe of the surface electronic structure of crystalline solids. Within the sudden approximation of the one-step model, the differential photoemission cross section $d\sigma/d\Omega(k_f, \Omega_{\boldsymbol{k}_f}; h\nu, \boldsymbol{\epsilon})$, i.e., the probability density to observe after irradiation with photons of energy $h\nu$ and polarization vector $\boldsymbol{\epsilon}$ a photoelectron of kinetic energy $E_{\text{kin}} = \hbar^2 k_f^2/2m$ and wave vector $\boldsymbol{k}_f$ at solid angle $\Omega_{\boldsymbol{k}_f} = (\theta, \phi)$, where θ is the inclination and ϕ the azimuth, can be decomposed into a product of two terms [43, 44]: the one-electron removal spectral function and the photoemission matrix element $M_{\boldsymbol{k}_f,i}$. Usually, the spectral function is of primary interest, because it provides access to band dispersions as well as self-energies and many-body interactions [44, 45]. Often, however, the photoemission cross section is strongly modulated by the matrix element $M_{\boldsymbol{k}_f,i}$, given in the dipole approximation and velocity gauge by

$$M_{\boldsymbol{k}_f,i} = \left\langle \psi_{\boldsymbol{k}_f} | \boldsymbol{\epsilon} \cdot \boldsymbol{\nabla} | \psi_i \right\rangle, \tag{6.1}$$

through the latter's dependence on the single-particle initial (ψ_i) and final state ($\psi_{\boldsymbol{k}_f}$) wave functions, as well as on the polarization $\boldsymbol{\epsilon}$ of the incoming photon field. On the one hand, this makes the experimental determination of the spectral function more difficult; on the other hand, the matrix element itself is a rich source of additional experimental information—especially regarding the initial-state wave function [46, 403].

A particularly simple connection with the initial state follows when approximating the final state by a plane wave [83, 404]. Then, the matrix element becomes proportional to the Fourier transform of the initial state times a momentum-dependent prefactor: $\boldsymbol{\epsilon} \cdot \boldsymbol{k}_f \times \mathcal{F}[\psi_i(\boldsymbol{r})](\boldsymbol{k}_f)$. In the field of organic molecular films, this plane-wave approximation (PWA) turned out to be particularly fruitful, and the ability to determine molecular orbital densities in momentum and real space from ARPES on such films—becoming known as photoemission orbital tomography [405, 403, 401]—has found wide-spread applications [46, 406, 389, 54, 407, 47, 51, 48, 262]. Moreover, the PWA has also been applied to extended solid-state systems [403, 408] and has provided insights into orbital angular momentum [409, 410, 411] and its topological manifestation in the Berry curvature [291, 412, 413].

Yet, one can rightly argue that the relationship between the initial state and the matrix element is in fact more complex than the PWA suggests [79]. Examples where the limitations of the PWA become evident are manifold and include photoelectron diffraction [414, 415], linear and circular dichroism [403, 416, 411], and photon-energy-dependent photoemission intensity modulations that have been tentatively attributed to final-state scattering effects [55, 417]. Theoretically, there is a long history of computational approaches aiming at a more exact description of the photoemission process. These include sophisticated quantum-coherent one-step models such as implemented, e.g., in the spin-polarized relativistic Korringa-Kohn-Rostoker technique [252, 253, 254] and multiple-scattering approaches [418, 415, 287, 417], but also real-time simulations in the framework of time-dependent density functional theory (TDDFT) [419, 86]. While all these methods adequately capture the photoemission process on a microscopic level, they

hide the underlying physical mechanisms in the computational complexity, thus rendering it impractical to establish any simple and intuitive connection between the matrix element and the initial state. Still, such a connection is vital for the physical understanding of photoemission, in particular in the context of orbital tomography.

In this paper, we present an economical extension of the plane-wave final state in photoemission from two-dimensional (2D) materials that takes into account all essential physical effects while retaining an intuitive link to the initial state. We used the photoemission intensity close to the $\overline{\mathrm{K}}$ point of quasi-freestanding monolayer graphene (QFMLG) [420, 421, 422], prepared on Si-terminated 6H-SiC(0001), as a benchmarking case (see Paragraph 6.4.1 for details of sample preparation). Varying the photon energy $h\nu$ in small steps, we measured the influence of the corresponding final state on the differential photoemission cross section of a constant initial state within the Dirac bands. We found that real-time TDDFT calculations employing the surface flux method [86] corroborate our benchmarking experiment. Crucially, we then introduce an intuitive *scattered-wave approximation* (SWA) of the photoemission final state that involves the interference of two dipole-allowed partial waves emitted from each C $2p_z$ orbital, and optionally their nearest-neighbor scattering at both sublattices of graphene as well ($\mathrm{SWA}^{\mathrm{NN}}$). This final state model describes the experimental results and the TDDFT calculations very well. Because of its generic nature, it can be readily used for a graphene-based determination of the absolute photon flux for variable energies, arbitrary experimental geometries and light polarizations typical for synchrotron-radiation experiments. Ultimately, the model can be further adapted to other (quasi-) 2D materials, such as films of π-conjugated molecules or (topological) surface states, to correct for deficiencies of the PWA in the description of their circular dichroism and photon-energy dependence, properties that in turn massively influence the extraction of the quantum metric and the Berry curvature [291, 412, 413].

6.2 Results

In our ARPES experiment, we employ a toroidal electron analyzer to measure the photoelectron intensity distribution $I(k_f, \Omega_0, \varphi; h\nu, \boldsymbol{\epsilon})$ at the detector, with $\Omega_0 = (\theta, \phi = 0)$ and $k_f = \sqrt{2mE_{\mathrm{kin}}/\hbar^2} = \sqrt{2m(h\nu + \varepsilon_i - \Phi)/\hbar^2}$, where Φ is the work function, and where φ is the azimuthal rotation of the sample (see Paragraph 6.4.2 for details). The index f denotes the final state, as defined by the fixed initial-state energy ε_i 1.35 eV below the Dirac point, and by the varying photon energy $h\nu$. Apart from an efficiency factor of the analyzer, I is proportional to the differential photoemission cross section $d\sigma/d\Omega(k_f, \Omega_0, \varphi; h\nu, \boldsymbol{\epsilon})$ and the photon intensity $I_{\mathrm{ph}}(h\nu, \boldsymbol{\epsilon})$ (see Paragraph 6.4.3 for details). Recovering $d\sigma/d\Omega$ from the photoelectron intensity distribution thus requires a division by an absolutely calibrated I_{ph}, which was readily provided by the insertion device beam-line at the Metrology Light Source in Berlin [399] for photon energies from 15 to 110 eV (see Paragraph 6.4.2 for details). Converting (θ, φ) to (k_x, k_y) and plotting the corresponding measured *momentum maps* in Figure 6.2 (a,b), we identify graphene's characteristic *horseshoe signatures* around the $\overline{\mathrm{K}}$ and $\overline{\mathrm{K}}'$ points [423, 424]. They arise from the structural interference of the two sublattices in the initial-state Bloch wave function and are thus characteristic for the honeycomb lattice. Specifically, the lattice sites' relative geometric phases $\vartheta_{\boldsymbol{k}} = \arg\sum_{j=0}^{2} e^{i\boldsymbol{n}_j \cdot \boldsymbol{k}}$ (Figure 6.2 (c) and Figure 6.3 (a)), where the $\boldsymbol{n}_j$ connect neighboring carbon atoms, produce a structure factor $(1 + e^{i\vartheta_{\boldsymbol{k}}})$ that suppresses valence band intensity along *dark corridors* [424] in momentum space (Figure 6.2 (a) and Paragraph 6.4.4). While in the PWA, both horseshoe and dark corridor are not expected to change, the experimental intensity around the horseshoes clearly redistributes as a function of final-state kinetic energy [424], as illustrated

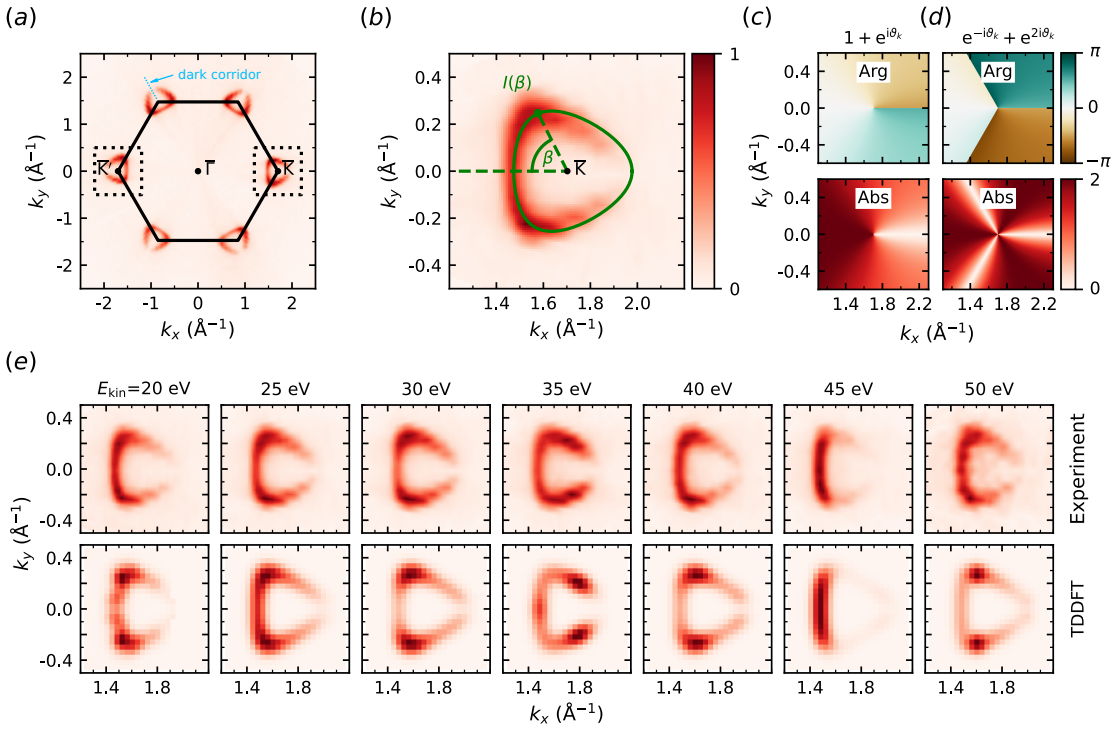

Figure 6.2: **Angle-resolved photoemission spectroscopy of graphene**. Overview (a) and close-up (b) of the typical horseshoe pattern arising in momentum maps close to the $\overline{\mathrm{K}}$ and $\overline{\mathrm{K}}'$ points, recorded at initial-state energy 1.35 eV below the Dirac point at $E_{\mathrm{kin}} = 30$ eV. Panel (b) also displays the contour (green line) and angle β along which the experimental data are plotted in Figure 6.3 (c-e). (c) Amplitude (bottom) and phase (top) of the initial-state structure factor that gives rise to the horseshoe. (d) Nearest-neighbor scattering factor that gives rise to intensity redistributions around the horseshoe. (e) Experimental horseshoe patterns around $\overline{\mathrm{K}}$ for seven representative kinetic energies measured in normal incidence geometry (top), compared to TDDFT calculations in precisely the same geometry (bottom).

in Figure 6.2 (e). Importantly, similar intensity redistributions as in experiment are also observed in our TDDFT simulations (Figure 6.2 (e), see Paragraph 6.4.5 for details), suggesting their source to be found in the final state.

To aid the quantitative analysis of the momentum maps, we plotted the photoelectron intensity as a function of the angle β around the green contour in Figure 6.2 (b) for E_{kin} between 15 and 80 eV (leftmost column of Figure 6.3 (c-e)), in normal light incidence (NI, Figure 6.3 (a)) and oblique light incidence (OI, Figure 6.3 (b)) geometries, both with p polarization. In NI geometry (Figure 6.3 (c)), the intensity appears predominantly below $E_{\mathrm{kin}} \lesssim 50$ eV, contracted along two streaks at $\beta \sim \pm\pi/3$ and interrupted by homogeneous intensity distributions between these angles at ~ 44 eV and below 20 eV. Further, between 30 and 40 eV we find the intensity to shift towards higher angles $\beta = \pm 2\pi/3$, an effect that we attribute to nearest-neighbor final-state scattering, as shall be seen in the following. In contrast, the angular intensity distribution in the OI geometry (Figure 6.3 (d,e)) is spread out more evenly between $\beta = \pm\pi/3$, because in this geometry nearest-neighbor scattering turns out to be less prevalent (see below). Moreover, the intensity distribution reaches up to kinetic energies of about 60 eV, with a suppression around 44 eV in the backward emission direction (BWD, Figure 6.3 (d)) that is not observed in forward emission (FWD, Figure 6.3 (e)).

As mentioned above, the PWA (second column in Figure 6.3 (c-e)) does not reproduce the rich structure observed in experiment: it predicts a monotonous decay of intensity with increasing kinetic energy, without any redistribution around the horseshoe. Also, the polarization factor $|\boldsymbol{\epsilon} \cdot \boldsymbol{k}_f|^2$ of the PWA incorrectly suppresses the overall intensity in the OI BWD geometry, in which the photoemission occurs (nearly) perpendicular to the polarization vector of light (Figures 6.3 (b,d)). In contrast, our TDDFT results (third column in Figure 6.3 (c-e)) are in remarkable agreement with the experiment in all three geometries, apart from an overall ~ 3 eV kinetic energy shift with respect to the experiment. Because the TDDFT simulations were performed for a freestanding and perfectly flat graphene layer, the pronounced structure must originate from graphene itself, and thus alternative explanations for the experimentally observed features in the photoemission cross section, such as hybridization with the substrate, photoelectron scattering from the underlying substrate atoms, or buckling of the graphene layer, can be ruled out. As TDDFT, however, accurately models graphene's surface potential, it also fully accounts for scattering of the outgoing photoelectron in the graphene lattice itself, apart from an overall offset of the surface potential because of the missing SiC substrate, to which we attribute the above-mentioned overall kinetic energy shift.

To clarify the physical origin of the kinetic energy and wave vector dependence of the differential cross section, we developed an improved model for the final state, the scattered-wave approximation (SWA). In this model, scattering effects are included via angular-momentum-dependent and kinetic-energy-dependent amplitudes and phase shifts between partial waves of the outgoing Coulomb wave (see Paragraph 6.4.6 and Reference [411]). As a result, k_f-dependent interference effects in the final state between the two dipole-allowed $l \pm 1$ partial waves become possible. While this description has in fact a long history in the simulation of the photoemission process of gas-phase molecules [425, 426, 427, 282], we formally extended it to a periodic system, including the Bloch nature of the initial state as well as on-site, and, in a second step, nearest-neighbor scattering of the outgoing photoelectron.

Without nearest-neighbor scattering, the photoemission intensity from the C $2p_z$-derived valence band of graphene becomes (Paragraph 6.4.6)

$$\begin{aligned} I(k_f, \Omega_{\boldsymbol{k}_f}\, h\nu, \boldsymbol{\epsilon}) &\propto |M_{\boldsymbol{k}_f,\boldsymbol{k}}|^2 \\ &= \delta_{\boldsymbol{k},\boldsymbol{k}_{f\parallel}} \left|\boldsymbol{\epsilon} \cdot \boldsymbol{M}_{210}(\boldsymbol{k}_f)(1 + e^{i\vartheta_{\boldsymbol{k}}})\right|^2, \end{aligned} \tag{6.2}$$

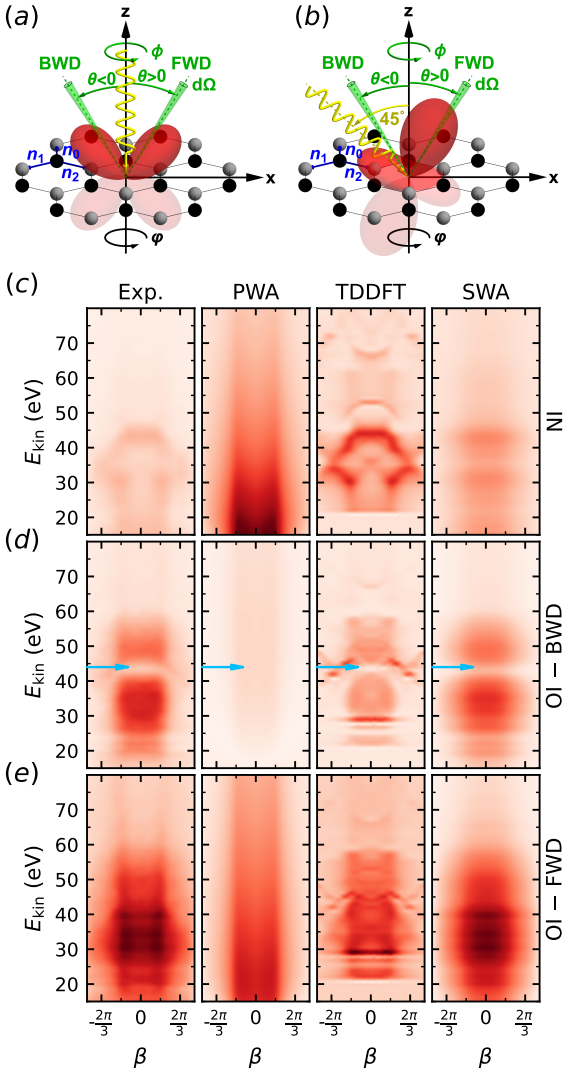

Figure 6.3: **Kinetic-energy-dependent photoemission intensities around the horseshoe.** (a) Normal incidence (NI) geometry. (b) Oblique incidence (OI) geometry. The incident light polarization is shown by the yellow sine wave. Angle-resolved detection in $d\Omega$ around inclination θ and azimuth ϕ is illustrated in green. The red lobes visualize the angular distributions of the pure d channels, d^2_{NI} and d^2_{OI}, respectively (cf. Equations 6.4 and 6.5). In our experiment, only photoelectrons emitted into the (x, z) plane, where $\phi = 0$, are detected. To obtain the momentum maps in Figure 6.2, the sample is rotated around the z axis by varying φ. (c-e) Experimental photoemission intensities in three geometries as indicated, extracted along the green contour in Figure 6.2 (b) and compiled for densely sampled kinetic energies between 15 and 80 eV (first column), compared to predictions of the PWA (second column), TDDFT (third column, shifted by 3 eV) and SWA without nearest-neighbor scattering (fourth column). Intensities in each column are plotted to scale, with dark red corresponding to high intensity. Between the columns the scaling is arbitrary. The blue arrows mark an intensity minimum that arises from a node in the d channel.

where the Kronecker $\delta_{\boldsymbol{k},\boldsymbol{k}_{f\parallel}}$ describes momentum conservation (modulo reciprocal lattice translations) and $(1+e^{i\vartheta_k})$ is the initial-state structure factor. Remarkably, the term $\boldsymbol{\epsilon}\cdot\boldsymbol{M}_{nlm}(\boldsymbol{k}_f)$ now replaces $\boldsymbol{\epsilon}\cdot\boldsymbol{k}_f\times\mathcal{F}[\phi_{nlm}](\boldsymbol{k}_f)$ in the PWA that we discussed in the introduction. For a $2p_z$ orbital with quantum numbers $\{nlm\}=\{210\}$, it is given by

$$\boldsymbol{M}_{210}(\boldsymbol{k}_f) \;=\; \underbrace{\widetilde{g}(k_f)\,\boldsymbol{Y}_{1,0,0}(\theta,\phi)}_{s\text{ channel}} - \underbrace{\widetilde{f}(k_f)\,\boldsymbol{Y}_{1,2,0}(\theta,\phi)}_{d\text{ channel}} \tag{6.3}$$

and therefore embodies the dipole selection rule and the corresponding angular distribution in the differential cross section for photoemission from C $2p_z$ orbitals. The complex-valued quantities $\widetilde{g}(k_f)$ and $\widetilde{f}(k_f)$ are determined by the effective on-site scattering potential and contain the k_f-dependent amplitude and phase of the s and d photoemission partial waves, respectively. The photoemission angular distribution in these two channels is given by the vector spherical harmonics $\boldsymbol{Y}_{l,l\mp1,m}$ [278], whose components can be individually addressed by the principal components of the light polarization vector $\boldsymbol{\epsilon}$.

In our experimental geometry (Figure 6.3 (a,b)), the NI and OI intensities simplify to (see Paragraph 6.4.6)

$$I_{\mathrm{NI}} \propto |\widetilde{f}(k_f)|^2 d_{\mathrm{NI}}(\theta,\phi)^2 |1+e^{i\vartheta_{k_{f\parallel}}}|^2, \tag{6.4}$$

$$\begin{aligned} I_{\mathrm{OI}} \propto \Big[& |\widetilde{f}(k_f)|^2 d_{\mathrm{OI}}(\theta,\phi)^2 + 8|\widetilde{g}(k_f)|^2 \\ & + 4\sqrt{2}|\widetilde{f}(k_f)||\widetilde{g}(k_f)| d_{\mathrm{OI}}(\theta,\phi)\cos\Delta\sigma \Big] \\ & \times |1+e^{i\vartheta_{k_{f\parallel}}}|^2, \end{aligned} \tag{6.5}$$

where $d_{\mathrm{NI}}(\theta,\phi) = \sin 2\theta\cos\phi$ and $d_{\mathrm{OI}}(\theta,\phi) = 3\sin 2\theta\cos\phi + 3\cos 2\theta + 1$ describe the angular intensity distributions of the pure d channel in the respective polarization geometries, and where $\Delta\sigma = \arg(\widetilde{f}/\widetilde{g})$ describes the relative phase between s and d partial waves. In the symmetric NI geometry, the s channel is suppressed and emission in the d channel is symmetric in θ. In contrast, I_{OI} is determined by the interference between the isotropic s and the anisotropic d channels. We note that in our experiments the plane of light incidence (spanned by the wave vector and light polarization) and the plane of detected photoemission coincide, i.e., $\phi = 0$ always. Hence, for $\beta = 0$ the above equations apply directly to our experiment, while for $\beta \neq 0$ (equivalent to $\phi \neq 0$ in Figure 6.3 (a,b) and Equation 6.4) the sample and with it the initial state need to be rotated by changing φ away from 0 while keeping $\phi = 0$. In contrast, both the TDDFT and the SWA calculations in Figure 6.3 (c-e) vary ϕ and keep $\varphi = 0$. Because the variations of φ (experiments) and ϕ (calculations) along the horseshoe trajectory β are small, deviations between the two detection geometries are negligible, as is also illustrated by the excellent agreement between experiment and theory in Figure 6.3 (c-e).

In analyzing the predictions of the SWA, we first focus on the kinetic energy (k_f) dependence. Since $d_{\mathrm{OI}}(\phi=0,\theta)^2$ vanishes for backward emission at $\theta_0^- \approx -29.3°$, we expect a minimum in I_{OI} at this angle. Close to the $\overline{\mathrm{K}}$ point of graphene we have $k_\parallel \approx 1.7$ Å^{-1}. Photoelectrons with this $k_{f\parallel}$ will be emitted at the angle θ_0^- if $k_f = k_{f\parallel}/\sin\theta_0^-$, yielding a kinetic energy $E_{\mathrm{kin}} \approx 44$ eV. This agrees with the observed intensity minimum in backward emission displayed in Figure 6.3 (d) (blue arrows), which can therefore be assigned to a node in the d channel (red lobe in Figure 6.3 (b)). Note that the second root of $d_{\mathrm{OI}}(\phi=0,\theta)^2$ appears in forward direction at $\theta_0^+ \approx 74.3°$, corresponding to a kinetic energy of only 11.4 eV for electrons from the vicinity of the $\overline{\mathrm{K}}$ point, which is outside our measurement range.

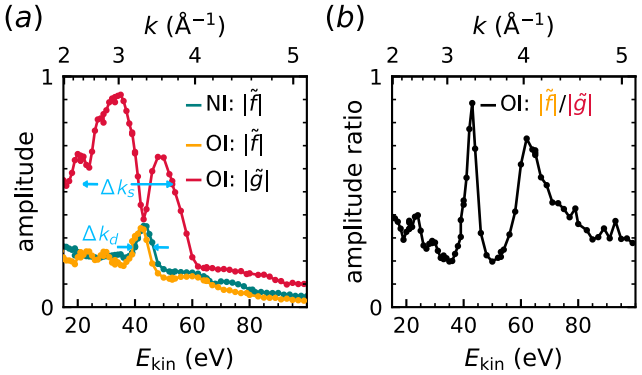

Figure 6.4: **Photoemission into s and d channels as a function of final-state kinetic energy.** (a) Amplitudes $|\widetilde{g}|$ and $|\widetilde{f}|$ of the s and d channels, respectively; (b) their ratio in the OI geometry. The curves were extracted from experimental data at $\beta = 0$ in NI and OI geometries as indicated, using the SWA without nearest-neighbor scattering. Positive real values were obtained only for in-phase photoemission in the s and d channels, i.e., $\Delta\sigma = 0$.

With the help of Equations 6.4 and 6.5 it is in fact possible to reconstruct the functions $|\widetilde{g}(k_f)|$ and $|\widetilde{f}(k_f)|$. To this end, we divided the NI experimental data in Figure 6.3 (c) at fixed angle $\beta = 0$ by $\sin^2 2\theta$ and thereby extracted the amplitude $|\widetilde{f}(k_f)|$ of the d channel (at $\beta = 0$, we also have $\phi = 0$). The green curve in Figure 6.4 (a) displays the result. Similarly, the BWD and FWD OI geometries (Figure 6.3 (d,e)) at $\beta = 0$ deliver two linearly independent equations for $I_{\mathrm{OI}}(k_f)$. Solving these for $|\widetilde{f}(k_f)|$ (orange in Figure 6.4 (a)) and $|\widetilde{g}(k_f)|$ (red in Figure 6.4 (a)), we find positive real values only if $\Delta\sigma = 0$, i.e., for an in-phase emission in the s and d channels. Quite remarkably, the $|\widetilde{f}(k_f)|$ obtained from the OI geometry matches the curve obtained from the NI geometry absolutely, i.e., without any scaling correction, thereby underlining the excellent photon intensity calibration provided by the Metrology Light Source. Plotting the ratio $|\widetilde{f}|/|\widetilde{g}|$ in Figure 6.4 (b), we find the s channel to be the predominant photoelectron source throughout the entire energy regime, except for regions around 43 eV and 63 eV, where the s and d channel contributions are of the same order.

Inserting the so-obtained amplitudes $|\widetilde{f}(k_f)|$ and $|\widetilde{g}(k_f)|$ as well as the phase shift $\Delta\sigma = 0$ back into the model of Equation 6.2, we can calculate the expected intensity distribution in the horseshoe for our three experimental configurations (varying θ and ϕ and keeping $\varphi = 0$). The results are shown in the rightmost column of Figure 6.3 (c-e). Regarding the OI data (d,e), which exhibit relatively little structure in β, the agreement between experiment and SWA is very satisfactory and clearly much better than for the PWA. For the NI data, however, the SWA model does not capture the distinctive redistribution of the intensity in k-space that is observed in experiment. Specifically, the kinetic-energy-dependent modulation along β is not reproduced.

To amend this deficiency, we thus extended the model to include, in addition to on-site scattering, also nearest-neighbor (NN) scattering in the final state, i.e., scattering of photoelectrons emitted from sublattice A into the Coulomb partial waves centered at one of the neighboring B

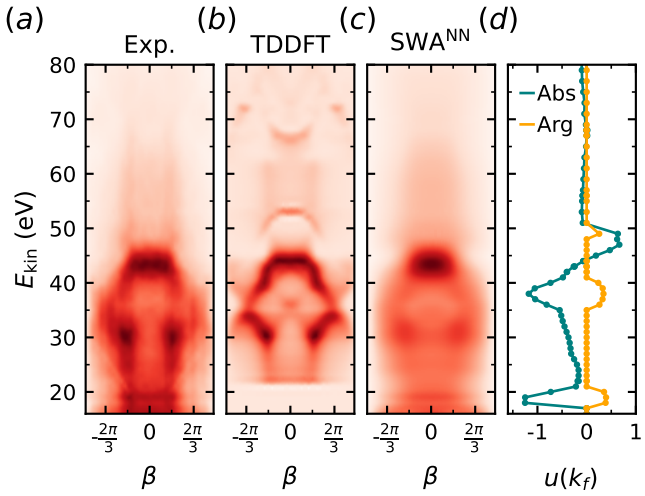

Figure 6.5: **Influence of nearest-neighbor scattering.** (a) Experimental photoemission intensity in the NI geometry reproduced from Figure 6.3 (c) with a different contrast scaling. (b) Corresponding TDDFT simulations from Figure 6.3 (c). (c) $\mathrm{SWA}^{\mathrm{NN}}$ prediction including nearest-neighbor final-state scattering. (d) k_f-dependent scattering amplitude and phase of $u(k_f)$ that best fits the data in (a). For a compact display we have plotted Abs $\equiv |u| \times \mathrm{sgn}(\arg u)$ and Arg $\equiv \mod(\arg u, \pi)$.

sites. Adapting Equation 6.2 accordingly, we find (see Paragraph 6.4.6)

$$I(k_f, \Omega_{\boldsymbol{k}_f}\, h\nu, \boldsymbol{\epsilon}) \propto \left|\boldsymbol{\epsilon}\cdot\boldsymbol{M}_{210}(\boldsymbol{k}_f)\times\left[1+e^{i\vartheta_k}+\right.\right. \\ \left.\left.+\left(e^{-i\vartheta_{k_{f\parallel}}}+e^{i\vartheta_k}e^{i\vartheta_{k_{f\parallel}}}\right)u(\boldsymbol{k}_f)\right]\right|^2\delta_{\boldsymbol{k},\boldsymbol{k}_{f\parallel}}. \tag{6.6}$$

NN final-state scattering thus leads to an additional term $(e^{-i\vartheta_{k_{f\parallel}}}+e^{i\vartheta_k}e^{i\vartheta_{k_{f\parallel}}})u(\boldsymbol{k}_f)$, which collapses to $(e^{-i\vartheta_{k_{f\parallel}}}+e^{i2\vartheta_{k_{f\parallel}}})u(\boldsymbol{k}_f)$ due to momentum conservation. Because $u(\boldsymbol{k}_f)$ varies only slowly on the photoemission hemisphere $\Omega_{\boldsymbol{k}_f}$, for a given k_f it can be approximated in Equation 6.6 as a merely kinetic-energy-dependent (but not momentum-vector-dependent) fit parameter $u(k_f)$ that is constant around the horseshoe, i.e., $u(\boldsymbol{k}_f) \approx |u(k_f)|e^{i\arg u(k_f)}$. Fitting Equation 6.6 under this assumption to the experimental data of Figure 6.3 (c), we obtained the intensity distribution shown in Figure 6.5 (c), with the corresponding $u(k_f)$ displayed in Figure 6.5 (d). Given the simplicity of our scattering model, the agreement with the experiment in Figure 6.5 (a) (and with TDDFT in Figure 6.5 (b)) is very satisfactory: In particular, the shift of the intensity to $\beta \approx \pm 2\pi/3$ in the kinetic energy range between 30 and 40 eV and also below 20 eV, as well as the concurrent depletion of the intensity in the interval $[-\pi/3, +\pi/3]$, are well reproduced. As Figure 6.2 (d) reveals, these redistributions are a direct consequence of the minima and maxima of $|e^{-i\vartheta_{k_{f\parallel}}}+e^{i2\vartheta_{k_{f\parallel}}}|$ at $\beta = \pm\pi/3$ and $\beta = \pm 2\pi/3$, respectively, and the maxima of $|u(k_f)|$ in the respective kinetic energy ranges. This demonstrates that the SWA in conjunction with nearest-neighbor final-state scattering ($\mathrm{SWA}^{\mathrm{NN}}$) captures the essence of the observed intensity distribution, in both kinetic energy and k-space.

Looking back at the overall intensity distributions in β of the three experimental geometries

in Figure 6.3 (c-e), we note that nearest-neighbor final-state scattering is most prevalent in the NI geometry, to a much lesser extent also in the OI-FWD, but essentially absent in OI-BWD, where the intensity is essentially confined in the interval $[-\pi/3, +\pi/3]$, as predicted by the bare initial-state structure factor $|1 + e^{i\vartheta_k}|$ (Figure 6.2 (c)). In other words, experimental geometries that have significant d channel contributions (NI, OI-FWD, cf. Equations 6.4 and 6.5) show NN scattering, while those with a dominant s channel (OI-BWD) do not. We rationalize this observation by the emission channels' k_f dependences. Estimating the d and s wave resonances in Figure 6.4 (a) to exhibit widths of $\Delta k_d \approx 0.3$ Å^{-1} and $\Delta k_s \approx 1.5$ Å^{-1}, respectively, Heisenberg's uncertainty principle $\Delta k \Delta r \geq \hbar/2$ suggests real-space distributions of the corresponding Coulomb partial waves of the order $\Delta r_d \approx 1.7$ Å and $\Delta r_s \approx 0.3$ Å around the carbon nucleus. Taking into account a carbon-carbon distance of 1.42 Å, a significant overlap between partial waves emanating from nearest neighbors is thus only expected for the d channel.

6.3 Conclusion

In summary, we measured angle-resolved photoemission intensities of the horseshoe of quasi-freestanding monolayer graphene (QFMLG) for a wide range of photon energies using a calibrated photon flux. Varying the final-state kinetic energy for a fixed initial state, we found a complex intensity modulation that is well reproduced by simulations using the surface-flux method within the framework of TDDFT, but goes beyond the predictions of the plane-wave final state approximation. In order to understand these findings in terms of an intuitive physical picture, we developed the scattered-wave approximation for the photoemission final state which allows for the interference of the dipole-allowed s and d photoemission channels, where the latter experiences also significant scattering from the neighboring carbon atoms. In this way, we extracted the kinetic-energy-dependent amplitude and phase of both s and d partial waves, which present a benchmark for *ab initio* theories that focus on a more sophisticated description of the photoemission process and are pivotal for the understanding of dichroism. Our wide-energy-range $\widetilde{f}(k_f)$, $\widetilde{g}(k_f)$ data provided in Figure 6.4 (a) (see Supplemental Material Ref. [402]) along with Equations 6.2 and 6.3 also allow for an easy calculation of the horseshoe intensities with arbitrary polarized light. A prospective application thereof could be an absolute normalization of photon flux in any photoemission measurement with variable photon energy and geometry purely based on the photoemission response of the robust 2D material QFMLG. Going beyond graphene, our model further promises an intuitive description of complex kinetic-energy-dependent intensity modulations and dichroism in layers of π conjugated organic molecules, or even in (quasi-) 2D quantum materials with more complex orbital low-energy electronic structures, including strong spin orbit coupling.

6.4 Appendix

6.4.1 Sample Preparation

The preparation of quasi-freestanding monolayer graphene (QFMLG) was performed in two steps [428, 429, 420, 430]: First, a Si-terminated 6H-SiC(0001) surface was thermally decomposed to create zero-layer graphene (ZLG). Subsequently, the ZLG is decoupled from the substrate by annealing at 550° C in hydrogen atmosphere (880 mbar) to obtain QFMLG. The quality of the QFMLG was controlled with low-energy electron diffraction (LEED) and x-ray photoemission spectroscopy (XPS) with Al K_α radiation. After preparation, the sample was transferred through

air to the synchrotron for ARPES experiments. Before the ARPES experiments, the sample was cleaned by outgassing in ultrahigh vacuum ($<10^{-9}$ mbar) at 350° C for 30 min. ARPES experiments with 45 eV photon energy revealed band maps typical for p-doped graphene with the Fermi level 0.1 eV below the Dirac point [420].

6.4.2 Photoemission Experiments

Photon-energy-dependent ARPES experiments were conducted at the calibrated insertion device beam-line [399] of the Metrology Light Source at the Physikalisch-Technische Bundesanstalt (PTB), the German national metrology institute in Berlin. Measurements in two experimental geometries were carried out, labeled as normal incidence (NI) and oblique incidence (OI), with incidence angles of, respectively, 0° and 45° relative to the sample surface normal. In both geometries, the incident light was p-polarized.

The photon energy was varied in small steps (1 eV for $h\nu < 50$ eV, 2 eV for $h\nu > 50$ eV) from $h\nu = 15$ to 110 eV. To this end, several different undulator/monochromator/filter settings of the beam-line were employed: (1) In the photon energy range from 15 to 31 eV, the third undulator harmonic with normal incidence onto the grating monochromator was employed; (2) in the range from 25 to 45 eV, the third harmonic with grazing incidence in combination with a Mg filter was used; (3) from 45 to 60 eV, the sixth harmonic with grazing incidence in combination with an Al filter was employed; (4) for 60 to 71 eV, the tenth harmonic with grazing incidence in combination with an Al filter was used; (5) for 71 to 87 eV, the tenth harmonic with grazing incidence in combination with a Be filter was employed; (6) and finally, for 87 to 110 eV the same setting as in (5) but in wiggler operation mode was used. The filters served to suppress both parasitic light from higher grating orders and stray light from the monochromator, reducing the false-light contribution to below 1% of the total [399].

Special care was taken regarding the calibration of the photon intensity I_{ph}. To this end, we employed the drain current caused by photoemission at the beam-line mirror. This current was referenced to an absolutely calibrated semiconductor photodiode, yielding an $h\nu$-dependent photon intensity curve measured in photons per seconds and nanoampere mirror current [55]. During the photoemission experiments from graphene, the mirror current was constantly monitored, yielding the calibrated photon intensity $I_{\mathrm{ph}}(h\nu, \boldsymbol{\epsilon})$ which was further used in Equation 6.14.

To detect the photoelectrons, a toroidal electron analyzer [400] was used. The instrument simultaneously collects photoelectrons emitted into a wide angular range of $-85° \leq \theta \leq 85°$ within the plane of incidence, i.e., the plane spanned by the incident light beam and the sample normal (see Figure 6.3 (a)), and an energy dispersion range of ≈ 1 eV. Additionally rotating the sample around its azimuth φ in steps of 1°, we obtained $I(k_f, \Omega_0, \varphi; h\nu, \boldsymbol{\epsilon})$ with $\Omega_0 \equiv (\theta, \phi = 0)$, and thus a complete experimental data cube, which was transformed into experimental momentum maps of the photoemission intensity $I(k_x, k_y)$. Note that unlike momentum maps that would be obtained from the intensity $I(k_f, \Omega_{\boldsymbol{k}_f}; h\nu, \boldsymbol{\epsilon})$ by converting $\Omega_{\boldsymbol{k}_f} = (\theta, \phi)$ into (k_x, k_y), the experimental momentum map in this paper was measured with constant azimuth $\phi = 0$. To obtain photoemission intensities deriving from the fixed initial-state energy of $\epsilon_i = -1.25$ eV, i.e., 1.35 eV below the Dirac point, the kinetic energy E_{kin} at which photoelectrons were detected was varied with photon energy $h\nu$ such that $E_{\mathrm{kin}} = h\nu - E_c$. E_c was determined by comparing the experimentally measured diameter of the horseshoe to the TDDFT-calculated one. For $E_c = 1.6$ eV, the experimentally measured horseshoes had the same diameter as the TDDFT-calculated horseshoes 1.35 eV below the Dirac point. While the absolute photoelectron-to-counts conversion rate of the toroidal electron analyzer is unknown, we expect the response $\chi(k_f)$ to be linear and independent of k_f, i.e., of kinetic energy. The cross sections reported in

this work are thus given apart from a constant factor χ, i.e., only in relative terms, and were thus normalized arbitrarily in Figure 6.4.

6.4.3 Photoemission Differential Cross Section

In the sudden approximation of the one-step model of photoemission, the probability per unit time (or transition rate) $W_{i,\boldsymbol{k}_f}$ that a photoelectron with wave vector $\boldsymbol{k}_f$ is emitted from the single-particle initial state i is given by Fermi's golden rule

$$\begin{aligned} W_{i,\boldsymbol{k}_f} &= \frac{2\pi}{\hbar}\left|\left\langle \psi_{\boldsymbol{k}_f}\left|\frac{e}{m}\boldsymbol{A}\cdot\hat{\boldsymbol{p}}\right|\psi_i\right\rangle\right|^2 \delta\left(\varepsilon_i-\varepsilon_{\boldsymbol{k}_f}-\Phi+h\nu\right) \\ &= \frac{2\pi e^2\hbar|A_0|^2}{m^2}\left|\left\langle \psi_{\boldsymbol{k}_f}\left|\boldsymbol{\epsilon}\cdot\nabla\right|\psi_i\right\rangle\right|^2 \delta\left(\varepsilon_i-\varepsilon_{\boldsymbol{k}_f}-\Phi+h\nu\right), \end{aligned} \tag{6.7}$$

where $|\psi_i\rangle$ is the initial (bound) state vector with energy $\varepsilon_i < 0$ and $|\psi_{\boldsymbol{k}_f}\rangle$ is the final (unbound) state vector with kinetic energy $E_{\text{kin}} = \varepsilon_{\boldsymbol{k}_f}$, and $\Phi > 0$ is the work function. $\boldsymbol{A}$ is the vector potential of the photon field, $\boldsymbol{\epsilon}$ its polarization vector, $\hat{\boldsymbol{p}}$ the momentum operator of the (photo)electron, and e and m are the electron's charge and mass, respectively. The perturbing operator $\boldsymbol{A}\cdot\hat{\boldsymbol{p}}$ arises from the minimal coupling principle by taking into account that the momentum operator commutes with the vector potential in the Coulomb gauge.

The probability per unit time P_{i,k_f} that a photoelectron with kinetic energy $E_{\text{kin}} = \hbar^2k_f^2/2m$ is emitted from initial state i into any direction $\Omega_{\boldsymbol{k}_f} = (\theta,\phi)$ can be calculated as

$$P_{i,k_f} = \frac{1}{v_{\boldsymbol{k}_f}}\int_{|\boldsymbol{k}'_f|=k_f} d^3\boldsymbol{k}'_f W_{i,\boldsymbol{k}'_f}, \tag{6.8}$$

where $v_{\boldsymbol{k}_f} = (2\pi)^3/V$ is the $\boldsymbol{k}_f$-space volume per $\boldsymbol{k}_f$ vector. V is the (illuminated) real-space volume of the sample, in which $\int_V \psi^*_{\boldsymbol{k}_f}\psi_{\boldsymbol{k}_f}d^3\boldsymbol{r} = 1$. Note that for a given initial state ψ_i with energy ε_i and due to energy conservation enforced by the delta function in Equation 6.7, the integration in Equation 6.8 projects out the angular dependence at a fixed absolute value k_f, i.e., kinetic energy as described earlier [46]. Using Equation 6.7, this becomes

$$\begin{aligned} P_{i,k_f} &= \frac{V}{(2\pi)^2}\frac{e^2\hbar|A_0|^2}{m^2}\int_{2\pi} d\Omega_{\boldsymbol{k}'_f}\int {k'_f}^2 dk'_f \left|\left\langle \psi_{\boldsymbol{k}'_f}\left|\boldsymbol{\epsilon}\cdot\nabla\right|\psi_i\right\rangle\right|^2 \delta(k'_f-k_f)\frac{1}{|s'(k_f)|} \\ &= \frac{V}{(2\pi)^2}\frac{e^2|A_0|^2k_f}{\hbar m}\int_{2\pi} d\Omega_{\boldsymbol{k}_f}\left|\left\langle \psi_{\boldsymbol{k}_f}\left|\boldsymbol{\epsilon}\cdot\nabla\right|\psi_i\right\rangle\right|^2, \end{aligned} \tag{6.9}$$

where $s(k'_f) \equiv \varepsilon_i - \hbar{k'_f}^2/2m - \Phi + h\nu$.

The total cross section σ_{i,k_f} of the photoemission process from initial state i is related to P_{i,k_f} by

$$\frac{\sigma_{i,k_f}}{A_\square} \equiv n_{i,k_f} = P_{i,k_f}\Delta t, \tag{6.10}$$

where $A_\square$ is the illuminated area on the sample and n_{i,k_f} is the fraction of emitted photoelectrons per photon hitting the area $A_\square$ in the time interval Δt. Evidently, $A_\square$ is given by $V_{\text{ph}}/(c\Delta t)$, where V_{ph} is the volume in which the energy of the photon field amounts to $h\nu$ and c the velocity of light. After differentiation with respect to the solid angle Ω we thus find for the differential cross section

$$\frac{d\sigma_{i,k_f}}{d\Omega} = \frac{V_{\text{ph}}}{c}\frac{dP_{i,k_f}}{d\Omega}. \tag{6.11}$$

Note that both $\frac{d\sigma_{i,k_f}}{d\Omega}$ and $\frac{dP_{i,k_f}}{d\Omega}$ are functions not only of k_f and $\Omega_{\boldsymbol{k}_f} = (\theta, \phi)$, but also of photon energy $h\nu$ (which—because of the delta function in Equation 6.7—selects possible initial states i according to their ε_i) and light polarization $\boldsymbol{\epsilon}$. Hence, we write $\frac{d\sigma}{d\Omega}(k_f, \Omega_{\boldsymbol{k}_f}; h\nu, \boldsymbol{\epsilon})$ from now on.

The normalization of the light field to the energy of one photon in the volume V_{ph} fixes the amplitude A_0 of the vector field to

$$|A_0|^2 = \frac{\hbar}{\pi V_{\mathrm{ph}} \epsilon_0 \nu}. \tag{6.12}$$

According to Equations 6.9 and 6.11, this finally yields the differential photoemission cross section

$$\frac{d\sigma}{d\Omega}(k_f, \Omega_{\boldsymbol{k}_f}; h\nu, \boldsymbol{\epsilon}) = \frac{d\sigma_{i,k_f}}{d\Omega} = \frac{V}{4\pi^3} \frac{e^2 k_f}{cm\epsilon_0 \nu} \left| \left\langle \psi_{\boldsymbol{k}_f} \left| \boldsymbol{\epsilon} \cdot \nabla \right| \psi_i \right\rangle \right|^2. \tag{6.13}$$

In experiment, we measure the photoelectron intensity $I(k_f, \Omega_{\boldsymbol{k}_f}; h\nu, \boldsymbol{\epsilon})$ at the detector in a finite solid angle $\Delta\Omega$, originating from the area $A_\square$ on the sample which contains N photoemitters. The calibrated beamline produces a known monochromatic photon flux $F_{\mathrm{ph}}(h\nu, \boldsymbol{\epsilon})$, yielding a photon intensity $I_{\mathrm{ph}}(h\nu, \boldsymbol{\epsilon}) = F(h\nu, \boldsymbol{\epsilon}) A_\square$ on the area $A_\square$. Photoelectrons are detected with efficiency $\chi(k_f)$. Therefore, the photoelectron intensity is given by

$$I(k_f, \Omega_{\boldsymbol{k}_f}; h\nu, \boldsymbol{\epsilon}) = \chi(k_f)\, I_{\mathrm{ph}}(h\nu, \boldsymbol{\epsilon})\, N\, \frac{\frac{d\sigma}{d\Omega}(k_f, \Omega_{\boldsymbol{k}_f}; h\nu, \boldsymbol{\epsilon})}{A_\square}\, \Delta\Omega. \tag{6.14}$$

Thus, the intensity ratio $I(k_f, \Omega_{\boldsymbol{k}_f}; h\nu, \boldsymbol{\epsilon}) / I_{\mathrm{ph}}(h\nu, \boldsymbol{\epsilon})$, if obtained at a carefully calibrated beamline with a carefully characterized linear response $\chi(k_f)$ of the analyzer, is a direct measure of the differential photoemission cross section. If we assume that the volume density of the photoemitters in the sample is ϱ, we can replace the ratio $N/A_\square$ in the above equation by ϱd, where d is the effective sampling depth.

6.4.4 Photoemission Initial State

The unit cell of graphene contains two carbon atoms, one in each of the two sublattices A and B. The respective atoms are located at $\boldsymbol{R}_{\mathrm{A}} = \frac{a}{2\sqrt{3}}(0, -1)^\top$ and $\boldsymbol{R}_{\mathrm{B}} = \frac{a}{2\sqrt{3}}(0, 1)^\top$ within the unit cell (see Figure 6.6). Each of these carbon atoms contributes one $2p_z$ orbital to the formation of aromatic π bonds. The nearest neighbors of carbon atoms in sublattice A are atoms in sublattice B; they are located at $\boldsymbol{n}_0 = (0, a/\sqrt{3})^\top$ within the same unit cell and at $\boldsymbol{n}_1 = C_3^1 \boldsymbol{n}_0 = (-a/2, -a/2\sqrt{3})^\top$ and $\boldsymbol{n}_2 = C_3^2 \boldsymbol{n}_0 = (a/2, -a/2\sqrt{3})^\top$ in adjacent unit cells, where C_3 is a threefold rotation around the sample normal. In the orbital basis $\{|R_A, 2p_z\rangle, |R_B, 2p_z\rangle\}$, the tight-binding Hamiltonian with nearest-neighbor hopping reads

$$\hat{H} = t \begin{pmatrix} 0 & h(\boldsymbol{k}) \\ h^*(\boldsymbol{k}) & 0 \end{pmatrix}, \tag{6.15}$$

where

$$h(\boldsymbol{k}) = \sum_{j=0}^{2} e^{i\boldsymbol{n}_j \cdot \boldsymbol{k}} \equiv |h(\boldsymbol{k})| e^{i\vartheta_{\boldsymbol{k}}} \tag{6.16}$$

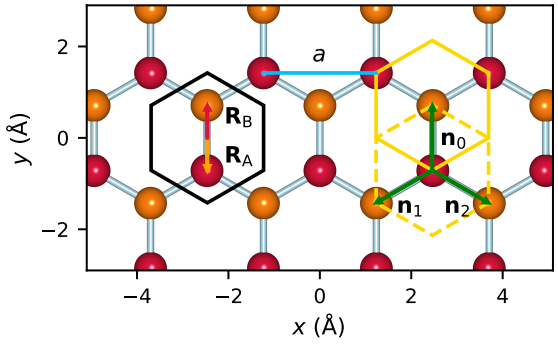

Figure 6.6: **Atomic structure of graphene.** Carbon atoms of the two sublattices A and B are displayed in red and orange, respectively. The primitive unit cell containing one atom each of both sublattices is shown in black. The three vectors $\boldsymbol{n}_0$, $\boldsymbol{n}_1$ and $\boldsymbol{n}_2$ from an atom in sublattice A to its nearest neighbors in sublattice B are indicated in green. Non primitive unit cells that contain all nearest neighbors of a sublattice representative are shown in yellow. In the SWA$^{\mathrm{NN}}$ including nearest-neighbor scattering, the total photoemission intensity is given by the sum of identical contributions from the two yellow unit cells.

describes the coupling between sublattices A and B, and where $t < 0$ is the nearest-neighbor hopping energy [283]. Diagonalizing $\hat{H}$, one finds eigenvalues

$$\begin{aligned} \varepsilon_{\boldsymbol{k}}^{\pm} &= \pm t|h(\boldsymbol{k})| \\ &= \pm t\sqrt{3+2\cos(ak_x)+4\cos(ak_x/2)\cos(a\sqrt{3}k_y/2)} \end{aligned} \tag{6.17}$$

with eigenvectors $\boldsymbol{c}^{\pm} = (c_{\mathrm{A}}^{\pm}, c_{\mathrm{B}}^{\pm})^{\top} = \frac{1}{\sqrt{2}}(1, \pm e^{i\vartheta_{\boldsymbol{k}}})^{\top}$, where $e^{i\vartheta_{\boldsymbol{k}}} = h(\boldsymbol{k})/|h(\boldsymbol{k})|$, and where the superscripts $+$ and $-$ label the negative and positive energy solutions, i.e., the valence and the conduction band, respectively. The argument $\vartheta_{\boldsymbol{k}}$ of $h(\boldsymbol{k})$ is plotted in Figure 6.7. Hence, the initial state of the photoemission process from the aromatic π bands of graphene is the Bloch state

$$\Psi_{\boldsymbol{k}}^{\pm}(\boldsymbol{r}) = \frac{1}{\sqrt{V}}\sum_{\boldsymbol{R}} e^{i\boldsymbol{k}\cdot\boldsymbol{R}}\frac{1}{\sqrt{2}}\left(|R_{\mathrm{A}}, 2p_z\rangle \pm e^{i\vartheta_{\boldsymbol{k}}}|R_{\mathrm{B}}, 2p_z\rangle\right), \tag{6.18}$$

where the sum runs over all graphene lattice sites $\boldsymbol{R}$, and $\boldsymbol{k}$ is defined within the first Brillouin zone of graphene. Because in the experiment we measure only the horseshoe within the valence band of graphene, we exclusively select the $+$ and drop the $-$ solution in the main text.

6.4.5 TDDFT Calculations

For the ab initio simulations of photoemission from graphene, we restricted ourselves to a single layer with a carbon-carbon distance of $n_j = 1.421$ Å, extended in the x, y plane. The TDDFT simulations were carried out with the real-space real-time code OCTOPUS [177, 431, 432, 433], using in-plane periodic boundary conditions and an out-of-plane simulation box of 70 Å (D_z) in both directions. To avoid spurious reflections of electron density in both non-periodic directions ($\pm z$ directions), we inserted a complex absorbing potential [434] (CAP), starting at a distance of ± 15 Å from the graphene layer, with $\mathrm{i}\xi\sin^2(\frac{z\pi}{2D_z})$ behavior and $\xi = -1$ a.u. We used a grid spacing in the simulation box of 0.18 Å and approximated the influence of the core electrons by

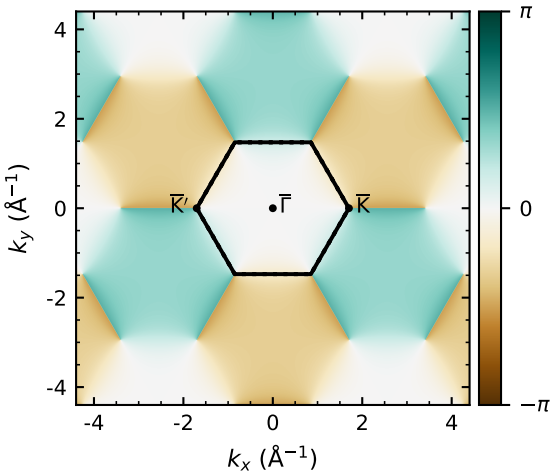

Figure 6.7: **Phase ϑ_k of graphene**. The black hexagon indicates the first Brillouin zone. $\overline{\Gamma}$, $\overline{\mathrm{K}}$ and $\overline{\mathrm{K}}'$ points are labeled.

norm-conserving Hartwigsen-Goedecker-Hutter pseudopotentials [435]. Exchange-correlation effects were treated in the adiabatic local density approximation (ALDA) [101, 103].

After the electronic ground state had been calculated, the system was subjected to an electromagnetic field for 30 fs. It was coupled to the Hamiltonian in the velocity gauge. This pulse was modeled by a $\cos(\omega t)$ function and shaped by a $\sin^2$ hull function, thus ensuring gradual on- and off-switching. Over all times, we recorded the flux of electron density through a surface located at the onset of the CAP, which is a direct numerical simulation of the ARPES experiment [85, 86]. In order to guarantee a normalized photon flux, the maximum amplitude of the pulse was varied for each photon energy, corresponding to a laser with a constant intensity of 10^8 W/cm^2.

6.4.6 Photoemission Final State

General Framework

Following Ref. [411], we write the photoelectron final state in terms of unbound solutions of the Schrödinger equation in a central Coulomb potential (Coulomb wave equation), i.e., in terms of unbound (positive energy) hydrogen-like atomic orbitals $|\boldsymbol{R}_j, \eta l m\rangle$ centered at site $\boldsymbol{R}_j$. These orbitals are the partial waves in the expansion of the Coulomb wave $|\boldsymbol{k}_f\rangle$ with wave vector $\boldsymbol{k}_f$ and as such are characterized by quantum numbers l and m, as well as the dimensionless Sommerfeld parameter $\eta = Z/(a_0 k_f)$, which describes the distortion of the outgoing photoelectron wave with spherical wave vector k_f in the Coulomb field of the ion that is left behind. a_0 is the Bohr radius. Note that the Sommerfeld parameter takes the role of the principal quantum number n that characterizes bound solutions.

The partial waves are given by [436, 437, 438, 439]

$$\chi_{\eta l m}(\boldsymbol{r}) = \langle \boldsymbol{r}|\chi_{\eta l m}\rangle = R_{\eta l}(r)\langle \boldsymbol{r}|lm\rangle = R_{\eta l}(r) Y_l^m(\Omega_{\boldsymbol{r}}). \tag{6.19}$$

In the far field, the radial functions $k_f r R_{\eta l}(r)$ normalize to a sine wave of unit amplitude,

$$R_{\eta l}(r \to \infty) \to \frac{\sin[k_f r - \eta \ln(2k_f r) - l\pi/2 + \sigma_l]}{k_f r}, \tag{6.20}$$

where $\sigma_l = \arg\Gamma(l + 1 + i\eta)$ is the Coulomb phase. The sine wave is phase-shifted with respect to the free electron wave, signifying the impact of the ionic Coulomb potential on the partial electron wave with angular momentum l far away from the atomic site.

The Coulomb wave $|\boldsymbol{k}_f\rangle$ of the outgoing photoelectron emitted with wave vector $\boldsymbol{k}_f$ from an atomic site in a specific direction, expanded in terms of partial waves for all l and m, is given by [279, 440]

$$|\boldsymbol{k}_f\rangle = 4\pi \sum_{l=0}^{\infty} \sum_{m=-l}^{l} i^l \, e^{i\sigma_l} \langle lm|\boldsymbol{k}_f\rangle |\chi_{\eta lm}\rangle, \tag{6.21}$$

yielding

$$\begin{aligned} \chi_{\boldsymbol{k}_f}(\boldsymbol{r}) &= \langle \boldsymbol{r}|\boldsymbol{k}_f\rangle \\ &= 4\pi \sum_{l=0}^{\infty} \sum_{m=-l}^{l} i^l \, e^{i\sigma_l} R_{\eta l}(r, k_f) \langle \boldsymbol{r}|lm\rangle \langle lm|\boldsymbol{k}_f\rangle \\ &= 4\pi \sum_{l=0}^{\infty} \sum_{m=-l}^{l} i^l \, e^{i\sigma_l} R_{\eta l}(r, k_f) Y_l^m(\Omega_{\boldsymbol{r}}) Y_l^{m*}(\Omega_{\boldsymbol{k}_f}). \end{aligned} \tag{6.22}$$

This expression should be compared to the partial-wave expansion of the plane-wave final state

$$e^{i\boldsymbol{k}_f \cdot \boldsymbol{r}} = 4\pi \sum_{l=0}^{\infty} \sum_{m=-l}^{l} i^l j_l(k_f r) Y_l^{m*}(\Omega_{\boldsymbol{r}}) Y_l^m(\Omega_{\boldsymbol{k}_f}) \tag{6.23}$$

where the j_l are spherical Bessel functions.

The final-state wave function of a photoelectron with wave vector $\boldsymbol{k}_f$ from a lattice of atoms is given by a coherent superposition of outgoing states $|\boldsymbol{k}_f\rangle$ emanating from all sites,

$$\Psi_{\boldsymbol{k}_f}(\boldsymbol{r}) = \frac{1}{\sqrt{V}} \sum_{\boldsymbol{R}} e^{i\boldsymbol{k}_f \cdot \boldsymbol{R}} \sum_{\boldsymbol{R}_j} e^{i\boldsymbol{k}_f \cdot \boldsymbol{R}_j} \chi_{\boldsymbol{k}_f}(\boldsymbol{r} - \boldsymbol{R} - \boldsymbol{R}_j), \tag{6.24}$$

where the sums are carried out over all lattice vectors $\boldsymbol{R}$ and basis sites $\boldsymbol{R}_j$ within a unit cell of the lattice, respectively. The prefactor involving the normalization volume (=sample volume) V safeguards that $\langle \Psi_{\boldsymbol{k}_f} | \Psi_{\boldsymbol{k}_f} \rangle = 1$. In the case of graphene, this becomes

$$\Psi_{\boldsymbol{k}_f}(\boldsymbol{r}) = \frac{1}{\sqrt{V}} \sum_{\boldsymbol{R}} e^{i\boldsymbol{k}_f \cdot \boldsymbol{R}} \sum_{j=\{A,B\}} e^{i\boldsymbol{k}_f \cdot \boldsymbol{R}_j} \chi_{\boldsymbol{k}_f}(\boldsymbol{r} - \boldsymbol{R} - \boldsymbol{R}_j), \tag{6.25}$$

where all $\boldsymbol{R}$, $\boldsymbol{R}_j$ are 2D vectors in the plane of graphene.

Before turning to the special case of photoemission from the C 2 p_z orbitals of graphene, we derive a general expression for the matrix element in Equation 6.13 between an initial Bloch state with band index κ,

$$|\Psi_{\boldsymbol{k}}^{\kappa}\rangle = \frac{1}{\sqrt{V}} \sum_{\boldsymbol{R}} e^{i\boldsymbol{k} \cdot \boldsymbol{R}} \sum_{\boldsymbol{R}_j} \sum_{nlm} c_{jnlm}^{\kappa}(\boldsymbol{k}) |\boldsymbol{R} + \boldsymbol{R}_j, nlm\rangle, \tag{6.26}$$

and the final state as given in Equation 6.24. The initial-state Bloch state can be expanded in terms of atomic states with quantum numbers $\{nlm\}$ centered at sites $\boldsymbol{R} + \boldsymbol{R}_j$. The latter are given by bound atomic orbitals (negative energy)

$$\Phi_{nlm}(\boldsymbol{r}) = \langle \boldsymbol{r} | \boldsymbol{0}, nlm \rangle = R_{nl}(r) Y_l^m(\Omega_{\boldsymbol{r}}). \tag{6.27}$$

Note that for graphene, the Bloch wave vectors in Equation 6.26 are 2D and oriented in the surface plane, i.e., $\boldsymbol{k} = \boldsymbol{k}_\parallel$. For the photoemission matrix element $M^\kappa_{\boldsymbol{k}_f \boldsymbol{k}}$ between the initial-state wave function $\Psi^\kappa_{\boldsymbol{k}}(\boldsymbol{r})$ and the final-state wave function $\Psi_{\boldsymbol{k}_f}(\boldsymbol{r})$ we obtain from Equation 6.24 and Equation 6.26

$$\begin{aligned}
M^\kappa_{\boldsymbol{k}_f \boldsymbol{k}} &= \int d^3r\, \Psi^*_{\boldsymbol{k}_f}(\boldsymbol{r})\, \boldsymbol{\epsilon} \cdot \nabla \Psi^\kappa_{\boldsymbol{k}}(\boldsymbol{r}) \\
&= \frac{1}{V} \sum_{\boldsymbol{R'}} e^{-i\boldsymbol{k}_f \cdot \boldsymbol{R'}} \sum_{\boldsymbol{R}'_j} e^{-i\boldsymbol{k}_f \cdot \boldsymbol{R}'_j} \sum_{\boldsymbol{R}} e^{i\boldsymbol{k} \cdot \boldsymbol{R}} \sum_{\boldsymbol{R}_j} \sum_{nlm} c^\kappa_{jnlm}(\boldsymbol{k}) \\
&\quad \times \int d^3r\, \chi^*_{\boldsymbol{k}_f}(\boldsymbol{r} - \boldsymbol{R'} - \boldsymbol{R}'_j)\, \boldsymbol{\epsilon} \cdot \nabla \Phi_{nlm}(\boldsymbol{r} - \boldsymbol{R} - \boldsymbol{R}_j) \\
&= \frac{1}{V} \sum_{\boldsymbol{R'}} e^{-i\boldsymbol{k}_f \cdot \boldsymbol{R'}} \sum_{\boldsymbol{R}'_j} e^{-i\boldsymbol{k}_f \cdot \boldsymbol{R}'_j} \sum_{\boldsymbol{R}} e^{i\boldsymbol{k} \cdot \boldsymbol{R}} \sum_{\boldsymbol{R}_j} \sum_{nlm} c^\kappa_{jnlm}(\boldsymbol{k}) \\
&\quad \times \int d^3r\, \chi^*_{\boldsymbol{k}_f}(\boldsymbol{r} - \boldsymbol{R'} - \boldsymbol{R}'_j + \boldsymbol{R} + \boldsymbol{R}_j)\, \boldsymbol{\epsilon} \cdot \nabla \Phi_{nlm}(\boldsymbol{r}) \\
&\approx \frac{1}{V} \sum_{\boldsymbol{R}} e^{i(\boldsymbol{k} - \boldsymbol{k}_f) \cdot \boldsymbol{R}} \sum_{\boldsymbol{R}_j} \sum_{nlm} c^\kappa_{jnlm}(\boldsymbol{k}) e^{-i\boldsymbol{k}_f \cdot \boldsymbol{R}_j} \int d^3r\, \chi^*_{\boldsymbol{k}_f}(\boldsymbol{r})\, \boldsymbol{\epsilon} \cdot \nabla \Phi_{nlm}(\boldsymbol{r}) \\
&= \frac{N}{V} \sum_{\boldsymbol{G}} \delta_{(\boldsymbol{k} - \boldsymbol{k}_f)_\parallel, \boldsymbol{G}} \sum_{\boldsymbol{R}_j} \sum_{nlm} c^\kappa_{jnlm}(\boldsymbol{k}) e^{-i\boldsymbol{k}_f \cdot \boldsymbol{R}_j}\, \boldsymbol{\epsilon} \cdot \boldsymbol{M}_{nlm}(\boldsymbol{k}_f) \\
&= \frac{1}{V_0} \sum_{\boldsymbol{G}} \delta_{(\boldsymbol{k} - \boldsymbol{k}_f)_\parallel, \boldsymbol{G}}\, \boldsymbol{\epsilon} \cdot \boldsymbol{\mathcal{M}} \cdot \boldsymbol{c} \\
&\approx \frac{\delta_{\boldsymbol{k}, \boldsymbol{k}_{f\parallel}}}{V_0}\, \boldsymbol{\epsilon} \cdot \boldsymbol{\mathcal{M}} \cdot \boldsymbol{c},
\end{aligned} \tag{6.28}$$

where $\boldsymbol{\mathcal{M}}$ is a $3 \times \dim(\boldsymbol{c})$ matrix that couples the polarization (row) vector $\boldsymbol{\epsilon}$ of the incoming light to the initial state (column) vector $\boldsymbol{c}(\boldsymbol{k}) = (\ldots, c^\kappa_{jnlm}(\boldsymbol{k}), \ldots)^\top$, and where the indices $\{\kappa jnlm\}$ run over all available coordinates and quantum numbers. From the second to the third lines of Equation 6.28, a coordinate transformation $\boldsymbol{r} - \boldsymbol{R} - \boldsymbol{R}_j \to \boldsymbol{r}$ was carried out. Also, from the third to the fourth lines we excluded transitions between initial-state orbitals at one site $\Phi_{nlm}(\boldsymbol{r} - \boldsymbol{R} - \boldsymbol{R}_j)$ and final-state waves $\chi_{\boldsymbol{k}_f}(\boldsymbol{r} - \boldsymbol{R'} - \boldsymbol{R}'_j)$ emerging from another site, i.e., we assumed $\boldsymbol{R} = \boldsymbol{R'}$ and $\boldsymbol{R}_j = \boldsymbol{R}'_j$. This amounts to an explicit exclusion of inter-site final-state scattering (see below) and is commonly referred to as the *independent center approximation*. From the fourth to the fifth lines, we further identified the Fourier series in $\boldsymbol{R}$ as Dirac comb with 2D reciprocal lattice periodicity $\boldsymbol{G}$, and hence recover momentum conservation. Here, N is the number of unit cells in the sample volume and V_0 the unit cell volume.

The column 3-vectors $\boldsymbol{M}_{nlm}(\boldsymbol{k}_f)$ in Equation 6.28 are defined as

$$\boldsymbol{M}_{nlm}(\boldsymbol{k}_f) \equiv \int d^3r\, \chi^*_{\boldsymbol{k}_f}(\boldsymbol{r})\, \nabla \Phi_{nlm}(\boldsymbol{r}), \tag{6.29}$$

where the gradient of atomic orbitals is given in Ref. [278] by

$$\begin{aligned}\nabla\Phi_{nlm}(\boldsymbol{r}) &= \nabla[R_{nl}(r)Y_l^m(\Omega_{\boldsymbol{r}})] \\ &= -\sqrt{\frac{l+1}{2l+1}}\left[\frac{\partial}{\partial r}-\frac{l}{r}\right]R_{nl}(r)\boldsymbol{Y}_{l,l+1,m}(\Omega_{\boldsymbol{r}}) + \\ &\quad +\sqrt{\frac{l}{2l+1}}\left[\frac{\partial}{\partial r}+\frac{l+1}{r}\right]R_{nl}(r)\boldsymbol{Y}_{l,l-1,m}(\Omega_{\boldsymbol{r}}),\end{aligned} \tag{6.30}$$

and where $\boldsymbol{Y}_{J,L,M}(\Omega_r)$ are the vector spherical harmonics defined as [278]

$$\boldsymbol{Y}_{J,L,M}(\Omega_{\boldsymbol{r}}) = \sum_{m=-L}^{L}\sum_{m'=-1}^{1}\langle L,m;1,m'|J,M\rangle Y_L^m(\Omega_{\boldsymbol{r}})\,\boldsymbol{\epsilon}_{m'}, \tag{6.31}$$

with Clebsch-Gordon coefficients $\langle j_1,m_1;j_2,m_2|J,M\rangle$. $\boldsymbol{Y}_{J,L,M}$ thus emerges from the angular-momentum coupling of the ordinary spherical harmonic Y_L^m with angular momentum quantum number L to the complex vector $\boldsymbol{u} = x\boldsymbol{e}_x + y\boldsymbol{e}_y + z\boldsymbol{e}_z$, $(x,y,z)\in\mathbb{C}^3$, which has the angular momentum quantum number 1. The eigenstates of the $\hat{L}_z$ operator in the three-dimensional complex space of $\boldsymbol{u}$ are the $\boldsymbol{\epsilon}_{m'}$, given by $\boldsymbol{\epsilon}_{+1} = (-1/\sqrt{2},-i/\sqrt{2},0)^\top$, $\boldsymbol{\epsilon}_0 = (0,0,1)^\top$, and $\boldsymbol{\epsilon}_{-1} = (1/\sqrt{2},-i/\sqrt{2},0)^\top$ [278]. Defining

$$\begin{aligned}f_{nl}(r) &\equiv \left[\frac{\partial}{\partial r}-\frac{l}{r}\right]R_{nl}(r), \\ g_{nl}(r) &\equiv \left[\frac{\partial}{\partial r}+\frac{l+1}{r}\right]R_{nl}(r),\end{aligned} \tag{6.32}$$

we obtain

$$\nabla\Phi_{nlm}(\boldsymbol{r}) = -\sqrt{\frac{l+1}{2l+1}}f_{nl}(r)\,\boldsymbol{Y}_{l,l+1,m}(\Omega_{\boldsymbol{r}}) + \sqrt{\frac{l}{2l+1}}g_{nl}(r)\,\boldsymbol{Y}_{l,l-1,m}(\Omega_{\boldsymbol{r}}), \tag{6.33}$$

which, if inserted into Equation 6.29, yields

$$\begin{aligned}\boldsymbol{M}_{nlm}(\boldsymbol{k}_f) &= \int d^3r\,\chi^*_{\boldsymbol{k}_f}(\boldsymbol{r})\left(-\sqrt{\frac{l+1}{2l+1}}f_{nl}(r)\,\boldsymbol{Y}_{l,l+1,m}(\Omega_{\boldsymbol{r}}) + \sqrt{\frac{l}{2l+1}}g_{nl}(r)\,\boldsymbol{Y}_{l,l-1,m}(\Omega_{\boldsymbol{r}})\right) \\ &= -\sqrt{\frac{l+1}{2l+1}}e^{-i\sigma_{l+1}}\widetilde{f}_{n,l,l+1}(k_f)\,\boldsymbol{Y}_{l,l+1,m}(\Omega_{\boldsymbol{k}_f}) + \\ &\quad +\sqrt{\frac{l}{2l+1}}e^{-i\sigma_{l-1}}\widetilde{g}_{n,l,l-1}(k_f)\,\boldsymbol{Y}_{l,l-1,m}(\Omega_{\boldsymbol{k}_f}),\end{aligned} \tag{6.34}$$

where we exploited the orthogonality of spherical harmonics to resolve the spatial integral and introduced

$$\begin{aligned}\widetilde{f}_{n,l,l+1}(k_f) &\equiv 4\pi(-i)^{l+1}\int dr\,r^2R^*_{\eta l+1}(r)f_{nl}(r), \\ \widetilde{g}_{n,l,l-1}(k_f) &\equiv 4\pi(-i)^{l-1}\int dr\,r^2R^*_{\eta l-1}(r)g_{nl}(r).\end{aligned} \tag{6.35}$$

The two summands in Equation 6.34 correspond to the two dipole-allowed photoemission channels $l\to l\pm1$. The $\widetilde{f}_{n,l,l+1}(k_f)$ and $\widetilde{g}_{n,l,l-1}(k_f)$ are the kinetic-energy-dependent (through k_f) amplitudes of the photoemission $l+1$ and $l-1$ channels, respectively, for photoemission from an initial state with quantum numbers $\{nlm\}$. The σ_{l+1} and σ_{l-1} are their corresponding Coulomb phases.

Photoemission from C $2p_z$ Orbitals Without Nearest-neighbor Scattering

We now focus on photoemission from the π band of graphene and calculate $M^{\pm}_{\boldsymbol{k}_f \boldsymbol{k}}$ for this explicit case. Then, the matrix $\boldsymbol{\mathcal{M}}$ is a 3×2 matrix, and $\boldsymbol{c}$ is given by $\boldsymbol{c}^{\pm} = \frac{1}{\sqrt{2}}(1, \pm e^{i\vartheta_k})^{\top}$. Since the orbitals in the two sublattices are identical, the two columns of $\boldsymbol{\mathcal{M}}$ are also identical. Because a specific choice of the basis in $\mathbb{C}^3$ is implicit in the definition of the vector spherical harmonics, and thus also in $\boldsymbol{M}_{nlm}$, we also need to express both the polarization vector $\boldsymbol{\epsilon}$ of the light and the initial state vector $\boldsymbol{c}$ in this basis. Since the π bands of graphene involve only C $2p_z$ states, this is trivial with regard to $\boldsymbol{c}$; we consider only the $\boldsymbol{M}_{210}$ vector. Regarding the polarization vector of the incoming light, we have to choose the basis of eigenstates of the complex vector $\boldsymbol{u}$, i.e., $\boldsymbol{\epsilon}_+$, $\boldsymbol{\epsilon}_0$ and $\boldsymbol{\epsilon}_-$ as defined above. In fact, this basis coincides with circular polarized light of two opposite directions in the x, y plane ($\boldsymbol{\epsilon}_+ \equiv \boldsymbol{\epsilon}_{\circlearrowleft}$ and $\boldsymbol{\epsilon}_- \equiv \boldsymbol{\epsilon}_{\circlearrowright}$) and linearly polarized light in the z direction ($\boldsymbol{\epsilon}_0$).

Applying Equation 6.34 to the C $2p_z$ orbital with quantum numbers $\{nlm\} = \{210\}$, we find

$$\begin{aligned} \boldsymbol{M}_{210}(\boldsymbol{k}_f) &= -\sqrt{\frac{2}{3}} e^{-i\sigma_2} \widetilde{f}_{2,1,2}(k_f)\, \boldsymbol{Y}_{1,2,0}(\Omega_{\boldsymbol{k}_f}) + \sqrt{\frac{1}{3}} e^{-i\sigma_0} \widetilde{g}_{2,1,0}(k_f)\, \boldsymbol{Y}_{1,0,0}(\Omega_{\boldsymbol{k}_f}) \\ &\equiv -\widetilde{f}(k_f)\, \boldsymbol{Y}_{1,2,0}(\Omega_{\boldsymbol{k}_f}) + \widetilde{g}(k_f)\, \boldsymbol{Y}_{1,0,0}(\Omega_{\boldsymbol{k}_f}), \end{aligned} \tag{6.36}$$

where for clarity we absorbed the constants as well as the k_f-dependent amplitudes ($\widetilde{g}_{2,1,0}$ and $\widetilde{f}_{2,1,2}$) and phases ($e^{-i\sigma_2}$ and $e^{-i\sigma_0}$) in the complex functions $\widetilde{f}(k_f)$ and $\widetilde{g}(k_f)$, respectively. According to Equation 6.28, $M^{\pm}_{\boldsymbol{k}_f \boldsymbol{k}}$ then becomes

$$\begin{aligned} M^{\pm}_{\boldsymbol{k}_f \boldsymbol{k}} &= \delta_{\boldsymbol{k}, \boldsymbol{k}_{f\parallel}}\, \boldsymbol{\epsilon} \cdot \boldsymbol{\mathcal{M}}(\boldsymbol{k}_f) \cdot \boldsymbol{c}^{\pm} \\ &= \delta_{\boldsymbol{k}, \boldsymbol{k}_{f\parallel}} \begin{pmatrix} \epsilon_+ & \epsilon_0 & \epsilon_- \end{pmatrix} \cdot \begin{pmatrix} \boldsymbol{M}_{210}(\boldsymbol{k}_f) & \boldsymbol{M}_{210}(\boldsymbol{k}_f) \end{pmatrix} \cdot \frac{1}{\sqrt{2}} \begin{pmatrix} 1 \\ \pm e^{i\vartheta_k} \end{pmatrix} \\ &= \delta_{\boldsymbol{k}, \boldsymbol{k}_{f\parallel}} \begin{pmatrix} \epsilon_+ & \epsilon_0 & \epsilon_- \end{pmatrix} \cdot \boldsymbol{M}_{210}(\boldsymbol{k}_f) \cdot \begin{pmatrix} 1 & 1 \end{pmatrix} \cdot \begin{pmatrix} 1 \\ \pm e^{i\vartheta_k} \end{pmatrix} \\ &= \Bigg(\underbrace{-\widetilde{f}(k_f) \left(\sqrt{\frac{3}{10}} \epsilon_- Y^1_2(\Omega_{\boldsymbol{k}_f}) - \sqrt{\frac{2}{5}} \epsilon_0 Y^0_2(\Omega_{\boldsymbol{k}_f}) + \sqrt{\frac{3}{10}} \epsilon_+ Y^{-1}_2(\Omega_{\boldsymbol{k}_f}) \right)}_{d \text{ channel}} + \\ &\quad + \underbrace{\widetilde{g}(k_f)\, \epsilon_0 Y^0_0(\Omega_{\boldsymbol{k}_f})}_{s \text{ channel}} \Bigg) \times \frac{1}{\sqrt{2}} (1 \pm e^{i\vartheta_{\boldsymbol{k}_{f\parallel}}}), \end{aligned} \tag{6.37}$$

where we used the vector spherical harmonics,

$$\boldsymbol{Y}_{1,2,0}(\Omega_{\boldsymbol{k}_f}) = \left(\sqrt{\frac{3}{10}} Y^{-1}_2(\Omega_{\boldsymbol{k}_f}), -\sqrt{\frac{2}{5}} Y^0_2(\Omega_{\boldsymbol{k}_f}), \sqrt{\frac{3}{10}} Y^1_2(\Omega_{\boldsymbol{k}_f}) \right)^{\top}, \tag{6.38}$$

and

$$\boldsymbol{Y}_{1,0,0}(\Omega_{\boldsymbol{k}_f}) = (0, Y^0_0(\Omega_{\boldsymbol{k}_f}), 0)^{\top}, \tag{6.39}$$

according to Equation 6.31.

First, we note that circular dichroism in this approximation vanishes, as

$$|Y^1_2(\Omega_{\boldsymbol{k}_f})| = |Y^{-1}_2(\Omega_{\boldsymbol{k}_f})|. \tag{6.40}$$

Next, we consider the two experimental geometries NI and OI that are employed in our work. For NI and a vector potential along $\boldsymbol{\epsilon}_x$, we have $\epsilon_+ = -\frac{1}{\sqrt{2}}$, $\epsilon_- = \frac{1}{\sqrt{2}}$, and $\epsilon_0 = 0$. Using the explicit expressions for the spherical harmonics,

$$\begin{aligned} Y_0^0(\Omega_{\boldsymbol{k}_f}) &= \frac{1}{2\sqrt{\pi}}, \\ Y_2^0(\Omega_{\boldsymbol{k}_f}) &= \sqrt{\frac{5}{4\pi}}(\frac{3}{2}\cos^2\theta - \frac{1}{2}), \\ Y_2^1(\Omega_{\boldsymbol{k}_f}) &= -\sqrt{\frac{15}{8\pi}}\sin\theta\cos\theta e^{+i\phi} \qquad \text{and} \\ Y_l^{-m} &= (-1)^m Y_l^{m*}, \end{aligned} \tag{6.41}$$

Equation 6.37 then becomes

$$M^{\pm}_{\boldsymbol{k}_f\boldsymbol{k},\mathrm{NI}} = \delta_{\boldsymbol{k},\boldsymbol{k}_{f\parallel}}\frac{3}{8\sqrt{\pi}}\widetilde{f}(k_f)\sin 2\theta\cos\phi(1\pm e^{i\vartheta_k}) \tag{6.42}$$

and the corresponding photoemission intensity reads

$$I^{\pm}(k_f,\theta,\phi;h\nu,\boldsymbol{\epsilon}_{\mathrm{NI}}) \propto |M^{\pm}_{\boldsymbol{k}_f\boldsymbol{k},\mathrm{NI}}|^2 = \delta_{\boldsymbol{k},\boldsymbol{k}_{f\parallel}}\frac{9}{64\pi}|\widetilde{f}(k_f)|^2\sin^2 2\theta\cos^2\phi|1\pm e^{i\vartheta_k}|^2. \tag{6.43}$$

This expression corresponds to Equation 6.4. Thus, we find that in the NI geometry with the polarization vector in the surface plane, the photoemission is strictly suppressed in the s channel. This geometry can therefore be used to determine the (square) modulus of the complex, kinetic-energy-dependent photoemission amplitude in the d channel.

In the OI geometry, with 45° angle of light incidence in the $-x,z$ half plane, we have $(\epsilon_+,\epsilon_0,\epsilon_-) = (-\frac{1}{2},\frac{1}{\sqrt{2}},\frac{1}{2})$. Equation 6.37 then yields

$$M^{\pm}_{\boldsymbol{k}_f\boldsymbol{k},\mathrm{OI}} = \delta_{\boldsymbol{k},\boldsymbol{k}_{f\parallel}}\frac{1}{8\sqrt{2\pi}}\left(\widetilde{f}(k_f)\ (3\sin 2\theta\cos\phi + 3\cos 2\theta + 1) + 2\sqrt{2}\widetilde{g}(k_f)\right)\times(1\pm e^{i\vartheta_k}), \tag{6.44}$$

and

$$\begin{aligned} I^{\pm}(k_f,\theta,\phi;h\nu,\boldsymbol{\epsilon}_{\mathrm{OI}}) &\propto |M^{\pm}_{\boldsymbol{k}_f\boldsymbol{k},\mathrm{OI}}|^2 \\ &= \delta_{\boldsymbol{k},\boldsymbol{k}_{f\parallel}}\frac{1}{128\pi}\Big(|\widetilde{f}(k_f)|^2\ (3\sin 2\theta\cos\phi + 3\cos 2\theta + 1)^2 + 8|\widetilde{g}(k_f)|^2 \\ &\quad +4\sqrt{2}|\widetilde{f}(k_f)||\widetilde{g}(k_f)|\ (3\sin 2\theta\cos\phi + 3\cos 2\theta + 1)\cos\Delta\sigma\Big) \\ &\quad \times|1\pm e^{i\vartheta_k}|^2. \end{aligned} \tag{6.45}$$

which corresponds to Equation 6.5, and where $\Delta\sigma(k_f) \equiv \arg\frac{\widetilde{f}(k_f)}{\widetilde{g}(k_f)}$ is the kinetic-energy-dependent relative phase between the d and s photoemission channels.

Photoemission from π Bands of Graphene Including Nearest-neighbor Scattering

To account for nearest-neighbor (NN) scattering, we reconsider the matrix element between the full initial- and final-state Bloch functions (Equation 6.28)

$$\begin{aligned} M^{\kappa}_{\boldsymbol{k}_f\boldsymbol{k}} &= \int d^3r\, \Psi^*_{\boldsymbol{k}_f}(\boldsymbol{r})\, \boldsymbol{\epsilon}\cdot\nabla\Psi^{\kappa}_{\boldsymbol{k}}(\boldsymbol{r}) \\ &= \frac{1}{V}\sum_{\boldsymbol{R'}} e^{-i\boldsymbol{k}_f\cdot\boldsymbol{R'}} \sum_{\boldsymbol{R}'_j} e^{-i\boldsymbol{k}_f\cdot\boldsymbol{R}'_j} \sum_{\boldsymbol{R}} e^{i\boldsymbol{k}\cdot\boldsymbol{R}} \sum_{\boldsymbol{R}_j}\sum_{nlm} c^{\kappa}_{jnlm}(\boldsymbol{k})\cdot \\ &\quad \cdot \int d^3r\, \chi^*_{\boldsymbol{k}_f}(\boldsymbol{r}-\boldsymbol{R'}-\boldsymbol{R}'_j+\boldsymbol{R}+\boldsymbol{R}_j)\, \boldsymbol{\epsilon}\cdot\nabla\Phi_{nlm}(\boldsymbol{r}). \end{aligned} \tag{6.46}$$

In the previous section, we assumed $\boldsymbol{R'} = \boldsymbol{R}$ and $\boldsymbol{R}'_j = \boldsymbol{R}_j$ before proceeding with this equation; the initial-state orbital and final-state partial wave were required to be centered on the same carbon atom, i.e., we employed the independent center approximation. Now we will relax this condition and allow an electron originating from a certain basis atom to be emitted in a partial wave centered on *another* basis atom ($\boldsymbol{R}'_j \neq \boldsymbol{R}_j$) in the same unit cell ($\boldsymbol{R'} = \boldsymbol{R}$). Clearly, this allows for nearest-neighbor scattering within the unit cell during the photoemission process. Then the above equation becomes

$$\begin{aligned} M^{\kappa}_{\boldsymbol{k}_f\boldsymbol{k}} &\approx \frac{1}{V}\sum_{\boldsymbol{R}} e^{i(\boldsymbol{k}-\boldsymbol{k}_f)\cdot\boldsymbol{R}} \sum_{\boldsymbol{R}'_j} e^{-i\boldsymbol{k}_f\cdot\boldsymbol{R}'_j} \sum_{\boldsymbol{R}_j}\sum_{nlm} c^{\kappa}_{jnlm}(\boldsymbol{k}) \int d^3r\, \chi^*_{\boldsymbol{k}_f}(\boldsymbol{r}-\boldsymbol{R}'_j+\boldsymbol{R}_j)\, \boldsymbol{\epsilon}\cdot\nabla\Phi_{nlm}(\boldsymbol{r}) \\ &= \frac{1}{V_0}\sum_{\boldsymbol{G}} \delta_{(\boldsymbol{k}-\boldsymbol{k}_f)_{\parallel},\boldsymbol{G}} \sum_{\boldsymbol{R}'_j} e^{-i\boldsymbol{k}_f\cdot\boldsymbol{R}'_j} \sum_{\boldsymbol{R}_j}\sum_{nlm} c^{\kappa}_{jnlm}(\boldsymbol{k}) \int d^3r\, \chi^*_{\boldsymbol{k}_f}(\boldsymbol{r}-\boldsymbol{R}'_j+\boldsymbol{R}_j)\, \boldsymbol{\epsilon}\cdot\nabla\Phi_{nlm}(\boldsymbol{r}). \end{aligned} \tag{6.47}$$

In the above equation the integral cannot any more be written as $\boldsymbol{\epsilon}\cdot\boldsymbol{M}_{nlm}(\boldsymbol{k}_f)$ for a single set of quantum numbers $\{nlm\}$ as in Equation 6.34. Rather, the shift $\boldsymbol{\Delta} = \boldsymbol{R}_j - \boldsymbol{R}'_j$ between the centers of the $\chi_{\boldsymbol{k}_f}$ and Φ_{nlm} requires the expansion of the integral in terms of angular momentum eigenfunctions for all quantum numbers $\{n'l'm'\}$, with so-called Shibuya-Wulfmann integrals [441, 442] $S^{\boldsymbol{R}'_j n'l'm'}_{\boldsymbol{R}_j nlm}$ as expansion coefficients,

$$\int d^3r\, \chi^*_{\boldsymbol{k}_f}(\boldsymbol{r}-\boldsymbol{R}'_j+\boldsymbol{R}_j)\, \boldsymbol{\epsilon}\cdot\nabla\Phi_{nlm}(\boldsymbol{r}) = \sum_{n'l'm'} S^{\boldsymbol{R}'_j n'l'm'}_{\boldsymbol{R}_j nlm}\, \boldsymbol{\epsilon}\cdot\boldsymbol{M}_{n'l'm'}(\boldsymbol{k}_f) \tag{6.48}$$

where $\boldsymbol{M}_{n'l'm'}$ is given by Equation 6.34. This expansion yields

$$\begin{aligned} M^{\kappa}_{\boldsymbol{k}_f\boldsymbol{k}} &\approx \frac{1}{V_0}\sum_{\boldsymbol{G}} \delta_{(\boldsymbol{k}-\boldsymbol{k}_f)_{\parallel},\boldsymbol{G}} \sum_{\boldsymbol{R}'_j} e^{-i\boldsymbol{k}_f\cdot\boldsymbol{R}'_j} \sum_{\boldsymbol{R}_j}\sum_{nlm} c^{\kappa}_{jnlm}(\boldsymbol{k}) \sum_{n'l'm'} S^{\boldsymbol{R}'_j n'l'm'}_{\boldsymbol{R}_j nlm}\, \boldsymbol{\epsilon}\cdot\boldsymbol{M}_{n'l'm'}(\boldsymbol{k}_f) \\ &= \frac{1}{V_0}\sum_{\boldsymbol{G}} \delta_{(\boldsymbol{k}-\boldsymbol{k}_f)_{\parallel},\boldsymbol{G}} \sum_{j\in\{\mathrm{A,B}\}} c^{\pm}_j(\boldsymbol{k}) \sum_{j'\in\{\mathrm{A,B}\}} \sum_{\forall j'\neq j:i'=0}^{2} e^{-i\boldsymbol{k}_f\cdot\boldsymbol{n}_{ji'}} \sum_{n'l'm'} S^{j'n'l'm'}_{j210}(\boldsymbol{n}_{ji'})\boldsymbol{\epsilon}\cdot\boldsymbol{M}_{n'l'm'}(\boldsymbol{k}_f), \end{aligned} \tag{6.49}$$

where in the second line we have adjusted the nomenclature to the case of photoemission from the π bands with band index $\kappa = \pm$ and quantum numbers $\{nlm\} = \{210\}$ of graphene with its two sublattices A and B. Note that in the case of graphene (Figure 6.6) we have to consider a non-primitive (larger) unit cell to include all nearest neighbors of the two sublattice atoms into one

unit cell. The $\boldsymbol{n}_{ji'}$ are the vectors pointing from an atom in sublattice j to nearest neighbors i' in the other sublattice. Generally, $S_{jnlm}^{jn'l'm'} = \delta_{nn'}\delta_{ll'}\delta_{mm'}$. Moreover, since both sublattices host the same C_3-symmetric C p_z orbitals, $S_{A210}^{Bn'l'm'} = S_{B210}^{An'l'm'}$ for equivalent $\boldsymbol{n}_{ji'}$. We therefore leave out the sublattice indices j, j' in the Shibuya-Wulfmann integrals, which according to Equation 78 in Reference [442] are proportional to

$$S_{210}^{n'l'm'}(\boldsymbol{n}_{i'}) \propto \sum_{N,L} \sqrt{6n'N(2l'+1)}\langle l', -m'; 1, 0|L, -m'\rangle f_{NL}(n_{i'}) Y_L^{-m'}(\boldsymbol{\Omega}_{n_{i'}}). \tag{6.50}$$

The Shibuya-Wulfmann integrals perform a basis change between C $2p_z$ orbitals centered at sublattice B to a linear combination of orbitals $\{n'l'm'\}$ centered at sublattice A and vice versa [441, 442]. The radial contributions f_{NL} decay exponentially with orbital distance, i.e., $f_{NL} \propto e^{-\frac{2Z}{a_0 n'}|\boldsymbol{n}_{i'}|/2}$ with effective nuclear charge Z and Bohr radius a_0, where $|\boldsymbol{n}_{i'}|$ in our nearest-neighbor model is equivalent to the sublattice distance $n_{i'} = 1.421$ Å, which justifies our nearest-neighbor scattering approximation.

Evaluating Equation 6.49 leads to

$$\begin{aligned} M_{\boldsymbol{k}_f\boldsymbol{k}}^{\pm} &\approx \frac{\delta_{\boldsymbol{k},\boldsymbol{k}_{f\parallel}}}{\sqrt{2}V_0}\boldsymbol{\epsilon}\cdot\Bigg[\quad (1 \pm e^{i\vartheta_k})\boldsymbol{M}_{210}(\boldsymbol{k}_f) + \textstyle\sum_{i'=0}^{2}\sum_{n'l'm'} \boldsymbol{M}_{n'l'm'}(\boldsymbol{k}_f)\cdot \\ &\qquad \cdot\left(S_{210}^{n'l'm'}(\boldsymbol{n}_{i'})e^{-i\boldsymbol{k}_f\cdot\boldsymbol{n}_{i'}} \pm e^{i\vartheta_k}S_{210}^{n'l'm'}(-\boldsymbol{n}_{i'})e^{i\boldsymbol{k}_f\cdot\boldsymbol{n}_{i'}}\right)\Bigg] \\ &= \frac{\delta_{\boldsymbol{k},\boldsymbol{k}_{f\parallel}}}{\sqrt{2}V_0}\boldsymbol{\epsilon}\cdot\Bigg[\quad (1 \pm e^{i\vartheta_k})\boldsymbol{M}_{210}(\boldsymbol{k}_f) + \textstyle\sum_{n'l'm'} S_{210}^{n'l'm'}(\boldsymbol{n}_0)\boldsymbol{M}_{n'l'm'}(\boldsymbol{k}_f)\cdot \\ &\qquad \cdot\textstyle\sum_{i'=0}^{2} e^{-i\pi\frac{2i'}{3}m'}\left(e^{-i\boldsymbol{k}_f\cdot\boldsymbol{n}_{i'}} \pm e^{i\vartheta_k}e^{-i\pi m'}e^{i\boldsymbol{k}_f\cdot\boldsymbol{n}_{i'}}\right)\Bigg], \end{aligned} \tag{6.51}$$

where we have employed $c_{\mathrm{A}}^{\pm}(\boldsymbol{k}) = \frac{1}{\sqrt{2}}$ and $c_{\mathrm{B}}^{\pm}(\boldsymbol{k}) = \pm\frac{1}{\sqrt{2}}e^{i\vartheta_k}$. In the second line we have used that the angular components $Y_L^{-m'}$ in Equation 6.50 transform as $C_\nu^{i'}Y_L^{-m'} = e^{-i2\pi/\nu i'm'}Y_L^{-m'}$ under ν-fold rotation C_ν, thus yielding $S_{210}^{n'l'm'}(\boldsymbol{n}_{i'}) = C_3^{i'}S_{210}^{n'l'm'}(\boldsymbol{n}_0) = e^{-i\pi\frac{2i'}{3}m'}S_{210}^{n'l'm'}(\boldsymbol{n}_0)$ and $S_{210}^{n'l'm'}(-\boldsymbol{n}_0) = C_2 S_{210}^{n'l'm'}(\boldsymbol{n}_0) = e^{-i\pi m'}S_{210}^{n'l'm'}(\boldsymbol{n}_0)$. Further, since the 2 p_z orbital possesses a node in the graphene x, y plane and the vectors $\boldsymbol{n}_i'$ connecting the sublattices lie within this plane, the $S_{210}^{n'l'm'}$ are necessarily zero for $l' + m' = 0 \mod 2$, i.e., for orbitals l', m' that are nonzero within the x, y plane.

For electrons to effectively scatter into channels with angular momentum l', they further must overcome the centrifugal barrier, i.e., $k_f^2 \geq l'(l'+1)/a^2$, where a is the atomic radius. With $a_{\mathrm{carbon}} \sim 0.7$ Å and $k_f^{\max} \leq 3$ Å^{-1} in the energy region where we observe scattering, we find only channels with $l' < 1.67$ to significantly contribute to this process. The lowest orbital

order contributions thus results from $l' = 1$ and $m' = 0$, and we find

$$\begin{aligned}
M^{\pm}_{\boldsymbol{k}_f \boldsymbol{k}} &\approx \frac{\delta_{\boldsymbol{k},\boldsymbol{k}_{f\parallel}}}{\sqrt{2}V_0}\boldsymbol{\epsilon}\cdot\left[(1\pm e^{i\vartheta_k})\boldsymbol{M}_{210}(\boldsymbol{k}_f) + \sum_{n'} S^{n'10}_{210}(\boldsymbol{n}_0)\boldsymbol{M}_{n'10}(\boldsymbol{k}_f)\sum_{i'=0}^{2}\left(e^{-i\boldsymbol{k}_f\cdot\boldsymbol{n}_{i'}} \pm e^{i\vartheta_k}e^{i\boldsymbol{k}_f\cdot\boldsymbol{n}_{i'}}\right)\right] \\
&= \frac{\delta_{\boldsymbol{k},\boldsymbol{k}_{f\parallel}}}{\sqrt{2}V_0}\boldsymbol{\epsilon}\cdot\left[(1\pm e^{i\vartheta_k})\boldsymbol{M}_{210}(\boldsymbol{k}_f) + \left(h^*(\boldsymbol{k}_{f\parallel}) \pm e^{i\vartheta_k}h(\boldsymbol{k}_{f\parallel})\right)\sum_{n'} S^{n'10}_{210}(\boldsymbol{n}_0)\boldsymbol{M}_{n'10}(\boldsymbol{k}_f)\right] \\
&= \frac{\delta_{\boldsymbol{k},\boldsymbol{k}_{f\parallel}}}{\sqrt{2}V_0}\boldsymbol{\epsilon}\cdot\left[(1\pm e^{i\vartheta_k})\boldsymbol{M}_{210}(\boldsymbol{k}_f) + \left(e^{-i\vartheta_{\boldsymbol{k}_{f\parallel}}} \pm e^{i\vartheta_k}e^{i\vartheta_{\boldsymbol{k}_{f\parallel}}}\right)|h^*(\boldsymbol{k}_{f\parallel})|\sum_{n'} S^{n'10}_{210}(\boldsymbol{n}_0)\boldsymbol{M}_{n'10}(\boldsymbol{k}_f)\right] \\
&= \frac{\delta_{\boldsymbol{k},\boldsymbol{k}_{f\parallel}}}{\sqrt{2}V_0}\boldsymbol{\epsilon}\cdot\boldsymbol{M}_{210}(\boldsymbol{k}_f)\left[(1\pm e^{i\vartheta_k}) + \left(e^{-i\vartheta_{\boldsymbol{k}_{f\parallel}}} \pm e^{i\vartheta_k}e^{i\vartheta_{\boldsymbol{k}_{f\parallel}}}\right)u(\boldsymbol{k}_f)\right] \\
&= \frac{1}{\sqrt{2}V_0}\underbrace{\boldsymbol{\epsilon}\cdot\boldsymbol{M}_{210}(\boldsymbol{k}_f)}_{\text{dipole selection}}\left[\underbrace{(1\pm e^{i\vartheta_{\boldsymbol{k}_{f\parallel}}})}_{\text{horseshoe}} + \underbrace{\left(e^{-i\vartheta_{\boldsymbol{k}_{f\parallel}}} \pm e^{i2\vartheta_{\boldsymbol{k}_{f\parallel}}}\right)u(\boldsymbol{k}_f)}_{\text{NN scattering}}\right].
\end{aligned} \tag{6.52}$$

Here we absorbed the last sum into a complex function $u(\boldsymbol{k}_f)$ that essentially describes the overlap between initial-state $2p_z$ orbitals and scattered Coulomb waves on neighboring sites. $u(\boldsymbol{k}_f)$ varies only slowly on the photoemission hemisphere Ω_{k_f} if compared to $h(\boldsymbol{k}_f)$ and thus for a given photoelectron momentum $k_f = \sqrt{2mE_{\text{kin}}/\hbar^2}$ can be approximated as a merely kinetic-energy-dependent fit parameter that is constant across the horseshoe: $u(\boldsymbol{k}_f) \sim |u(k_f)|e^{i\arg u(k_f)}$.

The first term in the square brackets of this expression represents the structure factor producing a photoemission intensity that is proportional to $|\frac{1}{\sqrt{2}}(1\pm e^{i\vartheta_k})|^2 = 1 \pm \cos\vartheta_k$ and gives rise to the ubiquitous horseshoe pattern, reflecting the interference of the initial state Bloch wave residing at the graphene sublattices A and B. The second term represents nearest-neighbor scattering in the final state, essentially dictated by $(e^{-i\vartheta_{\boldsymbol{k}_{f\parallel}}} \pm e^{i\vartheta_k}e^{i\vartheta_{\boldsymbol{k}_{f\parallel}}})$ that reflects the structural interference between initial *and* final state wave functions. We note that nearest-neighbor final-state scattering now introduces interference terms between $\boldsymbol{M}_{210}(\boldsymbol{k}_f)$ and $\boldsymbol{M}_{n'10}(\boldsymbol{k}_f)$, and circular dichroism hence does not vanish any longer.

Chapter 7

Photoemission Orbital Tomography for Excitons in Organic Molecules

PHYSICAL REVIEW B **108**, 085132 (2023)

Photoemission orbital tomography for excitons in organic molecules

C. S. Kern, A. Windischbacher, and P. Puschnig*
Institute of Physics, NAWI Graz, University of Graz, 8010 Graz, Austria

Figure 7.1: **Header of the article as published in *PRB* [443].**

Significance Statement

POT is a very successful technique in which momentum space signatures from photoemission experiments can be brought into relation with theoretical quantum mechanical wave functions and thereby allows a precise characterization of, for instance, ordered organic molecules on surfaces. In recent years, the experimental scope has been enlarged to the time domain by so-called *pump-probe* photoemission spectroscopy. Here, systems are excited by an optical pulse and, subsequently, those excited states can be probed by a second pulse. For excitations below the band-gap of non-metallic systems, bound electron-hole pairs—the excitons—form, which are not described by POT due to their entangled character.

In this work, we tackled this problem by a many-body formulation of the photoemission matrix element in terms of Dyson orbitals. In this way, we could incorporate exciton wave functions in a second quantization formalism and found that the photoemission from an exciton can indeed be integrated into the formalism of POT. The resulting equation suggests that the hole contribution of an exciton fixes the measured kinetic energy of the photoelectron. At each allowed kinetic energy, the momentum distribution can be simulated by respecting the entangled character of the exciton. To further validate our derivation, we also simulated the photoemission from excitons by a TDDFT approach, which naturally allows for pump-probe setups and where no assumptions on the final state need to be made. We found very good

agreement for the two approaches and discussed the implications of the method for generic exciton structures on the examples of three organic molecules in the gas-phase.

Author Contributions

Following an initial idea for this work that emerged in discussions between Andreas Windischbacher, Peter Puschnig and me, real-time TDDFT calculations executed by myself could confirm the theoretical model. Subsequently, I wrote the code to simulate exciton photoemission from Casida calculations, with the help of Andreas Windischbacher, who wrote a similar code for the analysis of results from the Bethe-Salpeter Equation, which, however, were not used in the final paper for consistency reasons. The manuscript of the paper was drafted by myself, with significant contributions from Andreas Windischbacher and Peter Puschnig.

Abstract

Driven by recent developments in time-resolved photoemission spectroscopy, we extend the successful method of photoemission orbital tomography (POT) to excitons. Our theory retains the intuitive orbital picture of POT, while respecting both the entangled character of the exciton wave function and the energy conservation in the photoemission process. Analyzing results from three organic molecules, we classify generic exciton structures and give a simple interpretation in terms of natural transition orbitals. We validate our findings by directly simulating pump-probe experiments with time-dependent density functional theory.

7.1 Introduction

In the past decade, photoemission orbital tomography (POT) [46, 406, 407, 405, 401, 48] has emerged as a powerful technique that relates the measured photoemission angular distribution (PAD) from oriented films of organic molecules with the orbitals from which the electron has been emitted. This direct connection arises from modeling photoelectrons by plane waves. While this plane wave assumption has been debated [79, 80] and, in fact, demonstrated to be insufficient in certain circumstances [81, 82], POT has led to valuable insights, for instance, into the hybridization between organic layers and the substrate [50, 51, 52], the geometry of adsorbate layers [47, 48, 49], the nature of reaction products [53] or real space images of orbitals [**?**, 55, 56, 57, 58]. Particularly the latter aspect has also stimulated discussions on how to build a formal bridge between quantum mechanical wave functions and the experimentally observed momentum space distributions [246, 98].

Despite these numerous achievements, until very recently, POT could only be applied to study occupied molecular orbitals by photoexciting electrons from the ground state. With the advent of laser high-harmonic generation and free-electron lasers, it has become possible to study also the dynamics of excited states in time- and angle-resolved photoemission spectroscopy (trARPES) experiments. On the one hand, band structure movies of crystalline solids have shown the temporal evolution of the electron system over the complete Brillouin zone [444, 445, 446]. On the other hand, for molecular systems, optically excited states, involving transitions from HOMO to LUMO, have recently been observed with trARPES on their intrinsic temporal and spatial scales [262, 447, 448]. In more complex systems however, the simple HOMO-LUMO picture breaks down and excitons may involve multiple transitions as, for instance, observed in van der Waals heterostructures [449, 450, 451, 452, 453, 454, 455] and

defects therein [456, 457, 458]. In organic semiconductor crystals, the multi-orbital nature of excitons is crucial [459] and also relevant for understanding singlet fission [448]. Thus, an exciton must be generally treated as an entangled state composed of multiple electron-hole transitions for which a theoretical foundation of POT is still lacking.

The aim of this work is to fill this gap and establish a consistent framework that allows us to interpret measured PAD maps from excitons. Specifically, we assume that the exciton wave function is represented in a product basis of valence and conduction states, as typically done when solving the electron-hole Bethe-Salpeter equation (BSE) [261] or Casida's equation in time-dependent density functional theory (TDDFT) [174, 215]. Expanding the concept of Dyson orbitals [244, 98, 245] to excited states, we arrive at the result that the PAD can be interpreted as the Fourier-transformed coherent sum of the electronic part of the exciton wave function. These relations, as well as the unexpected consequences of the photohole's state for the measured kinetic energy spectrum, are illustrated for generic cases of exciton compositions in a series of organic molecules in the gas phase. We further show how exciton photoemission can be interpreted in terms of the established concept of natural transition orbitals (NTOs)s [218] and, underpinning our findings, the PAD is also simulated directly by means of a TDDFT approach where no assumptions on the final state are made whatsoever.

7.2 Theory

Bound electron-hole pairs, excitons, are the fundamental optical excitations for energies below the band gap in molecules and non-metallic solids. For such correlated electron-hole pairs, we assume that the wave function of the m-th exciton, with excitation energy Ω_m, can be expanded in the single-particle electron $\{\chi_c(\boldsymbol{r}_e)\}$ and hole basis $\{\phi_v(\boldsymbol{r}_h)\}$ as

$$\psi_m(\boldsymbol{r}_h, \boldsymbol{r}_e) = \sum_{v,c} X_{vc}^{(m)} \phi_v^*(\boldsymbol{r}_h)\chi_c(\boldsymbol{r}_e). \tag{7.1}$$

Here, the sum runs over all pairs of valence and conduction states $\{v, c\}$, respectively, and $X_{vc}^{(m)}$ is the transition density matrix that describes the character of the exciton. Note that here and in the following derivations, we use the Tamm-Dancoff approximation [460] for better readability. In the general case and in our calculations, however, we also consider de-excitations.

7.2.1 Photoemission from Excitons

Our goal is to find a consistent expression that connects the exciton wave function as defined in Equation 7.1 with measured photoemission momentum maps. In the spirit of POT, we describe the photoelectron probability with Fermi's golden rule as the transition from an initial N-particle state Ψ_i^N to a final state Ψ_f^N, triggered by the photon field $\boldsymbol{A}$ with energy ω. We couple this classical field to the electrons' momenta $\boldsymbol{P}$ in the dipole approximation and use the Coulomb gauge as well as Hartree atomic units unless stated otherwise. Denoting the energy of the states Ψ_i^N and Ψ_f^N with E_i and E_f respectively, the photoelectron probability is

$$W_{\mathrm{i}\to\mathrm{f}} = 2\pi \left| \left\langle \Psi_\mathrm{f}^N \middle| \boldsymbol{A}\boldsymbol{P} \middle| \Psi_\mathrm{i}^N \right\rangle \right|^2 \delta\left(\omega + E_\mathrm{i} - E_\mathrm{f}\right). \tag{7.2}$$

In contrast to earlier work on photoemission from the electronic ground state $\Psi_{\mathrm{i},0}^N$, now the initial state is given by the the m-th exciton which can also be expressed in a second quantization formulation as

$$\left| \Psi_{\mathrm{i},m}^N \right\rangle = \sum_{v,c} X_{vc}^{(m)} a_c^\dagger a_v \left| \Psi_{\mathrm{i},0}^N \right\rangle. \tag{7.3}$$

Here, a_v and $a_c^\dagger$ create a hole and an electron in state v and c, respectively. Its energy $E_{\mathrm{i},m}^N$ is the sum of the ground state energy $E_{\mathrm{i},0}^N$ and the excitation energy Ω_m.

For the final state Ψ_f^N, one commonly assumes the sudden approximation, in which the correlation between the emitted electron $\gamma_{\boldsymbol{k}}$ and the remaining system can be neglected [44], and Ψ_f^N can be written as the anti-symmetrized product of the $(N-1)$ electron state $\Psi_{\mathrm{f},j}^{N-1}$ and the photoemitted electron with momentum $\boldsymbol{k}$ in state $\gamma_{\boldsymbol{k}}$:

$$\Psi_{\mathrm{f},j,\boldsymbol{k}}^N = \mathcal{A}\Psi_{\mathrm{f},j}^{N-1}\gamma_{\boldsymbol{k}}. \tag{7.4}$$

Like the initial state, $\Psi_{\mathrm{f},j}^{N-1}$ may be expressed in Fock space, i.e. as the N-electron ground state from which the j-th electron has been removed:

$$\left|\Psi_{\mathrm{f},j}^{N-1}\right\rangle = a_j \left|\Psi_{\mathrm{i},0}^N\right\rangle. \tag{7.5}$$

Under these assumptions, we can identify the total energy of this final state as the sum of $E_{\mathrm{f},j}^{N-1}$ and the photoelectron's kinetic energy, $E_\mathrm{kin} = k^2/2$. The energy conservation from Equation 7.2 then demands

$$E_\mathrm{kin} = \omega - (E_{\mathrm{f},j}^{N-1} - E_{\mathrm{i},0}^N) + \Omega_m = \omega - \varepsilon_j + \Omega_m, \tag{7.6}$$

where we have introduced the j-th ionization potential ε_j as the energy difference between the j-th excited state of the $(N-1)$-electron system and the N electron ground state. In taking the overlap between the two wave functions for the N-electron and the $(N-1)$-electron system, we utilize the Dyson orbital for electron detachment $D_{j,m}$, in the usual way [244, 263, 98], with the only modification that in our case the Dyson amplitudes have to be spanned over both the basis sets $\{\varphi_{v'}\}$ and $\{\chi_{c'}\}$:

$$\begin{aligned} D_{j,m}(\mathbf{r}) = &\sum_{v'} \left\langle \Psi_{\mathrm{i},m}^N \middle| a_{v'}^\dagger \middle| \Psi_{\mathrm{f},j}^{N-1} \right\rangle \phi_{v'}(\mathbf{r}) + \\ &+ \sum_{c'} \left\langle \Psi_{\mathrm{i},m}^N \middle| a_{c'}^\dagger \middle| \Psi_{\mathrm{f},j}^{N-1} \right\rangle \chi_{c'}(\mathbf{r}). \end{aligned} \tag{7.7}$$

It is accepted that Dyson orbitals represent the most appropriate way to describe photoemission in a single-orbital picture [263, 243, 280, 246, 98], however, their computation from correlated wave functions in a multi-reference framework [247, 248] is often not feasible. Therefore, and with weakly-correlated systems in mind, we approximate $\Psi_{\mathrm{i},0}^N$ by a single Slater determinant. Inserting the N-electron wave function, Equation 7.3, and the $(N-1)$-electron wave function, Equation 7.5, into the expression for the Dyson orbital, we get

$$\begin{aligned} D_{j,m}(\mathbf{r}) = &\sum_{v'}\sum_{v,c} X_{vc}^{(m)} \left\langle \Psi_{\mathrm{i},0}^N \middle| a_v^\dagger a_c a_{v'}^\dagger a_j \middle| \Psi_{\mathrm{i},0}^N \right\rangle \phi_{v'}(\mathbf{r}) + \\ &+ \sum_{c'}\sum_{v,c} X_{vc}^{(m)} \left\langle \Psi_{\mathrm{i},0}^N \middle| a_v^\dagger a_c a_{c'}^\dagger a_j \middle| \Psi_{\mathrm{i},0}^N \right\rangle \chi_{c'}(\mathbf{r}), \end{aligned} \tag{7.8}$$

where all integrals in the sum over v' vanish due to orthogonality. In the sum over c', we get no contributions for $c \neq c'$ by the same argument and thus arrive at our final result for the j-th

Dyson orbital (up to normalization constants):

$$\begin{aligned} D_{j,m}(\mathbf{r}) &= \sum_{v,c} X_{vc}^{(m)} \left\langle \Psi_{\mathrm{i},0}^{N} \middle| a_v^\dagger a_c a_c^\dagger a_j \middle| \Psi_{\mathrm{i},0}^{N} \right\rangle \chi_c(\mathbf{r}) = \\ &= \sum_{c} X_{jc}^{(m)} \left\langle \Psi_{\mathrm{i},0}^{N} \middle| a_j^\dagger a_j a_c a_c^\dagger \middle| \Psi_{\mathrm{i},0}^{N} \right\rangle \chi_c(\mathbf{r}) = \\ &= \sum_{c} X_{jc}^{(m)} \chi_c(\mathbf{r}). \end{aligned} \tag{7.9}$$

Note that exploiting the orthogonality relations between many-body wave functions in different states is possible here, since $\Psi_{\mathrm{i},0}^{N}$ is represented by a single Slater determinant only. However, we remark that the above derivation could be extended to multi-configuration methods, albeit at the expense of an additional summation over configuration space in Equation 7.9.

With the help of the Dyson orbitals, we can avoid the explicit treatment of the $N-1$ passive electrons in the process and thereby reduce the matrix element of Equation 7.2 to an integral over a single coordinate only:

$$\begin{aligned} \left\langle \Psi_{\mathrm{f},j}^{N} \middle| \boldsymbol{AP} \middle| \Psi_{\mathrm{i},m}^{N} \right\rangle &\approx \boldsymbol{A} \int \mathrm{d}^3 r \, \overline{\gamma}_{\boldsymbol{k}}(\boldsymbol{r}) \, \boldsymbol{p} \, D_{j,m}(\boldsymbol{r}) \\ &\propto (\boldsymbol{Ak}) \, \mathcal{F}\left[D_{j,m}\right](\boldsymbol{k}). \end{aligned} \tag{7.10}$$

In the second line, we make use of the plane wave approximation, $\gamma_{\boldsymbol{k}}(\boldsymbol{r}) \propto \mathrm{e}^{\mathrm{i}\boldsymbol{kr}}$, that is inherent to POT [46, 401] and that naturally introduces the Fourier transform of the Dyson orbital, modulated by a weakly angle-dependent polarization factor $\boldsymbol{Ak}$. Importantly, only the j-th row of the transition density matrix $X_{vc}^{(m)}$ contributes to the j-th Dyson orbital in Equation 7.9, thereby fixing the hole position in the orbital ϕ_j. Finally, the photoemission angular distribution arising from the m-th exciton is obtained by summing over all possible final state hole configurations as follows

$$\begin{aligned} I_m(\boldsymbol{k}) &\propto |\boldsymbol{Ak}|^2 \sum_j \left| \sum_c X_{jc}^{(m)} \mathcal{F}\left[\chi_c\right](\boldsymbol{k}) \right|^2 \\ &\times \delta\left(\omega - E_{\mathrm{kin}} - \varepsilon_j + \Omega_m\right). \end{aligned} \tag{7.11}$$

From this expression, which we refer to as "exPOT" (exciton POT) in the remainder of this work, we expect the photoemission signal from a general exciton to have contributions at multiple kinetic energies that are in concordance with the energy conservation and thus depend on the hole's position after electron detachment described by the ionization energy ε_j. At each allowed kinetic energy, momentum maps take the form of a Fourier transform of the *coherent* sum over unoccupied states, weighted by the corresponding transition density matrix elements.

7.2.2 Formulation with Natural Transition Orbitals

While the orbitals χ_c and the transition density matrix X_{vc} appearing in the photoemission intensity expression for exPOT (Equation 7.11) can be readily computed from a BSE or Casida calculation, physical intuition about the character of the exciton can be enhanced by introducing *natural transition orbitals* (NTOs) [218, 98].

Let us assume that in the exciton calculation there are N_v occupied orbitals ϕ_v, and a number of N_c unoccupied (or virtual) orbitals χ_c. Then, the transition density matrix X_{vc} is a matrix with

N_v rows and N_c columns, whose singular value decomposition can be written in the following way

$$X = V \Lambda C^T. \tag{7.12}$$

Here, V and C are quadratic matrices of sizes $N_v \times N_v$ and $N_c \times N_c$, respectively, and the rectangular $(N_v \times N_c)$-matrix Λ has only non-vanishing elements $\lambda_1, \lambda_2, \ldots \lambda_{N_v}$ in the diagonal. These singular values are ordered according to their magnitude, thus $\lambda_1 > \lambda_2 > \cdots > \lambda_{N_v}$, and fulfill the normalization condition

$$\sum_{i=1}^{N_v} \lambda_i^2 = 1. \tag{7.13}$$

Note that we have assumed that $N_v < N_c$ as is typically the case in the calculation of optically excited states. By making use of the transformations

$$\widetilde{\phi}_\lambda = \sum_{v=1}^{N_v} V_{\lambda v}^T \phi_v \tag{7.14}$$

$$\widetilde{\chi}_\lambda = \sum_{c=1}^{N_c} C_{\lambda c}^T \chi_c, \tag{7.15}$$

we obtain a new set of orbitals, the NTOs $\widetilde{\phi}_\lambda$ and $\widetilde{\chi}_\lambda$, respectively, which can be used to express the exciton wave function in the electron-hole-basis (Equation 7.1):

$$\psi(\boldsymbol{r}_h, \boldsymbol{r}_e) = \sum_{\lambda=1}^{N_v} \Lambda_\lambda \widetilde{\phi}_\lambda^*(\boldsymbol{r}_h) \widetilde{\chi}_\lambda(\boldsymbol{r}_e). \tag{7.16}$$

Inserting Equation 7.12 into Equation 7.11—and by making use of the fact that the Fourier transform $\mathcal{F}$ is a linear operator—we can rewrite the exPOT formula for the photoemission intensity in the NTO basis as follows:

$$\begin{aligned} I_m(\boldsymbol{k}) &\propto |A\boldsymbol{k}|^2 \sum_j \left| \sum_\lambda V_{j\lambda} \Lambda_\lambda \mathcal{F}\left[\widetilde{\chi}_\lambda\right](\boldsymbol{k}) \right|^2 \\ &\times \delta\left(\omega + E_{\text{kin}} - \varepsilon_j + \Omega_m\right). \end{aligned} \tag{7.17}$$

At first sight, it seems that we have not gained much: we have just replaced the summation over c with the summation over λ and replaced the prefactors. In practice, however, a given exciton is often characterized by just a few NTOs and one can easily control the accuracy of the exciton's representation in terms of NTOs by introducing a threshold for the Λ_λ. Moreover, it is our believe that NTOs are useful when dealing with excitons, since the character of the transition is encoded in just a few single-particle orbitals and with introducing Equation 7.17, we can assign physical meaning to these orbitals as actual observables of the excited-state photoemission experiment.

7.2.3 Generic Exciton Structures

Before presenting our numerical results, we explain the implications of Equation 7.11 on the example of four prototypical exciton structures that are collected in Table 7.1 and schematically depicted in Figure 7.2. For educational reasons, here only $N_v = 2$ occupied and $N_c = 2$ unoccupied orbitals are taken into account for setting up the transition density matrix such that all matrices are simple 2×2 matrices.

Table 7.1: Transition density matrices X_{vc} as well as their singular value decompositions $X = V\Lambda C^T$ for the four simple exciton structures defined in Figure 7.2. Additionally, the exciton wave functions ψ are given in terms of the NTOs $\widetilde{\phi}$ and $\widetilde{\chi}$, respectively.

	Case (i)	Case (ii)	Case (iii)	Case (iv)
$X =$	$\begin{pmatrix} 1 & 0 \\ 0 & 0 \end{pmatrix}$	$\begin{pmatrix} 0 & \frac{1}{\sqrt{2}} \\ \frac{1}{\sqrt{2}} & 0 \end{pmatrix}$	$\begin{pmatrix} \frac{1}{\sqrt{2}} & 0 \\ \frac{1}{\sqrt{2}} & 0 \end{pmatrix}$	$\begin{pmatrix} \frac{1}{\sqrt{2}} & \frac{1}{\sqrt{2}} \\ 0 & 0 \end{pmatrix}$
$\Lambda =$	$\begin{pmatrix} 1 & 0 \\ 0 & 0 \end{pmatrix}$	$\begin{pmatrix} \frac{1}{\sqrt{2}} & 0 \\ 0 & \frac{1}{\sqrt{2}} \end{pmatrix}$	$\begin{pmatrix} 1 & 0 \\ 0 & 0 \end{pmatrix}$	$\begin{pmatrix} 1 & 0 \\ 0 & 0 \end{pmatrix}$
$V =$	$\begin{pmatrix} 1 & 0 \\ 0 & 1 \end{pmatrix}$	$\begin{pmatrix} 0 & 1 \\ 1 & 0 \end{pmatrix}$	$\begin{pmatrix} \frac{1}{\sqrt{2}} & -\frac{1}{\sqrt{2}} \\ \frac{1}{\sqrt{2}} & \frac{1}{\sqrt{2}} \end{pmatrix}$	$\begin{pmatrix} 1 & 0 \\ 0 & 1 \end{pmatrix}$
$C =$	$\begin{pmatrix} 1 & 0 \\ 0 & 1 \end{pmatrix}$	$\begin{pmatrix} 1 & 0 \\ 0 & 1 \end{pmatrix}$	$\begin{pmatrix} 1 & 0 \\ 0 & 1 \end{pmatrix}$	$\begin{pmatrix} \frac{1}{\sqrt{2}} & -\frac{1}{\sqrt{2}} \\ \frac{1}{\sqrt{2}} & \frac{1}{\sqrt{2}} \end{pmatrix}$
$\psi =$	$\widetilde{\phi}_1\widetilde{\chi}_1$	$\frac{1}{\sqrt{2}}\widetilde{\phi}_1\widetilde{\chi}_1 + \frac{1}{\sqrt{2}}\widetilde{\phi}_2\widetilde{\chi}_2$	$\widetilde{\phi}_1\widetilde{\chi}_1$	$\widetilde{\phi}_1\widetilde{\chi}_1$
$\widetilde{\phi}_1 =$	ϕ_1	ϕ_2	$\frac{1}{\sqrt{2}}(\phi_1 + \phi_2)$	ϕ_1
$\widetilde{\phi}_2 =$	—	ϕ_1	—	—
$\widetilde{\chi}_1 =$	χ_1	χ_1	χ_1	$\frac{1}{\sqrt{2}}(\chi_1 + \chi_2)$
$\widetilde{\chi}_2 =$	—	χ_2	—	—

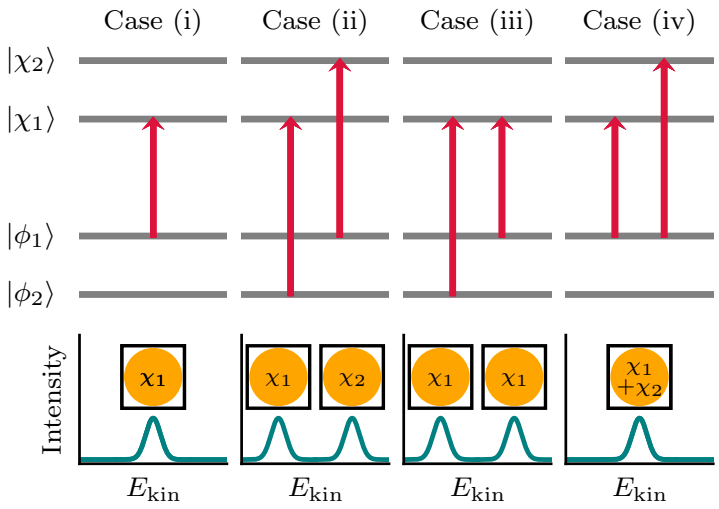

Figure 7.2: Four prototypical exciton structures and the corresponding predictions of exPOT for the observed PAD maps as detailed in the text.

In case (i), the exciton involves only a single transition from the highest occupied orbital ϕ_1 to the lowest unoccupied orbital χ_1, which is, in fact, a common case for the lowest exciton in some organic molecules [262]. Evidently, exPOT predicts that the observed PAD is given by the Fourier transform of χ_1 appearing at the kinetic energy $E_{\mathrm{kin}} = \omega - \varepsilon_1 + \Omega_1$, where ω is the probe photon energy, ε_1 the ionization potential corresponding to ϕ_1, and Ω_1 denotes the exciton energy, i.e. the pump photon energy. This is also illustrated in the bottom part of Figure 7.2, where the the square above the peak in the sketched kinetic energy spectrum should represent the expected PAD map of χ_1. Also note that the NTOs coincide with the original orbitals in this case. For case (ii), we assume the exciton wave function as $\psi = \frac{1}{\sqrt{2}}(\phi_2\chi_1 + \phi_1\chi_2)$. Here, Equation 7.11 leads to PAD maps of both χ_1 and χ_2, however, appearing at kinetic energies corresponding to the ionization levels of ϕ_2 and ϕ_1, respectively, as also illustrated in Figure 7.2. Note that this exciton represents a truly entangled state [461] which can also be seen after transforming to the NTO basis (see Table 7.1). The situation is somewhat different for case (iii), where we assume $\psi = \frac{1}{\sqrt{2}}(\phi_2\chi_1 + \phi_1\chi_1)$. Here, we expect to observe two identical PADs appearing at two different kinetic energies, depending on whether, after the electron has been emitted, the hole resides in state ϕ_1 or ϕ_2. While the unoccupied NTO $\widetilde{\chi}_1$ equals χ_1, the two occupied orbitals can now be represented by a single NTO. Finally in case (iv), the exciton is described by $\psi = \frac{1}{\sqrt{2}}(\phi_1\chi_1 + \phi_1\chi_2)$ and Equation 7.11 suggests that the PAD is proportional to the Fourier transform of a *coherent* sum of the unoccupied orbitals χ_1 and χ_2, the NTO $\widetilde{\chi}_1$, which appears at $E_{\mathrm{kin}} = \omega - \varepsilon_1 + \Omega_1$. In the following, we want to give examples for the non-trivial cases (ii)–(iv) by actual numerical simulations.

7.3 Results and Discussion

Let us now compare the predictions of our exPOT approach for organic molecules with computationally more demanding, but accurate TDDFT calculations as implemented in the real-space code OCTOPUS [176, 177]. Here, photoemission spectra and PAD maps are obtained by recording the flux of photoelectron density through a detector surface (t-SURFF) [85, 86], which seamlessly allows for pump-probe setups and where no assumptions on the final state need to be made.

For a better comparability of the two theoretical approaches, exPOT vs. t-SURFF, we take several precautions. First, we focus on planar molecules for which the plane wave approximation has already been well tested [54, 48]. Second, we choose the probe field in z-direction, that is perpendicular to the molecular plane, which is also known to minimize possible deficiencies of the PWA [81]. Third, we ensure that pump pulses are long enough to only excite the specific exciton in question, since for ultrashort pulses considerable energy broadening needs to be taken into account [462, 463]. Equivalently, we keep our probe pulses long enough for a resonable kinetic energy resolution in the spectra and choose probe energies in the XUV regime for the sake of the sudden approximation [464]. Fourth, we limit ourselves to the adiabatic local density approximation (ALDA) since more advanced functionals, such as hybrids, would be computationally too demanding for the real-time propagation utilized for the t-SURFF method. We emphasize, however, that for the application of our exPOT formalism, the latter restriction is not necessary and any method for excited states that provides a transition density matrix in terms of single-particle orbitals can be used.

With the aim to find real-life examples for the cases (ii)–(iv) outlined above, we have selected three prototypical π-conjugated molecules, namely tetracyanoquinodimethane (TCNQ), porphine and perylenetetracarboxylic dianhydride (PTCDA), and perform linear-response TDDFT calculations within the Casida formalism in OCTOPUS. The details of those calulations are described in Paragraph 7.5.1. For TCNQ, the solution reveals an exciton with $\Omega_m = 6.76$ eV which is strongly allowed for y-polarization (molecular geometry and choice of axis are depicted in Paragraph 7.5.1). Its exciton wave function has major contributions from $\phi_3\chi_2$ (0.44), $\phi_2\chi_3$ (0.35) and $\phi_1\chi_6$ (0.07) (see Table 7.2 for more details). Thus it represents an entangled state as in case (ii). In the t-SURFF calculations, we set the pump energy $\omega_{\text{pump}} = \Omega_m$ and employ a probe energy of $\omega = 35$ eV (details in Paragraph 7.5.2). The resulting kinetic energy spectrum of the emitted electrons is depicted in panel (a) of Figure 7.3. It is dominated by emissions from the three highest occupied orbitals ϕ_1, ϕ_2 and ϕ_3 indicated by the green, orange and blue dashed vertical lines, respectively. Importantly, however, we also observe three emission peaks at kinetic energies larger by precisely ω_{pump}. This behavior, already qualitatively illustrated in the second column of Figure 7.2, is in perfect accordance with the energy conservation of Equation 7.11. Despite the orders of magnitude smaller peak heights for the exciton emission, we obtain three distinct PAD maps (at the kinetic energies marked by vertical full lines), which are displayed in panel (b). Comparing with our exPOT theory, indeed, the Fourier transforms of the first three NTOs of this entangled exciton, as depicted in panel (c), are in very good agreement with the PAD maps from t-SURFF.

Next, we present our results for the optical excitation in porphin at $\Omega_m = 3.94$ eV in x-direction, which serves as an example for case (iii) defined in Figure 7.2. From the t-SURFF calculation, we obtain two identical momentum maps at the kinetic energies corresponding to the hole in state ϕ_1 and ϕ_4 (left and middle column of panel (a) in Figure 7.4). Note that here, in contrast to the above PADs from TCNQ, we have projected the t-SURFF ARPES intensities on the respective ground-state orbitals, since the total photoelectron yield is also affected by other contributions which are not relevant for our case (see also Paragraph 7.5.2). The Casida

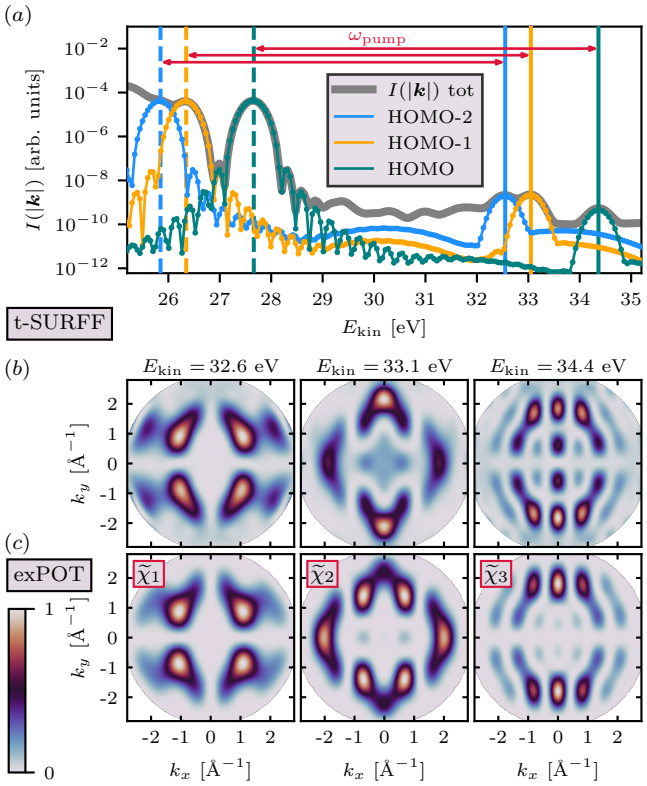

Figure 7.3: **Comparison of exPOT with results from t-SURFF for TCNQ.** (a) total angle-integrated photoelectron intensity from t-SURFF (grey) and its projection onto the HOMO (v=1, green), HOMO-1 (v=2, orange) and HOMO-2 (v=3, blue) states, with corresponding kinetic energy positions $\omega - \varepsilon_j$ indicated by the vertical dashed lines in the same colors. Red arrows mark the energy of the pump pulse ω_{pump}, full vertical lines $\omega - \varepsilon_j + \omega_{\mathrm{pump}}$ respectively. (b) PAD maps from t-SURFF at the kinetic energies indicated by the full vertical lines in panel (a). (c) PAD maps obtained from the exPOT approach with the first three NTOs.

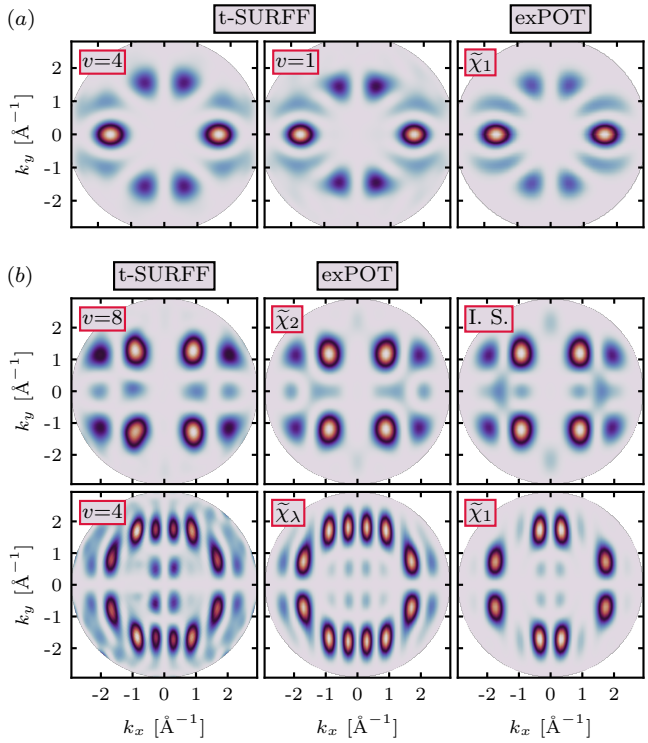

Figure 7.4: **Comparison of exPOT with results from t-SURFF for porphin and PTCDA.** (a) PADs for porphin from t-SURFF at different kinetic energies (left and middle column) compared to the exPOT map of the first NTO (right column). (b) Different methods for PTCDA, showing contributions from $v = 4$ (top row) and $v = 8$ (bottom row), see text for details.

calculation leads to almost equal contributions of $\phi_1\chi_2$ (0.27) and $\phi_4\chi_2$ (0.25) to the exciton wave function, which can be written as a single NTO $\widetilde{\chi}_1$ (see Table 7.2), resulting in the PAD depicted in the rightmost column of panel (a) in Figure 7.4. The excellent agreement with the corresponding t-SURFF maps further validates the exPOT predictions. Remarkably, while a single NTO might be enough to explain photoemission from an excited state of such character, it can be comprised of contributions from different valance states, which then lead to photoemission signatures of the same conduction state at different kinetic energies.

Conversely, in case (iv), we consider an exciton structure with transitions involving only a single hole state v but multiple conduction states c. For PTCDA at an excitation energy of $\Omega_m = 4.45$ eV (polarized in y-direction), we encounter even two such transitions: $\phi_8\chi_4$ (0.29), $\phi_8\chi_3$ (0.03) and $\phi_4\chi_8$ (0.06), $\phi_4\chi_2$ (0.06). The top row of panel (b) of Figure 7.4 is devoted to the contribution from $v = 8$, with the state-projected result from t-SURFF in the left column agreeing very well with the exPOT result in the middle column, evaluated with the contribution from $\widetilde{\chi}_2$ only. Importantly, the computation of the latter implicitly involves a *coherent* sum over the unoccupied states χ_4 and χ_3, while wrongly performing an *incoherent* summation worsens the agreement for with the t-SURFF reference (see right panel labeled I. S.). The second major set of contributions to this exciton, $\phi_4\chi_8$ and $\phi_4\chi_2$, leads to a PAD at the kinetic energy corresponding to ε_4 and is shown in the bottom row of Figure 7.4, panel (b). Again, the t-SURRF result (left

column) agrees well with exPOT (middle column). This time however, we need to take into account a sum over multiple NTOs ($\widetilde{\chi}_\lambda$) while the PAD from a single NTO ($\widetilde{\chi}_1$, right column) is not sufficiently accurate. This is due to the fact that, in general, the electron or hole contributions can contribute to different NTOs and only the coherent sum over λ is equivalent to the coherent sum of Equation 7.11 (see also comparison of PADs in Paragraph 7.5.3). In summary, we have not only proven excellent agreement of the exPOT theory with *ab-initio* simulations for case (iv), but could also emphasize the necessity of the *coherent* superposition of the electron orbitals for such a case.

7.4 Conclusions

We demonstrate an extension of photoemission orbital tomography to excitons, termed exPOT, and thereby provide the theoretical foundations to interpret photoemission angular distributions maps as measured in pump-probe ARPES experiments of oriented organic molecules in terms of exciton wave functions. We illustrate the consequences of exPOT on the example of three organic molecules, covering a range of prototypical exciton structures, and validate our findings by real-time TDDFT calculations that directly incorporate the pump and probe fields. In our method, the simplicity of the orbital interpretation can be retained by identifying Fourier-transformed NTOs as the observables in photoemission of excitons. The evaluation of the ARPES intensity, however, demands a coherent sum over electron contributions to reflect the entangled character of an exciton wave function, as well as an incoherent sum over hole contributions to fulfill energy conservation. While in this work, we have restricted ourselves to organic molecules in the gas phase, the extension of exPOT to periodic systems and magnetic materials is straight-forward. Moreover, our method can also be combined with any common excited state description, e.g. including electron-hole correlations within the framework of the Bethe-Salpeter equation.

7.5 Appendix

7.5.1 Ground state and linear response calculations

The structures of the three molecules TCNQ ($C_{12}H_4N_4$), porphin ($C_{20}H_{14}N_4$) and PTCDA ($C_{24}H_8O_6$) were optimized using the real-space mode of GPAW [465, 466] in conjunction with the BGFS minimization routine from the Atomic Simulation Environment (ASE) [467].

We used a simulation box with 0.2 Å spacing, 8 Å vacuum around each molecule and set the maximum force criterion to 0.02 eV/Å. These relaxed geometries were then used in all further calculations and are depicted in Figure **??** together with the Cartesian coordinate system and the direction of the pump field incidence.

In order to solve Casida's equation and perform the NTO analysis, we employed the linear-response TDDFT (LR-TDDFT) implementation of the real-space code OCTOPUS [176, 177]. For the three molecules, we used a simulation domain with spheres of radius 8 Å around each atom and a spacing of 0.2 Å. While the latter value for the spacing may not lead to fully converged results for the geometry optimization described before, as well as for the optical spectra in the following, we choose 0.2 Å none the less for all calculations to be consistent with the numerically very demanding ARPES simulations. For the same reason, we used the local density approximation (LDA) [101] for LR-TDDFT calculations with the Perdew-Zunger implementation of correlation [103] and norm-conserving Troullier-Martins pseudopotentials [468]. Having computed the respective groundstate of the three molecules this way, we solved Casida's equation

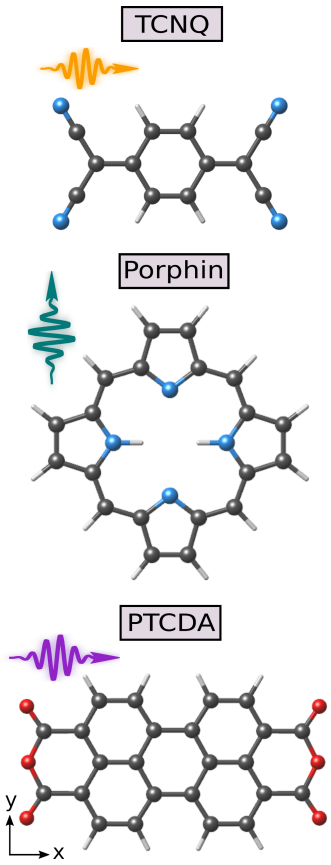

Figure 7.5: Geometries of the three molecules used in our investigation (TCNQ, porphin and PTCDA), arrows mark the incident direction of the pump pulse in the photoemission simulation

Table 7.2: Casida excitation energies, Ω_m, their corresponding single particle contributions in terms of the inital Kohn-Sham molecular orbitals, X^2_{vc}, and the eigenvalues (magnitudes) of the natural transition orbitals, Λ^2_λ, for the three molecules presented in the main text. All contributions greater than 0.01 are shown, those referenced in our investigation are highlighted, with the exception of the NTOs for PTCDA, since here a full sum over λ was necessary (see text for details)

TCNQ $\Omega_m = 6.76$ eV		porphin $\Omega_m = 3.52$ eV		PTCDA $\Omega_m = 5.51$ eV	
$\phi_v \to \chi_c$	X^2_{vc}	$\phi_v \to \chi_c$	X^2_{vc}	$\phi_v \to \chi_c$	X^2_{vc}
3 → 2	**0.44**	2 → 1	0.36	**8 → 4**	**0.29**
2 → 3	**0.35**	**1 → 2**	**0.27**	11 → 2	0.23
1 → 6	**0.07**	**4 → 2**	**0.25**	7 → 7	0.17
5 → 4	0.03	**8 → 2**	**0.05**	**4 → 8**	**0.06**
17 → 2	0.02	3 → 3	0.04	**4 → 2**	**0.06**
11 → 3	0.02			1 → 5	0.05
				8 → 3	**0.03**
				16 → 1	0.02
				7 → 1	0.02
				9 → 2	0.02
$\widetilde{\phi}_\lambda \to \widetilde{\chi}_\lambda$	Λ^2_λ	$\widetilde{\phi}_\lambda \to \widetilde{\chi}_\lambda$	Λ^2_λ	$\widetilde{\phi}_\lambda \to \widetilde{\chi}_\lambda$	Λ^2_λ
1 → 1	**0.46**	**1 → 1**	**0.57**	**1 → 1**	**0.32**
2 → 2	**0.39**	2 → 2	0.36	**2 → 2**	**0.32**
3 → 3	**0.07**	3 → 3	0.05	3 → 3	0.20
4 → 4	0.04			4 → 4	0.06
5 → 5	0.01			5 → 5	0.05
				6 → 6	0.03

with the same numerical parameter and considered an energy window of 32 eV, 28 eV and 30 eV for TCNQ, Porphin and PTCDA, respectively. In this range combinations of occupied and unoccupied states were considered, thereby obtaining the transition density matrices $X^{(m)}_{vc}$ for the m-th exciton. Note that our calculations also include de-excitations beyond the Tamm-Dancoff approximation. For the NTOs, we computed the singular value decomposition of Equation 7.12 with python's numpy package [469]. The results of the LR-TDDFT calculations are shown in Table 7.2 and optical spectra are shown in Figure 7.6 for comparison with the real-time TDDFT calculations of the next section.

7.5.2 Real-time TDDFT calculations

In this section, we describe the methods to obtain the ab-initio simulations of photoemission from real-time TDDFT (RT-TDDFT) with OCTOPUS. While in the last section, the results for linear-response calculations already delivered the desired excitation energies, we also employed a RT-TDDFT method for optical spectra [175]. Using the ground state calculations with the same parameter as described in the previous section, we perturbed the system at initial time

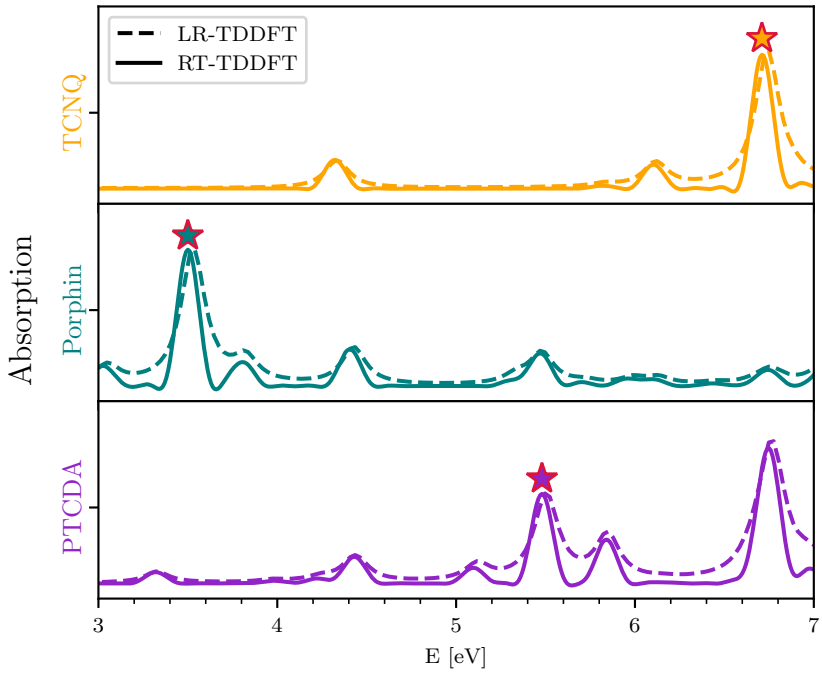

Figure 7.6: Absorption spectra of the molecules TCNQ, porphin and PTCDA calculated with OCTOPUS in RT-TDDFT (full curves) and within the linear-response Casida formalism (dashed curves). Excitation energies used in the pump-probe photoemission simulations are marked with an asterisk.

$t = 0$ with a Dirac-δ pulse (pulse strength: 0.01 Å^{-1}) that equally excites all optically allowed transitions. We then evolved the system for further 30 fs, with a time steps of 2 as, and Fourier transformed the time-dependent dipole-moment to get the optical spectrum [202]. In Figure 7.6, we compare the optical spectra from RT-TDDFT with those from the LR-TDDFT calculations of the previous section. For all three molecules, we find very good agreement, thus assuring the comparability of our methods. Since we also use TDDFT in the real-time fashion for the ARPES simulations, we use the excitation energies (marked by $\star$ symbols) from RT-TDDFT.

Having obtained the excitation energies of interest, we now describe the method used for the pump-probe ARPES simulations with t-SURFF [85, 86]. For all three molecules, we first computed the ground state as described above, with the only difference that we used a spherical simulation box around the center of the molecules with $R = 35$ Å radius. Then, the systems were subjected to pump pulses with respective energies Ω_m for $t_{\text{pump}} = 20$ fs, followed by $t_{\text{probe}} = 15$ fs of propagation time with the probe pulse. While the energy and direction of the pump pulses were varied according to the excitations within the different molecules, we always probed with z-polarized fields and a photon energy of $\omega = 35$ eV. For both types of pulses, we used a $\cos(\omega t)$ function, shaped by a hull function of $\sin^2$-type to ensure gradual on- and off-switching of the fields, thereby avoiding non-resonant excitations. The field amplitudes were varied such that the radiation would correspond to a laser with intensity 10^8 W/cm^2. In order to avoid spurious effects of reflected electron density at the border of our simulation region, we inserted a complex absorbing potential (CAP) [434] described by $\mathrm{i}\xi \sin^2(\frac{\Theta(r-R_0)\pi}{2R})$,

with magnitude $\xi = -0.2$ a.u. and onset at $R_0 = 20$ Å. Over all times, we recorded the flux of electron density through a spherical surface [85, 86] at R_0 and thus obtained energy- and angle-resolved photoemission intesities in an *ab-inito* way as a direct numerical simulation of the experiment.

7.5.3 Complementing results

In the following, we give additional results that complement those of the main text for all three molecules. For each molecule in Figure 7.7–7.9, we show the kinetic energy spectra from t-SURFF (panels (a)) in conjunction with momentum maps from the different methods presented for a series of orbitals that are relevant for the respective excitons (panels (b)). For TCNQ in Figure 7.7, all results between the different theoretical descriptions agree well, with the exception of maps for $v = 11$, where the results from t-SURFF are different to exPOT. Interestingly, it seems that the t-SURFF map for $v = 11$ depicts what seems to be missing for the exPOT map for $v = 2$, i.e. the accentuation of the main feature at $k_x = 0$ Å^{-1}, $k_y \geq 2$ Å^{-1}. The additional results for porphin in Figure 7.8 show very good agreement as well, with the one exception of $v = 8$, which does not agree at all. For the two pathological cases, $v = 11$ in TCNQ and $v = 8$ in porphin, we wish to remark that for both cases the contributions to the transition matrix are alread quite small (1-2 %) such that better converged LR-TDDFT calculations might give other results. The same argument is valid for the t-SURFF calculations, where it can be seen in the kinetic energy-resolved spectra that the peaks stemming from these two transitions are by approximately an order of magnitude smaller than those of the main contributions and would hardly be detectable in an actual experiment.

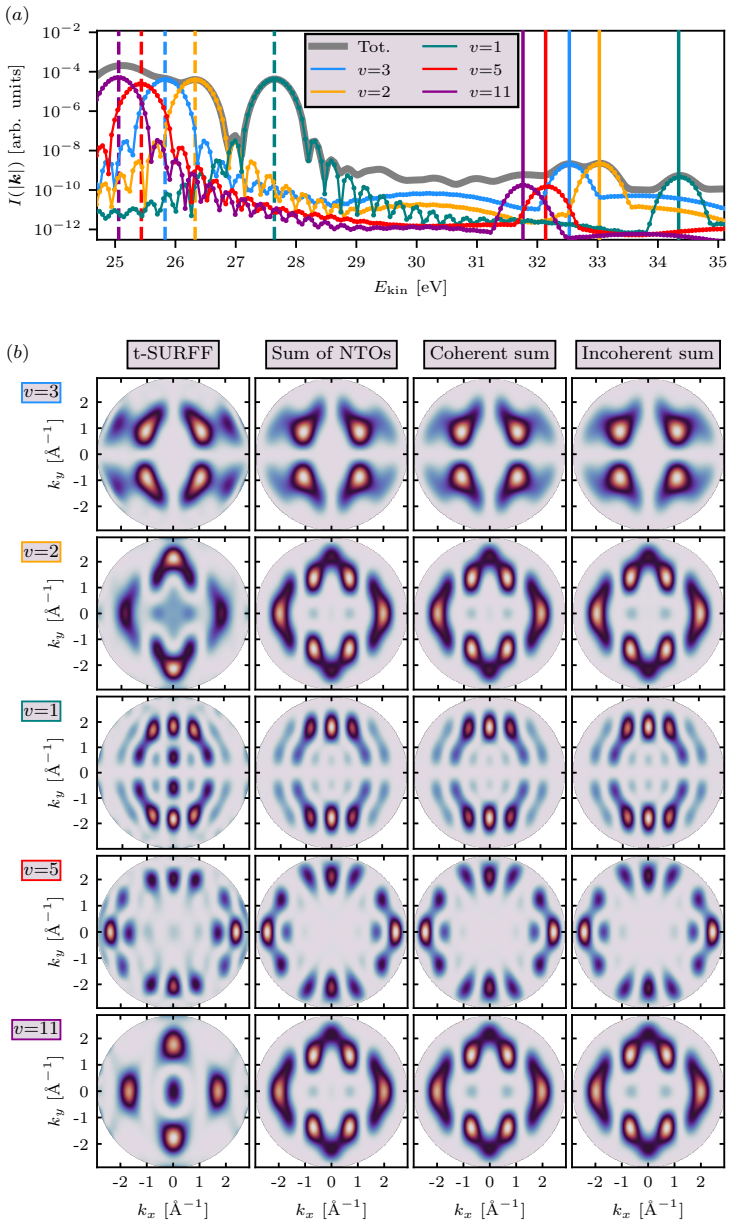

Figure 7.7: **Summary of results for TCNQ excited with 6.7 eV in y-direction.** The kinetic energy spectrum from t-SURFF is shown in panel (a) with $I(|\boldsymbol{k}|)$ in grey, as well as the projection on states $v = \{3, 2, 1, 5, 11\}$. In the same colors, we show E_v in dashed lines and $E_v + \omega_{\mathrm{pump}}$ in full lines. In panel (b), the corresponding momentum maps of the state-projected photoemission intensities from t-SURFF are shown in each line of the leftmost column. In the left-middle column, we show the results from exPOT for the sum over NTOs (Equation 7.17) and the equal results from exPOT with the coherent sum over $X_{vc}\chi_c$ (Equation 7.11) in the middle-right column. For comparison, the results with a wrongly performed incoherent sum are shown in the rightmost column (see text for details).

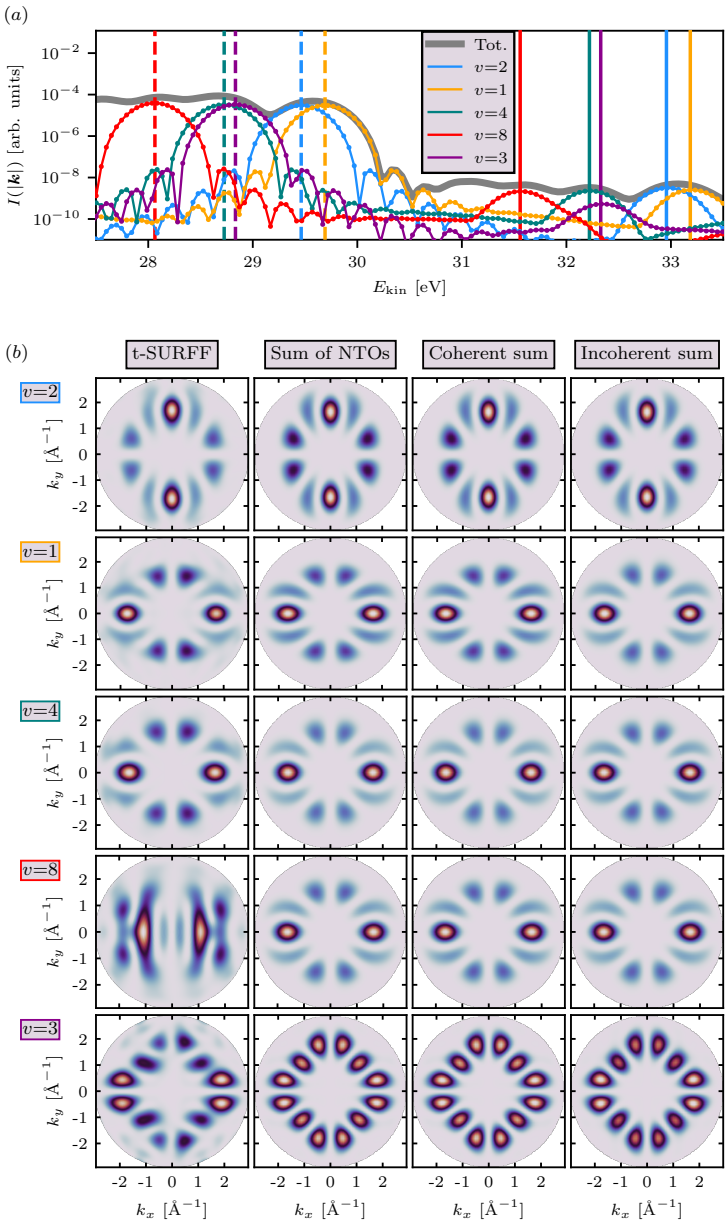

Figure 7.8: **Summary of results for porphin excited with 3.5 eV in x-direction.** The kinetic energy spectrum from t-SURFF is shown in panel (a) with $I(|\boldsymbol{k}|)$ in grey, as well as the projection on states $v = \{2, 1, 4, 8, 3\}$. In the same colors, we show E_v in dashed lines and $E_v + \omega_{\mathrm{pump}}$ in full lines. In panel (b), the corresponding momentum maps of the state-projected photoemission intensities from t-SURFF are shown in each line of the leftmost column. In the left-middle column, we show the results from exPOT for the sum over NTOs (Equation 7.17) and the equal results from exPOT with the coherent sum over $X_{vc}\chi_c$ (Equation 7.11) in the middle-right column. For comparison, the results with a wrongly performed incoherent sum are shown in the rightmost column (see text for details).

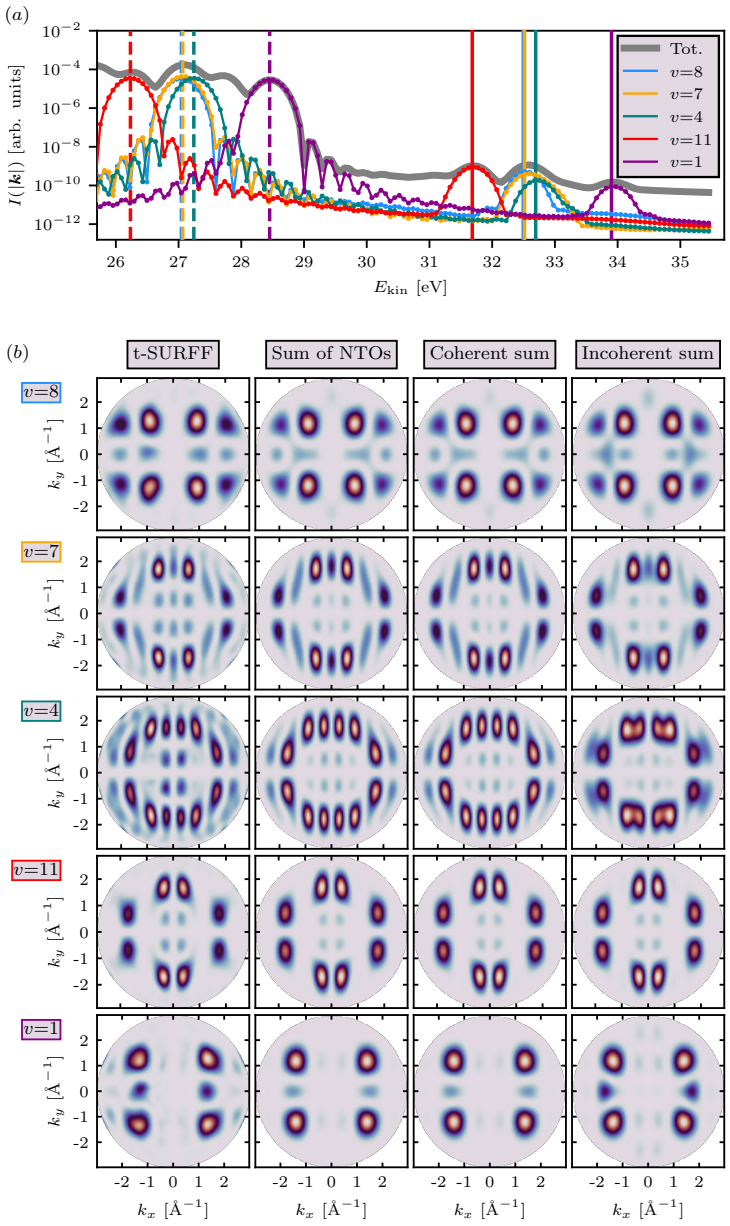

Figure 7.9: **Summary of results for PTCDA excited with 5.45 eV in y-direction.** The kinetic energy spectrum from t-SURFF is shown in panel (a) with $I(|\boldsymbol{k}|)$ in grey, as well as the projection on states $v = \{8, 7, 4, 11, 1\}$. In the same colors, we show E_v in dashed lines and $E_v + \omega_{\mathrm{pump}}$ in full lines. In panel (b), the corresponding momentum maps of the state-projected photoemission intensities from t-SURFF are shown in each line of the leftmost column. In the left-middle column, we show the results from exPOT for the sum over NTOs (Equation 7.17) and the equal results from exPOT with the coherent sum over $X_{vc}\chi_c$ (Equation 7.11) in the middle-right column. For comparison, the results with a wrongly performed incoherent sum are shown in the rightmost column (see text for details).

Chapter 8

Conclusions

In Chapters 3 and 4 it was shown that tetra-phenyl-porphyrine and porphin self-metalate when adsorbed on 2 monolayers of MgO on Ag(100). This process was found to be irrespective of the charge transfer to the molecule in case of the flat, closely-adsorbed porphin, but is mediated by the charge transfer in case of tetra-phenyl-porphyrine, due to the larger adsorption height in the latter case. In both cases the metalation reaction cannot be observed directly in POT, since the experimentally accessible orbitals are not sensitive to the ion-exchange. The most appropriate comparison for the electronic structure calculations to experimental findings was therefore an analysis of the energy balance for the metalation reaction. It turned out that such mixed metal-oxide-organic frameworks pose a serious challenge for van der Waals-correctedDFT calculations and that the experimentally observed metalation could be reproduced only in the case of porphin with a functional of the "vdW-DF" family. Since the MgO/Ag(100) interface offers the unique possibility to tune the surface work function, and thereby control the charge transfer into adsorbed molecules, this system is of great importance for POT but also challenging for van der Waals-corrected DFT.

On the same surface and in Chapter 5, the adsorption of PTCDA showed a remarkable bending of the molecules that had not been observed on metal surfaces so far. This could be explained by the interplay between the surface Mg^{2+}-ions and oxygen atoms in the molecule, and is therefore a special characteristic of this system. For the general case, however, it was shown that POT is sensitive to detect such conformal changes via the momentum space signatures of the molecular orbitals. This capability is beyond other surface science methods for detecting inter-atomic distances, since it is not restricted to chemically distinct atomic species within a molecule, as, for instance, in the x-ray standing waves method. In comparison to theory, we found that by varying the molecular bend in the simulations ad libidum, the experimental results could be well-reproduced and that the method is very sensitive to small changes above a certain threshold. When simulating the molecular bend from first principles, however, it turned out that the van der Waals corrections in DFT could not perfectly reproduce the experimentally observed bending. It thus has to be concluded again that, for organic molecular layers on the MgO/Ag(100) surface, the choice and assessment of van der Waals corrections is crucial in DFT and, therefore, for the initial state of POT in these systems as well.

The previous results had shown that the frontiers of POT lie rather in its underlying electronic structure calculations and not in its formulation, at least as far as the initial state is concerned. Conversely, this does not hold for the final state any longer. In Chapter 6 the plane wave final state was put to test from different perspectives. With carefully calibrated synchrotron radiation over a wide range of incident photon energies, strong modulations in the photoemission

intensity from graphene's Dirac bands could be experimentally observed. Using a plane wave final state, on the other hand, one is not able to capture these observed intensity modulations, but they are well rendered by simulations of photoemission from TDDFT. In developing an additional model that describes the final state as spherical waves interfering from different, dipole-allowed angular-momentum channels in the initial state, the experimental data could be reproduced. With the comparison of data measured from different incidence directions, it was furthermore shown that the scattering of the outgoing photoelectron from next-neighbors must be included, in order to describe the correct physics of the photoemission process. In this way, we could extend the realm of POT to cases that require a more sophisticated treatment of the final state to fully reproduce experimental data. With the SWA, important matrix element effects can thus be considered for the de-convolution of the material's spectral function from experimental measurements.

In the last part of this thesis (Chapter 7), we extended the formalism of POT to excited states. This enabled the simulation of photoemission from excitons, as experimentally measured in recent pump-probe experiments. From our theory, termed "exPOT", we found remarkable consequences for the photoemission from such bound electron-hole pairs. In particular and depending on the transitions occurring in the exciton, its photoemission signatures can be found at multiple kinetic energies. At each allowed kinetic energy, the momentum space signature was found to respect the entangled character of the exciton by a coherent summation of contributions from different unoccupied states. These consequences could be exemplified by the simulation of photoemission from excitons in three different organic molecules and, moreover, be confirmed by subsequent TDDFT calculations, which thus served as a numerical control experiment. We could furthermore show that our formulation can also be expressed in terms of NTOs, which allow for a more compact representation of the transitions that form an exciton. This assignes a physical meaning to the NTOs as the actually observed quantities in a photoemission experiment of excitons in the context of POT. With its extension to excited states, we could therefore considerably enlarge the frontiers of POT.

With the heterogeneous record of topics touched in this thesis, future work in multiple directions seem possible and expedient. For the description of metal-ionic-organic frameworks with DFT, more state-of-the art van der Waals corrections could be explored, such as many-body dispersion [151], and a systematic comparison of theoretical methods for a variety of different molecules on the MgO/Ag(100) surface would be helpful to deliver the best possible initial state for the POT technique in such cases. For the final state in photoemission, the SWA is expected to improve results in other areas where a correct final state is demanded, for instance in the phenomenon of circular dichroism [282]. Regarding our exPOT theory, experimental validation is already feasible, as e.g. in shown with experiments on excitons in buckminsterfullerene thin films [459]. Especially in this direction, experimental effort is expected to increase in the next decade and behind the current frontiers of photoemission orbital tomography, *terra incognita* is still waiting to be explored.

List of Publications

(i) Larissa Egger, Michael Hollerer, Christian S. Kern, Hannes Herrmann, Philipp Hurdax, Anja Haags, Xiaosheng Yang, Alexander Gottwald, Mathias Richter, Serguei Soubatch, F. Stefan Tautz, Georg Koller, Peter Puschnig, Michael G. Ramsey, and Martin Sterrer. Charge-promoted self-metalation of porphyrins on an oxide surface. *Angewandte Chemie International Edition* **60** (10), 5078-5082, 2021.

(ii) Anthony Thomas, Thomas Leoni, Olivier Siri, Conrad Becker, Martin Unzog, Christian S. Kern, Peter Puschnig, and Peter Zeppenfeld. A one-dimensional high-order commensurate phase of tilted molecules. *Physical Chemistry Chemical Physics* **24**, 9118-9122, 2022.

(iii) Francesco Presel, Christian S. Kern, Thomas G. Boné, Florian Schwarz, Peter Puschnig, Michael G. Ramsey, and Martin Sterrer. Charge and adsorption height dependence of the self-metalation of porphyrins on ultrathin MgO(001) films. *Physical Chemistry Chemical Physics* **24**, 28540-28547, 2022.

(iv) Philipp Hurdax, Christian S. Kern, Thomas Boné, Anja Haags, Larissa Egger, Xiaosheng Yang, Hans Kirschner, Mathias Richter, Serguei Soubatch, Georg Koller, Frank Stefan Tautz, Martin Sterrer, Peter Puschnig, and Michael G. Ramsey. Large distortion of fused aromatics on dielectric interlayers quantified by photoemission orbital tomography. *ACS Nano* **16**, 17435-17443, 2022.

(v) Christian S. Kern, Anja Haags, Larissa Egger, Xiaosheng Yang, Hans Kirschner, Susanne Wolff, Thomas Seyller, Alexander Gottwald, Mathias Richter, Umberto De Giovannini, Angel Rubio, Michael G. Ramsey, François C. Bocquet, Serguei Soubatch, F. Stefan Tautz, Peter Puschnig, and Simon Moser. Simple extension of the plane-wave final state in photoemission: Bringing understanding to the photon-energy dependence of two-dimensional materials. *Physical Review Research* **5**, 033075, 2023.

(vi) Christian S. Kern, Andreas Windischbacher, and Peter Puschnig. Photoemission orbital tomography for excitons in organic molecules. *Physical Review B* **108**, 085132, 2023.

(vii) Wiebke Bennecke, Andreas Windischbacher, David Schmitt, Jan Philipp Bange, Ralf Hemm, Christian S. Kern, Gabriele D'Avino, Xavier Blase, Daniel Steil, Sabine Steil, Martin Aeschlimann, Benjamin Stadtmüller, Marcel Reutzel, Peter Puschnig, G. S. Matthijs Jansen, and Stefan Mathias. Multiorbital exciton formation in an organic semiconductor. *Under review.*

(viii) Christian S. Kern, Xiaosheng Yang, Giovanni Zamborlini, Vitaliy Feyer, Umberto De Giovannini, François C. Bocquet, Serguei Soubatch, Angel Rubio, Michael G. Ramsey, F. Stefan Tautz, and Peter Puschnig. Circular dichroism in the photoelectron angular distribution of organic molecules. *In preparation.*

Appendices

A: Additional Derivations

Equation of motion for the difference in current densities

In this paragraph, a detailed derivation for the difference in current densities in the equation of motion, i.e. Equation 2.50, is given in order to complement the proof of the Runge-Gross theorem. We first define the quantum mechanical current operator with the anti-commutator $[.,.]_+$ as

$$\begin{aligned}\boldsymbol{J}(\boldsymbol{r}) &= \frac{1}{2\mathrm{i}}\sum_j^N \left[\nabla_j \delta(\boldsymbol{r}-\boldsymbol{r}_j) + \delta(\boldsymbol{r}-\boldsymbol{r}_j)\nabla_j\right] \\ &= \frac{1}{2\mathrm{i}}\sum_j^N \left[\nabla_j, \delta(\boldsymbol{r}-\boldsymbol{r}_j)\right]_+ ,\end{aligned}$$

and $\mathrm{d}\Omega := \mathrm{d}\boldsymbol{r}_1 \ldots \mathrm{d}\boldsymbol{r}_N$ as the integral measure for the many-body wave function $\Psi(\boldsymbol{r}_1, \ldots, \mathrm{d}\boldsymbol{r}_N)$, where we neglect spin degrees of freedom. Starting from Equation 2.50 times the imaginary unit, and defining $\boldsymbol{H}(t_0) - \boldsymbol{H}'(t_0) =: \Delta\boldsymbol{H}_0$ we get

$$\begin{aligned}\mathrm{i}\partial_t \left\{\boldsymbol{j}(\boldsymbol{r},t) - \boldsymbol{j}'(\boldsymbol{r},t)\right\}\Big|_{t=t_0} &= \langle\Psi_0|\left[\boldsymbol{J}(\boldsymbol{r}), \Delta\boldsymbol{H}_0\right]|\Psi_0\rangle = \frac{1}{2\mathrm{i}}\sum_j^N \langle\Psi_0|\left[\left[\nabla_j, \delta(\boldsymbol{r}-\boldsymbol{r}_j)\right]_+, \Delta\boldsymbol{H}_0\right]|\Psi_0\rangle \\ &= \frac{1}{2\mathrm{i}}\sum_j^N \left\{\langle\Psi_0|\left[\nabla_j\delta(\boldsymbol{r}-\boldsymbol{r}_j), \Delta\boldsymbol{H}_0\right]|\Psi_0\rangle + \langle\Psi_0|\left[\delta(\boldsymbol{r}-\boldsymbol{r}_j)\nabla_j, \Delta\boldsymbol{H}_0\right]|\Psi_0\rangle\right\} \\ &= \frac{1}{2\mathrm{i}}\sum_j^N \big\{\langle\Psi_0|\nabla_j\delta(\boldsymbol{r}-\boldsymbol{r}_j)\Delta\boldsymbol{H}_0|\Psi_0\rangle - \langle\Psi_0|\Delta\boldsymbol{H}_0\nabla_j\delta(\boldsymbol{r}-\boldsymbol{r}_j)|\Psi_0\rangle + \\ &\qquad + \langle\Psi_0|\delta(\boldsymbol{r}-\boldsymbol{r}_j)\nabla_j\Delta\boldsymbol{H}_0|\Psi_0\rangle - \langle\Psi_0|\Delta\boldsymbol{H}_0\delta(\boldsymbol{r}-\boldsymbol{r}_j)\nabla_j|\Psi_0\rangle\big\}.\end{aligned}$$

In the next step, we write the scalar products as real-space integrals and apply the product rule for the nabla operator and collect terms, such that

$$\begin{aligned}\mathrm{i}\partial_t \left\{\boldsymbol{j}(\boldsymbol{r},t) - \boldsymbol{j}'(\boldsymbol{r},t)\right\}\Big|_{t=t_0} = \frac{1}{2\mathrm{i}}\sum_j^N \int \mathrm{d}\Omega\, \{&\Psi_0^*\Delta\boldsymbol{H}_0\Psi_0\nabla_j\delta(\boldsymbol{r}-\boldsymbol{r}_j) + \Psi_0^*\delta(\boldsymbol{r}-\boldsymbol{r}_j)\Psi_0\nabla_j\Delta\boldsymbol{H}_0 + \\ &+\Psi_0^*\delta(\boldsymbol{r}-\boldsymbol{r}_j)\Delta\boldsymbol{H}_0\nabla_j\Psi_0 - \Psi_0^*\Delta\boldsymbol{H}_0\Psi_0\nabla_j\delta(\boldsymbol{r}-\boldsymbol{r}_j) + \\ &-\Psi_0^*\Delta\boldsymbol{H}_0\delta(\boldsymbol{r}-\boldsymbol{r}_j)\nabla_j\Psi_0 + \Psi_0^*\delta(\boldsymbol{r}-\boldsymbol{r}_j)\Psi_0\nabla_j\Delta\boldsymbol{H}_0 + \\ &+\Psi_0^*\delta(\boldsymbol{r}-\boldsymbol{r}_j)\Delta\boldsymbol{H}_0\nabla_j\Psi_0 - \Psi_0^*\Delta\boldsymbol{H}_0\delta(\boldsymbol{r}-\boldsymbol{r}_j)\nabla_j\Psi_0\} \\ = \frac{1}{\mathrm{i}}\sum_j^N \int \mathrm{d}\Omega\, &\Psi_0^*\delta(\boldsymbol{r}-\boldsymbol{r}_j)\Psi_0\nabla_j\Delta\boldsymbol{H}_0.\end{aligned}$$

Recall that $\Delta\boldsymbol{H}_0$ means the difference between two Hamiltonians at time t_0, which is only due to different potentials, such that

$$\Delta\boldsymbol{H}_0 = v(\boldsymbol{r},t_0) - v'(\boldsymbol{r},t_0),$$

and therefore

$$\mathrm{i}\partial_t \left\{\boldsymbol{j}(\boldsymbol{r},t) - \boldsymbol{j}'(\boldsymbol{r},t)\right\}\Big|_{t=t_0} = \frac{1}{\mathrm{i}}\sum_j^N \int \mathrm{d}\Omega\, \Psi_0^*\delta(\boldsymbol{r}-\boldsymbol{r}_j)\Psi_0\nabla_j \left\{v(\boldsymbol{r},t_0) - v'(\boldsymbol{r},t_0)\right\}.$$

List of Abbreviations

ACFD adiabatic connection fluctuation-dissipation.

AFM atomic force microscopy.

ALDA adiabatic local density approximation.

ARPES angular-resolved photoemission spectroscopy.

BSE Bethe-Salpter equation.

DFT density functional theory.

GGA generalized-gradient approximation.

HEG homogeneous electron gas.

HF Hartree-Fock.

HOMO highest occupied molecular orbital.

HSE Heyd, Scuseria and Ernzerhof.

KS Kohn-Sham.

LCAO local combination of atomic orbitals.

LDA local density approximation.

LSDA local spin density approximation.

LUMO lowest unoccupied molecular orbital.

MGGA Meta-GGA.

NTOs natural transition orbitals.

OT-RSH optimially-tuned range-separated hybrid.

PBE Perdew, Burke and Ernzerhof.

POT photoemission orbital tomography.

PTCDA perylene-tetracarboxylic dianhydride.

PWA plane wave approximation.

RPA random phase approximation.

RSH range-separated hybrid.

SE Schrödinger equation.

STM scanning tunneling microscopy.

STS scanning tunneling spectroscopy.

SWA scattered wave approximation.

TDDFT time-dependent DFT.

TDKS time-dependent Kohn-Sham.

TDSE time-dependent Schrödinger equation.

trARPES time- and angle-resolved photoemission spectroscopy.

vdW-DF van der Waals density functional.

XPS x-ray photoelectron spectroscopy.

Bibliography

[1] A. G. J. MacFarlane, Jonathan P. Dowling, and Gerard J. Milburn. Quantum technology: the second quantum revolution. *Philosophical Transactions of the Royal Society of London. Series A: Mathematical, Physical and Engineering Sciences*, 361(1809):1655–1674, 2003.

[2] Vlatko Vedral. *Introduction to Quantum Information Science*. Oxford University Press, 2006.

[3] Michael A. Nielsen and Isaac L. Chuang. *Quantum Computation and Quantum Information: 10th Anniversary Edition*. Cambridge University Press, 2010.

[4] *Philosophy of Quantum Information and Entanglement*. Cambridge University Press, 2010.

[5] Maximilian Schlosshauer. Decoherence, the measurement problem, and interpretations of quantum mechanics. *Rev. Mod. Phys.*, 76:1267–1305, 2005.

[6] Dave Morris Bacon and K. Birgitta Whaley. *Decoherence, Control, and Symmetry in Quantum Computers*. PhD thesis, 2001. University of California, Berkeley.

[7] C. Monroe, W. C. Campbell, L.-M. Duan, Z.-X. Gong, A. V. Gorshkov, P. W. Hess, R. Islam, K. Kim, N. M. Linke, G. Pagano, P. Richerme, C. Senko, and N. Y. Yao. Programmable quantum simulations of spin systems with trapped ions. *Rev. Mod. Phys.*, 93:025001, 2021.

[8] Immanuel Bloch, Jean Dalibard, and Sylvain Nascimbène. Quantum simulations with ultracold quantum gases. *Nature Physics*, 8(4):267–276, 2012.

[9] Christian Gross and Immanuel Bloch. Quantum simulations with ultracold atoms in optical lattices. *Science*, 357(6355):995–1001, 2017.

[10] G. S. Paraoanu. Recent Progress in Quantum Simulation Using Superconducting Circuits. *Journal of Low Temperature Physics*, 175(5):633–654, 2014.

[11] Rosario Fazio. Quantum Simulations with Superconducting Networks. *Journal of Superconductivity and Novel Magnetism*, 34(6):1643–1646, 2021.

[12] Olivier Ezratty. Perspective on superconducting qubit quantum computing. *The European Physical Journal A*, 59(5):94, 2023.

[13] Gary Wolfowicz, F. Joseph Heremans, Christopher P. Anderson, Shun Kanai, Hosung Seo, Adam Gali, Giulia Galli, and David D. Awschalom. Quantum guidelines for solid-state spin defects. *Nature Reviews Materials*, 6(10):906–925, 2021.

[14] Giordano Scappucci, Christoph Kloeffel, Floris A. Zwanenburg, Daniel Loss, Maksym Myronov, Jian-Jun Zhang, Silvano De Franceschi, Georgios Katsaros, and Menno Veldhorst. The germanium quantum information route. *Nature Reviews Materials*, 6(10):926–943, 2021.

[15] Karsten Flensberg, Felix von Oppen, and Ady Stern. Engineered platforms for topological superconductivity and Majorana zero modes. *Nature Reviews Materials*, 6(10):944–958, 2021.

[16] Daniel Douglas Eley. Phthalocyanines as Semiconductors. *Nature*, 162(4125):819–819, 1948.

[17] C. K. Chiang, C. R. Fincher, Y. W. Park, A. J. Heeger, H. Shirakawa, E. J. Louis, S. C. Gau, and Alan G. MacDiarmid. Electrical Conductivity in Doped Polyacetylene. *Phys. Rev. Lett.*, 39:1098–1101, 1977.

[18] Gilles Horowitz. *Organic Transistors*. John Wiley & Sons, Ltd, 2006.

[19] Yang Yang and Fred Wudl. Organic Electronics: From Materials to Devices. *Advanced Materials*, 21(14-15):1401–1403, 2009.

[20] He Yan, Zhihua Chen, Yan Zheng, Christopher Newman, Jordan R. Quinn, Florian Dötz, Marcel Kastler, and Antonio Facchetti. A high-mobility electron-transporting polymer for printed transistors. *Nature*, 457(7230):679–686, 2009.

[21] Qing Hua Wang, Kourosh Kalantar-Zadeh, Andras Kis, Jonathan N. Coleman, and Michael S. Strano. Electronics and optoelectronics of two-dimensional transition metal dichalcogenides. *Nature Nanotechnology*, 7(11):699–712, 2012.

[22] Kazuhiko Seki, Naoki Hayashi, Hiroshi Oji, Eisuke Ito, Yukio Ouchi, and Hisao Ishii. Electronic structure of organic/metal interfaces. *Thin Solid Films*, 393(1):298–303, 2001. Proceedings from the 4th International Conference on Nano-Molecular Electronics.

[23] Jierui Wang, He Zhu, and Shiping Zhu. Shaping of metal–organic frameworks at the interface. *Chemical Engineering Journal*, 466:143106, 2023.

[24] Kang-Jun Baeg, Maddalena Binda, Dario Natali, Mario Caironi, and Yong-Young Noh. Organic Light Detectors: Photodiodes and Phototransistors. *Advanced Materials*, 25(31):4267–4295, 2013.

[25] Hao Ren, Jing-De Chen, Yan-Qing Li, and Jian-Xin Tang. Recent Progress in Organic Photodetectors and their Applications. *Advanced Science*, 8(1):2002418, 2021.

[26] Tong Shan, Xiao Hou, Xiaokuan Yin, and Xiaojun Guo. Organic photodiodes: device engineering and applications. *Frontiers of Optoelectronics*, 15(1):49, 2022.

[27] C. W. Tang and S. A. VanSlyke. Organic electroluminescent diodes. *Applied Physics Letters*, 51(12):913–915, 1987.

[28] J. H. Burroughes, D. D. C. Bradley, A. R. Brown, R. N. Marks, K. Mackay, R. H. Friend, P. L. Burns, and A. B. Holmes. Light-emitting diodes based on conjugated polymers. *Nature*, 347(6293):539–541, 1990.

[29] Seungsuk Han and David R. Yarkony. A Lippmann–Schwinger approach for the determination of photoionization and photodetachment cross sections based on a partial wave Green's function expansion and configuration interaction wave functions. *Molecular Physics*, 110(9-10):845–859, 2012.

[30] Hisahiro Sasabe and Junji Kido. Development of high performance OLEDs for general lighting. *J. Mater. Chem. C*, 1:1699–1707, 2013.

[31] Shi-Jie Zou, Yang Shen, Feng-Ming Xie, Jing-De Chen, Yan-Qing Li, and Jian-Xin Tang. Recent advances in organic light-emitting diodes: toward smart lighting and displays. *Mater. Chem. Front.*, 4:788–820, 2020.

[32] Lin X. Chen. Organic Solar Cells: Recent Progress and Challenges. *ACS Energy Letters*, 4(10):2537–2539, 2019.

[33] R. O. Kesinro, A. O Boyo, M. L. Akinyemi, M. E. Emetere, and A. P. Aizebeokhai. Progress on Organic Solar Cells: A Short Review. *IOP Conference Series: Earth and Environmental Science*, 665(1):012036, 2021.

[34] Ebru Kondolot Solak and Erdal Irmak. Advances in organic photovoltaic cells: a comprehensive review of materials, technologies, and performance. *RSC Adv.*, 13:12244–12269, 2023.

[35] G. Binnig, H. Rohrer, Ch. Gerber, and E. Weibel. Tunneling through a controllable vacuum gap. *Applied Physics Letters*, 40(2):178–180, 1982.

[36] J. Tersoff and D. R. Hamann. Theory of the scanning tunneling microscope. *Phys. Rev. B*, 31:805–813, 1985.

[37] G. Binnig, C. F. Quate, and Ch. Gerber. Atomic Force Microscope. *Phys. Rev. Lett.*, 56:930–933, 1986.

[38] Jian Zhong and Juan Yan. Seeing is believing: atomic force microscopy imaging for nanomaterial research. *RSC Adv.*, 6:1103–1121, 2016.

[39] M. P. Seah. The quantitative analysis of surfaces by XPS: A review. *Surface and Interface Analysis*, 2(6):222–239, 1980.

[40] Noel H. Turner. *X-Ray Photoelectron and Auger Electron Spectroscopy*. John Wiley & Sons, Ltd, 2006.

[41] Kai Siegbahn. ESCA: atomic, molecular and solid state structure studies by means of electron spectroscopy. *Nova acta Regiae Societatis Scientiarum Upsaliensis*, 1967.

[42] K. Siegbahn. Electron spectroscopy - an outlook. *Journal of Electron Spectroscopy and Related Phenomena*, 5(1):3–97, 1974. The International Journal on Theoretical and Experimental Aspects of Electron Spectroscopy.

[43] Stefan Hüfner. *Photoelectron Spectroscopy*. Springer, Berlin, 2003.

[44] Andrea Damascelli. Probing the Electronic Structure of Complex Systems by ARPES. *Physica Scripta*, 2004(T109):61, 2004.

[45] Jonathan A. Sobota, Yu He, and Zhi-Xun Shen. Angle-resolved photoemission studies of quantum materials. *Reviews of Modern Physics*, 93(2):025006, 2021.

[46] Peter Puschnig, Stephen Berkebile, Alexander J. Fleming, Georg Koller, Konstantin Emtsev, Thomas Seyller, John D. Riley, Claudia Ambrosch-Draxl, Falko P. Netzer, and Michael G. Ramsey. Reconstruction of Molecular Orbital Densities from Photoemission Data. *Science*, 326:702–706, 2009.

[47] M. Graus, M. Grimm, C. Metzger, M. Dauth, C. Tusche, J. Kirschner, S. Kümmel, A. Schöll, and F. Reinert. Electron-Vibration Ccoupling in Molecular Materials: Assignment of Vibronic Modes from Photoelectron Momentum Mapping. *Physical Review Letters*, 116:147601, 2016.

[48] Pavel Kliuiev, Giovanni Zamborlini, Matteo Jugovac, Yeliz Gurdal, Karin von Arx, Kay Waltar, Stephan Schnidrig, Roger Alberto, Marcella Iannuzzi, Vitaliy Feyer, Matthias Hengsberger, and Jürg Osterwalderand Luca Castiglioni. Combined orbital tomography study of multi-configurational molecular adsorbate systems. *Nature Communications*, 10:5255, 2019.

[49] Philipp Hurdax, Christian S. Kern, Thomas Boné, Anja Haags, Larissa Egger, Xiaosheng Yang, Hans Kirschner, Mathias Richter, Serguei Soubatch, Georg Koller, Frank Stefan Tautz, Martin Sterrer, Peter Puschnig, and Michael Ramsey. Large Distortion of Fused Aromatics on Dielectric Interlayers Quantified by Photoemission Orbital Tomography. *ACS Nano*, 16:17435–17443, 2022.

[50] J. Ziroff, F. Forster, A. Schöll, P. Puschnig, and F. Reinert. Hybridization of Organic Molecular Orbitals with Substrate States at Interfaces: PTCDA on Silver. *Phys. Rev. Lett.*, 104:233004, 2010.

[51] Giovanni Zamborlini, Daniel Lüftner, Zhijing Feng, Bernd Kollmann, Peter Puschnig, Carlo Dri, Mirko Panighel, Giovanni Di Santo, Andrea Goldoni, Giovanni Comelli, Matteo Jugovac, Vitaliy Feyer, and Claus Michael Schneider. Multi-orbital charge transfer at highly oriented organic/metal interfaces. *Nature Communications*, 8:335, 2017.

[52] Xiaosheng Yang, Matteo Jugovac, Giovanni Zamborlini, Vitaliy Feyer, Georg Koller, Peter Puschnig, Serguei Soubatch, Michael G. Ramsey, and F. Stefan Tautz. Momentum-selective orbital hybridization. *Nature Communications*, 13:5148, 2022.

[53] Anja Haags, Alexander Reichmann, Qitang Fan, Larissa Egger, Hans Kirschner, Tim Naumann, Simon Werner, Tobias Vollgraff, Jörg Sundermeyer, Lukas Eschmann, Xiaosheng Yang, Dominik Brandstetter, François C. Bocquet, Georg Koller, Alexander Gottwald, Mathias Richter, Michael G. Ramsey, Michael Rohlfing, Peter Puschnig, J. Michael Gottfried, Serguei Soubatch, and F. Stefan Tautz. Kekulene: On-Surface Synthesis, Orbital Structure, and Aromatic Stabilization. *ACS Nano*, 14(11):15766–15775, 2020.

[54] Daniel Lüftner, Thomas Ules, Eva Maria Reinisch, Georg Koller, Serguei Soubatch, F. Stefan Tautz, Michael G. Ramsey, and Peter Puschnig. Imaging the wave functions of adsorbed molecules. *Proceedings of the National Academy of Sciences*, 111(2):605–610, 2014.

[55] S. Weiß, D. Lüftner, Thomas Ules, E. M. Reinisch, H. Kaser, A. Gottwald, M. Richter, S. Soubatch, Georg Koller, M. G. Ramsey, F. S. Tautz, and Peter Puschnig. Exploring three-dimensional orbital imaging with energy-dependent photoemission tomography. *Nature Communications*, 6:8287, 2015.

[56] Pavel Kliuiev, Tatiana Latychevskaia, Juerg Osterwalder, Matthias Hengsberger, and Luca Castiglioni. Application of iterative phase-retrieval algorithms to ARPES orbital tomography. *New J. Phys.*, 18:093041, 2016.

[57] Martin Graus, Christian Metzger, Manuel Grimm, Pascal Nigge, Vitaliy Feyer, Achim Schöll, and Friedrich Reinert. Three-dimensional tomographic imaging of molecular orbitals by photoelectron momentum microscopy. *The European Physical Journal B*, 92(4):80.

[58] Matthijs Jansen, Marius Keunecke, Marten Düvel, Christina Möller, David Schmitt, Wiebke Bennecke, Jasmin Kappert, Daniel Steil, D. Russell Luke, Sabine Steil, and Stefan Mathias. Efficient orbital imaging based on ultrafast momentum microscopy and sparsity-driven phase retrieval. *New Journal of Physics*, 22:063012, 2020.

[59] P. Hohenberg and W. Kohn. Inhomogeneous Electron Gas. *Phys. Rev.*, 136:B864–B871, 1964.

[60] W. Kohn. Nobel Lecture: Electronic structure of matter—wave functions and density functionals. *Rev. Mod. Phys.*, 71:1253–1266, 1999.

[61] R. M. Dreizler and E. K. U. Gross. *Density functional theory: an approach to the quantum many-body problem*. Springer, Berlin, 1990.

[62] Robert G Parr. *Density-functional theory of atoms and molecules*. The international series of monographs on chemistry. 1. issued as an oxford univ. press paperback. edition, 1994.

[63] Klaus Capelle. A bird's-eye view of density-functional theory. *Braz. J. Phys.*, 36, 2002.

[64] C. Fiolhais, F. Nogueira, and M.A.L. Marques. *A Primer in Density Functional Theory*. Lecture Notes in Physics. Springer Berlin Heidelberg, 2003.

[65] F. London. Zur Theorie und Systematik der Molekularkräfte. *Zeitschrift für Physik*, 63(3):245–279, 1930.

[66] Jan Hermann, Robert A. Jr. DiStasio, and Alexandre Tkatchenko. First-Principles Models for van der Waals Interactions in Molecules and Materials: Concepts, Theory, and Applications. *Chemical Reviews*, 117(6):4714–4758, 2017.

[67] Priya Sony, Peter Puschnig, Dmitrii Nabok, and Claudia Ambrosch-Draxl. Importance of Van Der Waals Interaction for Organic Molecule-Metal Junctions: Adsorption of Thiophene on Cu(110) as a Prototype. *Phys. Rev. Lett.*, 99:176401, 2007.

[68] Reinhard J. Maurer, Victor G. Ruiz, Javier Camarillo-Cisneros, Wei Liu, Nicola Ferri, Karsten Reuter, and Alexandre Tkatchenko. Adsorption structures and energetics of molecules on metal surfaces: Bridging experiment and theory. *Progress in Surface Science*, 91(2):72–100, 2016.

[69] H. Rydberg, M. Dion, N. Jacobson, E. Schröder, P. Hyldgaard, S. I. Simak, D. C. Langreth, and B. I. Lundqvist. Van der Waals Density Functional for Layered Structures. *Phys. Rev. Lett.*, 91:126402, 2003.

[70] A. K. Geim and I. V. Grigorieva. Van der Waals heterostructures. *Nature*, 499(7459):419–425, 2013.

[71] Getachew G. Kebede, Daniel Spångberg, Pavlin D. Mitev, Peter Broqvist, and Kersti Hermansson. Comparing van der Waals DFT methods for water on NaCl(001) and MgO(001). *The Journal of Chemical Physics*, 146(6):064703, 2017.

[72] Carl M Frostenson, Erik Jedvik Granhed, Vivekanand Shukla, Pär A T Olsson, Elsebeth Schröder, and Per Hyldgaard. Hard and soft materials: putting consistent van der Waals density functionals to work. *Electronic Structure*, 4(1):014001, 2022.

[73] Kellar Autumn, Yiching A. Liang, S. Tonia Hsieh, Wolfgang Zesch, Wai Pang Chan, Thomas W. Kenny, Ronald Fearing, and Robert J. Full. Adhesive force of a single gecko foot-hair. *Nature*, 405(6787):681–685, 2000.

[74] Robert A. Distasio, O. Anatole von Lilienfeld, and Alexandre Tkatchenko. Collective many-body van der Waals interactions in molecular systems. *Proceedings of the National Academy of Sciences*, 109:14791 – 14795, 2012.

[75] K. Kendall and A. D. Roberts. van der Waals forces influencing adhesion of cells. *Philosophical Transactions of the Royal Society B: Biological Sciences*, 370(1661):20140078, 2015.

[76] Michael Hollerer, Daniel Lüftner, Philipp Hurdax, Thomas Ules, Serguei Soubatch, Frank Stefan Tautz, Georg Koller, Peter Puschnig, Martin Sterrer, and Michael G. Ramsey. Charge Transfer and Orbital Level Alignment at Inorganic/Organic Interfaces: The Role of Dielectric Interlayers. *ACS Nano*, 11(6):6252–6260, 2017.

[77] Willi Auwärter, David Écija, Florian Klappenberger, and Johannes V. Barth. Porphyrins at interfaces. *Nature Chemistry*, 7(2):105–120, 2015.

[78] J. Michael Gottfried. Surface chemistry of porphyrins and phthalocyanines. *Surface Science Reports*, 70(3):259–379, 2015.

[79] A M Bradshaw and D P Woodruff. Molecular orbital tomography for adsorbed molecules: Is a correct description of the final state really unimportant? *New Journal of Physics*, 17(1):013033, 2015.

[80] Larissa Egger, Bernd Kollmann, Philipp Hurdax, Daniel Lüftner, Xiaosheng Yang, Simon Weiß, Alexander Gottwald, Mathias Richter, Georg Koller, Serguei Soubatch, F. Stefan Tautz, Peter Puschnig, and Michael G. Ramsey. Can photoemission tomography be useful for small, strongly-interacting adsorbate systems? *New J. Phys.*, 21:043003, 2019.

[81] M. Dauth, M. Graus, I. Schelter, M. Wießner, A. Schöll, F. Reinert, and S. Kümmel. Perpendicular Emission, Dichroism, and Energy Dependence in Angle-Resolved Photoemission: The Importance of The Final State. *Phys. Rev. Lett.*, 117:183001, 2016.

[82] C. Metzger, M. Graus, M. Grimm, G. Zamborlini, V. Feyer, M. Schwendt, D. Lüftner, P. Puschnig, A. Schöll, and F. Reinert. Plane-wave final state for photoemission from nonplanar molecules at a metal-organic interface. *Phys. Rev. B*, 101:165421, 2020.

[83] Peter J. Feibelman and D. E. Eastman. Photoemission spectroscopy—Correspondence between quantum theory and experimental phenomenology. *Phys. Rev. B*, 10:4932–4947, 1974.

[84] S. Moser. A toy model for dichroism in angle resolved photoemission. *Journal of Electron Spectroscopy and Related Phenomena*, 262:147278, 2023.

[85] Philipp Wopperer, Umberto De Giovannini, and Angel Rubio. Efficient and accurate modeling of electron photoemission in nanostructures with TDDFT. *The European Physical Journal B*, 90(3):51, 2017.

[86] Umberto De Giovannini, Hannes Hübener, and Angel Rubio. A First-Principles Time-Dependent Density Functional Theory Framework for Spin and Time-Resolved Angular-Resolved Photoelectron Spectroscopy in Periodic Systems. *Journal of Chemical Theory and Computation*, 13(1):265–273, 2017.

[87] Richard M. Martin. *Electronic Structure: Basic Theory and Practical Methods*. Cambridge University Press, 1 edition, 2004.

[88] D.S. Sholl and J.A. Steckel. *Density Functional Theory: A Practical Introduction*. Wiley, 2011.

[89] R. O. Jones. Density functional theory: Its origins, rise to prominence, and future. *Rev. Mod. Phys.*, 87:897–923, 2015.

[90] Mel Levy. Electron densities in search of Hamiltonians. *Physical Review A*, 26(3):1200 – 1208, 1982.

[91] Elliott H. Lieb. Density functionals for coulomb systems. *International Journal of Quantum Chemistry*, 24(3):243–277, 1983.

[92] W. Kohn. v-Representability and Density Functional Theory. *Phys. Rev. Lett.*, 51:1596–1598, 1983.

[93] H. Englisch and R. Englisch. Hohenberg-Kohn theorem and non-V-representable densities. *Physica A: Statistical Mechanics and its Applications*, 121(1):253–268, 1983.

[94] Mel Levy. Universal variational functionals of electron densities, first-order density matrices, and natural spin-orbitals and solution of the v-representability problem. *Proc. Natl. Acad. Sci. USA*, 76:6062, 1979.

[95] Robert van Leeuwen. *Density functional approach to the many-body problem: Key concepts and exact functionals*, volume 43, pages 25–94. Academic Press, 2003.

[96] W. Kohn and L. J. Sham. Self-Consistent Equations Including Exchange and Correlation Effects. *Phys. Rev.*, 140:A1133–A1138, 1965.

[97] Magnus R. Hestenes and Eduard Stiefel. Methods of conjugate gradients for solving linear systems. *Journal of research of the National Bureau of Standards*, 49:409–435, 1952.

[98] Anna I. Krylov. From orbitals to observables and back. *J. Chem. Phys.*, 153:080901, 2020.

[99] T. Koopmans. Über die Zuordnung von Wellenfunktionen und Eigenwerten zu den einzelnen Elektronen eines Atoms. *Physica*, 1(1):104–113, 1934.

[100] J. F. Janak. Proof that $\frac{\partial E}{\partial n_i} = \epsilon$ in density-functional theory. *Phys. Rev. B*, 18:7165–7168, 1978.

[101] P. A. M. Dirac. Note on Exchange Phenomena in the Thomas Atom. *Mathematical Proceedings of the Cambridge Philosophical Society*, 26(3):376–385, 1930.

[102] D. M. Ceperley and B. J. Alder. Ground State of the Electron Gas by a Stochastic Method. *Phys. Rev. Lett.*, 45:566–569, 1980.

[103] J. P. Perdew and Alex Zunger. Self-interaction correction to density-functional approximations for many-electron systems. *Phys. Rev. B*, 23:5048–5079, 1981.

[104] John P. Perdew and Yue Wang. Accurate and simple analytic representation of the electron-gas correlation energy. *Phys. Rev. B*, 45:13244–13249, 1992.

[105] Philipp Haas, Fabien Tran, and Peter Blaha. Calculation of the lattice constant of solids with semilocal functionals. *Phys. Rev. B*, 79:085104, 2009.

[106] Takeyce K. Whittingham and Kieron Burke. Relations between coordinate and potential scaling in the high-density limit. *The Journal of Chemical Physics*, 122(13):134108, 2005.

[107] U von Barth and L Hedin. A local exchange-correlation potential for the spin polarized case. i. *Journal of Physics C: Solid State Physics*, 5(13):1629, 1972.

[108] John P. Perdew and Karla Schmidt. Jacob's ladder of density functional approximations for the exchange-correlation energy. *AIP Conference Proceedings*, 577(1):1–20, 2001.

[109] A. D. Becke. Density-functional exchange-energy approximation with correct asymptotic behavior. *Phys. Rev. A*, 38:3098–3100, 1988.

[110] John P. Perdew, Kieron Burke, and Matthias Ernzerhof. Generalized Gradient Approximation Made Simple. *Phys. Rev. Lett.*, 77:3865–3868, 1996.

[111] Viktor N. Staroverov, Gustavo E. Scuseria, Jianmin Tao, and John P. Perdew. Comparative assessment of a new nonempirical density functional: Molecules and hydrogen-bonded complexes. *The Journal of Chemical Physics*, 119(23):12129–12137, 2003.

[112] Viktor N. Staroverov, Gustavo E. Scuseria, Jianmin Tao, and John P. Perdew. Tests of a ladder of density functionals for bulk solids and surfaces. *Phys. Rev. B*, 69:075102, 2004.

[113] John P. Perdew, Stefan Kurth, Aleš Zupan, and Peter Blaha. Accurate Density Functional with Correct Formal Properties: A Step Beyond the Generalized Gradient Approximation. *Phys. Rev. Lett.*, 82:2544–2547, 1999.

[114] Jianmin Tao, John P. Perdew, Viktor N. Staroverov, and Gustavo E. Scuseria. Climbing the Density Functional Ladder: Nonempirical Meta–Generalized Gradient Approximation Designed for Molecules and Solids. *Phys. Rev. Lett.*, 91:146401, 2003.

[115] Jianwei Sun, Adrienn Ruzsinszky, and John P. Perdew. Strongly Constrained and Appropriately Normed Semilocal Density Functional. *Phys. Rev. Lett.*, 115:036402, 2015.

[116] Axel D. Becke. Density-functional thermochemistry. III. The role of exact exchange. *The Journal of Chemical Physics*, 98(7):5648–5652, 1993.

[117] P. J. Stephens, F. J. Devlin, C. F. Chabalowski, and M. J. Frisch. Ab Initio Calculation of Vibrational Absorption and Circular Dichroism Spectra Using Density Functional Force Fields. *The Journal of Physical Chemistry*, 98(45):11623–11627, 1994.

[118] Chengteh Lee, Weitao Yang, and Robert G. Parr. Development of the Colle-Salvetti correlation-energy formula into a functional of the electron density. *Phys. Rev. B*, 37:785–789, 1988.

[119] Jochen Heyd, Gustavo E. Scuseria, and Matthias Ernzerhof. Hybrid functionals based on a screened Coulomb potential. *The Journal of Chemical Physics*, 118(18):8207–8215, 2003.

[120] Aliaksandr V. Krukau, Oleg A. Vydrov, Artur F. Izmaylov, and Gustavo E. Scuseria. Influence of the exchange screening parameter on the performance of screened hybrid functionals. *The Journal of Chemical Physics*, 125(22):224106, 2006.

[121] Tamar Stein, Helen Eisenberg, Leeor Kronik, and Roi Baer. Fundamental Gaps in Finite Systems from Eigenvalues of a Generalized Kohn-Sham Method. *Phys. Rev. Lett.*, 105:266802, 2010.

[122] Andreas Karolewski, Leeor Kronik, and Stephan Kümmel. Using optimally tuned range separated hybrid functionals in ground-state calculations: Consequences and caveats. *The Journal of Chemical Physics*, 138(20):204115, 2013.

[123] Leeor Kronik, Tamar Stein, Sivan Refaely-Abramson, and Roi Baer. Excitation Gaps of Finite-Sized Systems from Optimally Tuned Range-Separated Hybrid Functionals. *Journal of Chemical Theory and Computation*, 8(5):1515–1531, 2012.

[124] Dahvyd Wing, Guy Ohad, Jonah B. Haber, Marina R. Filip, Stephen E. Gant, Jeffrey B. Neaton, and Leeor Kronik. Band gaps of crystalline solids from Wannier-localization–based optimal tuning of a screened range-separated hybrid functional. *Proceedings of the National Academy of Sciences*, 118(34):e2104556118, 2021.

[125] Filipp Furche. Molecular tests of the random phase approximation to the exchange-correlation energy functional. *Phys. Rev. B*, 64:195120, 2001.

[126] Karen Johnston, Jesper Kleis, Bengt I. Lundqvist, and Risto M. Nieminen. Influence of van der Waals forces on the adsorption structure of benzene on silicon studied using density functional theory. *Phys. Rev. B*, 77:121404, 2008.

[127] Alexandre Tkatchenko, Lorenz Romaner, Oliver T. Hofmann, Egbert Zojer, Claudia Ambrosch-Draxl, and Matthias Scheffler. Van der Waals Interactions Between Organic Adsorbates and at Organic/Inorganic Interfaces. *MRS Bulletin*, 35(6):435–442, 2010.

[128] Sriharsha V. Aradhya, Michael Frei, Mark S. Hybertsen, and L. Venkataraman. Van der Waals interactions at metal/organic interfaces at the single-molecule level. *Nature Materials*, 11(10):872–876, 2012.

[129] Sebastian Zuluaga, Pieremanuele Canepa, Kui Tan, Yves J Chabal, and Timo Thonhauser. Study of van der Waals bonding and interactions in metal organic framework materials. *Journal of Physics: Condensed Matter*, 26(13):133002, 2014.

[130] João P. Prates Ramalho, José R. B. Gomes, and Francesc Illas. Accounting for van der Waals interactions between adsorbates and surfaces in density functional theory based calculations: selected examples. *RSC Adv.*, 3:13085–13100, 2013.

[131] Per Hyldgaard, Kristian Berland, and Elsebeth Schröder. Interpretation of van der Waals density functionals. *Phys. Rev. B*, 90:075148, 2014.

[132] Kristian Berland, Valentino R Cooper, Kyuho Lee, Elsebeth Schröder, T Thonhauser, Per Hyldgaard, and Bengt I Lundqvist. van der Waals forces in density functional theory: a review of the vdW-DF method. *Reports on Progress in Physics*, 78(6):066501, 2015.

[133] Martin Stöhr, Troy Van Voorhis, and Alexandre Tkatchenko. Theory and practice of modeling van der Waals interactions in electronic-structure calculations. *Chem. Soc. Rev.*, 48:4118–4154, 2019.

[134] R. Eisenschitz and F. London. Über das Verhältnis der van der Waalsschen Kräfte zu den homöopolaren Bindungskräften. *Zeitschrift für Physik*, 60(7):491–527, 1930.

[135] J E Lennard-Jones. Cohesion. *Proceedings of the Physical Society*, 43(5):461, 1931.

[136] Stefan Grimme. Accurate description of van der Waals complexes by density functional theory including empirical corrections. *Journal of Computational Chemistry*, 25(12):1463–1473, 2004.

[137] Stefan Grimme, Jens Antony, Stephan Ehrlich, and Helge Krieg. A consistent and accurate ab initio parametrization of density functional dispersion correction (DFT-D) for the 94 elements H-Pu. *The Journal of Chemical Physics*, 132(15):154104, 2010.

[138] Torsten Kerber, Marek Sierka, and Joachim Sauer. Application of semiempirical long-range dispersion corrections to periodic systems in density functional theory. *Journal of Computational Chemistry*, 29(13):2088–2097, 2008.

[139] X. Chu and A. Dalgarno. Linear response time-dependent density functional theory for van der Waals coefficients. *The Journal of Chemical Physics*, 121(9):4083–4088, 2004.

[140] Alexandre Tkatchenko and Matthias Scheffler. Accurate Molecular Van Der Waals Interactions from Ground-State Electron Density and Free-Atom Reference Data. *Phys. Rev. Lett.*, 102:073005, 2009.

[141] V. P. Osinga, S. J. A. van Gisbergen, J. G. Snijders, and E. J. Baerends. Density functional results for isotropic and anisotropic multipole polarizabilities and C_6, C_7, and C_8 Van der Waals dispersion coefficients for molecules. *The Journal of Chemical Physics*, 106(12):5091–5101, 1997.

[142] K. T. Tang and M. Karplus. Padé-Approximant Calculation of the Nonretarded van der Waals Coefficients for Two and Three Helium Atoms. *Phys. Rev.*, 171:70–74, 1968.

[143] P.W. Langhoff and M. Karplus. Chapter 2 Application of Padé Approximants to Dispersion Force and Optical Polarizability Computations. In *The Padé Approximant in Theoretical Physics*, pages 41–97. Elsevier, 1970.

[144] Tore Brinck, Jane S Murray, and Peter Politzer. Polarizability and volume. *The Journal of chemical physics*, 98(5):4305–4306, 1993.

[145] F. L. Hirshfeld. Bonded-atom fragments for describing molecular charge densities. *Theoretica chimica acta*, 44(2):129–138, 1977.

[146] Tkatchenko-Scheffler method. `https://www.vasp.at/wiki/index.php/Tkatchenko-Scheffler_method`. Accessed: 2023-04-03.

[147] Patrick Bultinck, Christian Van Alsenoy, Paul W. Ayers, and Ramon Carbó-Dorca. Critical analysis and extension of the Hirshfeld atoms in molecules. *The Journal of Chemical Physics*, 126(14):144111, 2007.

[148] Tomáášš Bučko, Sébastien Lebègue, Jürgen Hafner, and János G. Ángyán. Improved Density Dependent Correction for the Description of London Dispersion Forces. *Journal of Chemical Theory and Computation*, 9(10):4293–4299, 2013. PMID: 26589148.

[149] Tomáš Bučko, Sébastien Lebègue, Jürgen Hafner, and János G. Ángyán. Extending the applicability of the Tkatchenko-Scheffler dispersion correction via iterative Hirshfeld partitioning. *The Journal of Chemical Physics*, 141(3):034114, 2014.

[150] B.T. Thole. Molecular polarizabilities calculated with a modified dipole interaction. *Chemical Physics*, 59(3):341–350, 1981.

[151] Alexandre Tkatchenko, Robert A. DiStasio, Roberto Car, and Matthias Scheffler. Accurate and Efficient Method for Many-Body van der Waals Interactions. *Phys. Rev. Lett.*, 108:236402, 2012.

[152] Tomáš Bučko, Sébastien Lebègue, Jürgen Hafner, and János G. Ángyán. Tkatchenko-Scheffler van der Waals correction method with and without self-consistent screening applied to solids. *Phys. Rev. B*, 87:064110, 2013.

[153] Victor G. Ruiz, Wei Liu, and Alexandre Tkatchenko. Density-functional theory with screened van der Waals interactions applied to atomic and molecular adsorbates on close-packed and non-close-packed surfaces. *Phys. Rev. B*, 93:035118, 2016.

[154] Alberto Ambrosetti, Anthony M. Reilly, Jr. DiStasio, Robert A., and Alexandre Tkatchenko. Long-range correlation energy calculated from coupled atomic response functions. *The Journal of Chemical Physics*, 140(18):18A508, 2014.

[155] Tim Gould, Sébastien Lebègue, János G. Ángyán, and Tomáš Bučko. A Fractionally Ionic Approach to Polarizability and van der Waals Many-Body Dispersion Calculations. *Journal of Chemical Theory and Computation*, 12(12):5920–5930, 2016.

[156] Tomáš Bučko, Sébastien Lebègue, Tim Gould, and János G. Ángyán. Many-body dispersion corrections for periodic systems: an efficient reciprocal space implementation. *Journal of Physics: Condensed Matter*, 28(4):045201, 2016.

[157] C. Ullrich. *Time-Dependent Density-Functional Theory: Concepts and Applications*. Oxford Graduate Texts. OUP Oxford, 2012.

[158] D.C. Langreth and J.P. Perdew. The exchange-correlation energy of a metallic surface. *Solid State Communications*, 17(11):1425–1429, 1975.

[159] O. Gunnarsson and B. I. Lundqvist. Exchange and correlation in atoms, molecules, and solids by the spin-density-functional formalism. *Phys. Rev. B*, 13:4274–4298, 1976.

[160] David C. Langreth and John P. Perdew. Exchange-correlation energy of a metallic surface: Wave-vector analysis. *Phys. Rev. B*, 15:2884–2901, 1977.

[161] T. Miyake, F. Aryasetiawan, T. Kotani, M. van Schilfgaarde, M. Usuda, and K. Terakura. Total energy of solids: An exchange and random-phase approximation correlation study. *Phys. Rev. B*, 66:245103, 2002.

[162] Filipp Furche and Troy Van Voorhis. Fluctuation-dissipation theorem density-functional theory. *The Journal of Chemical Physics*, 122(16):164106, 2005.

[163] Andrea Marini, P. García-González, and Angel Rubio. First-Principles Description of Correlation Effects in Layered Materials. *Phys. Rev. Lett.*, 96:136404, 2006.

[164] P. García-González, J. J. Fernández, Andrea Marini, and Angel Rubio. Advanced Correlation Functionals: Application to Bulk Materials and Localized Systems. *The Journal of Physical Chemistry A*, 111(49):12458–12465, 2007.

[165] Judith Harl and Georg Kresse. Cohesive energy curves for noble gas solids calculated by adiabatic connection fluctuation-dissipation theory. *Phys. Rev. B*, 77:045136, 2008.

[166] Huy-Viet Nguyen and Giulia Galli. A first-principles study of weakly bound molecules using exact exchange and the random phase approximation. *The Journal of Chemical Physics*, 132(4):044109, 2010.

[167] M. Dion, H. Rydberg, E. Schröder, D. C. Langreth, and B. I. Lundqvist. Van der Waals Density Functional for General Geometries. *Phys. Rev. Lett.*, 92:246401, 2004.

[168] Kyuho Lee, Éamonn D. Murray, Lingzhu Kong, Bengt I. Lundqvist, and David C. Langreth. Higher-accuracy van der Waals density functional. *Phys. Rev. B*, 82:081101, 2010.

[169] Jiří Klimeš, David R Bowler, and Angelos Michaelides. Chemical accuracy for the van der Waals density functional. *Journal of Physics: Condensed Matter*, 22(2):022201, 2009.

[170] Jiří Klimeš, David R. Bowler, and Angelos Michaelides. Van der Waals density functionals applied to solids. *Phys. Rev. B*, 83:195131, 2011.

[171] Oleg A. Vydrov and Troy Van Voorhis. Nonlocal van der Waals density functional: The simpler the better. *The Journal of Chemical Physics*, 133(24):244103, 2010.

[172] Riccardo Sabatini, Tommaso Gorni, and Stefano de Gironcoli. Nonlocal van der Waals density functional made simple and efficient. *Phys. Rev. B*, 87:041108, 2013.

[173] Haowei Peng, Zeng-Hui Yang, John P. Perdew, and Jianwei Sun. Versatile van der Waals Density Functional Based on a Meta-Generalized Gradient Approximation. *Phys. Rev. X*, 6:041005, 2016.

[174] Mark E. Casida. Time-Dependent Density Functional Response Theory for Molecules. In *Recent Advances in Density Functional Methods*, pages 155–192.

[175] K. Yabana and G. F. Bertsch. Time-dependent local-density approximation in real time. *Phys. Rev. B*, 54:4484–4487, 1996.

[176] Xavier Andrade, David Strubbe, Umberto De Giovannini, Ask Hjorth Larsen, Micael J T Oliveira, Joseba Alberdi-Rodriguez, Alejandro Varas, Iris Theophilou, Nicole Helbig, Matthieu J Verstraete, Lorenzo Stella, Fernando Nogueira, Alán Aspuru-Guzik, Alberto Castro, Miguel A L Marques, and Angel Rubio. Real-space grids and the Octopus code as tools for the development of new simulation approaches for electronic systems. *Physical Chemistry Chemical Physics*, 17(47):31371–31396, 2015.

[177] Nicolas Tancogne-Dejean, Micael J. T. Oliveira, Xavier Andrade, Heiko Appel, and et. al. Octopus, a computational framework for exploring light-driven phenomena and quantum dynamics in extended and finite systems. *The Journal of Chemical Physics*, 152(12):124119, 2020.

[178] Erich Runge and E. K. U. Gross. Density-Functional Theory for Time-Dependent Systems. *Phys. Rev. Lett.*, 52:997–1000, 1984.

[179] E.K.U. Gross and W. Kohn. Time-Dependent Density-Functional Theory. In Per-Olov Löwdin, editor, *Density Functional Theory of Many-Fermion Systems*, volume 21 of *Advances in Quantum Chemistry*, pages 255–291. Academic Press, 1990.

[180] Robert Van Leeuwen. Key Concepts in Time-dependent Density-Functional Theory. *International Journal of Modern Physics B*, 15(14):1969–2023, 2001.

[181] Yonghui Li and C. A. Ullrich. Time-dependent V-representability on lattice systems. *The Journal of Chemical Physics*, 129(4), 2008.

[182] Claudio Verdozzi. Time-Dependent Density-Functional Theory and Strongly Correlated Systems: Insight from Numerical Studies. *Phys. Rev. Lett.*, 101:166401, 2008.

[183] M. Ruggenthaler, M. Penz, and D. Bauer. On the existence of effective potentials in time-dependent density functional theory. *Journal of Physics A: Mathematical and Theoretical*, 42(42):425207, 2009.

[184] M. Ruggenthaler, M. Penz, and D. Bauer. General Runge-Gross-type theorem for dipole laser-matter interaction. *Phys. Rev. A*, 81:062108, 2010.

[185] N. T. Maitra, T. N. Todorov, C. Woodward, and K. Burke. Density-potential mapping in time-dependent density-functional theory. *Phys. Rev. A*, 81:042525, 2010.

[186] J. Crank and P. Nicolson. A practical method for numerical evaluation of solutions of partial differential equations of the heat-conduction type. *Mathematical Proceedings of the Cambridge Philosophical Society*, 43(1):50–67, 1947.

[187] Alberto Castro, Miguel A. L. Marques, and Angel Rubio. Propagators for the time-dependent Kohn–Sham equations. *The Journal of Chemical Physics*, 121(8):3425–3433, 2004.

[188] M. Ruggenthaler, S. E. B. Nielsen, and R. van Leeuwen. Analytic density functionals with initial-state dependence and memory. *Phys. Rev. A*, 88:022512, 2013.

[189] Sheng-Lun Liao, Tak-San Ho, Herschel Rabitz, and Shih-I. Chu. Exact-exchange optimized effective potential and memory effect in time-dependent density functional theory. *The European Physical Journal B*, 91(7):147, 2018.

[190] Yasumitsu Suzuki, Ryo Nagai, and Jun Haruyama. Machine learning exchange-correlation potential in time-dependent density-functional theory. *Phys. Rev. A*, 101:050501, 2020.

[191] David J. Tozer and Nicholas C. Handy. On the determination of excitation energies using density functional theory. *Phys. Chem. Chem. Phys.*, 2:2117–2121, 2000.

[192] Robert J. Cave, Fan Zhang, Neepa T. Maitra, and Kieron Burke. A dressed TDDFT treatment of the 21Ag states of butadiene and hexatriene. *Chemical Physics Letters*, 389(1):39–42, 2004.

[193] H. O. Wijewardane and C. A. Ullrich. Real-Time Electron Dynamics with Exact-Exchange Time-Dependent Density-Functional Theory. *Phys. Rev. Lett.*, 100:056404, 2008.

[194] Bradley F. Habenicht, Noriyuki P. Tani, Makenzie R. Provorse, and Christine M. Isborn. Two-electron Rabi oscillations in real-time time-dependent density-functional theory. *The Journal of Chemical Physics*, 141(18), 2014. 184112.

[195] Daniele Varsano, Leonardo A. Espinosa-Leal, Xavier Andrade, Miguel A. L. Marques, Rosa di Felice, and Angel Rubio. Towards a gauge invariant method for molecular chiroptical properties in TDDFT. *Phys. Chem. Chem. Phys.*, 11:4481–4489, 2009.

[196] C.D. Pemmaraju, F.D. Vila, J.J. Kas, S.A. Sato, J.J. Rehr, K. Yabana, and David Prendergast. Velocity-gauge real-time TDDFT within a numerical atomic orbital basis set. *Computer Physics Communications*, 226:30–38, 2018.

[197] J. Franck and E. G. Dymond. Elementary processes of photochemical reactions. *Trans. Faraday Soc.*, 21:536–542, 1926.

[198] Edward Condon. A Theory of Intensity Distribution in Band Systems. *Phys. Rev.*, 28:1182–1201, 1926.

[199] C A Ullrich, P-G Reinhard, and E Suraud. Metallic clusters in strong femtosecond laser pulses. *Journal of Physics B: Atomic, Molecular and Optical Physics*, 30(21):5043, 1997.

[200] Takashi Nakatsukasa and Kazuhiro Yabana. Photoabsorption spectra in the continuum of molecules and atomic clusters. *The Journal of Chemical Physics*, 114(6):2550–2561, 2001.

[201] G. F. Bertsch, J.-I. Iwata, Angel Rubio, and K. Yabana. Real-space, real-time method for the dielectric function. *Phys. Rev. B*, 62:7998–8002, 2000.

[202] K. Yabana, T. Nakatsukasa, J.-I. Iwata, and G. F. Bertsch. Real-time, real-space implementation of the linear response time-dependent density-functional theory. *physica status solidi (b)*, 243(5):1121–1138, 2006.

[203] Nicolas Tancogne-Dejean and Angel Rubio. Atomic-like high-harmonic generation from two-dimensional materials. *Science Advances*, 4(2):eaao5207, 2018.

[204] M. Lucchini, S. A. Sato, A. Ludwig, J. Herrmann, M. Volkov, L. Kasmi, Y. Shinohara, K. Yabana, L. Gallmann, and U. Keller. Attosecond dynamical Franz-Keldysh effect in polycrystalline diamond. *Science*, 353(6302):916–919, 2016.

[205] E. K. U. Gross, J. F. Dobson, and M. Petersilka. *Density functional theory of time-dependent phenomena*, pages 81–172. Springer Berlin Heidelberg, Berlin, Heidelberg, 1996.

[206] M.A.L. Marques and E.K.U. Gross. TIME-DEPENDENT DENSITY FUNCTIONAL THEORY. *Annual Review of Physical Chemistry*, 55(1):427–455, 2004.

[207] Peter Elliott, Filipp Furche, and Kieron Burke. *Excited States from Time-Dependent Density Functional Theory*, chapter 3, pages 91–165. John Wiley & Sons, Ltd, 2008.

[208] Carsten A. Ullrich and Zeng-hui Yang. A Brief Compendium of Time-Dependent Density Functional Theory. *Brazilian Journal of Physics*, 44(1):154–188, 2014.

[209] Paul Geerlings, Stijn Fias, Zino Boisdenghien, and Frank De Proft. Conceptual DFT: chemistry from the linear response function. *Chem. Soc. Rev.*, 43:4989–5008, 2014.

[210] Carsten A. Ullrich and Zeng-hui Yang. *Excitons in Time-Dependent Density-Functional Theory*, pages 185–217. Springer International Publishing, Cham, 2016.

[211] E. K. U. Gross and Walter Kohn. Local density-functional theory of frequency-dependent linear response. *Phys. Rev. Lett.*, 55:2850–2852, 1985.

[212] M. Petersilka, U. J. Gossmann, and E. K. U. Gross. Excitation Energies from Time-Dependent Density-Functional Theory. *Phys. Rev. Lett.*, 76:1212–1215, 1996.

[213] Gunnar Källén. On the definition of the Renormalization Constants in Quantum Electrodynamics. *Helvetica Physica Acta*, 25:509–527, 1952.

[214] Hein Lehmann. Über Eigenschaften von Ausbreitungsfunktionen und Renormierungskonstanten quantisierter Felder. *Il Nuovo Cimento (1943-1954)*, 11:342–357, 1954.

[215] Giovanni Onida, Lucia Reining, and Angel Rubio. Electronic excitations: density-functional versus many-body Green's-function approaches. *Rev. Mod. Phys.*, 74:601–659, 2002.

[216] S. Sharma, J. K. Dewhurst, A. Sanna, and E. K. U. Gross. Bootstrap Approximation for the Exchange-Correlation Kernel of Time-Dependent Density-Functional Theory. *Phys. Rev. Lett.*, 107:186401, 2011.

[217] P. Romaniello, D. Sangalli, J. A. Berger, F. Sottile, L. G. Molinari, L. Reining, and G. Onida. Double excitations in finite systems. *The Journal of Chemical Physics*, 130(4), 2009.

[218] Richard L. Martin. Natural transition orbitals. *The Journal of Chemical Physics*, 118(11):4775–4777, 2003.

[219] Ingo Schelter and Stephan Kümmel. Accurate Evaluation of Real-Time Density Functional Theory Providing Access to Challenging Electron Dynamics. *Journal of Chemical Theory and Computation*, 14(4):1910–1927, 2018.

[220] Joaquim Jornet-Somoza and Irina Lebedeva. Real-Time Propagation TDDFT and Density Analysis for Exciton Coupling Calculations in Large Systems. *Journal of Chemical Theory and Computation*, 15(6):3743–3754, 2019.

[221] H. Hertz. Üeber einen Einfluss des ultravioletten Lichtes auf die electrische Entladung. *Annalen der Physik*, 267(8):983–1000, 1887.

[222] A. Einstein. Über einen die Erzeugung und Verwandlung des Lichtes betreffenden heuristischen Gesichtspunkt. *Annalen der Physik*, 322(6):132–148, 1905.

[223] Max Planck. Über das Gesetz der Energieverteilung im Normalspectrum. *Annalen der Physik*, 309(3):553–563, 1901.

[224] R. A. Millikan. A Direct Photoelectric Determination of Planck's "h". *Phys. Rev.*, 7:355–388, 1916.

[225] Fedor Ivanovich Vilesov, BL Kurbatov, and Aleksandr Nikolaevich Terenin. Electron distribution over energies in the photoionization of aromatic amines in the gaseous phase. In *Doklady Akademii Nauk*, volume 138, pages 1329–1332. Russian Academy of Sciences, 1961.

[226] D. W. Turner and M. I. Al Jobory. Determination of Ionization Potentials by Photoelectron Energy Measurement. *The Journal of Chemical Physics*, 37(12):3007–3008, 1962.

[227] R.C.G. Leckey and J.D. Riley. A toroidal angle-resolving electron spectrometer for surface studies. *Applications of Surface Science*, 22-23:196–205, 1985.

[228] M. Escher, N. Weber, M. Merkel, C. Ziethen, P. Bernhard, G. Schönhense, S. Schmidt, F. Forster, F. Reinert, B. Krömker, and D. Funnemann. NanoESCA: a novel energy filter for imaging x-ray photoemission spectroscopy. *Journal of Physics: Condensed Matter*, 17(16):S1329, 2005.

[229] G. D. Mahan. Theory of Photoemission in Simple Metals. *Phys. Rev. B*, 2:4334–4350, 1970.

[230] Norman Haag. *Exploring the Potential of Orbital Tomography for 3D Molecules*. PhD thesis, Technische Universität Kaiserslautern, 2017.

[231] Shinji Hasegawa, Takayuki Miyamae, Kyuya Yakushi, Hiroo Inokuchi, Kazuhiko Seki, and Nobuo Ueno. Origin of the photoemission intensity oscillation of C_{60}. *Phys. Rev. B*, 58:4927–4933, 1998.

[232] Norman Haag, Daniel Lüftner, Florian Haag, Johannes Seidel, Leah L. Kelly, Giovanni Zamborlini, Matteo Jugovac, Vitaliy Feyer, Martin Aeschlimann, Peter Puschnig, Mirko Cinchetti, and Benjamin Stadtmüller. Signatures of an atomic crystal in the band structure of a C_{60} thin film. *Phys. Rev. B*, 101:165422, 2020.

[233] C. N. Berglund and W. E. Spicer. Photoemission Studies of Copper and Silver: Theory. *Phys. Rev.*, 136:A1030–A1044, 1964.

[234] W.L. Schaich and N.W. Ashcroft. Theory of photoemission. *Solid State Communications*, 8(23):1959–1963, 1970.

[235] C. Caroli, D. Lederer-Rozenblatt, B. Roulet, and D. Saint-James. Inelastic Effects in Photoemission: Microscopic Formulation and Qualitative Discussion. *Phys. Rev. B*, 8:4552–4569, 1973.

[236] Carl-Olof Almbladh and Lars Hedin. *Beyond the One-Electron Model. Many-Body Effects in Atoms, Molecules, and Solids, in Handbook of Synchrotron Radiation vol. 1b, ed. by E.-E. Koch, North-Holland 1983, pp 607-904*, pages 607–904. 1983.

[237] Carl-Olof Almbladh. Photoemission beyond the sudden approximation. *Journal of Physics: Conference Series*, 35(1):127, 2006.

[238] Dorothea Golze, Marc Dvorak, and Patrick Rinke. The GW Compendium: A Practical Guide to Theoretical Photoemission Spectroscopy. *Frontiers in Chemistry*, 7, 2019.

[239] M. Feidt, S. Mathias, and M. Aeschlimann. Development of an analytical simulation framework for angle-resolved photoemission spectra. *Phys. Rev. Mater.*, 3:123801, 2019.

[240] Iulia Emilia Brumboiu, Olle Eriksson, and Patrick Norman. Photoelectron Spectroscopy of Molecules Beyond the Electric Dipole Approximation. *Journal of Chemical Theory and Computation*, 15(10):5483–5494, 2019.

[241] J Maurer and U Keller. Ionization in intense laser fields beyond the electric dipole approximation: concepts, methods, achievements and future directions. *Journal of Physics B: Atomic, Molecular and Optical Physics*, 54(9):094001, 2021.

[242] F. Schwabl. *Quantum Mechanics*. Springer Berlin Heidelberg, 2007.

[243] M Dauth, M Wiessner, V Feyer, A Schöll, P Puschnig, F Reinert, and S Kümmel. Angle resolved photoemission from organic semiconductors: orbital imaging beyond the molecular orbital interpretation. *New Journal of Physics*, 16(10):103005, 2014.

[244] Barry T. Pickup. On the theory of fast photoionization processes. *Chemical Physics*, 19(2):193–208, 1977.

[245] J. V. Ortiz. Dyson-orbital concepts for description of electrons in molecules. *The Journal of Chemical Physics*, 153(7):070902, 2020.

[246] Donald G. Truhlar, Philippe C. Hiberty, Sason Shaik, Mark S. Gordon, and David Danovich. Orbitals and the Interpretation of Photoelectron Spectroscopy and (e,2e) Ionization Experiments. *Angewandte Chemie*, 131(36):12460–12466, 2019.

[247] C. Melania Oana and Anna I. Krylov. Cross sections and photoelectron angular distributions in photodetachment from negative ions using equation-of-motion coupled-cluster Dyson orbitals. *The Journal of Chemical Physics*, 131(12):124114, 2009.

[248] Marta L. Vidal, Anna I. Krylov, and Sonia Coriani. Dyson orbitals within the fc-CVS-EOM-CCSD framework: theory and application to X-ray photoelectron spectroscopy of ground and excited states. *Phys. Chem. Chem. Phys.*, 22:2693–2703, 2020.

[249] Daniel Lüftner, Simon Weiß, Xiaosheng Yang, Philipp Hurdax, Vitaliy Feyer, Alexander Gottwald, Georg Koller, Serguei Soubatch, Peter Puschnig, Michael G. Ramsey, and F. Stefan Tautz. Understanding the photoemission distribution of strongly interacting two-dimensional overlayers. *Phys. Rev. B*, 96:125402, 2017.

[250] B. A. Lippmann and Julian Schwinger. Variational Principles for Scattering Processes. I. *Phys. Rev.*, 79:469–480, 1950.

[251] Seungsuk Han and David R. Yarkony. Determining partial differential cross sections for low-energy electron photodetachment involving conical intersections using the solution of a Lippmann-Schwinger equation constructed with standard electronic structure techniques. *The Journal of Chemical Physics*, 134(17):174104, 2011.

[252] H. Ebert, D. Ködderitzsch, and J. Minár. Calculating condensed matter properties using the KKR-Green's function method—recent developments and applications. *Reports on Progress in Physics*, 74(9):096501, 2011.

[253] Jürgen Braun, Ján Minár, and Hubert Ebert. Correlation, temperature and disorder: Recent developments in the one-step description of angle-resolved photoemission. *Physics Reports*, 740:1–34, 2018.

[254] S. Beaulieu, J. Schusser, S. Dong, M. Schüler, T. Pincelli, M. Dendzik, J. Maklar, A. Neef, H. Ebert, K. Hricovini, M. Wolf, J. Braun, L. Rettig, J. Minár, and R. Ernstorfer. Revealing Hidden Orbital Pseudospin Texture with Time-Reversal Dichroism in Photoelectron Angular Distributions. *Physical Review Letters*, 125:216404, 2020.

[255] Richard Y. Koyama and Neville V. Smith. Photoemission Properties of Simple Metals. *Phys. Rev. B*, 2:3049–3059, 1970.

[256] J.B. Pendry. Theory of photoemission. *Surface Science*, 57(2):679–705, 1976.

[257] Daniel Lueftner. *Orbital tomography: Understanding photoemission of organic molecular films*. PhD thesis, University of Graz, 2015.

[258] M. J. Frisch, G. W. Trucks, H. B. Schlegel, G. E. Scuseria, M. A. Robb, J. R. Cheeseman, G. Scalmani, V. Barone, G. A. Petersson, H. Nakatsuji, X. Li, M. Caricato, A. V. Marenich, J. Bloino, B. G. Janesko, R. Gomperts, B. Mennucci, H. P. Hratchian, J. V. Ortiz, A. F. Izmaylov, J. L. Sonnenberg, D. Williams-Young, F. Ding, F. Lipparini, F. Egidi, J. Goings, B. Peng, A. Petrone, T. Henderson, D. Ranasinghe, V. G. Zakrzewski, J. Gao, N. Rega, G. Zheng, W. Liang, M. Hada, M. Ehara, K. Toyota, R. Fukuda, J. Hasegawa, M. Ishida, T. Nakajima, Y. Honda, O. Kitao, H. Nakai, T. Vreven, K. Throssell, J. A. Montgomery, Jr., J. E. Peralta, F. Ogliaro, M. J. Bearpark, J. J. Heyd, E. N. Brothers, K. N. Kudin, V. N. Staroverov, T. A. Keith, R. Kobayashi, J. Normand, K. Raghavachari, A. P. Rendell, J. C. Burant, S. S. Iyengar, J. Tomasi, M. Cossi, J. M. Millam, M. Klene, C. Adamo, R. Cammi, J. W. Ochterski, R. L. Martin, K. Morokuma, O. Farkas, J. B. Foresman, and D. J. Fox. Gaussian 16 Revision C.01, 2016. Gaussian Inc. Wallingford CT.

[259] E. Aprà, E. J. Bylaska, W. A. de Jong, N. Govind, K. Kowalski, T. P. Straatsma, M. Valiev, H. J. J. van Dam, Y. Alexeev, J. Anchell, V. Anisimov, F. W. Aquino, R. Atta-Fynn,

J. Autschbach, N. P. Bauman, J. C. Becca, D. E. Bernholdt, K. Bhaskaran-Nair, S. Bogatko, P. Borowski, J. Boschen, J. Brabec, A. Bruner, E. Cauët, Y. Chen, G. N. Chuev, C. J. Cramer, J. Daily, M. J. O. Deegan, T. H. Dunning, M. Dupuis, K. G. Dyall, G. I. Fann, S. A. Fischer, A. Fonari, H. Früchtl, L. Gagliardi, J. Garza, N. Gawande, S. Ghosh, K. Glaesemann, A. W. Götz, J. Hammond, V. Helms, E. D. Hermes, K. Hirao, S. Hirata, M. Jacquelin, L. Jensen, B. G. Johnson, H. Jónsson, R. A. Kendall, M. Klemm, R. Kobayashi, V. Konkov, S. Krishnamoorthy, M. Krishnan, Z. Lin, R. D. Lins, R. J. Littlefield, A. J. Logsdail, K. Lopata, W. Ma, A. V. Marenich, J. Martin del Campo, D. Mejia-Rodriguez, J. E. Moore, J. M. Mullin, T. Nakajima, D. R. Nascimento, J. A. Nichols, P. J. Nichols, J. Nieplocha, A. Otero-de-la Roza, B. Palmer, A. Panyala, T. Pirojsirikul, B. Peng, R. Peverati, J. Pittner, L. Pollack, R. M. Richard, P. Sadayappan, G. C. Schatz, W. A. Shelton, D. W. Silverstein, D. M. A. Smith, T. A. Soares, D. Song, M. Swart, H. L. Taylor, G. S. Thomas, V. Tipparaju, D. G. Truhlar, K. Tsemekhman, T. Van Voorhis, Á. Vázquez-Mayagoitia, P. Verma, O. Villa, A. Vishnu, K. D. Vogiatzis, D. Wang, J. H. Weare, M. J. Williamson, T. L. Windus, K. Woliński, A. T. Wong, Q. Wu, C. Yang, Q. Yu, M. Zacharias, Z. Zhang, Y. Zhao, and R. J. Harrison. NWChem: Past, present, and future. *The Journal of Chemical Physics*, 152(18):184102, 2020.

[260] Dominik Brandstetter, Xiaosheng Yang, Daniel Lüftner, F. Stefan Tautz, and Peter Puschnig. kMap.py: A Python program for simulation and data analysis in photoemission tomography. *Comp. Phys. Commun.*, 263:107905, 2021.

[261] Michael Rohlfing and Steven G. Louie. Electron-hole excitations and optical spectra from first principles. *Phys. Rev. B*, 62:4927–4944, 2000.

[262] Robert Wallauer, Miriam Raths, Klaus Stallberg, Lasse Münster, Dominik Brandstetter, Xiaosheng Yang, Jens Güdde, Peter Puschnig, Serguei Soubatch, Christian Kumpf, Francois C. Bocquet, Frank Stefan Tautz, and Ulrich Höfer. Tracing orbital images on ultrafast time scales. *Science*, 371:1056–1059, 2021.

[263] C. Melania Oana and Anna I. Krylov. Dyson orbitals for ionization from the ground and electronically excited states within equation-of-motion coupled-cluster formalism: Theory, implementation, and examples. *The Journal of Chemical Physics*, 127(23):234106, 2007.

[264] Bruno Nunes Cabral Tenorio, Aurora Ponzi, Sonia Coriani, and Piero Decleva. Photoionization Observables from Multi-Reference Dyson Orbitals Coupled to B-Spline DFT and TD-DFT Continuum. *Molecules*, 27(4), 2022.

[265] A. Liebsch. Theory of Angular Resolved Photoemission from Adsorbates. *Phys. Rev. Lett.*, 32:1203–1206, 1974.

[266] A. Liebsch. Theory of the angular-resolved photoemission from TaS2. *Solid State Communications*, 19(12):1193–1196, 1976.

[267] Ansgar Liebsch. Theory of Angle-Resolved Photoemission from Ordered Overlayers. *Phys. Rev. Lett.*, 38:248–251, 1977.

[268] James W. Davenport. Ultraviolet Photoionization Cross Sections for N_2 and CO. *Phys. Rev. Lett.*, 36:945–949, 1976.

[269] James W. Davenport. Multiple scattering theory of photoemission. *International Journal of Quantum Chemistry*, 12(S11):89–96, 1977.

[270] J. W. Davenport. Determination of adsorbate bond geometry using photoemission. *Journal of Vacuum Science and Technology*, 15(2):433–439, 1978.

[271] Warren D. Grobman. Angle-resolved photoemission from molecules in the independent-atomic-center approximation. *Phys. Rev. B*, 17:4573–4585, 1978.

[272] M. Scheffler, K. Kambe, and F. Forstmann. Angle resolved photoemission from adsorbates: Theoretical considerations of polarization effects and symmetry. *Solid State Communications*, 25(2):93–99, 1978.

[273] N J Shevchik. Atomic dipole theory of photoemission from molecules adsorbed on surfaces. *Journal of Physics C: Solid State Physics*, 11(16):3521, 1978.

[274] S.M. Goldberg, C.S. Fadley, and S. Kono. Photoelectric cross-sections for fixed-orientation atomic orbitals: Relationship to the plane-wave final state approximation and angle-resolved photoemission. *Solid State Communications*, 28(6):459–463, 1978.

[275] S.M. Goldberg, C.S. Fadley, and S. Kono. Photoionization cross-sections for atomic orbitals with random and fixed spatial orientation. *Journal of Electron Spectroscopy and Related Phenomena*, 21(4):285–363, 1981.

[276] K. Kambe and M. Scheffler. Theory of photoexcitation of adsorbates: An analysis of atomic, adlayer, and substrate effects. *Surface Science*, 89(1):262–273, 1979.

[277] N.V. Richardson. Comments on angle-resolved photoemission from oriented films of lead phthalocyanine on a Cu100 surface. *Chemical Physics Letters*, 102(4):390–391, 1983.

[278] George B. Arfken, Hans J. Weber, and Frank E. Harris. *Mathematical Methods for Physicists*. Elsevier Academic Press, 7th edition, 2013.

[279] Albert Messiah. *Quantum Mechanics Volume I+II*. Elsevier Science B.V., 1961.

[280] Samer Gozem, Anastasia O. Gunina, Takatoshi Ichino, David L. Osborn, John F. Stanton, and Anna I. Krylov. Photoelectron Wave Function in Photoionization: Plane Wave or Coulomb Wave? *The Journal of Physical Chemistry Letters*, 6(22):4532–4540, 2015.

[281] William J. Thompson. A concise derivation of the plane-wave partial-wave expansion. *American Journal of Physics*, 60(4):378–379, 1992.

[282] Gerd Schönhense. Circular Dichroism and Spin Polarization in Photoemission from Adsorbates and Non-Magnetic Solids. *Physica Scripta*, 1990(T31):255, 1990.

[283] Cristina Bena and Gilles Montambaux. Remarks on the tight-binding model of graphene. *New Journal of Physics*, 11(9):095003, 2009.

[284] Hiroaki Tanaka, Kenta Kuroda, and Tomohiro Matsushita. SPADExp: A photoemission angular distribution simulator directly linked to first-principles calculations. *Journal of Electron Spectroscopy and Related Phenomena*, 264:147297, 2023.

[285] S. Nagamatsu, S. Kera, K. Okudaira, T. Fujikawa, and N. Ueno. Multiple-Scattering Approach to Angle-Resolved Ultraviolet Photoelectron Spectroscopy of Large Molecules. *e-Journal of Surface Science and Nanotechnology*, 3:461–465, 2005.

[286] Hiroshi Shinotsuka, Hiroko Arai, and Takashi Fujikawa. Depth distribution function calculated by quantum scattering theory. *Phys. Rev. B*, 77:085404, 2008.

[287] N. Komiya, K. Hatada, F. Ota, P. Krüger, T. Fujikawa, and K. Niki. Multiple scattering approach to photoemission from the highest occupied molecular orbital of pentacene. *Journal of Electron Spectroscopy and Related Phenomena*, 220:21–24, 2017. Proceedings of the 39th International Conference on Vacuum Ultraviolet and X-ray Physics (VUVX-2016).

[288] Liang Tao and Armin Scrinzi. Photo-electron momentum spectra from minimal volumes: the time-dependent surface flux method. *New Journal of Physics*, 14(1):013021, 2012.

[289] Umberto De Giovannini, Gustavo Brunetto, Alberto Castro, Jessica Walkenhorst, and Angel Rubio. Simulating Pump–Probe Photoelectron and Absorption Spectroscopy on the Attosecond Timescale with Time-Dependent Density Functional Theory. *ChemPhysChem*, 14(7):1363–1376, 2013.

[290] Shunsuke A. Sato, Hannes Hübener, Angel Rubio, and Umberto De Giovannini. First-principles simulations for attosecond photoelectron spectroscopy based on time-dependent density functional theory. *The European Physical Journal B*, 91(6):126, 2018.

[291] Michael Schüler, Umberto De Giovannini, Hannes Hübener, Angel Rubio, Michael A. Sentef, and Philipp Werner. Local Berry curvature signatures in dichroic angle-resolved photoelectron spectroscopy from two-dimensional materials. *Science Advances*, 6(9):eaay2730, 2020.

[292] A Crawford-Uranga, U De Giovannini, D J Mowbray, S Kurth, and A Rubio. Modelling the effect of nuclear motion on the attosecond time-resolved photoelectron spectra of ethylene. *Journal of Physics B: Atomic, Molecular and Optical Physics*, 47(12):124018, 2014.

[293] Umberto De Giovannini. *Pump-Probe Photoelectron Spectra*, pages 293–311. Springer International Publishing, Cham, 2020.

[294] Andrea Trabattoni, Joss Wiese, Umberto De Giovannini, Jean-François Olivieri, Terry Mullins, Jolijn Onvlee, Sang-Kil Son, Biagio Frusteri, Angel Rubio, Sebastian Trippel, and Jochen Küpper. Setting the photoelectron clock through molecular alignment. *Nature Communications*, 11(1):2546, 2020.

[295] Ofer Neufeld, Wenwen Mao, Hannes Hübener, Nicolas Tancogne-Dejean, Shunsuke A. Sato, Umberto De Giovannini, and Angel Rubio. Time- and angle-resolved photoelectron spectroscopy of strong-field light-dressed solids: Prevalence of the adiabatic band picture. *Phys. Rev. Res.*, 4:033101, 2022.

[296] Larissa Egger, Michael Hollerer, Christian S. Kern, Hannes Herrmann, Philipp Hurdax, Anja Haags, Xiaosheng Yang, Alexander Gottwald, Mathias Richter, Serguei Soubatch, F. Stefan Tautz, Georg Koller, Peter Puschnig, Michael G. Ramsey, and Martin Sterrer. Charge-Promoted Self-Metalation of Porphyrins on an Oxide Surface. *Angewandte Chemie International Edition*, 60(10):5078–5082, 2021.

[297] K. Diller, F. Klappenberger, F. Allegretti, A. C. Papageorgiou, S. Fischer, A. Wiengarten, S. Joshi, K. Seufert, D. Écija, W. Auwärter, and J. V. Barth. Investigating the molecule-substrate interaction of prototypic tetrapyrrole compounds: Adsorption and self-metalation of porphine on Cu(111). *The Journal of Chemical Physics*, 138(15):154710, 2013.

[298] Hubertus Marbach. Surface-Mediated in Situ Metalation of Porphyrins at the Solid-Vacuum Interface. *Accounts of Chemical Research*, 48(9):2649–2658, 2015.

[299] Philipp Hurdax, Michael Hollerer, Peter Puschnig, Daniel Lüftner, Larissa Egger, Michael G. Ramsey, and Martin Sterrer. Controlling the Charge Transfer across Thin Dielectric Interlayers. *Advanced Materials Interfaces*, 7(14):2000592, 2020.

[300] Julia Köbl, Tao Wang, Cici Wang, Martin Drost, Fan Tu, Qian Xu, Huanxin Ju, Daniel Wechsler, Matthias Franke, Haibin Pan, Hubertus Marbach, Hans-Peter Steinrück, Junfa Zhu, and Ole Lytken. Hungry Porphyrins: Protonation and Self-Metalation of Tetraphenylporphyrin on TiO2(110)-1 $\times$ 1. *ChemistrySelect*, 1(19):6103–6105, 2016.

[301] Cici Wang, Qitang Fan, Yong Han, José I. Martínez, José A. Martín-Gago, Weijia Wang, Huanxin Ju, J. Michael Gottfried, and Junfa Zhu. Metalation of tetraphenylporphyrin with nickel on a TiO2(110)-1 $\times$ 2 surface. *Nanoscale*, 8:1123–1132, 2016.

[302] Giacomo Lovat, Daniel Forrer, Mikel Abadia, Marcos Dominguez, Maurizio Casarin, Celia Rogero, Andrea Vittadini, and Luca Floreano. On-Surface Synthesis of a Pure and Long-Range-Ordered Titanium(IV)-Porphyrin Contact Layer on Titanium Dioxide. *The Journal of Physical Chemistry C*, 121(25):13738–13746, 2017.

[303] Daniel Wechsler, Cynthia C. Fernández, Quratulain Tariq, Nataliya Tsud, Kevin C. Prince, Federico J. Williams, Hans-Peter Steinrück, and Ole Lytken. Interfacial Reactions of Tetraphenylporphyrin with Cobalt-Oxide Thin Films. *Chemistry – A European Journal*, 25(57):13197–13201, 2019.

[304] Johannes Schneider, Matthias Franke, Martin Gurrath, Michael Röckert, Thomas Berger, Johannes Bernardi, Bernd Meyer, Hans-Peter Steinrück, Ole Lytken, and Oliver Diwald. Porphyrin Metalation at MgO Surfaces: A Spectroscopic and Quantum Mechanical Study on Complementary Model Systems. *Chemistry – A European Journal*, 22(5):1744–1749, 2016.

[305] Johannes Schneider, Fabian Kollhoff, Johannes Bernardi, Andre Kaftan, Jörg Libuda, Thomas Berger, Mathias Laurin, and Oliver Diwald. Porphyrin Metalation at the MgO Nanocube/Toluene Interface. *ACS Applied Materials & Interfaces*, 7(41):22962–22969, 2015.

[306] Gianluca Di Filippo, Andrej Classen, Rebecca Pöschel, and Thomas Fauster. Interaction of free-base tetraphenylporphyrin with magnesium oxide: Influence of MgO morphology on metalation. *The Journal of Chemical Physics*, 146(6):064702, 2017.

[307] Stefan Mohnani and Davide Bonifazi. Supramolecular architectures of porphyrins on surfaces: The structural evolution from 1D to 2D to 3D to devices. *Coordination Chemistry Reviews*, 254(19):2342–2362, 2010. Supramolecular approaches to nano and molecular electronics.

[308] Katharina Diller, Anthoula C. Papageorgiou, Florian Klappenberger, Francesco Allegretti, Johannes V. Barth, and Willi Auwärter. In vacuo interfacial tetrapyrrole metallation. *Chem. Soc. Rev.*, 45:1629–1656, 2016.

[309] J. Michael Gottfried, Ken Flechtner, Andreas Kretschmann, Thomas Lukasczyk, and Hans-Peter Steinrück. Direct Synthesis of a Metalloporphyrin Complex on a Surface. *Journal of the American Chemical Society*, 128(17):5644–5645, 2006.

[310] Willi Auwärter, Alexander Weber-Bargioni, Susan Brink, Andreas Riemann, Agustin Schiffrin, Mario Ruben, and Johannes V. Barth. Controlled Metalation of Self-Assembled Porphyrin Nanoarrays in Two Dimensions. *ChemPhysChem*, 8(2):250–254, 2007.

[311] Niklas Nilius, Martin Sterrer, Markus Heyde, and Hans-Joachim Freund. *Atomic Scale Characterization of Defects on Oxide Surfaces*, pages 29–80. Springer International Publishing, Cham, 2015.

[312] Florian Buchner, Ina Kellner, Wolfgang Hieringer, Andreas Görling, Hans-Peter Steinrück, and Hubertus Marbach. Ordering aspects and intramolecular conformation of tetraphenylporphyrins on Ag(111). *Phys. Chem. Chem. Phys.*, 12:13082–13090, 2010.

[313] Gianfranco Pacchioni, Livia Giordano, and Matteo Baistrocchi. Charging of Metal Atoms on Ultrathin MgO/Mo(100) Films. *Phys. Rev. Lett.*, 94:226104, 2005.

[314] Martin Sterrer, Thomas Risse, Umberto Martinez Pozzoni, Livia Giordano, Markus Heyde, Hans-Peter Rust, Gianfranco Pacchioni, and Hans-Joachim Freund. Control of the Charge State of Metal Atoms on Thin MgO Films. *Phys. Rev. Lett.*, 98:096107, 2007.

[315] Andrej Classen, Rebecca Pöschel, Gianluca Di Filippo, Thomas Fauster, Osman Barış Malcıoğlu, and Michel Bockstedte. Electronic structure of tetraphenylporphyrin layers on Ag(100). *Phys. Rev. B*, 95:115414, 2017.

[316] Philipp Hurdax, Michael Hollerer, Larissa Egger, Georg Koller, Xiaosheng Yang, Anja Haags, Serguei Soubatch, Frank Stefan Tautz, Mathias Richter, Alexander Gottwald, Peter Puschnig, Martin Sterrer, and Michael G. Ramsey. Controlling the electronic and physical coupling on dielectric thin films. *Beilstein Journal of Nanotechnology*, 11:1492–1503, 2020.

[317] Jagriti Pal, Marco Smerieri, Edvige Celasco, Letizia Savio, Luca Vattuone, and Mario Rocca. Morphology of Monolayer MgO Films on Ag(100): Switching from Corrugated Islands to Extended Flat Terraces. *Phys. Rev. Lett.*, 112:126102, 2014.

[318] M. Valiev, E.J. Bylaska, N. Govind, K. Kowalski, T.P. Straatsma, H.J.J. Van Dam, D. Wang, J. Nieplocha, E. Apra, T.L. Windus, and W.A. de Jong. NWChem: A comprehensive and scalable open-source solution for large scale molecular simulations. *Computer Physics Communications*, 181(9):1477–1489, 2010.

[319] John P. Perdew, Kieron Burke, and Matthias Ernzerhof. Generalized Gradient Approximation Made Simple. *Phys. Rev. Lett.*, 77:3865–3868, 1996.

[320] G. Kresse and J. Furthmüller. Efficient iterative schemes for ab initio total-energy calculations using a plane-wave basis set. *Phys. Rev. B*, 54:11169–11186, 1996.

[321] G. Kresse and D. Joubert. From ultrasoft pseudopotentials to the projector augmented-wave method. *Phys. Rev. B*, 59:1758–1775, 1999.

[322] Sanliang Ling, Matthew B. Watkins, and Alexander L. Shluger. Effects of atomic scale roughness at metal/insulator interfaces on metal work function. *Phys. Chem. Chem. Phys.*, 15:19615–19624, 2013.

[323] J. Pal, M. Smerieri, E. Celasco, L. Savio, L. Vattuone, R. Ferrando, S. Tosoni, L. Giordano, G. Pacchioni, and M. Rocca. How Growing Conditions and Interfacial Oxygen Affect the Final Morphology of MgO/Ag(100) Films. *The Journal of Physical Chemistry C*, 118(45):26091–26102, 2014.

[324] T. Jaouen, P. Aebi, S. Tricot, G. Delhaye, B. Lépine, D. Sébilleau, G. Jézéquel, and P. Schieffer. Induced work function changes at Mg-doped MgO/Ag(001) interfaces: Combined Auger electron diffraction and density functional study. *Phys. Rev. B*, 90:125433, 2014.

[325] Martin Sterrer, Thomas Risse, and Hans-Joachim Freund. Low temperature infrared spectra of CO adsorbed on the surface of MgO(001) thin films. *Surface Science*, 596(1):222–228, 2005.

[326] Y. D. Kim, T. Wei, J. Stultz, and D. W. Goodman. Dissociation of Water on a Flat, Ordered Silica Surface. *Langmuir*, 19(4):1140–1142, 2003.

[327] Gianfranco Pacchioni. Oxygen Vacancy: The Invisible Agent on Oxide Surfaces. *ChemPhysChem*, 4(10):1041–1047, 2003.

[328] Martin Sterrer, Markus Heyde, Marek Novicki, Niklas Nilius, Thomas Risse, Hans-Peter Rust, Gianfranco Pacchioni, and Hans-Joachim Freund. Identification of Color Centers on MgO(001) Thin Films with Scanning Tunneling Microscopy. *The Journal of Physical Chemistry B*, 110(1):46–49, 2006.

[329] Martin Sterrer, Esther Fischbach, Thomas Risse, and Hans-Joachim Freund. Geometric Characterization of a Singly Charged Oxygen Vacancy on a Single-Crystalline MgO(001) Film by Electron Paramagnetic Resonance Spectroscopy. *Phys. Rev. Lett.*, 94:186101, 2005.

[330] A. Kolmakov, J. Stultz, and D. W. Goodman. Characterization of surface defects on MgO thin films by ultraviolet photoelectron and metastable impact electron spectroscopies. *The Journal of Chemical Physics*, 113(17):7564–7570, 2000.

[331] J Kramer, W Ernst, C Tegenkamp, and H Pfnür. Mechanism and kinetics of color center formation on epitaxial thin films of MgO. *Surface Science*, 517(1):87–97, 2002.

[332] Oliver T. Hofmann, Patrick Rinke, Matthias Scheffler, and Georg Heimel. Integer versus Fractional Charge Transfer at Metal(/Insulator)/Organic Interfaces: Cu(/NaCl)/TCNE. *ACS Nano*, 9(5):5391–5404, 2015.

[333] Minho Kim, Won June Kim, Timothy Gould, Eok Kyun Lee, Sébastien Lebègue, and Hyungjun Kim. uMBD: A Materials-Ready Dispersion Correction That Uniformly Treats Metallic, Ionic, and van der Waals Bonding. *Journal of the American Chemical Society*, 142(5):2346–2354, 2020.

[334] Francesco Presel, Christian S. Kern, Thomas G. Boné, Florian Schwarz, Peter Puschnig, Michael G. Ramsey, and Martin Sterrer. Charge and adsorption height dependence of the self-metalation of porphyrins on ultrathin MgO(001) films. *Phys. Chem. Chem. Phys.*, 24:28540–28547, 2022.

[335] Stefan Mohnani and Davide Bonifazi. Supramolecular architectures of porphyrins on surfaces: The structural evolution from 1D to 2D to 3D to devices. *Coordination Chemistry Reviews*, 254(19):2342–2362, 2010. Supramolecular approaches to nano and molecular electronics.

[336] Maxence Urbani, Michael Grätzel, Mohammad Khaja Nazeeruddin, and Tomás Torres. Meso-Substituted Porphyrins for Dye-Sensitized Solar Cells. *Chemical Reviews*, 114(24):12330–12396, 2014.

[337] Rubén González-Moreno, Carlos Sánchez-Sánchez, Marta Trelka, Roberto Otero, Albano Cossaro, Alberto Verdini, Luca Floreano, Marta Ruiz-Bermejo, Aran García-Lekue, José Ángel Martín-Gago, and Celia Rogero. Following the Metalation Process of Protoporphyrin IX with Metal Substrate Atoms at Room Temperature. *The Journal of Physical Chemistry C*, 115(14):6849–6854, 2011.

[338] Andrea Goldoni, Carlo A. Pignedoli, Giovanni Di Santo, Carla Castellarin-Cudia, Elena Magnano, Federica Bondino, Alberto Verdini, and Daniele Passerone. Room Temperature Metalation of 2H-TPP Monolayer on Iron and Nickel Surfaces by Picking up Substrate Metal Atoms. *ACS Nano*, 6(12):10800–10807, 2012.

[339] Can Wang, Ruimei Wang, Jakob Hauns, and Thomas Fauster. Self-Metalation of Porphyrins by Cobalt Oxide: Photoemission Spectroscopic Investigation. *The Journal of Physical Chemistry C*, 124(26):14167–14175, 2020.

[340] Francesco Armillotta, Enrico D'Incecco, Manuel Corva, Matus Stredansky, Jean-Jacques Gallet, Fabrice Bournel, Andrea Goldoni, Alberto Morgante, Erik Vesselli, and Alberto Verdini. Self-Metalation of Porphyrins at the Solid–Gas Interface. *Angewandte Chemie International Edition*, 60(49):25988–25993, 2021.

[341] Jan Nowakowski, Christian Wäckerlin, Jan Girovsky, Dorota Siewert, Thomas A. Jung, and Nirmalya Ballav. Porphyrin metalation providing an example of a redox reaction facilitated by a surface reconstruction. *Chem. Commun.*, 49:2347–2349, 2013.

[342] Giacomo Lovat, Daniel Forrer, Mikel Abadia, Marcos Dominguez, Maurizio Casarin, Celia Rogero, Andrea Vittadini, and Luca Floreano. Hydrogen capture by porphyrins at the TiO2(110) surface. *Phys. Chem. Chem. Phys.*, 17:30119–30124, 2015.

[343] Luca Schio, Daniel Forrer, Maurizio Casarin, Andrea Goldoni, Celia Rogero, Andrea Vittadini, and Luca Floreano. On surface chemical reactions of free-base and titanyl porphyrins with r-TiO2(110): a unified picture. *Phys. Chem. Chem. Phys.*, 24:12719–12744, 2022.

[344] Markus K. Kremer, Daniel Forrer, Celia Rogero, Luca Floreano, and Andrea Vittadini. Digging Ti interstitials at the r-TiO2(110) surface: Mechanism of porphyrin Ti sequestration by iminic N nucleophilic attack. *Applied Surface Science*, 564:150403, 2021.

[345] Tobias Wähler, Ralf Schuster, and Jörg Libuda. Self-Metalation of Anchored Porphyrins on Atomically Defined Cobalt Oxide Surfaces: In situ Studies by Surface Vibrational Spectroscopy. *Chemistry – A European Journal*, 26(54):12445–12453, 2020.

[346] Kristin Werner, Susanne Mohr, Matthias Schwarz, Tao Xu, Max Amende, Tibor Döpper, Andreas Görling, and Jörg Libuda. Functionalized Porphyrins on an Atomically Defined Oxide Surface: Anchoring and Coverage-Dependent Reorientation of MCTPP on Co3O4(111). *The Journal of Physical Chemistry Letters*, 7(3):555–560, 2016.

[347] Johannes Schneider, Fabian Kollhoff, Torben Schindler, Stephan Bichlmaier, Johannes Bernardi, Tobias Unruh, Jörg Libuda, Thomas Berger, and Oliver Diwald. Adsorption, Ordering, and Metalation of Porphyrins on MgO Nanocube Surfaces: The Directional Role of Carboxylic Anchoring Groups. *The Journal of Physical Chemistry C*, 120(47):26879–26888, 2016.

[348] Cynthia C. Fernández, Daniel Wechsler, Tulio C.R. Rocha, Hans-Peter Steinrück, Ole Lytken, and Federico J. Williams. Adsorption geometry of carboxylic acid functionalized porphyrin molecules on TiO2(110). *Surface Science*, 689:121462, 2019.

[349] Tobias Wähler, Ralf Schuster, and Jörg Libuda. Surface Structure Controls Self-Metalation: In-Situ IR Studies of Anchored Porphyrins on Atomically-Defined Cobalt Oxide Surfaces. *The Journal of Physical Chemistry C*, 124(39):21538–21548, 2020.

[350] Fabian Kollhoff, Johannes Schneider, Thomas Berger, Oliver Diwald, and Jörg Libuda. Thermally Activated Self-metalation of Carboxy-functionalized Porphyrin Films on MgO Nanocubes. *ChemPhysChem*, 19(17):2272–2280, 2018.

[351] Fabian Kollhoff, Johannes Schneider, Gao Li, Sami Barkaoui, Wenjie Shen, Thomas Berger, Oliver Diwald, and Jörg Libuda. Anchoring of carboxyl-functionalized porphyrins on MgO, TiO2, and Co3O4 nanoparticles. *Phys. Chem. Chem. Phys.*, 20:24858–24868, 2018.

[352] Daniel Wechsler, Cynthia C. Fernández, Hans-Peter Steinrück, Ole Lytken, and Federico J. Williams. Covalent Anchoring and Interfacial Reactions of Adsorbed Porphyrins on Rutile TiO2(110). *The Journal of Physical Chemistry C*, 122(8):4480–4487, 2018.

[353] Feifei Xiang, Tobias Schmitt, Marco Raschmann, and M. Alexander Schneider. Adsorption and self-assembly of porphyrins on ultrathin CoO films on Ir(100). *Beilstein Journal of Nanotechnology*, 11:1516–1524, 2020.

[354] Maximilian Ammon, Andreas Raabgrund, and M. Alexander Schneider. Adsorption, self-assembly and self-metalation of tetra-cyanophenyl porphyrins on semiconducting CoO(100) films. *Surface Science*, 720:122044, 2022.

[355] Silviya Ninova, Osman Barış Malcıoğlu, Philipp Auburger, Matthias Franke, Ole Lytken, Hans-Peter Steinrück, and Michel Bockstedte. Morphology dependent interaction between Co(ii)-tetraphenylporphyrin and the MgO(100) surface. *Phys. Chem. Chem. Phys.*, 23:2105–2116, 2021.

[356] Osman Barış Malcıoğlu and Michel Bockstedte. Self-metalation of a free-base porphyrin on a metal oxide surface mediated by extended defects: Insight from ab initio molecular dynamics simulations. *Surface Science*, 723:122101, 2022.

[357] G. Kresse and J. Hafner. Ab initio molecular dynamics for liquid metals. *Phys. Rev. B*, 47:558–561, 1993.

[358] G. Kresse and J. Furthmüller. Efficiency of ab-initio total energy calculations for metals and semiconductors using a plane-wave basis set. *Computational Materials Science*, 6(1):15–50, 1996.

[359] Hendrik J. Monkhorst and James D. Pack. Special points for Brillouin-zone integrations. *Phys. Rev. B*, 13:5188–5192, 1976.

[360] Silvia Schintke, Stéphane Messerli, Marina Pivetta, Fran çois Patthey, Laurent Libioulle, Massimiliano Stengel, Alessandro De Vita, and Wolf-Dieter Schneider. Insulator at the Ultrathin Limit: MgO on Ag(001). *Phys. Rev. Lett.*, 87:276801, 2001.

[361] D. A. Duncan, P. Casado Aguilar, M. Paszkiewicz, K. Diller, F. Bondino, E. Magnano, F. Klappenberger, I. Píš, A. Rubio, J. V. Barth, A. Pérez Paz, and F. Allegretti. Local adsorption structure and bonding of porphine on Cu(111) before and after self-metalation. *The Journal of Chemical Physics*, 150(9):094702, 2019.

[362] C. Bürker, A. Franco-Cañellas, K. Broch, T.-L. Lee, A. Gerlach, and F. Schreiber. Self-Metalation of 2H-Tetraphenylporphyrin on Cu(111) Studied with XSW: Influence of the Central Metal Atom on the Adsorption Distance. *The Journal of Physical Chemistry C*, 118(25):13659–13666, 2014.

[363] Alberto Verdini, Prashant Shinde, Gian Luca Montanari, Simone Tommaso Suran-Brunelli, Marco Caputo, Giovanni Di Santo, Carlo A. Pignedoli, Luca Floreano, Daniele Passerone, and Andrea Goldoni. Water Formation for the Metalation of Porphyrin Molecules on Oxidized Cu(111). *Chemistry - A European Journal*, 22(41):14672–14677, 2016.

[364] Wei Yan, Wen-Yu He, Zhao-Dong Chu, Mengxi Liu, Lan Meng, Rui-Fen Dou, Yanfeng Zhang, Zhongfan Liu, Jia-Cai Nie, and Lin He. Strain and curvature induced evolution of electronic band structures in twisted graphene bilayer. *Nature Communications*, 4(1):2159, 2013.

[365] Nicholas J. Hestand and Frank C. Spano. The Effect of Chain Bending on the Photophysical Properties of Conjugated Polymers. *The Journal of Physical Chemistry B*, 118(28):8352–8363, 2014.

[366] Irene R. Márquez, Silvia Castro-Fernández, Alba Millán, and Araceli G. Campaña. Synthesis of distorted nanographenes containing seven- and eight-membered carbocycles. *Chem. Commun.*, 54:6705–6718, 2018.

[367] Yunbin Hu, Peng Xie, Marzio De Corato, Alice Ruini, Shen Zhao, Felix Meggendorfer, Lasse Arnt Straasø, Loic Rondin, Patrick Simon, Juan Li, Jonathan J. Finley, Michael Ryan Hansen, Jean-Sébastien Lauret, Elisa Molinari, Xinliang Feng, Johannes V. Barth, Carlos-Andres Palma, Deborah Prezzi, Klaus Müllen, and Akimitsu Narita. Bandgap Engineering of Graphene Nanoribbons by Control over Structural Distortion. *Journal of the American Chemical Society*, 140(25):7803–7809, 2018.

[368] Dibyajyoti Ghosh, Debdipto Acharya, Liujiang Zhou, Wanyi Nie, Oleg V. Prezhdo, Sergei Tretiak, and Amanda J. Neukirch. Lattice Expansion in Hybrid Perovskites: Effect on Optoelectronic Properties and Charge Carrier Dynamics. *The Journal of Physical Chemistry Letters*, 10(17):5000–5007, 2019.

[369] Daejin Eom and Ja-Yong Koo. Direct measurement of strain-driven Kekulé distortion in graphene and its electronic properties. *Nanoscale*, 12:19604–19608, 2020.

[370] Gergely Dobrik, Péter Nemes-Incze, Bruno Majérus, Péter Süle, Péter Vancsó, Gábor Piszter, Miklós Menyhárd, Benjámin Kalas, Péter Petrik, Luc Henrard, and Levente Tapasztó. Large-area nanoengineering of graphene corrugations for visible-frequency graphene plasmons. *Nature Nanotechnology*, 17(1):61–66, 2022.

[371] Jiye Luo, Xiaomin Xu, Renxin Mao, and Qian Miao. Curved Polycyclic Aromatic Molecules That Are π-Isoelectronic to Hexabenzocoronene. *Journal of the American Chemical Society*, 134(33):13796–13803, 2012.

[372] F. Matthias Bickelhaupt and Kendall N. Houk. Analyzing Reaction Rates with the Distortion/Interaction-Activation Strain Model. *Angewandte Chemie International Edition*, 56(34):10070–10086, 2017.

[373] Kenneth J. Shea and Jang Seob Kim. Influence of strain on chemical reactivity. Relative reactivity of torsionally distorted double bonds in MCPBA epoxidations. *Journal of the American Chemical Society*, 114(8):3044–3051, 1992.

[374] Dirk Schweitzer, Jason Shearer, Durrell K. Rittenberg, Steven C. Shoner, Jeffrey J. Ellison, Reza Loloee, Scott Lovell, David Barnhart, and Julie A. Kovacs. Enhancing Reactivity via Structural Distortion. *Inorganic Chemistry*, 41(12):3128–3136, 2002.

[375] Trevor A. Hamlin, Brian J. Levandowski, Ayush K. Narsaria, Kendall N. Houk, and F. Matthias Bickelhaupt. Structural Distortion of Cycloalkynes Influences Cycloaddition Rates both by Strain and Interaction Energies. *Chemistry – A European Journal*, 25(25):6342–6348, 2019.

[376] Oliver Bauer, Giuseppe Mercurio, Martin Willenbockel, Werner Reckien, Christoph Heinrich Schmitz, Benjamin Fiedler, Serguei Soubatch, Thomas Bredow, Frank Stefan Tautz, and Moritz Sokolowski. Role of functional groups in surface bonding of planar π-conjugated molecules. *Phys. Rev. B*, 86:235431, 2012.

[377] V. Geringer, M. Liebmann, T. Echtermeyer, S. Runte, M. Schmidt, R. Rückamp, M. C. Lemme, and M. Morgenstern. Intrinsic and extrinsic corrugation of monolayer graphene deposited on SiO_2. *Phys. Rev. Lett.*, 102:076102, 2009.

[378] A. Hauschild, K. Karki, B. C. C. Cowie, M. Rohlfing, F. S. Tautz, and M. Sokolowski. Molecular Distortions and Chemical Bonding of a Large π-Conjugated Molecule on a Metal Surface. *Phys. Rev. Lett.*, 94:036106, 2005.

[379] G. Mercurio, E. R. McNellis, I. Martin, S. Hagen, F. Leyssner, S. Soubatch, J. Meyer, M. Wolf, P. Tegeder, F. S. Tautz, and K. Reuter. Structure and Energetics of Azobenzene on Ag(111): Benchmarking Semiempirical Dispersion Correction Approaches. *Phys. Rev. Lett.*, 104:036102, 2010.

[380] Simon Weiß, Ina Krieger, Timo Heepenstrick, Serguei Soubatch, Moritz Sokolowski, and F. Stefan Tautz. Determination of the adsorption geometry of PTCDA on the Cu(100) surface. *Phys. Rev. B*, 96:075414, 2017.

[381] O. Bauer, J. Ikonomov, C. H. Schmitz, M. Willenbockel, S. Soubatch, F. S. Tautz, and M. Sokolowski. Adsorption of 3,4,9,10-Perylenetetracarboxylic Acid Dianhydride on the Cu3Au(111) Surface Studied by Normal-Incidence X-ray Standing Waves. *The Journal of Physical Chemistry C*, 122(20):10904–10917, 2018.

[382] S. Weiß, D. Gerbert, A. Stein, A. K. Schenk, X. Yang, C. Brülke, R. Kremring, S. Feldmann, F. C. Bocquet, M. Gille, S. Hecht, M. Sokolowski, P. Tegeder, S. Soubatch, and F. S. Tautz. Dependence of the adsorption height of graphenelike adsorbates on their dimensionality. *Phys. Rev. B*, 98:075410, 2018.

[383] Christine Brülke, Timo Heepenstrick, Ina Krieger, Beatrice Wolff, Xiaosheng Yang, Ali Shamsaddinlou, Simon Weiß, François C. Bocquet, F. Stefan Tautz, Serguei Soubatch, and Moritz Sokolowski. Quantitative analysis of the electronic decoupling of an organic semiconductor molecule at a metal interface by a monolayer of hexagonal boron nitride. *Phys. Rev. B*, 99:121404, 2019.

[384] A. Gerlach, F. Schreiber, S. Sellner, H. Dosch, I. A. Vartanyants, B. C. C. Cowie, T.-L. Lee, and J. Zegenhagen. Adsorption-induced distortion of $F_{16}CuPc$ on Cu(111) and Ag(111): An x-ray standing wave study. *Phys. Rev. B*, 71:205425, 2005.

[385] A. Gerlach, S. Sellner, F. Schreiber, N. Koch, and J. Zegenhagen. Substrate-dependent bonding distances of PTCDA: A comparative x-ray standing-wave study on Cu(111) and Ag(111). *Phys. Rev. B*, 75:045401, 2007.

[386] C. Stadler, S. Hansen, F. Pollinger, C. Kumpf, E. Umbach, T.-L. Lee, and J. Zegenhagen. Structural investigation of the adsorption of SnPc on Ag(111) using normal-incidence x-ray standing waves. *Phys. Rev. B*, 74:035404, 2006.

[387] E M Reinisch, T Ules, P Puschnig, S Berkebile, M Ostler, T Seyller, M G Ramsey, and G Koller. Development and character of gap states on alkali doping of molecular films. *New Journal of Physics*, 16(2):023011, 2014.

[388] M. Willenbockel, D. Lüftner, B. Stadtmüller, G. Koller, C. Kumpf, S. Soubatch, P. Puschnig, M. G. Ramsey, and F. S. Tautz. The interplay between interface structure, energy level alignment and chemical bonding strength at organic–metal interfaces. *Phys. Chem. Chem. Phys.*, 17:1530–1548, 2015.

[389] P. Puschnig, E.-M. Reinisch, T. Ules, G. Koller, S. Soubatch, M. Ostler, L. Romaner, F. S. Tautz, C. Ambrosch-Draxl, and M. G. Ramsey. Orbital tomography: Deconvoluting photoemission spectra of organic molecules. *Physical Review B*, 84:235427, 2011.

[390] M. Wießner, D. Hauschild, A. Schöll, F. Reinert, V. Feyer, K. Winkler, and B. Krömker. Electronic and geometric structure of the PTCDA/Ag(110) interface probed by angle-resolved photoemission. *Phys. Rev. B*, 86:045417, 2012.

[391] B. Stadtmüller, M. Willenbockel, E. M. Reinisch, T. Ules, F. C. Bocquet, S. Soubatch, P. Puschnig, G. Koller, M. G. Ramsey, F. S. Tautz, and C. Kumpf. Orbital tomography for highly symmetric adsorbate systems. *Europhysics Letters*, 100(2):26008, 2012.

[392] P. Puschnig, A. D. Boese, M. Willenbockel, M. Meyer, D. Lüftner, E. M. Reinisch, T. Ules, G. Koller, S. Soubatch, M. G. Ramsey, and F. S. Tautz. Energy Ordering of Molecular Orbitals. *The Journal of Physical Chemistry Letters*, 8(1):208–213, 2017.

[393] Daniel Lüftner, Simon Weiß, Xiaosheng Yang, Philipp Hurdax, Vitaliy Feyer, Alexander Gottwald, Georg Koller, Serguei Soubatch, Peter Puschnig, Michael G. Ramsey, and F. Stefan Tautz. Understanding the photoemission distribution of strongly interacting two-dimensional overlayers. *Phys. Rev. B*, 96:125402, 2017.

[394] Xiaosheng Yang, Ina Krieger, Daniel Lüftner, Simon Weiß, Timo Heepenstrick, Michael Hollerer, Philipp Hurdax, Georg Koller, Moritz Sokolowski, Peter Puschnig, Michael G. Ramsey, F. Stefan Tautz, and Serguei Soubatch. On the decoupling of molecules at metal surfaces. *Chem. Commun.*, 54:9039–9042, 2018.

[395] Jascha Repp, Gerhard Meyer, Sladjana M. Stojković, André Gourdon, and Christian Joachim. Molecules on Insulating Films: Scanning-Tunneling Microscopy Imaging of Individual Molecular Orbitals. *Phys. Rev. Lett.*, 94:026803, 2005.

[396] J. Wollschläger, J. Viernow, C. Tegenkamp, D. Erdös, K. M. Schröder, and H. Pfnür. Stoichiometry and morphology of MgO films grown reactively on Ag(100). *Applied Surface Science*, 142(1):129–134, 1999.

[397] Sung Beom Cho, Kyung-Han Yun, Dong Su Yoo, Kiyong Ahn, and Yong-Chae Chung. Work function tuning of an ultrathin MgO film on an Ag substrate by generating oxygen impurities at the interface. *Thin Solid Films*, 544:541–544, 2013. The 6th International Conference on Technological Advances of Thin Films & Surface Coatings.

[398] G. Mercurio, O. Bauer, M. Willenbockel, N. Fairley, W. Reckien, C. H. Schmitz, B. Fiedler, S. Soubatch, T. Bredow, M. Sokolowski, and F. S. Tautz. Adsorption height determination of nonequivalent C and O species of PTCDA on Ag(110) using x-ray standing waves. *Phys. Rev. B*, 87:045421, 2013.

[399] Alexander Gottwald, Hendrik Kaser, and Michael Kolbe. The U125 insertion device beamline at the Metrology Light Source. *Journal of Synchrotron Radiation*, 26(2):535–542, 2019.

[400] L. Broekman, A. Tadich, E. Huwald, J. Riley, R. Leckey, T. Seyller, K. Emtsev, and L. Ley. First results from a second generation toroidal electron spectrometer. *Journal of Electron Spectroscopy and Related Phenomena*, 144-147:1001–1004, 2005.

[401] P. Puschnig and M.G. Ramsey. Photoemission Tomography: Valence Band Photoemission as a Quantitative Method for Investigating Molecular Films. In Klaus Wandelt, editor, *Encyclopedia of Interfacial Chemistry*, pages 380 – 391. Elsevier, Oxford, 2018.

[402] Christian S. Kern, Anja Haags, Larissa Egger, Xiaosheng Yang, Hans Kirschner, Susanne Wolff, Thomas Seyller, Alexander Gottwald, Mathias Richter, Umberto De Giovannini, Angel Rubio, Michael G. Ramsey, François C. Bocquet, Serguei Soubatch, F. Stefan Tautz, Peter Puschnig, and Simon Moser. Simple extension of the plane-wave final state in photoemission: Bringing understanding to the photon-energy dependence of two-dimensional materials. *Phys. Rev. Res.*, 5:033075, 2023.

[403] Simon Moser. An experimentalist's guide to the matrix element in angle resolved photoemission. *Journal of Electron Spectroscopy and Related Phenomena*, 214:29–52, 2017.

[404] J. W. Gadzuk. Surface molecules and chemisorption. II. Photoemission angular distributions. *Physical Review B*, 10:5030–5044, 1974.

[405] Phil Woodruff. *Modern Techniques of Surface Science*. Cambridge University Press, Cambridge, 2016.

[406] M. Dauth, T. Körzdörfer, S. Kümmel, J. Ziroff, M. Wiessner, A. Schöll, F. Reinert, M. Arita, and K. Shimada. Orbital Density Reconstruction for Molecules. *Physical Review Letters*, 107:193002, 2011.

[407] Ngoc Linh Nguyen, Giovanni Borghi, Andrea Ferretti, Ismaila Dabo, and Nicola Marzari. First-Principles Photoemission Spectroscopy and Orbital Tomography in Molecules from Koopmans-Compliant Functionals. *Physical Review Letters*, 114:166405, 2015.

[408] Peter Puschnig and Daniel Lüftner. Simulation of angle-resolved photoemission spectra by approximating the final state by a plane wave: From graphene to polycyclic aromatic hydrocarbon molecules. *Journal of Electron Spectroscopy and Related Phenomena*, 200:193–208, 2015.

[409] Jin-Hong Park, Choong H. Kim, Jun-Won Rhim, and Jung Hoon Han. Orbital Rashba effect and its detection by circular dichroism angle-resolved photoemission spectroscopy. *Phys. Rev. B*, 85:195401, 2012.

[410] Maximilian Ünzelmann, Hendrik Bentmann, Philipp Eck, Tilman Kißlinger, Begmuhammet Geldiyev, Janek Rieger, Simon Moser, Raphael C. Vidal, Katharina Kißner, Lutz Hammer, M. Alexander Schneider, Thomas Fauster, Giorgio Sangiovanni, Domenico Di Sante, and Friedrich Reinert. Orbital-Driven Rashba Effect in a Binary Honeycomb Monolayer AgTe. *Physical Review Letters*, 124(17):176401, 2020.

[411] S. Moser. A toy model for dichroism in angle resolved photoemission. *Journal of Electron Spectroscopy and Related Phenomena*, 262(August 2022):147278, 2023.

[412] Michael Schüler, Umberto De Giovannini, Hannes Hübener, Angel Rubio, Michael A. Sentef, Thomas P. Devereaux, and Philipp Werner. How Circular Dichroism in Time- and Angle-Resolved Photoemission Can Be Used to Spectroscopically Detect Transient Topological States in sGraphene. *Physical Review X*, 10:041013, 2020.

[413] Michael Schüler, Tommaso Pincelli, Shuo Dong, Thomas P. Devereaux, Martin Wolf, Laurenz Rettig, Ralph Ernstorfer, and Samuel Beaulieu. Polarization-Modulated Angle-Resolved Photoemission Spectroscopy: Toward Circular Dichroism without Circular Photons and Bloch Wave-function Reconstruction. *Physical Review X*, 12:011019, 2022.

[414] S. Thevuthasan, G. S. Herman, A. P. Kaduwela, R. S. Saiki, Y. J. Kim, W. Niemczura, M. Burger, and C. S. Fadley. Electron emission holography at keV energies: Estimates of accuracy and limitations. *Physical Review Letters*, 67:469–472, 1991.

[415] P. Krüger, F. Da Pieve, and J. Osterwalder. Real-space multiple scattering method for angle-resolved photoemission and valence-band photoelectron diffraction and its application to Cu(111). *Physical Review B*, 83:115437, 2011.

[416] M. Dauth, M. Graus, I. Schelter, M. Wießner, A. Schöll, F. Reinert, and S. Kümmel. Perpendicular Emission, Dichroism, and Energy Dependence in Angle-Resolved Photoemission: The Importance of The Final State. *Physical Review Letters*, 117:183001, 2016.

[417] Peter Krüger and Fumihiko Matsui. Observation and theory of strong circular dichroism in angle-revolved photoemission from graphite. *Journal of Electron Spectroscopy and Related Phenomena*, 258(March):147219, 2022.

[418] S. Kera, S Tanaka, H Yamane, D Yoshimura, K K Okudaira, K Seki, and Nobuo Ueno. Quantitative analysis of photoelectron angular distribution of single-domain organic monolayer film: NTCDA on GeS(001). *Chemical Physics*, 325(1):113–120, 2006.

[419] M Dauth and S Kümmel. Predicting photoemission intensities and angular distributions with real-time density-functional theory. *Physical Review A*, 93(2):022502, 2016.

[420] C. Riedl, C. Coletti, T. Iwasaki, A. A. Zakharov, and U. Starke. Quasi-Free-Standing Epitaxial Graphene on SiC Obtained by Hydrogen Intercalation. *Physical Review Letters*, 103:246804, 2009.

[421] F. Speck, J. Jobst, F. Fromm, M. Ostler, D. Waldmann, M. Hundhausen, H. B. Weber, and Th Seyller. The quasi-free-standing nature of graphene on H-saturated SiC(0001). *Applied Physics Letters*, 99(12):122106, 2011.

[422] J. Sforzini, L. Nemec, T. Denig, B. Stadtmüller, T.-L. Lee, C. Kumpf, S. Soubatch, U. Starke, P. Rinke, V. Blum, F. C. Bocquet, and F. S. Tautz. Approaching Truly Freestanding Graphene: The Structure of Hydrogen-Intercalated Graphene on 6H-SiC(0001). *Physical Review Letters*, 114:106804, 2015.

[423] Aaron Bostwick, Taisuke Ohta, Thomas Seyller, Karsten Horn, and Eli Rotenberg. Quasiparticle dynamics in graphene. *Nature Physics*, 3(1):36–40, 2007.

[424] Isabella Gierz, Jürgen Henk, Hartmut Höchst, Christian R. Ast, and Klaus Kern. Illuminating the dark corridor in graphene: Polarization dependence of angle-resolved photoemission spectroscopy on graphene. *Physical Review B*, 83(12):121408, 2011.

[425] Warren D Grobman. Angle-resolved photoemission from molecules in the independent-atomic-center approximation. *Physical Review B*, 17(12):4573–4585, 1978.

[426] Nobuo Ueno, Katsumi Suzuki, Shinji Hasegawa, Koji Kamiya, Kazuhiko Seki, and Hiroo Inokuchi. Angle-resolved photoemission spectroscopy of ultrathin films of H2-phthalocyanine on MoS2 surfaces. *The Journal of Chemical Physics*, 99(9):7169, 1993.

[427] Nobuo Ueno, Akinori Kitamura, Koji K Okudaira, Takayuki Miyamae, Yoshiya Harada, Sinji Hasegawa, Hisao Ishii, Hiroo Inokuchi, Takashi Fujikawa, Takafumi Miyazaki, and Kazuhiko Seki. Angle-resolved ultraviolet photoelectron spectroscopy of thin films of bis(1,2,5-thiadiazolo)-p-quinobis (1,3-dithiole) on the MoS_2 surface. *The Journal of Chemical Physics*, 107(6):2079, 1997.

[428] K. V. Emtsev, F. Speck, Th. Seyller, L. Ley, and J. D. Riley. Interaction, growth, and ordering of epitaxial graphene on SiC{0001} surfaces: A comparative photoelectron spectroscopy study. *Physical Review B*, 77:155303, 2008.

[429] Konstantin V. Emtsev, Aaron Bostwick, Karsten Horn, Johannes Jobst, Gary L. Kellogg, Lothar Ley, Jessica L. McChesney, Taisuke Ohta, Sergey A. Reshanov, Jonas Röhrl, Eli Rotenberg, Andreas K. Schmid, Daniel Waldmann, Heiko B. Weber, and Thomas Seyller. Towards wafer-size graphene layers by atmospheric pressure graphitization of silicon carbide. *Nature Materials*, 8(3):203–207, 2009.

[430] S. Forti, K. V. Emtsev, C. Coletti, A. A. Zakharov, C. Riedl, and U. Starke. Large-area homogeneous quasifree standing epitaxial graphene on SiC(0001): Electronic and structural characterization. *Physical Review B*, 84(12):125449, 2011.

[431] Miguel A.L. Marques, Alberto Castro, George F. Bertsch, and Angel Rubio. octopus: a first-principles tool for excited electron-ion dynamics. *Computer Physics Communications*, 151(1):60–78, 2003.

[432] Alberto Castro, Heiko Appel, Micael Oliveira, Carlo A. Rozzi, Xavier Andrade, Florian Lorenzen, M. A. L. Marques, E. K. U. Gross, and Angel Rubio. octopus: a tool for the application of time-dependent density functional theory. *physica status solidi (b)*, 243(11):2465–2488, 2006.

[433] Xavier Andrade, Joseba Alberdi-Rodriguez, David A Strubbe, Micael J T Oliveira, Fernando Nogueira, Alberto Castro, Javier Muguerza, Agustin Arruabarrena, Steven G Louie, Alán Aspuru-Guzik, Angel Rubio, and Miguel A L Marques. Time-dependent density-functional theory in massively parallel computer architectures: the octopus project. *Journal of Physics: Condensed Matter*, 24(23):233202, 2012.

[434] Umberto De Giovannini, Ask Hjorth Larsen, and Angel Rubio. Modeling electron dynamics coupled to continuum states in finite volumes with absorbing boundaries. *The European Physical Journal B*, 88(3):56, 2015.

[435] C Hartwigsen, S Goedecker, and J Hutter. Relativistic separable dual-space Gaussian pseudopotentials from H to Rn. *Physical Review B*, 58(7):3641–3662, 1998.

[436] N. Mukunda. Completeness of the Coulomb wave functions in quantum mechanics. *American Journal of Physics*, 46(9):910–913, 1978.

[437] L.D. Landau and E.M. Lifshitz. SCHRÖDINGER'S EQUATION. In *Quantum Mechanics*, pages 50–81. Elsevier, 1977.

[438] Milton Abramowitz, Irene A. Stegun, and Robert H. Romer. Handbook of Mathematical Functions with Formulas, Graphs, and Mathematical Tables. *American Journal of Physics*, 56(10):958–958, 1988.

[439] James Avery and John Avery. *Generalized Sturmians and Atomic Spectra*. WORLD SCIENTIFIC, 2006.

[440] J. Humblet. Analytical structure and properties of Coulomb wave functions for real and complex energies. *Annals of Physics*, 155(2):461–493, 1984.

[441] Vincenzo Aquilanti and Andrea Caligiana. Sturmian approach to one-electron many-center systems: integrals and iteration schemes. *Chemical Physics Letters*, 366(1-2):157–164, 2002.

[442] John Avery. Many-center Coulomb Sturmians and Shibuya-Wulfman integrals. *International Journal of Quantum Chemistry*, 100(2):121–130, 2004.

[443] C. S. Kern, A. Windischbacher, and P. Puschnig. Photoemission orbital tomography for excitons in organic molecules. *Phys. Rev. B*, 108:085132, 2023.

[444] Timm Rohwer, Stefan Hellmann, Martin Wiesenmayer, Christian Sohrt, Ankatrin Stange, Bartosz Slomski, Adra Carr, Yanwei Liu, Luis Miaja Avila, Matthias Kalläne, Stefan Mathias, Lutz Kipp, Kai Rossnagel, and Michael Bauer. Collapse of long-range charge order tracked by time-resolved photoemission at high momenta. *Nature*, 471:490–493, 2011.

[445] Steffen Eich, Moritz Plötzing, Markus Rollinger, Sebastian Emmerich, Roman Adam, Cong Chen, Henry Cornelius Kapteyn, Margaret M. Murnane, Lukasz Plucinski, Daniel Steil, Benjamin Stadtmüller, Mirko Cinchetti, Martin Aeschlimann, Claus M. Schneider, and Stefan Mathias. Band structure evolution during the ultrafast ferromagnetic-paramagnetic phase transition in cobalt. *Science Advances*, 3(3):e1602094, 2017.

[446] C. W. Nicholson, A. Lücke, W. G. Schmidt, M. Puppin, L. Rettig, R. Ernstorfer, and M. Wolf. Beyond the molecular movie: Dynamics of bands and bonds during a photoinduced phase transition. *Science*, 362:821–825, 2018.

[447] Kiana Baumgärtner, Marvin Reuner, Christian Metzger, Dmytro Kutnyakhov, Michael Heber, Federico Pressacco, Chul-Hee Min, Thiago R. F. Peixoto, Mario Reiser, Chan Kim, Wei Lu, Roman Shayduk, Manuel Izquierdo, Günter Brenner, Friedrich Roth, Achim Schöll, Serguei Molodtsov, Wilfried Wurth, Friedrich Reinert, Anders Madsen, Daria Popova-Gorelova, and Markus Scholz. Ultrafast orbital tomography of a pentacene film using time-resolved momentum microscopy at a FEL. *Nature Communications*, 13(1):2741, 2022.

[448] Alexander Neef, Samuel Beaulieu, Sebastian Hammer, Shuo Dong, Julian Maklar, Tommaso Pincelli, R. Patrick Xian, Martin Wolf, Laurenz Rettig, Jens Pflaum, and Ralph Ernstorfer. Orbital-resolved observation of singlet fission. *Nature*, 616(7956):275–279, 2023.

[449] R. Wallauer, J. Reimann, N. Armbrust, J. Güdde, and U. Höfer. Intervalley scattering in MoS_2 imaged by two-photon photoemission with a high-harmonic probe. *Applied Physics Letters*, 109(16), 2016. 162102.

[450] R. Bertoni, C. W. Nicholson, L. Waldecker, H. Hübener, C. Monney, U. De Giovannini, M. Puppin, M. Hoesch, E. Springate, R. T. Chapman, C. Cacho, M. Wolf, A. Rubio, and R. Ernstorfer. Generation and Evolution of Spin-, Valley-, and Layer-Polarized Excited Carriers in Inversion-Symmetric WSe_2. *Phys. Rev. Lett.*, 117:277201, 2016.

[451] Julien Madéo, Michael K. L. Man, Chakradhar Sahoo, Marshall Campbell, Vivek Pareek, E. Laine Wong, Abdullah Al-Mahboob, Nicholas S. Chan, Arka Karmakar, Bala Murali Krishna Mariserla, Xiaoqin Li, Tony F. Heinz, Ting Cao, and Keshav M. Dani. Directly visualizing the momentum-forbidden dark excitons and their dynamics in atomically thin semiconductors. *Science*, 370(6521):1199–1204, 2020.

[452] Robert Wallauer, Raul Perea-Causin, Lasse Münster, Sarah Zajusch, Samuel Brem, Jens Güdde, Katsumi Tanimura, Kai-Qiang Lin, Rupert Huber, Ermin Malic, and Ulrich Höfer. Momentum-Resolved Observation of Exciton Formation Dynamics in Monolayer WS_2. *Nano Letters*, 21(13):5867–5873, 2021. PMID: 34165994.

[453] Joakim Hagel, Samuel Brem, Christopher Linderälv, Paul Erhart, and Ermin Malic. Exciton landscape in van der Waals heterostructures. *Phys. Rev. Res.*, 3:043217, 2021.

[454] Jan Philipp Bange, Paul Werner, David Schmitt, Wiebke Bennecke, Giuseppe Meneghini, AbdulAziz AlMutairi, Marco Merboldt, Kenji Watanabe, Takashi Taniguchi, Sabine Steil, Daniel Steil, R Thomas Weitz, Stephan Hofmann, G S Matthijs Jansen, Samuel Brem, Ermin Malic, Marcel Reutzel, and Stefan Mathias. Ultrafast dynamics of bright and dark excitons in monolayer WSe2 and heterobilayer WSe2/MoS2. *2D Materials*, 10(3):035039, 2023.

[455] Jan Philipp Bange, David Schmitt, Wiebke Bennecke, Giuseppe Meneghini, Abdul Aziz AlMutairi, Kenji Watanabe, Takashi Taniguchi, Daniel Steil, Sabine Steil, R. Thomas Weitz, G. S. Matthijs Jansen, Stephan Hofmann, Samuel Brem, Ermin Malic, Marcel Reutzel, and Stefan Mathias. Probing correlations in the exciton landscape of a moiré heterostructure. *arXiv: 2303.17886*, 2023.

[456] Sivan Refaely-Abramson, Diana Y. Qiu, Steven G. Louie, and Jeffrey B. Neaton. Defect-Induced Modification of Low-Lying Excitons and Valley Selectivity in Monolayer Transition Metal Dichalcogenides. *Phys. Rev. Lett.*, 121:167402, 2018.

[457] Elmar Mitterreiter, Bruno Schuler, Ana Micevic, Daniel Hernangómez-Pérez, Katja Barthelmi, Katherine A. Cochrane, Jonas Kiemle, Florian Sigger, Julian Klein, Edward Wong, Edward S. Barnard, Kenji Watanabe, Takashi Taniguchi, Michael Lorke, Frank Jahnke, Johnathan J. Finley, Adam M. Schwartzberg, Diana Y. Qiu, Sivan Refaely-Abramson, Alexander W. Holleitner, Alexander Weber-Bargioni, and Christoph Kastl. The role of chalcogen vacancies for atomic defect emission in MoS2. *Nature Communications*, 12(1):3822, 2021.

[458] A. Hötger, T. Amit, J. Klein, K. Barthelmi, T. Pelini, A. Delhomme, S. Rey, M. Potemski, C. Faugeras, G. Cohen, D. Hernangómez-Pérez, T. Taniguchi, K. Watanabe, C. Kastl, J. J. Finley, S. Refaely-Abramson, A. W. Holleitner, and A. V. Stier. Spin-defect characteristics of single sulfur vacancies in monolayer MoS2. *npj 2D Materials and Applications*, 7(1), 2023.

[459] Wiebke Bennecke, Andreas Windischbacher, David Schmitt, Jan Philipp Bange, Ralf Hemm, Christian S. Kern, Gabriele D'Avino, Xavier Blase, Daniel Steil, Sabine Steil, Martin Aeschlimann, Benjamin Stadtmueller, Marcel Reutzel, Peter Puschnig, G. S. Matthijs Jansen, and Stefan Mathias. Multiorbital exciton formation in an organic semiconductor. *arXiv: 2303.13904*, 2023.

[460] Lorin X. Benedict, Eric L. Shirley, and Robert B. Bohn. Optical Absorption of Insulators and the Electron-Hole Interaction: An Ab Initio Calculation. *Phys. Rev. Lett.*, 80:4514–4517, 1998.

[461] Felix Plasser. Entanglement entropy of electronic excitations. *The Journal of Chemical Physics*, 144(19):194107, 2016.

[462] Daria Popova-Gorelova, Jochen Küpper, and Robin Santra. Imaging electron dynamics with time- and angle-resolved photoelectron spectroscopy. *Phys. Rev. A*, 94:013412, 2016.

[463] Marvin Reuner and Daria Popova-Gorelova. Attosecond imaging of photoinduced dynamics in molecules using time-resolved photoelectron momentum microscopy. *Phys. Rev. A*, 107:023101, 2023.

[464] Sebastian Hammon and Stephan Kümmel. Pump-probe photoemission simulated in real time: Revealing many-particle signatures. *Phys. Rev. A*, 104:012815, 2021.

[465] J. J. Mortensen, L. B. Hansen, and K. W. Jacobsen. Real-space grid implementation of the projector augmented wave method. *Phys. Rev. B*, 71:035109, 2005.

[466] J Enkovaara, C Rostgaard, J J Mortensen, J Chen, M Dulak, L Ferrighi, J Gavnholt, C Glinsvad, V Haikola, H A Hansen, H H Kristoffersen, M Kuisma, A H Larsen, L Lehtovaara, M Ljungberg, O Lopez-Acevedo, P G Moses, J Ojanen, T Olsen, V Petzold, N A Romero, J Stausholm-Moller, M Strange, G A Tritsaris, M Vanin, M Walter, B Hammer, H Häkkinen, G K H Madsen, R M Nieminen, J K Norskov, M Puska, T T Rantala, J Schiotz, K S Thygesen, and K W Jacobsen. Electronic structure calculations with GPAW: a real-space implementation of the projector augmented-wave method. *Journal of Physics: Condensed Matter*, 22(25):253202, 2010.

[467] Ask Hjorth Larsen, Jens Jorgen Mortensen, Jakob Blomqvist, Ivano E Castelli, Rune Christensen, Marcin Dulak, Jesper Friis, Michael N Groves, Bjork Hammer, Cory Hargus, Eric D Hermes, Paul C Jennings, Peter Bjerre Jensen, James Kermode, John R Kitchin, Esben Leonhard Kolsbjerg, Joseph Kubal, Kristen Kaasbjerg, Steen Lysgaard, Jon Bergmann Maronsson, Tristan Maxson, Thomas Olsen, Lars Pastewka, Andrew Peterson, Carsten Rostgaard, Jakob Schiotz, Ole Schütt, Mikkel Strange, Kristian S Thygesen, Tejs Vegge, Lasse Vilhelmsen, Michael Walter, Zhenhua Zeng, and Karsten W Jacobsen. The atomic simulation environment—a Python library for working with atoms. *Journal of Physics: Condensed Matter*, 29(27):273002, 2017.

[468] N. Troullier and José Luís Martins. Efficient pseudopotentials for plane-wave calculations. *Phys. Rev. B*, 43:1993–2006, 1991.

[469] Charles R. Harris, K. Jarrod Millman, St'efan J. van der Walt, Ralf Gommers, Pauli Virtanen, David Cournapeau, Eric Wieser, Julian Taylor, Sebastian Berg, Nathaniel J. Smith, Robert Kern, Matti Picus, Stephan Hoyer, Marten H. van Kerkwijk, Matthew Brett, Allan Haldane, Jaime Fern'andez del R'10, Mark Wiebe, Pearu Peterson, Pierre G'erard-Marchant, Kevin Sheppard, Tyler Reddy, Warren Weckesser, Hameer Abbasi, Christoph Gohlke, and Travis E. Oliphant. Array programming with NumPy. *Nature*, 585(7825):357–362, 2020.